"High-resolution soil moisture mapping by a proximal ground penetrating radar : a numerical, laboratory and field evaluation"

Minet, Julien

Abstract

Soil moisture is an important state variable acting in many environmental, hydrologic and climatic processes. There is thus a pressing scientific demand for revealing the soil moisture dynamics in the biosphere at various temporal and spatial scales. Despite the huge development of remote sensing of soil moisture techniques, there is still a lack of soil moisture measurement techniques available at high spatial resolution (~ m). This thesis aimed to validate and apply advanced proximal ground penetrating radar (GPR) for soil moisture sensing at the field scale. For field acquisition, the GPR system was mounted on a mobile platform that allowed for a fast acquisition rate at high resolution. The impact of shallow soil layering on the GPR backscattered signal was investigated in numerical and laboratory experiments and the best GPR data inversions strategies for dealing with shallow soil layering were determined. Then, coherent two-layered and continuous soil moisture profiles could be...

Référence bibliographique

Minet, Julien. *High-resolution soil moisture mapping by a proximal ground penetrating radar : a numerical, laboratory and field evaluation.* Prom. : Lambot, Sébastien

Université catholique de Louvain
Faculté d'Ingénierie Biologique, Agronomique et Environnementale
Earth and Life Institute - Environmental Sciences

High-resolution soil moisture mapping by a proximal ground penetrating radar

A numerical, laboratory and field evaluation

Julien Minet

Mai 2011

Thèse présentée en vue de l'obtention
du grade de Docteur en Sciences Agronomiques
et Ingénierie Biologique

Promoteur: S. Lambot

Composition du jury:
Président: Pr Jacques Mahillon (UCL, Belgique)
Promoteur: Pr Sébastien Lambot (UCL, Belgique)
Lecteurs: Pr Marnik Vanclooster (UCL, Belgique)
Pr Pierre Defourny (UCL, Belgique)
Pr Niko Verhoest (UGent, Belgique)
Dr Johan A. Huisman (FZJ, Allemagne)
Dr Laurent Pfister (CRP, Luxembourg)

Parce que ça sert à quelque chose
de mesurer l'humidité du sol?

Philippe Navet, 2010

Remerciements

Mes remerciements vont tout d'abord à mon promoteur Sébastien Lambot. J'ai pu profiter de ses encouragements, de son inépuisable optimisme, de son credo "vite fait, bien fait" et de son expérience autant pratique que théorique, autant les pieds dans la terre qu'en chevauchant une onde électromagnétique. Je lui suis reconnaissant de m'avoir fait très vite confiance et de m'avoir permis de participer à de nombreuses conférences.

Je remercie chaleureusement le Professeur Marnik Vanclooster, d'abord d'avoir soumis un si beau projet de recherche, de m'avoir fait nagé dans le monde de l'hydrologie mais aussi de m'avoir invité à des missions répétées au Maroc et en Tunisie et de m'avoir fait partagé autant que possible les arcanes de l'institution UCL et la Recherche scientifique. Merci également aux autres membres de mon Jury, Pierre Defourny, Niko Verhoest, Sander Huisman et Laurent Pfister pour leurs remarques qui m'ont aidé à améliorer ce document, ainsi qu'à tous les co-auteurs de nos papiers, Patrick Bogaert, Géraldine Delaide, Eric Laloy, Evert Slob, Harry Vereecken et Agung Wahyudi.

Je remercie également tous les collègues du GERU de tout âge et toutes origines, tant les administratifs, académiques que scientifiques. Je suis spécialement reconnaissant à Carine Demeyer pour son écoute et son engagement, ainsi qu'à Guido Rentmeesters pour sa patiente distillation de son savoir technique, pré-requis indispensable à tout savoir théorique et à la compréhension du monde. Merci à tous les autres pour les partages de tuyaux, de morceaux de codes, d'idées, d'opinions, de valeurs, de musique, de gîte et couverts, et de bureau.

Je remercie finalement Géraldine, ma famille, amis et colocataires, de vous être intéressés, malgré tout, à l'humidité du sol...

Contents

Remerciements **iii**
Remerciements iii
Contents v

List of Figures **ix**

List of Tables **xvii**

Introduction **1**
Scientific context 1
Objectives 5
Outline of the thesis 6

1 A frequency domain reflectometry technique for soil electrical properties determination **9**
1.1 Outline 9
1.2 Introduction 10
1.3 Objectives 11
1.4 Materials and methods 12
1.4.1 Electromagnetic properties of materials 12
1.4.2 Modeling of the FDR system 12
1.4.3 Model inversion 17
1.4.4 Petrophysical models 17
1.4.5 Laboratory experiments setup 18
1.5 Laboratory experiments results 19
1.5.1 Probe transfer functions determination 19
1.5.2 Inversion of FDR measurements in salt water 21
1.5.3 Determination of the sand water content 25
1.6 Conclusions 27

2 Soil moisture estimation by ground penetrating radar in the presence of thin layers: Numerical and laboratory experiments **31**
2.1 Outline 31
2.2 Introduction 32
2.3 Objectives 33
2.4 Materials and methods 34

- 2.4.1 Theory 34
- 2.4.2 Numerical experiments 35
- 2.4.3 Laboratory experiments 36
- 2.5 Results and discussion 40
  - 2.5.1 Numerical experiments 40
  - 2.5.2 Laboratory experiments 48
- 2.6 Conclusions 57

3 Soil moisture mapping by ground penetrating radar in profile conditions: Numerical and field experiments 59

- 3.1 Outline 59
- 3.2 Introduction 60
- 3.3 Objectives 61
- 3.4 GPR forward and inverse modeling 62
  - 3.4.1 GPR system modeling 62
  - 3.4.2 Inversion of GPR data 62
  - 3.4.3 Multilayered medium models 63
- 3.5 Numerical experiments 65
  - 3.5.1 Model configurations 65
  - 3.5.2 Numerical results 65
- 3.6 GPR Field Measurements 68
  - 3.6.1 Materials and methods 68
  - 3.6.2 Field measurements results 71
  - 3.6.3 Error sources in field acquisition 81
- 3.7 Conclusions 83

4 Validation of ground penetrating radar full-waveform inversion for field scale soil moisture mapping 85

- 4.1 Outline 85
- 4.2 Introduction 86
- 4.3 Objectives 87
- 4.4 Materials and Methods 88
  - 4.4.1 Study site 88
  - 4.4.2 Soil moisture sensing by ground penetrating radar . . . 89
  - 4.4.3 Uncertainties assessment 92
- 4.5 Results 95
  - 4.5.1 Surface soil moisture maps 95
  - 4.5.2 Inversion uncertainties 97
  - 4.5.3 Repetition uncertainties 100
  - 4.5.4 Comparison with soil sampling measurements 100
- 4.6 Discussions 102
  - 4.6.1 Inversion uncertainties 102
  - 4.6.2 Repetition uncertainties 104
  - 4.6.3 Comparison with soil sampling measurements 104
  - 4.6.4 Comparison of the uncertainties 105
- 4.7 Conclusions 106

5 Temporal stability of soil moisture patterns measured by a proximal ground penetrating radar in an agricultural field 109
- 5.1 Outline 109
- 5.2 Introduction 110
- 5.3 Objectives 111
- 5.4 Materials and Methods 112
  - 5.4.1 Study site 112
  - 5.4.2 Soil moisture mapping by ground penetrating radar . . 113
  - 5.4.3 Temporal stability of soil moisture pattern identification 114
- 5.5 Soil moisture patterns 115
  - 5.5.1 Geostatistical analysis 115
  - 5.5.2 Line effect 119
  - 5.5.3 Comparison with soil core sampling measurements . . . 120
- 5.6 Temporal stability of soil moisture patterns 121
  - 5.6.1 Intersection of field-average soil moisture areas 121
  - 5.6.2 Relative difference to field-average 123
  - 5.6.3 Comparison of the two methods 125
  - 5.6.4 Temporal stability of soil moisture from soil core sampling measurements 125
  - 5.6.5 Comparison with previous studies 126
- 5.7 Conclusions 127

6 Effect of high-resolution spatial soil moisture variability on simulated runoff response using a distributed hydrologic model 129
- 6.1 Outline 129
- 6.2 Introduction 130
- 6.3 Objectives 132
- 6.4 Materials and Methods 132
  - 6.4.1 Agricultural fields 132
  - 6.4.2 Sensing of soil moisture by ground penetrating radar . . 133
  - 6.4.3 Antecedent soil moisture scenarios 134
  - 6.4.4 Hydrologic model 138
- 6.5 Results 139
  - 6.5.1 Soil moisture data measured by ground penetrating radar 139
  - 6.5.2 Effect of antecedent soil moisture on hydrographs 142
  - 6.5.3 Evaluation of soil moisture modeling scenarios 148
- 6.6 Discussions 152
  - 6.6.1 Effect of spatial variability of soil moisture on simulated runoff 152
  - 6.6.2 Soil moisture patterns and its relation with topographic wetness index 154
  - 6.6.3 Disaggregation of soil moisture 155
- 6.7 Conclusions 155

Conclusions and Perspectives **157**
Summary 157
Ground penetrating radar limitations and perspectives 160
Perspectives in soil moisture sensing 163

Appendices **165**

Bibliography **167**

Soil moisture maps **183**

Publications and Conferences **191**

List of Figures

1.1 Modeling of the frequency domain reflectometry (FDR) system by a one dimensional multilayered medium: (a) schematic of the measurement system with vector network analyzer (VNA), (b) corresponding representation as a multilayered medium, where S_{11} is the scatter function, R are reflection coefficients, and ε is the dielectric permittivity, σ is the electrical conductivity, and μ is the magnetic permeability at depths d, and (c) probe reflection and transmission coefficients R and T characterizing the FDR probe head. 14

1.2 Frequency domain reflectometry (FDR) probe transfer functions reflection coefficients $R_{C,0}(\omega)$ (a) and $R_{0,C}(\omega)$ (c) and transmission coefficients $T(\omega)$ (b) determined throughout the entire frequency range (f) from 10 MHz to 8 GHz, depicted in amplitude (upper graphs) and phase (lower graphs), for three different number of measurements (three, seven, and 17) used to solve the systems of equations. 20

1.3 Measured, predicted and inverted scatter functions $S_{11}(\omega)$ depicted in the frequency (a) and time domains (b) for water with a salt concentration of 0.154 gL^{-1}. 22

1.4 Measured, predicted and inverted global reflection coefficients $R_{0,N}(\omega)$ depicted in the frequency (a) and time domains (b) for water with a salt concentration of 0.154 gL^{-1}. 23

1.5 Inverted electrical conductivity (σ) at the minimal frequency (10 MHz) from frequency domain reflectometry (FDR) measurements as a function of the measured σ in the 10 different salt water solutions. 25

1.6 Relative dielectric permittivity (ε_r) estimated from time domain reflectometry (TDR) measurements and frequency domain reflectometry (FDR) inversions as a function of the sand water content (θ_v) measured by volumetric sampling. The model of Ledieu *et al.* (1986) was fitted over the TDR and FDR data. . 26

1.7 Frequency-dependent, apparent electrical conductivity (σ) retrieved from frequency domain reflectometry (FDR) inversions for sand media at 10 different water contents (WC) and for demineralized water depicted with theoretical values from the model of Debye (a); enlargement of the electrical conductivity of the sand media (b). 28

2.1 Model configuration used for the numerical experiments and inverse modeling flowchart. 36
2.2 Schematic of the laboratory experimental setup showing the GPR horn antenna above the two-layered sandbox (a) and picture of the experimental setup viewed from the top (b). 38
2.3 Time domain representation (b-scan) of the measured Green's functions for the 50 configurations in the laboratory experiments. Vertical lines delineate the configurations according to the 10 different first layer water content (θ_1). For each θ_1, five different first layer thicknesses were set. 39
2.4 Error on the dielectric permittivity of the first layer $\Delta\varepsilon_1$ for each top layer thickness h_1, with inversions performed with the two-layered model in the frequency domain. Results from the numerical experiments. 41
2.5 Error on the dielectric permittivity of the second layer $\Delta\varepsilon_2$ for each top layer thickness h_1, with inversions performed with the two-layered model in the frequency domain. Results from the numerical experiments. 42
2.6 Generated and inverted Green's functions for a first layer water content of 0.36, a second layer water content of 0 and a first layer thickness of 0.01 m, depicted in frequency (a) and time domain (b). Results from the numerical experiments. 43
2.7 Response surfaces of the objective function logarithm $\log_{10}(\phi)$ in the (a) ε_1-ε_2, (b) ε_1-$\log_{10}(\sigma_1)$, (c) ε_1-h_1, (d) ε_1-$\log_{10}(\sigma_2)$, (e) ε_2-h_1 and (f) h_1-$\log_{10}(\sigma_1)$ parameter planes. These objective functions are plotted for the particular case depicted in Fig. 2.6, i.e., $h_1 = 0.01$ m, $\theta_1 = 0.36$, and $\theta_2 = 0$. True parameter values are represented by the white star marker. Results from the numerical experiments. 44
2.8 Response surfaces of the objective function logarithm $\log_{10}(\phi)$ in the (a) ε_1-ε_2, (b) ε_1-$\log_{10}(\sigma_1)$, (c) ε_1-h_1, (d) ε_1-$\log_{10}(\sigma_2)$, (e) ε_2-h_1 and (f) h_1-$\log_{10}(\sigma_1)$ parameter planes. These objective functions are plotted for the case where $h_1 = 0.08$ m, $\theta_1 = 0.36$, and $\theta_2 = 0$. True parameter values are represented by the white star marker. Results from the numerical experiments. 45

2.9 Error distribution of the dielectric permittivity of the top layer, as a function of the contrast in water content between the layers. The box extent shows interquartile range (i.e., the range between the first and the third quartiles), while the median of the error distribution is represented by the horizontal line that cuts the box. Whiskers length is 1.5 times the vertical length of the boxes. Outlier error values are displayed as crosses outside of the whiskers. Comparison between inversions performed with the two-layered (a) and the one-layered (b) models in the frequency domain. Results from the numerical experiments. 46

2.10 Soil surface relative dielectric permittivity estimated from GPR data inversion ($\varepsilon_{1,GPR}$) as a function of soil volumetric water content θ_v. Dielectric permittivities are depicted with different symbols according to the top layer thickness. The model of Ledieu *et al.* (1986) is fitted on the observed data (solid line). The dotted vertical line at value $\theta_v = 0.064$ indicates the soil water content of the second layer (constant for all configurations). (a) Two-layered inversion in the frequency domain. (b) One-layered inversion in the frequency domain. (c) Two-layered inversion in the time domain. (d) One-layered inversion in the time domain. (e) Two-layered inversion in the time domain assuming no PEC as lower-halfspace. (f) Inversion in the time domain by focusing on the surface reflection only (Lambot *et al.*, 2006b). 49

2.11 Comparison between first layer thickness measured in the sandbox and derived from GPR signal inversion using the TIME 2L* scenario. 51

2.12 Response surfaces of the logarithm of the objective function in the ε_1-ε_2 (a), ε_1-σ_1 (b) and ε_1-h_1 (c) parameter planes for a GPR laboratory measurements inversion (FREQ 2L scenario) where $\theta_v = 0.115$ and $h_1 = 8$ cm. The unique value retrieved by the GMCS-NMS inversion is depicted with a star. Points of the parameter space sampled by the DREAM algorithm are projected (in red) over the response surfaces. Histograms of the posterior distributions are drawn along the axis of the parameters. Confidence intervals using a linear approximation of the slope of the objective functions are drawn in red rectangles. 52

2.13 Error between the ground measurements and GPR-derived soil surface water content as a function of the contrast between the two layers for TIME L-M inversion scenario. Coefficient of determination r^2 is depicted in the upper-left corner. 54

2.14 Absolute difference in the top-layer dielectric permittivities between one- and two-layered models in frequency domain as a function of the top-layer volumetric water content. Dielectric permittivities are depicted with different symbols according to the first-layer widths. The dotted vertical line at value $\theta_v = 0.064$ indicates the soil water content of the second layer. . . . 55

2.15 Measured and modeled Green's functions on the frequency bandwidth from 0.8 to 2.6 GHz, depicted (a) in the frequency and (b) time domain. 56
2.16 Error boxplots between the GPR-derived and the sampled volumetric soil water content of the top layer, for inversions with different frequency bandwidths. The box extent shows interquartile range (i.e., the range between the first and the third quartiles), while the median of the error distribution is represented by the horizontal line that cuts the box. Whiskers length is 1.5 times the vertical length of the boxes. Outlier error values are displayed as crosses outside of the whiskers. 57

3.1 Flowchart of the inversion of the Green's function $\mathbf{G}^{\uparrow}_{\mathbf{xx}}$ with the three different multilayered soil moisture models, that are, the one-layered, two-layered and profile models. 63
3.2 Numerically generated soil moisture profiles with the van Genuchten model (dotted lines) and two-layered profile (plain lines) retrieved by inversion using the two-layered model, for four different van Genuchten parametrizations ($n = 14$ and $\alpha = 16$, 20, 24 and 28 m^{-1}). Results from the numerical experiments. . . . 66
3.3 Comparison between the first layer thickness h_1 retrieved by inversion using the two-layered model and the position of the inflexion point z_i of the generated soil moisture profile. Results from the numerical experiments. 67
3.4 Study site for the GPR acquisitions near Walhain, Belgium. The 3741 GPR measurements are depicted over the field. 68
3.5 All-terrain vehicle holding the GPR system constituted of a horn antenna linked to a vector network analyzer, the DGPS device and the PC. Picture taken on the 23^{th} of March 2009 in a barley field near Walhain, Belgium. 69
3.6 Soil moisture map retrieved by one-layered model inversions from the field acquisition near Walhain on the 23^{th} of March 2009. Size of the symbols are inversely related to their uncertainty by the weight function, which is, $Weight = max(RMSE) - RMSE$. 72
3.7 Variogram for soil moisture computed on the whole field with a class distance from 0 to 200 m by a step of 5 m. Variogram along and perpendicular to the sampling line is denoted by circle and plus symbols, respectively. Exponential models are fitted for both variograms. The sampling variance is indicated by the horizontal dashed line. 73
3.8 Soil moisture maps from two-layered model inversions for the first layer (a) and the second layer (b) and from the profile model inversions for the top (c) and the bottom (d) of the profile for the 300 points outlined with the red polygon in Fig. 3.6. 74

3.9 Variograms for soil moisture computed on the 300 selected points for the first layer (a) and the second layer (b) from the two-layered model inversions and for the top (c) and the bottom (d) from the profile model inversions. Exponential models are fitted for all variograms. The total variance is indicated by the horizontal dashed line. 77
3.10 Soil moisture profiles retrieved from the two-layered inversion and the model inversion and unique soil moisture value retrieved from the one-layered model inversion for two GPR measured points ((a) and (b)). 78
3.11 Measured and modeled Green's functions in the frequency domain depicted in amplitude (a) and phase (b) and in time domain for the one-layered model (c) and for the two others models (d). The one-layered modeled Green's function is defined on the frequency range from 200 to 800 MHz. Two-layered and profile modeled Green's functions are defined on the frequency range from 200 to 1600 MHz. 79

4.1 Study site of Burnia near Louvain-la-Neuve, Belgium. The GPR acquisition was performed along 12 parallel lines. Soil core sampling was performed in 20 locations. 88
4.2 All-terrain vehicle holding the GPR system constituted of a horn antenna linked to a vector network analyzer, the DGPS device, an EM38 sensor and the PC. Picture taken on the 15^{th} of March 2010 in a Burnia near Louvain-la-Neuve, Belgium. 89
4.3 Measured and modeled Green's function depicted in the frequency domain in amplitude and phase (a) and in time domain (b). The time-window corresponding to the surface reflection is delineated in (b). 91
4.4 Soil moisture maps for the three acquisitions. Topographic contour lines with an interdistance of one meter are depicted in grey lines. The black arrows indicate the location and the direction of the slope of the main thalweg in the field. 95
4.5 Variogram for soil moisture computed along the acquisition lines for the three repetitions. An exponential model is fitted on the variogram estimates. The sampling variance is indicated by the horizontal dashed line. 96
4.6 Maps of the interpolated modeling error $\phi(\mathbf{b}^*)$. Topographic contour lines with an interdistance of one meter are depicted in grey lines. 97
4.7 Observed sensitivity of the electromagnetic model, expressed by the sum of the elements of the Jacobian matrix for the permittivity, as a function of inverted soil moisture. 98
4.8 Maps of the soil moisture uncertainty $\sigma_{\theta,GPR}$ [$\mathrm{m}^3\mathrm{m}^{-3}$] computed using Eqs (4.3) to (4.6). Topographic contour lines with an interdistance of one meter are depicted in grey lines. 99

4.9 Maps of the repetition uncertainties for the three acquisitions. The repetition uncertainty is computed as the difference between the interpolated values of each repetitions. The black lines delineated the zones where the two repetitions of the acquisition resulted in different soil moisture estimates, at 95 % of confidence. 101
4.10 Comparison between interpolated GPR-derived soil dielectric permittivity ε_{GPR} and volumetric sampling soil moisture θ_V. . . 102

5.1 Study site of Burnia near Louvain-la-Neuve, Belgium. The slope is expressed in percents. 112
5.2 Air temperature and precipitation depicted from the 04 March to 10 April 2010. 113
5.3 GPR-derived soil moisture point-measurements depicted with the same color scale for the five GPR surveys. 116
5.4 Variograms for soil moisture computed for the five field acquisitions along ('o') and perpendicular ('+') to the acquisition lines. Exponential models are fitted for the parallel variograms. The total variance is indicated by the horizontal dashed line. 118
5.5 Comparison between interpolated GPR-derived soil dielectric permittivity ε_{GPR} and volumetric sampling soil moisture θ_V for all dates. 120
5.6 Soil moisture maps for the five dates. The locations where soil moisture is equal to the field-average within a tolerance of ± 0.02 m^3m^{-3} are outlined by black lines. The intersection of these zones between the five dates are outlined by red lines. . . 122
5.7 Temporal stability of the field-average soil moisture computed by indicators based on the relative difference of soil moisture to the field-average. From top to bottom, the mean of the relative difference $\overline{\delta}_i$, the standard deviation of the relative difference $\sigma(\delta)_i$ and the RMSE of these differences RMSE_{δ_i} are presented. The time-stable zones determined by the first method are outlined by black lines. 123
5.8 Rank ordered mean relative difference of GPR-derived soil moisture to the field-average $\overline{\delta}_i$ (dashed line) depicted with standard deviation $\sigma(\delta)_i$ (in gray). The RMSE of the relative differences RMSE_{δ_i} is presented in a plain line. Results from GPR measurements. 125
5.9 Rank ordered mean relative difference of volumetric soil moisture to the field-average $\overline{\delta}_i$ (dashed line) depicted with standard deviation $\sigma(\delta)_i$ (in gray) for the 20 soil core sampling locations. The RMSE of the relative differences RMSE_{δ_i} is presented in a plain line. Results from soil core sampling measurements. The four sampling points that are within the time-stable area are depicted with a thick green errorbar. 126

6.1 Maps of soil moisture point-values retrieved by GPR inversions from the field acquisition in Marbaix, 15 April 2009. Contour lines with an interdistance of one meter are depicted in black lines. The outlet of the field is indicated by the black arrow. Projected coordinate system: Belgian Lambert 1972. 135
6.2 Antecedent soil moisture maps for Marbaix, 15 April 2009, used as an input in the hydrologic model with measured grided values (a), measured values rearranged according the TWI (b), measured values inversely rearranged according the TWI (c), randomly permuted values (d), simulated values using a variogram (e) and connected simulated values (f). The outlet location and direction are indicated with an arrow. 136
6.3 Variogram of soil moisture computed for the field campaign in Marbaix, 15 April 2009 with a class distance from 0 to 150 m by a step of 5 m. A variogram using an exponential model is fitted on the data. The total variance of soil moisture is depicted with the dashed line. 140
6.4 Hydrographs from hydrologic simulations using the antecedent soil moisture maps from all scenarios for 4 field campaigns: Walhain - 07/04/2008 (a), Marbaix - 15/04/2009 (b), Walsdorf - 21/07/2009 (c) and Burnia - 06/04/2010 (d). For stochastic soil moisture scenarios, i.e., *random*, *variogram*, *connected*, the average hydrographs on the 1000 realizations are depicted. The rainfall is depicted by the bars of the second Y-axis. 142
6.5 Relative difference between *structured* and $structured_{inv}$ runoff volume as a function of the mean soil moisture in the field. . . 145
6.6 Hydrographs from hydrologic simulation using the antecedent soil moisture maps from scenarios 1 to 5 for the field campaign in Marbaix, 15 April 2009. The average *random* hydrograph is depicted as a dotted line on top of the 1000 hydrographs from the random antecedent soil moisture maps. 146
6.7 Hydrographs from hydrologic simulation using the antecedent soil moisture maps from scenarios 1 to 4 and 6 for the field campaign in Marbaix, 15 April 2009. The average *variogram* hydrograph is depicted in a dashed line on top of the 1000 hydrographs from the simulated antecedent soil moisture maps. . 147
6.8 Hydrographs from hydrologic simulation using the antecedent soil moisture maps from scenarios 1 to 4 and 7 for the field campaign in Marbaix, 15 April 2009. The average *connected* hydrograph is depicted in a dashed-dotted line on top of the 1000 hydrographs from the simulated antecedent soil moisture maps. 147
6.9 Nash-Sutcliffe efficiency coefficients of the *structured* scenario with respect to the $reference$ scenario ($NSE_{structured}$) as a function of the correlation between measured soil moisture and the TWI ($r_{TWI,\theta}$). 150

List of Tables

1.1 Root mean square error RMSE of the fits according to the model of Ledieu *et al.* (1986) and coefficient of determination r^2 between the square root of the relative dielectric permittivity $\sqrt{\varepsilon_r}$ and the volumetric water content θ_v for time domain reflectometry (TDR) and frequency domain reflectometry (FDR) measurements. 27

2.1 Number of convergent configurations for time and frequency domains and for the one-layered and the two-layered inversion models in the numerical experiments. 48
2.2 Statistics on the comparison between ground measurements of volumetric water content and GPR-measured dielectric permittivities. 50

3.1 Summary of the inversions of GPR field data for the three models. 70
3.2 Statistics of GPR-derived soil moisture from the one-, two-layered and profile inversions for the 300 selected points. The mean (μ) and the standard deviation (σ) of soil moisture and three variogram parameters (Nugget effect, Sill and Range) are presented. 76

4.1 Statistics of GPR-derived volumetric soil moisture [$\mathrm{m^3m^{-3}}$] (non-interpolated values) 96
4.2 Summary of the soil moisture uncertainties [$\mathrm{m^3m^{-3}}$] determined by the different methods 105

5.1 Presentation of the five GPR acquisitions 114
5.2 Statistics of GPR-derived volumetric soil moisture expressed in [$\mathrm{m^3m^{-3}}$] and variograms parameters (Nugget [$\mathrm{m^3m^{-3}}$]^2, Sill [$\mathrm{m^3m^{-3}}$]^2 and Range [m]) 117
5.3 Soil moisture [$\mathrm{m^3m^{-3}}$] statistics from soil core sampling and RMSE of the petrophysical relationships 121

6.1 Description of the agricultural fields and resolutions used in hydrologic simulations 133

6.2 GPR soil moisture ([m^{3}m^{-3}]) acquisitions. The number of measured points, the duration of the acquisition, the mean (μ_θ) and standard deviation (σ_θ) of soil moisture, variogram parameters (Nugget effect [m^{3}m^{-3}]^2, Sill [m^{3}m^{-3}]^2 and Range), the ratio between the nugget effect and the sill (Nug./Sill), the coefficient of correlation between the TWI and soil moisture ($r_{TWI,\theta}$) and the resolution for hydrologic simulations are presented. 141
6.3 Runoff peak Q_{max} and total runoff volume V for each antecedent soil moisture scenario for the 10 field campaigns. For the stochastic scenarios, the average Q_{max} and V were computed and the standard deviations are depicted in brackets. Maximum and minimum values for each field campaign are highlighted in bold and italic, respectively. 144
6.4 Nash-Sutcliffe efficiency coefficients of the different scenarios of antecedent soil moisture maps compared to the $reference$ scenario for the 10 field campaigns. The mean and the standard deviation of normalized Nash-Sutcliffe coefficients were computed for the 10 field campaigns. Maximum and minimum values for each field campaign are highlighted in bold and italic, respectively. 149
6.5 Nash-Sutcliffe efficiency coefficients of the different scenarios of antecedent soil moisture maps compared to the $reference$ scenario for Marbaix, 15 April 2010 for varying grid sizes. The coefficients of correlation between the TWI and soil moisture ($r_{TWI,\theta}$) are presented in the second column. 151

Introduction

Scientific context

Surface soil moisture, i.e., the water held in the first centimeters of soils, plays an important role in many environmental, agricultural, hydrologic and climatic processes. In hydrology, soil moisture governs the partitioning of rainfall into runoff and infiltration, and neglecting its variability largely impacts on the prediction of solute leaching (e.g., Zhang *et al.*, 1996; Wendroth *et al.*, 1999), erosion (e.g., Fitzjohn *et al.*, 1998), runoff (e.g., Merz and Bardossy, 1998; Zehe *et al.*, 2005) and evaporation (e.g., Yang *et al.*, 2007). In agriculture and irrigation applications, plant growth and seed germination are largely controlled by soil water availability (e.g., Borgogno *et al.*, 2010), particularly when saline stress is encountered. Knowing the spatiotemporal distribution of soil moisture and soil water storage capacity is therefore an important asset for the optimization of irrigation under variable environment. Soil moisture also exerts a strong control on soil biogeochemistry (Robinson *et al.*, 2008b), especially with respect to the cycling of nitrogen and carbon from soil to the hydro-, bio- and atmosphere (Porporato *et al.*, 2003; D'Odorico *et al.*, 2003; Herbst *et al.*, 2009). In climatology and meteorology, the importance of the soil moisture in the water balance and land surface energy budget has been widely acknowledged (Seneviratne *et al.*, 2010), as it controls the evaporation and the sensible heat fluxes between soil and atmosphere. In digital soil mapping applications, transitory soil moisture measurements at the field scale may actually provide information about (nearly) time-invariant soil attributes as soil hydraulic properties, which are dependent on soil structure and texture. Facing environmental contamination and increasing scarcity of resources, knowing the spatial variability of soil properties at the field scale with a high resolution is considerably appealing for designing new optimal agricultural practices, in the framework of precision agriculture (Adamchuk *et al.*, 2004).

Soil moisture is known to vary drastically in time and space across many scales, especially in highly heterogeneous environments in terms of soil type, vegetation and topography. Hence, soil moisture appears sometimes as an ephemeral, erratic, imperceptible and capricious variable. When it is measured by an indirect method, over an uncertain extent and penetration depth, and in a complex soil environment made not only of soil particles, air and water but also roots and others biological features, it is worth claiming that the meaning of what is measured as "soil moisture" is actually ambiguous.

Determining temporal and spatial soil moisture variability is therefore essential for many scientific issues and applications from the field to the global scale. In that respect, a large number of soil moisture sensing techniques were used and developed in the last 50 years (Evett and Parkin, 2005; Robinson *et al.*, 2008a,b; Vereecken *et al.*, 2008). The reference and the only direct soil moisture measurement method is the gravimetric method, which consists in weighting a soil sample after and before oven-drying the sample at 105°C. The difference between the humid and dry weights gives the amount of soil water that was present in the sample. If the soil sample volume is known, the volumetric soil water content (m^3 of water m^{-3} of soil) can be determined, in addition to the gravimetric soil water content (g of water g^{-1} of soil).

In the field of hydrogeophysics, numerous indirect methods for soil moisture sensing exist and rely on the measurement of a physical variable that is a surrogate for soil moisture. Most of these methods are based on the measurement of the soil response when it is exposed under electric current or electromagnetic field, which is dependant on the soil electromagnetic properties. As the relative dielectric permittivity of water overwhelms the one of the other soil components, the soil electromagnetic response is principally determined by its water content. Two main categories of soil moisture measurement techniques are often distinguished: contact-based (or invasive) and contact-free methods (Vereecken *et al.*, 2008). The contact-based methods require direct contact with the soil medium and include time domain reflectometry methods (TDR) (Topp *et al.*, 1980; Robinson *et al.*, 2003), capacitance sensors (e.g., Bogena *et al.*, 2007), electrical resistivity tomography (ERT) (e.g., Michot *et al.*, 2003), neutron probes (e.g., Hupet and Vanclooster, 2002), heat pulse sensors (Campbell *et al.*, 1991) and fiber optics sensors (e.g., Garrido *et al.*, 1999). Recently, wireless sensor networks using clusters of invasive sensors were deployed, offering the potentiality of measuring soil moisture over large extent with high temporal resolution (Bogena *et al.*, 2010).

Among the contact-free or non-invasive methods, we may distinguish between spaceborne or airborne remote sensing and proximal (or ground-based) sensing methods. There has been a huge development in the recent years in spaceborne remote sensing instruments and platforms for soil moisture. Remote sensing of soil moisture methods include passive (radiometers, >5 km of resolution) and active (scatterometer and synthetic aperture radar, 3-30 m of resolution) microwave methods that operate at various spatial and temporal resolutions (Wigneron *et al.*, 2003; Wagner *et al.*, 2007). Probably the greatest asset of remote sensing methods is that they can cover large areas with a large temporal resolution. For instance, the Soil Moisture and Ocean Salinity (SMOS) mission launched by the European Space Agency in November 2009 intents to provide global soil moisture estimates at 50 km of spatial resolution and a 3 days revisiting time (ESA, 2002). However, remote sensing methods still suffer from several limitations. Measurements capabilities are limited over dense vegetation cover and by the scattering effect of surface soil roughness (Verhoest *et al.*, 2008) because of the relatively high frequencies at which these sensors usually operate. An important drawback is the shallow penetration depth of the remote sensing instruments (on the order of the cm), while a deeper characterization of soil moisture is desirable in many applications (Capehart and Carlson, 1997; Vereecken *et al.*, 2008). Finally, the large support scale of remote sensing technique hides the within-pixel soil moisture variability, which is generally resulting in a poor agreement with small-support scale calibrating measurements (e.g., Ceballos *et al.*, 2005). The difference in support scales between large-scale remote sensing methods and small-scale invasive sensors may indeed reach several orders of magnitude, therefore making these two methods hardly comparable.

Proximal soil moisture sensing methods, that are ground-based but non-invasive, may bridge the scale gap that remains in soil moisture sensing techniques, making possible the characterization of soil moisture at an intermediate scale between remote sensing and invasive sensors. Proximal soil moisture sensing includes ground penetrating radar (GPR), electromagnetic induction sensors (EMI) (e.g., Martinez *et al.*, 2010) and ground-based radiometers (e.g., Jonard *et al.*, 2010). Proximal soil moisture sensing can be seen as the counterpart of the spaceborne remote sensing but operating at ground. While GPR and radiometers are mostly sensitive to soil moisture, it is worth mentioning that EMI sensors are sensitive not only to soil moisture, but also to soil salinity, clay and organic matter contents. GPR for soil moisture sensing is based on the propagation of an electromagnetic wave into the soil, which is mainly governed by the soil water content. A review about recent GPR developments can be found in Slob *et al.* (2010) while a complete review of GPR applications for soil moisture sensing was given in Huisman *et al.* (2003). Several techniques were developed to infer soil moisture from GPR surface measurements:

The most commonly used surface GPR approach for soil moisture sensing is based on the analysis of the ground wave propagation velocity (Huisman *et al.*, 2002a; Grote *et al.*, 2003; Galagedara *et al.*, 2005; Lunt *et al.*, 2005; Grote *et al.*, 2010). The ground wave is the signal that travels directly from the emitting to the receiving antenna through the soil surface. Generally, three different acquisition types are used for acquiring the ground wave (Huisman *et al.*, 2003), which are: (1) wide angle reflection and refraction (WARR), (2) common mid point (CMP), and (3) fixed offset (FO) methods. The two first acquisition types are multi-offset acquisitions, namely, they consist in making several measurements over the same target by increasing the offset between emitter and receiver antennas, while a single offset is used in the fixed offset method. The ground wave method has proven its effectiveness and its accuracy in relatively simple soil conditions. However, the technique presents a number of drawbacks, including the following: 1) the required contact between the antennas and the soil; 2) the identification of the ground wave; which may be ambiguous or even impossible in some conditions; 3) the presence of ambiguous guided waves when near-surface layering is present (van der Kruk, 2006; Strobbia and Cassiani, 2007); and 4) the limited adequacy of the used straight-ray approximation for modeling electromagnetic wave propagation (Ernst *et al.*, 2007).

The second approach is the surface reflection coefficient method, which uses off-ground radar configurations (Chanzy *et al.*, 1996; Redman *et al.*, 2002; Serbin and Or, 2003, 2004). The soil surface dielectric permittivity (and correlated soil moisture) is derived from the Fresnel reflection coefficient, which is determined from the ratio between the amplitude of the reflection at the soil surface and the one obtained for a calibrating perfect electric conductor. However, this method still remains mostly unused nowadays for real-time mapping applications, mainly due to the requirement for such calibration (Lambot *et al.*, 2006b).

Recently, some authors proposed innovative soil moisture retrieval approaches using the same GPR sensors. In that respect, van der Kruk (2006) and van der Kruk *et al.* (2010) developed an inversion method of dispersed waveforms trapped into a surface waveguide (i.e., when soil is layered by freezing, thawing or by a wetting front) for retrieving its dielectric permittivity and thickness. Oden *et al.* (2008) used a catalog of finite-difference time-domain (FDTD) simulations of early-time waveforms received by the GPR system for various model parameters that is to be compared with received waveforms. Recently, Benedetto (2010) used a Rayleigh scattering based method for directly determining soil moisture, without the need of a petrophysical relationship and calibration of the GPR system.

While they have shown in general a relatively good accuracy in soil moisture sensing compared to spaceborne platforms, current GPR methods mainly suffer from the cumbersomeness of their application in field conditions and the resulting limited extent they can cover. For instance, a high resolution (∼dm) three-dimensional imaging of soil moisture can be achieved using borehole GPR (Binley *et al.*, 2001, 2002; Looms *et al.*, 2008), but this method necessitates the drilling of boreholes in the soil, that hampers its use for characterizing large areas with a high resolution. Using the ground wave method, multi-offset acquisitions (i.e., CMP and WARR acquisitions) might be necessary to correctly identify the ground wave. For a single soil moisture measurement, multiple GPR data acquisitions are then necessary, which is too time-consuming to perform mapping of large areas. Although fixed offset methods that uses single-offset configuration were developed (e.g., Steelman and Endres, 2010), the resulting accuracy might be lower compared to multi-offset measurements and the effectiveness in high-resolution mapping is still limited by the required contact of the antenna with soil.

The off-ground GPR system developed by Lambot *et al.* (2004b, 2006b) can be seen as an advanced surface reflection method and has shown particularly promising potentialities for soil moisture sensing and mapping. The use of an off-ground configuration is particularly suited for rapid soil moisture sensing in field conditions, as no contact with soil is required. The method is based on an accurate modeling of the GPR system by a three-dimensional solution of Maxwell's equations for wave propagation in multi-layered media and by an antenna calibration using frequency-dependent transfer functions including antenna-soil interactions. Soil dielectric permittivity and correlated soil moisture are retrieved by full-waveform inversion of the GPR data. Full-waveform inversion of ultra-wideband GPR data (i.e., acquired in a large frequency bandwidth) permits to maximize information retrieval capabilities. Low frequency antenna permits to avoid surface roughness scattering and vegetation attenuation. Although this GPR method appeared highly accurate in laboratory experiments, its effectiveness in field conditions, especially for real-time mapping, has to be demonstrated.

Objectives

This PhD research was performed in the framework of the HYDRASENS research project. This project aims at exploring new strategies to integrate radar remote sensing, hydrologic, and hydraulic modeling for water management purposes through data assimilation. In that context, we developed a GPR approach for high-resolution soil moisture mapping at the field scale.

The first main objective of this thesis is to test, validate and apply the off-ground GPR system developed by Lambot *et al.* (2004b, 2006b) for soil moisture sensing and mapping in field conditions. We aim at developing an operational GPR solution for real-time mapping of surface soil moisture in nearly-bare agricultural fields at high resolution over large extents (several ha). The applicability and reliability of the method is evaluated under usual and critical conditions through numerical, laboratory and field experiments. This overall goal was distributed in several specific objectives:

- to extend and validate the electromagnetic modeling approach to a frequency domain reflectometry application, i.e., on a TDR probe, for local soil moisture determination;
- to investigate by numerical experiments the well-posedness of the GPR inversion and to compare different inversion strategies to deal with shallow soil moisture layering and vertical profile;
- to test by laboratory experiments the reliability of the GPR method for soil moisture determination in the presence of shallow soil layering;
- to test in field conditions the capability of the GPR method to retrieve layered or continuously-varying vertical profiles of soil moisture;
- to comprehensively validate the GPR method and quantify the soil moisture measurements uncertainties by independent uncertainty assessment methods in field conditions, including the determination of inversion uncertainties, comparison with ground-truth measurements and repetitions of the acquisition.

Using the soil moisture maps measured by GPR, the second main objective is to study the spatiotemporal variability of soil moisture at the field scale and its implications in hydrological applications. The GPR method for soil moisture mapping developed in the first part of this thesis may bring new insights about the understanding of surface soil moisture dynamics and its implication in surface hydrology. In particular, the specific objectives are as follows:

- to study the spatiotemporal soil moisture patterns in a 2.5 ha agricultural field;
- to study the temporal stability of soil moisture patterns for determining time-stable areas;
- to investigate the effect of different measured soil moisture pattern organizations on simulated runoff response using a distributed hydrologic model;
- to determine which soil moisture pattern organization could be used for high resolution soil moisture modeling at the field scale.

Outline of the thesis

Chapter 1 starts with the development of a new frequency domain reflectometry application based on the electromagnetic modeling and calibration approaches used in this thesis for improving the determination of the soil electrical properties. A general description of electromagnetic wave propagation modeling in multi-layered media that is used in other parts of the thesis is presented in this chapter.

Chapter 2 deals with the impact of shallow soil layering on the soil moisture characterization by GPR through numerical and laboratory experiments. GPR data may be affected by interferences in the presence of shallow layering, which may be widely encountered in the environment under rapid soil wetting or drying. In chapter 3, we extend the issues raised in chapter 2 to real complex soil profile conditions in a field application. The purpose is to investigate the retrieval of vertical profile soil moisture information by continuously-varying soil moisture profile and two-layered model configurations in field conditions. The GPR method for soil moisture sensing and mapping in field conditions is then comprehensively validated in chapter 4, with different soil moisture uncertainties assessment methods. The uncertainties in surface soil moisture retrieved from surface reflection GPR data inversion are quantified and the reliability of the technique in field conditions is assessed.

Chapter 5 shows an application of the GPR technique for investigating high-resolution spatiotemporal patterns and their temporal stability in an agricultural field. In chapter 6, we use numerous soil moisture surveys by GPR to analyze the effect of antecedent soil moisture variability on the runoff response using a distributed hydrologic model. In these two last chapters, the high spatial resolution of the soil moisture measurements by GPR provides new insights about the investigation of soil moisture spatial variability at the field scale and its impacts in hydrologic modeling. Finally, a summary of the main findings of this thesis and perspectives for future researches in GPR development and soil moisture sensing are drawn in the conclusion of the thesis.

The organization of this thesis is based on articles published or submitted to international peer-reviewed journals (cf. Publications and Conferences). Redundancies were avoided, although the different chapters can still be read independently.

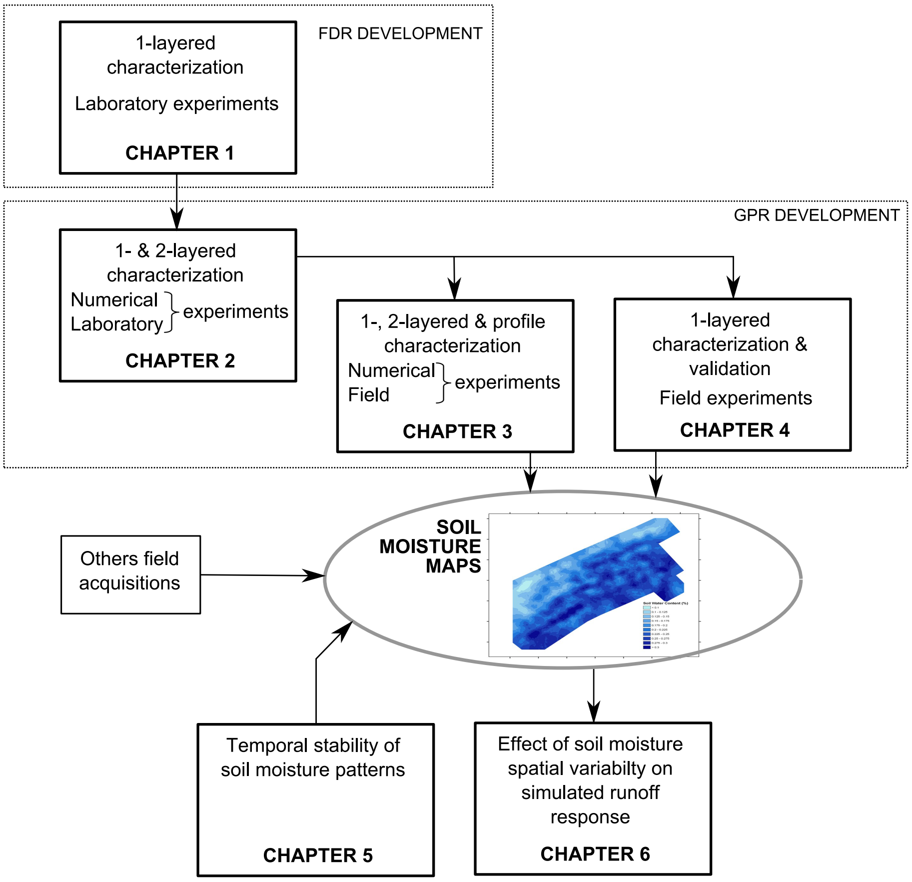
FDR DEVELOPMENT
1-layered characterization
Laboratory experiments
CHAPTER 1
GPR DEVELOPMENT
1- & 2-layered characterization
Numerical
Laboratory
experiments
CHAPTER 2
1-, 2-layered & profile characterization
Numerical
Field
experiments
CHAPTER 3
1-layered characterization & validation
Field experiments
CHAPTER 4
Others field acquisitions
SOIL MOISTURE MAPS
Temporal stability of soil moisture patterns
CHAPTER 5
Effect of soil moisture spatial variabilty on simulated runoff response
CHAPTER 6

Chapter 1

A frequency domain reflectometry technique for soil electrical properties determination*

1.1 Outline

We present a generalized frequency domain reflectometry (FDR) technique for soil electrical properties determination, which is based on an electromagnetic model decoupling the cable and probe head from the ground using frequency-dependent reflection and transmission transfer functions. The FDR model represents an exact solution of Maxwell's equations for wave propagation in one-dimensional multilayered media. The benefit of the decoupling is that the FDR probe can be fully described by its characteristic transfer functions, which are determined using only a few measurements. The soil properties are retrieved after removing the probe effects from the raw FDR data by inverting iteratively a global reflection coefficient. The proposed method was validated in laboratory conditions for measurements in water with different salt concentrations and sand with different water contents. For salt water, inversions of the data led to dielectric permittivity and electrical conductivity values very close to the expected theoretical or measured values. In the frequency range for which the probe is efficient, a good agreement was obtained between measured, inverted and theoretically-predicted signals. For sand, results were consistent with the different water contents and also in close agreement with traditional time domain reflectometry measurements. The proposed method offers great

---

*This chapter is adapted from:
Minet, J.; Lambot, S.; Delaide, G.; Huisman, J. A.; Vereecken, H. & Vanclooster, M. A generalized frequency domain reflectometry forward and inverse modeling technique for soil electrical properties determination, in *Vadose Zone Journal*, **2010**, 9(4), 1063-1072.

promise for accurate soil electrical characterization as it inherently permits to maximize the information that can be retrieved from the FDR data.

1.2 Introduction

Time domain reflectometry (TDR) has become a standard in geophysical applications for measuring the soil dielectric permittivity (and correlated soil moisture) and electrical conductivity. Since TDR for soil characterization was first developed by Topp *et al.* (1980, 2003) in the early 1980s, many applications and enhancements have been reported regarding (1) the development of the physical measurement system, e.g., in the design of the TDR probe (Robinson *et al.*, 2003) and by the multiplexing of several probes (Heimovaara and Bouten, 1990), and (2) the interpretation and modeling of the TDR waveform (Heimovaara, 1993; Noborio, 2001; Robinson *et al.*, 2003). The calibration of petrophysical relationships that link the dielectric permittivity and the soil water content has also received a specific attention (Topp *et al.*, 1980; Ledieu *et al.*, 1986; Sihvola and Kong, 1988; Yu *et al.*, 1999).

Traditionally, dielectric permittivity is derived from the TDR signal by the analysis of the travel time of the electromagnetic wave along the transmission line. Chung and Lin (2009) showed that different dielectric permittivity estimations can be obtained by comparing the methods that have been proposed to determine the reflection arrivals in the travel time analysis (e.g., the tangent method, the derivative method). Indeed, Hook and Livingston (1996) demonstrated that a dominant source of error in estimating soil water content using TDR was the uncertainty in determining the propagation travel time. High soil electrical conductivity in clay and/or saline soils can also significantly affect the propagation of the waveform and the determination of the travel time, leading to erroneous estimation of the real part of the dielectric permittivity if not taken into account (Pepin *et al.*, 1995; Sun *et al.*, 2000).

Soil electrical conductivity is usually retrieved from the TDR signal by depicting the reflection coefficient at long times and applying the Giese and Tiemann (1975) method. However, several authors have pointed out the limitations of this method (Lin *et al.*, 2008; Huisman *et al.*, 2008), as well as the dielectric permittivity determination methods above-cited. In addition, these methods are not suited for determining the frequency dependence of the soil electrical properties.

To overcome these limitations, more advanced forward and inverse modeling methods, usually performed in the frequency domain, have shown promising perspectives (Heimovaara, 1994; Lin, 2003; Schaap *et al.*, 2003; Huisman *et al.*, 2004; Heimovaara *et al.*, 2004; Mattei *et al.*, 2005; Shuai *et al.*, 2009). In addition, operating in the frequency domain permits to increase the bandwidth and, thereby, increases the information content in the data. As a result, frequency domain analysis offers more potential than the common time domain and travel time analysis methods for the determination of soil water content (Lin, 2003). In these previous studies, the FDR system was modeled using recursive scatter functions describing the propagation of the electromagnetic signal, accounting for transmission and reflection phenomena occurring at each change of impedance of the FDR system. Nevertheless, modeling of the FDR system could require numerous system calibrations with a high number of parameters to be determined (e.g., 40 as reported by Heimovaara *et al.* (2004)) and the necessity of disconnecting the elements of the FDR system, as stated by Shuai *et al.* (2009). In addition, in these previous studies, assumptions about the cable and probe impedances have to be made for modeling the FDR system.

Electromagnetic wave generation can be performed using other wave generator devices than the commonly used and commercialized cable testers. In particular, FDR systems that have been conceived with vector network analyzer (VNA) (Campbell, 1990; West *et al.*, 2003; Huisman *et al.*, 2004; Shuai *et al.*, 2009) have shown an unprecedented precision and control on the input generated signal as well as on the reception and the analysis of the returned waveform. In addition, the calibration of a VNA is well-defined, constituting an international standard, and thereby ensures repeatability of the measurements. Finally, unified models and techniques have been developed for soil electromagnetic characterization based on the same VNA technology but using different sensors (e.g., ground penetrating radar (GPR) (Lambot *et al.*, 2004b), electromagnetic induction (EMI) (Moghadas *et al.*, 2010)) operating with different frequency ranges and measuring at different scales.

1.3 Objectives

In this chapter, the electromagnetic modeling approach presented by Lambot *et al.* (2004b) for GPR is extended to a VNA-based FDR system in order to improve the retrieval capabilities of a TDR probe. A generalized FDR modeling approach is formulated and a practical probe calibration procedure is proposed. The approach is based on an electromagnetic model decoupling the cable and probe head from the ground using frequency-dependent reflection and transmission transfer functions. The FDR model represents an exact solution of Maxwell's equations for wave propagation in one-dimensional (1-D) multilayered media, and in particular, in transmission lines. The FDR probe is fully described by its characteristic transfer functions, which are determined using three or more measurements for known model configurations. The soil properties are retrieved after removing the probe effects from the raw FDR data by inverting iteratively a multilayered global reflection coefficient. This approach is not limited to the VNA-based FDR setup used here and could be extended to the traditional TDR cable testers.

In order to validate the method, we conducted laboratory experiments with measurements taken in salt water with increasing salt concentrations and sand with different moisture conditions. The results were compared to theoretical values and traditional TDR estimates. The advantage of the proposed approach compared to other existing methods is mainly the simple calibration procedure for determining the probe characteristics.

1.4 Materials and methods

1.4.1 Electromagnetic properties of materials

The electromagnetic parameters governing wave propagation are the dielectric permittivity ε, electrical conductivity σ and magnetic permeability μ. The magnetic permeability of the major natural materials encountered in the environment is assumed to be equal to the magnetic permeability of free space, namely, $\mu_0 = 4\pi 10^{-7}$ Hm^{-1}. However, soil with magnetic materials (e.g., iron oxides) may exhibit non negligible higher magnetic permeabilities (Robinson *et al.*, 1994; van Dam *et al.*, 2002; Stillman and Olhoeft, 2008; Mattei *et al.*, 2008).

Due to relaxation phenomena, the soil electromagnetic properties present a frequency dependence, which is usually described with the extended Debye relaxation model (e.g., Heimovaara, 1994; Feng *et al.*, 1999; Huisman *et al.*, 2004). It is worth noting that this model assumes only one single relaxation phenomenon, while the soil is a mix of air, soil particles and water and thus exhibits a complicated dielectric behavior due to the overlapping spectra of its different components (Logsdon, 2005). In the limited frequency range from 500 MHz to 3 GHz, however, it has been shown that the frequency dependence of the dielectric permittivity can be neglected for most soils (Zhou *et al.*, 2001; Weerts *et al.*, 2001; Huisman *et al.*, 2002b; Robinson *et al.*, 2005). Herein, we assume a constant dielectric permittivity in the frequency range 10 MHz - 1 GHz. Dielectric permittivity of sand can be assumed as constant in that frequency range (Kelleners *et al.*, 2005) and dielectric permittivity of water or salt water decreases as a function of the frequency above 2 GHz only (Meissner and Wentz, 2004).

Nevertheless, the frequency-dependence of the apparent electrical conductivity (which includes dielectric losses) in this frequency range can be significant, especially for high water contents. In a such limited frequency range, this dependence can be well accounted for using a linear model, thereby representing a local linear approximation of the full frequency-dependence function (Lambot *et al.*, 2004b):

$$\sigma(f) = \sigma_{f_{min}} + s(f - f_{min}) \tag{1.1}$$

where $\sigma_{f_{min}}$ is the apparent electrical conductivity at the minimal frequency f_{min} of the frequency range and s the slope of the linear function $\sigma(f)$.

1.4.2 Modeling of the FDR system

An FDR (or TDR) system is typically constituted by an electromagnetic wave generator, a coaxial cable and a FDR probe. The wave generator transmits an electromagnetic wave into the system and the FDR probe acts as a waveguide transmitting the wave into the medium in which the probe is inserted. The FDR rods thus emulate a coaxial medium where an alternating electric field oscillates between the central and the external rods, with the investigated medium acting as the insulating material of the coaxial line. Each sequential element of the FDR system is characterized by its internal electromagnetic properties, i.e., its dielectric permittivity ε, electrical conductivity σ, magnetic permeability μ, and dimensions, determining its complex impedance. A change in the characteristic properties above-cited produces a partial reflection and transmission of the wave. The FDR system thereby constitutes a transmission line or a 1-D multilayered medium.

An FDR measurement using VNA technology is represented by the frequency-dependent scatter function $S_{11}(\omega)$, defined as the complex ratio between the reflected and incident waves, namely:

$$S_{11}(\omega) = \frac{B(\omega)}{A(\omega)} \tag{1.2}$$

where $B(\omega)$ and $A(\omega)$ are the reflected and incident waves at the VNA calibration plane, respectively, and ω is the angular frequency. The subscripts of $S_{11}(\omega)$ refer to the fact that the same port of the VNA (i.e., port 1) is used for simultaneously transmitting (2^{nd} subscript) and receiving (1^{st} subscript) the waves. Electromagnetic wave propagation through the FDR probe results from a combination of infinite multiple reflections and transmissions, occurring at each change of impedance or interface.

In the time domain, using traditional TDR cable testers, the measured reflected wave $b(t)$ can be calculated by a convolution integral of the incident wave $a(t)$ and the system function $s(t)$ (Heimovaara, 1994):

$$b(t) = \int_{-\infty}^{+\infty} a(t-\tau)s(\tau)d\tau \tag{1.3}$$

where τ is the integration variable. The measured reflected wave $b(t)$ in the time domain can then be transformed in the frequency domain wave $B(\omega)$ using a Fourier transform (Heimovaara, 1994).

The overall FDR system is shown in Fig. 1.1(a) and its corresponding representation in terms of a 1-D multilayered medium is shown in Fig. 1.1(b). The variable $S_{11}(\omega)$ therefore represents a global reflection coefficient, measured at the calibration plane up to the end of the probe, formally referred to as $R_{C,N}(\omega)$, for fields incident from layer C (cable before the calibration plane) onto the interface with layer N (end of the rods). The probe head is defined here as the layered medium P, with unknown layers, situated between the calibration plane and the base of the FDR rods. The FDR probe head characteristics can only be determined owing to a decoupling of the probe head and rods in the electromagnetic model, in order to ensure that the probe head characteristics are independent from the measured medium. In order to mathematically decouple the probe head from the FDR rods, a fictive air layer (layer 0) is added in between, whose thickness d_0 tends to zero. This layer has therefore no effect on the wave propagation. The FDR rods are then discretized into a number of layers representing a multilayered medium, with each soil layer being characterized by its own electromagnetic parameters, and by extension, its soil properties. For non short-circuited probes, the end of the rods is modeled by an infinite half-space whose properties are defined such that they lead to a reflection coefficient $R_{N-1,N} = 1$. This can typically be emulated using $\varepsilon_r = 1$,

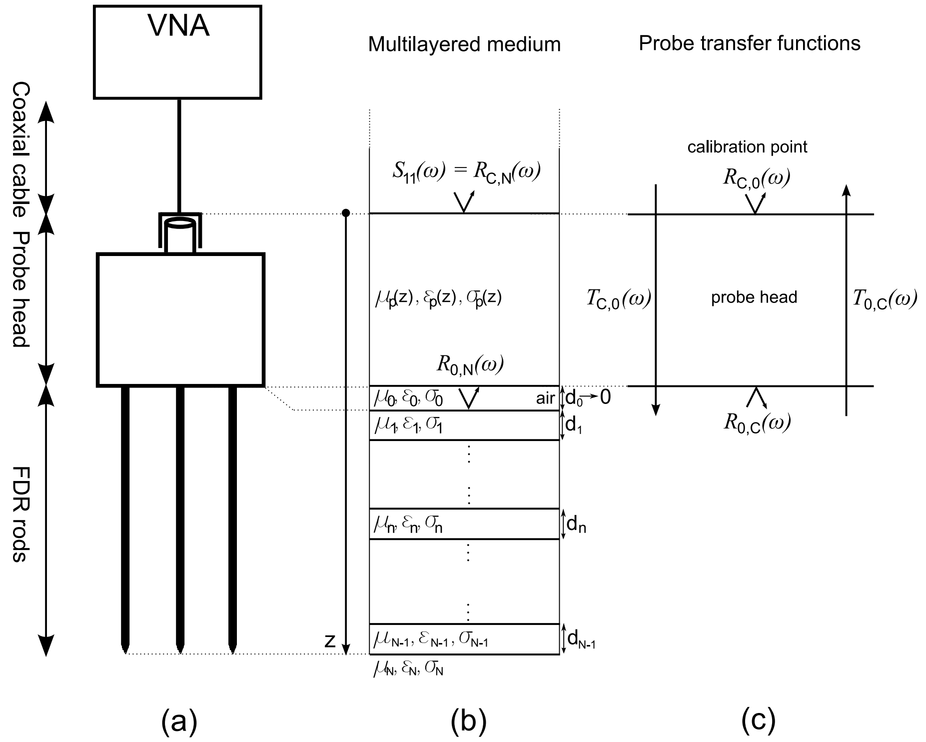

Figure 1.1: Modeling of the frequency domain reflectometry (FDR) system by a one dimensional multilayered medium: (a) schematic of the measurement system with vector network analyzer (VNA), (b) corresponding representation as a multilayered medium, where S_{11} is the scatter function, R are reflection coefficients, and ε is the dielectric permittivity, σ is the electrical conductivity, and μ is the magnetic permeability at depths d, and (c) probe reflection and transmission coefficients R and T characterizing the FDR probe head.

$\sigma = 0$, and $\mu_r \to \infty$ for layer N. The unknown layered medium P can be theoretically replaced by an equivalent medium with global reflection ($R_{C,0}(\omega)$ and $R_{0,C}(\omega)$) and transmission ($T_{C,0}(\omega)$ and $T_{0,C}(\omega)$) coefficients, defined as shown in Fig. 1.1(c), which fully characterize the probe head. Indeed, the presence of the fictive air layer permits to make independent these global functions from the soil properties. The scatter function $S_{11}(\omega)$ can then be derived as:

$$S_{11}(\omega) = R_{C,N}(\omega) = R_{C,0}(\omega) + \frac{T_{C,0}(\omega)R_{0,N}(\omega)T_{0,C}(\omega)}{1 - R_{0,C}(\omega)R_{0,N}(\omega)} \tag{1.4}$$

Defining $T(\omega) = T_{C,0}(\omega)T_{0,C}(\omega)$, the number of independent unknown characteristic probe head functions reduces to three, namely, $R_{C,0}(\omega)$, $R_{0,C}(\omega)$, and $T(\omega)$. It is worth noting that these characteristic probe transfer functions inherently contain the information about the probe characteristic as, e.g., the probe impedance, which is integrated in the $T(\omega)$ and $R_{0,C}(\omega)$ transfer functions. Once these probe characteristic functions are known, the probe effects can be filtered out from the $S_{11}(\omega)$ measurements and the response of the soil only can be derived, namely:

$$R_{0,N}(\omega) = \frac{S_{11}(\omega) - R_{C,0}(\omega)}{S_{11}(\omega)R_{0,C}(\omega) + T(\omega) - R_{C,0}(\omega)R_{0,C}(\omega)} \tag{1.5}$$

The three probe characteristic functions $R_{C,0}(\omega)$, $R_{0,C}(\omega)$, and $T(\omega)$ can be determined by solving a system of equations as (1.4), for which at least three independent measurements $S_{11}(\omega)$ should be performed and the corresponding $R_{0,N}(\omega)$ should be calculated. Practically, this can be realized using well known model configurations such as shortcuts at different sections of the rods (assuming $R_{n,n+1}(\omega)$ = -1 at the shortcut position) and a measurement with the probe in free space (air). To ensure independency of the calibrating equations for the whole frequency range, the system should be ideally overdetermined using more than three model configurations.

In case of time domain measurements using classical TDR devices, the scatter function $S_{11}(\omega)$ measured by the VNA in (1.4) can be replaced by the reflected wave $B(\omega)$, that is, the Fourier transform of $b(t)$ measured by the TDR cable tester. In that case, the incident wave $A(\omega)$ is integrated in the probe characteristic functions $R_{C,0}(\omega)$ and $T(\omega)$, therefore, it is not necessary to know it. In TDR system, the actual incident wave may differ from the one which is given by the TDR constructor because of distortions caused by internal electronics of the voltage generator and the transmission line (Mattei *et al.*, 2005).

The global reflection coefficient from the FDR rods ($R_{0,N}(\omega)$) can be recursively derived as (e.g., Feng *et al.*, 1999; Heimovaara *et al.*, 2004):

$$R_{n,N}(\omega) = \frac{R_{n,n+1}(\omega) + R_{n+1,N}(\omega)\exp(-2\gamma_{n+1}(\omega)d_{n+1})}{1 + R_{n,n+1}(\omega)R_{n+1,N}(\omega)\exp(-2\gamma_{n+1}(\omega)d_{n+1})} \tag{1.6}$$

where subscript n refers to the layer ($n = N-1, N-2, \cdots, 0$), $\gamma_n(\omega)$ is the propagation constant, $R_{n,n+1}(\omega)$ is the local reflection coefficient for fields incident from layer n onto the interface with layer $n+1$, and d_n is the layer thickness. The recursion is initiated assuming $R_{N-1,N}(\omega) = 1$ for an open-ended probe (Feng *et al.*, 1999; Schaap *et al.*, 2003). The electromagnetic wave is assumed to propagate in the transverse electromagnetic mode (TEM), meaning that the electric and magnetic fields are transverse to the direction of the propagation of the wave. The propagation constant γ depends on the dielectric permittivity ε, electrical conductivity σ and magnetic permeability μ of the medium. It is expressed as follows:

$$\gamma(\omega) = \sqrt{-\omega^2\mu(\varepsilon - \frac{j\sigma}{\omega})} \tag{1.7}$$

The propagation constant γ is a complex quantity which can also be expressed as:

$$\gamma = \alpha + \jmath\beta \tag{1.8}$$

The real part α is the attenuation constant

$$\alpha = \sqrt{\frac{\omega^2\mu\varepsilon}{2}\left(\sqrt{1+\tan^2\delta} - 1\right)} \tag{1.9}$$

and the imaginary part β is the phase constant

$$\beta = \sqrt{\frac{\omega^2\mu\varepsilon}{2}\left(\sqrt{1+\tan^2\delta} + 1\right)} \tag{1.10}$$

where

$$\tan\delta = \frac{\sigma}{\omega\varepsilon} \tag{1.11}$$

is defined as the loss tangent. The phase constant β determines wave propagation velocity v as:

$$v = \frac{\omega}{\beta} = \frac{1}{\sqrt{\frac{\mu\varepsilon}{2}\left(\sqrt{1+\tan^2\delta} + 1\right)}} \tag{1.12}$$

It is worth noting that for non-magnetic materials with a relatively low electrical conductivity and considering high frequencies, wave propagation velocity can be approximated by:

$$v \approx \frac{1}{\sqrt{\mu\varepsilon}} = \frac{c}{\sqrt{\varepsilon_r}} \tag{1.13}$$

where c is the wave velocity in free space and ε_r is the relative dielectric permittivity ($\varepsilon_r = \varepsilon/\varepsilon_0$ with ε_0 being the dielectric permittivity of free space). This assumption is commonly used when characterizing soil using classical TDR approaches. In our case, such an assumption is not applied.

The local reflection coefficient $R_{n,n+1}(\omega)$, resulting from the electromagnetic boundary conditions at an interface, is defined as :

$$R_{n,n+1}(\omega) = \frac{\mu_{n+1}\gamma_n(\omega) - \mu_n\gamma_{n+1}(\omega)}{\mu_{n+1}\gamma_n(\omega) + \mu_n\gamma_{n+1}(\omega)} \tag{1.14}$$

In previous studies, elements of the FDR system were modeled using characteristic impedances of the elements, assuming that they were known based on the system characteristics or that they could be retrieved by optimization (Heimovaara *et al.*, 2004). The cable impedance was usually assumed to be equal to 50 Ω and the probe impedance could be determined based on the probe geometry (i.e., with the inner and outer diameter of the coaxial medium (e.g., Heimovaara, 1994)). In this study, the probe head impedance and the FDR rods impedance are inherently accounted for in the probe transfer functions, i.e., they are determined by measurements in known media.

1.4.3 Model inversion

The unknown parameter vector **p** to be determined (containing the dielectric permittivity, frequency-dependent apparent electrical conductivity, and thickness of the investigated soil layers) is retrieved by a full-waveform inversion procedure, which is applied to the probe-filtered FDR signal (see Eq. (1.5)). The inverse problem is formulated in the least squares sense and the objective function is defined as follows:

$$\phi(\mathbf{p}) = \left|\mathbf{R}^*_{\mathbf{0},\mathbf{N}} - \mathbf{R}_{\mathbf{0},\mathbf{N}}\right|^T \left|\mathbf{R}^*_{\mathbf{0},\mathbf{N}} - \mathbf{R}_{\mathbf{0},\mathbf{N}}\right| \tag{1.15}$$

where $\mathbf{R}^*_{\mathbf{0},\mathbf{N}} = R^*_{0,N}(\omega)$ and $\mathbf{R}_{\mathbf{0},\mathbf{N}} = R_{0,N}(\omega, \mathbf{p})$ are the vectors containing, respectively, the observed and simulated global reflection coefficients of the soil. As these global reflection coefficients are complex vectors, the objective function is expressed by the amplitude of the difference of the filtered data in the complex plane.

Considering a multilayered soil sampled by the FDR probe, parameters for each soil layer can theoretically be retrieved by inversion, depending on the information content with respect to the number of parameters to optimize. Nevertheless, for thin layers compared to the signal wavelength and for small contrast between the layers, the information content in the waveform may be insufficient to distinguish the layers and to determine the layers properties, leading to non-unicity problems in the inversion, as it is shown in chapter 2 and Minet *et al.* (2010a). Although the optimization problem is generally simple for a single soil layer, the topography of the objective function to minimize can be relatively complex when considering several soil layers, including multiple local minima. To properly solve such inverse problems, a global optimization procedure is required. Following the approach of Lambot *et al.* (2002), we used the global multilevel coordinate search (GMCS) algorithm (Huyer and Neumaier, 1999) combined sequentially with the classical Nelder-Mead Simplex algorithm (Lagarias *et al.*, 1998).

1.4.4 Petrophysical models

A petrophysical model is necessary for translating the optimized dielectric permittivity ε_r into volumetric soil moisture θ. Two main approaches can be distinguished in the petrophysical models. The first approach is empiric and uses measurements of dielectric permittivity for a variety of soil types at different water contents to construct regressive polynomial formulas relating the water content with the dielectric permittivity. The most frequently used empirical formula is the relationship suggested by Topp *et al.* (1980):

$$\theta = -5.3 \times 10^{-2} + 2.92 \times 10^{-2}\varepsilon - 5.5 \times 10^{-4}\varepsilon^2 + 4.3 \times 10^{-6}\varepsilon^3 \tag{1.16}$$

This equation has been widely applied to predict soil moisture from TDR and GPR measurements and its validity was established in many studies (Roth *et al.*, 1992; Steelman and Endres, 2010).

The second approach is more theoretical and derives the water content from dielectric mixing models of soil. According to this approach, soil is a complex mixture of air, water and soil particles and the permittivity of soil is predicted from the permittivity of each component weighted by their volume fraction. Among these models, the complex refractive index model (CRIM) (Birchak *et al.*, 1974; Dobson *et al.*, 1985) appeared to be the most suitable in many studies. A combination of the two approaches consists in an empirical version of the CRIM model as developed by Ledieu *et al.* (1986) and Yu *et al.* (1999):

$$\theta = a\sqrt{\varepsilon_r} + b \tag{1.17}$$

with a and b being optimized soil specific parameters. This model was used in this chapter and further to fit the inversely-retrieved soil dielectric permittivity to the volumetric water content.

1.4.5 Laboratory experiments setup

The objective of the laboratory measurements was threefold: (1) to characterize the FDR probe transfer functions, (2) to validate these transfer functions in a well-known medium, i.e., salt water, and (3) to apply the inversion procedure in order to retrieve the electromagnetic properties of a humid sand in which the probe was inserted.

We set up the FDR system using a VNA (ZVT8, Rohde & Schwarz, Münich, Germany) as transmitter and receiver, which we connected to a homemade FDR probe with high quality N-type connectors and a 50 Ω impedance coaxial cable of 2.5 m length (Sucoflex 104PEA, Huber + Suhner AG, Herisau, Switzerland). The FDR probe was a 9.60 cm length, three-rod stainless steel device hold by an epoxy probe head and equipped with a N-type connector. The spacing between the two external rods was 28 mm and the diameter of the rods was 3 mm. The VNA was accurately calibrated with a high precision ($|S_{11}(\omega)| < -90$ dB for a “Match” measurement) with a 50 Ω OSM (Open, Short, Match) series of standard, N-type calibration kit (ZV-Z21, Rohde & Schwarz, Münich, Germany). The calibration of the VNA was made at the connector between the coaxial cable and the probe head, as illustrated in Fig. 1.1. It is worth noting that the calibration could have also been performed at port 1 of the VNA. In that case, the probe transfer functions would have also accounted for the coaxial cable.

For the probe transfer functions determination, $S_{11}(\omega)$ measurements were first performed in different well-known media, namely, in air and with the

FDR rods short-circuited at 16 different distances, accounting in total for 17 measurements, although three measurements are sufficient to determine the transfer functions. Probe length and position of short-cuts along the probe were precisely measured in order to compute the theoretical global reflection coefficient in these media. Second, measurements in 10 salt water solutions were made in order to validate the probe calibration and the inversion procedure. Lastly, we set up 10 different humid sand (Fontainebleau sand) media by mixing calculated volumes of dry sand and demineralized water to test the technique for the retrieval of the dielectric permittivities and frequency-dependent electrical conductivities. The same volume of water was added to the known volume of sand in order to obtain regularly increasing sand water content. These two last media (i.e., salt water and humid sand) were chosen as they permit to test the FDR method for the retrievals of the electrical conductivity and dielectric permittivity, respectively, as the water electrical properties are known.

The frequency dependent scatter function $S_{11}(\omega)$ was measured sequentially at 3996 stepped frequencies from 10 MHz to 8 GHz with a step of 2 MHz. Nevertheless, inversions of the measured signals were performed on a limited frequency range, namely, 10-1000 MHz, where the signal-to-noise ratio appeared to be optimal, especially due to the higher performances of the probe in that frequency range. It is worth mentioning that Lin (2003) suggested a similar optimal frequency range (500-1000 MHz).

For the measurements performed in humid sand, TDR measurements were also carried out using a Tektronix 1502C metallic cable tester (Tektronix, Inc., Beaverton, OR, USA) connected to a traditional TDR probe (95 mm long and 3 mm diameter with a 25 mm rod spacing). The dielectric permittivity was derived from the TDR waveforms using the WinTDR 6.0 software (Soil Physic Group, Utah State University, Logan, Utah, USA).

1.5 Laboratory experiments results

1.5.1 Probe transfer functions determination

The global reflection coefficients $R_{0,N}(\omega)$ corresponding to the 17 measurements (1 air + 16 short-cuts) performed for the probe transfer functions determination were first calculated using (1.6). The probe transfer functions were then retrieved by solving a system of equations as (1.4), assuming not only three model configurations but also more (seven and 17) to over-determine the system.

Figure 1.2 shows the amplitude and phase of the FDR probe transfer functions $R_{C,0}(\omega)$, $T(\omega)$, and $R_{0,C}(\omega)$ determined over the full frequency range from 10 MHz to 8 GHz. The transfer functions determined with the minimal number of measurements (i.e., three) show very good results for frequencies in which the probe is the most efficient (low $R(\omega)$ and high $T(\omega)$ values in the lower frequency range), yet, local errors appear for some frequencies, especially in the higher frequency range where the signal-to-noise ratio becomes poor as a result of lower probe efficiency and sensitivity to measurement errors (e.g., in the measurement of the distance between the probe head and the short-cut).

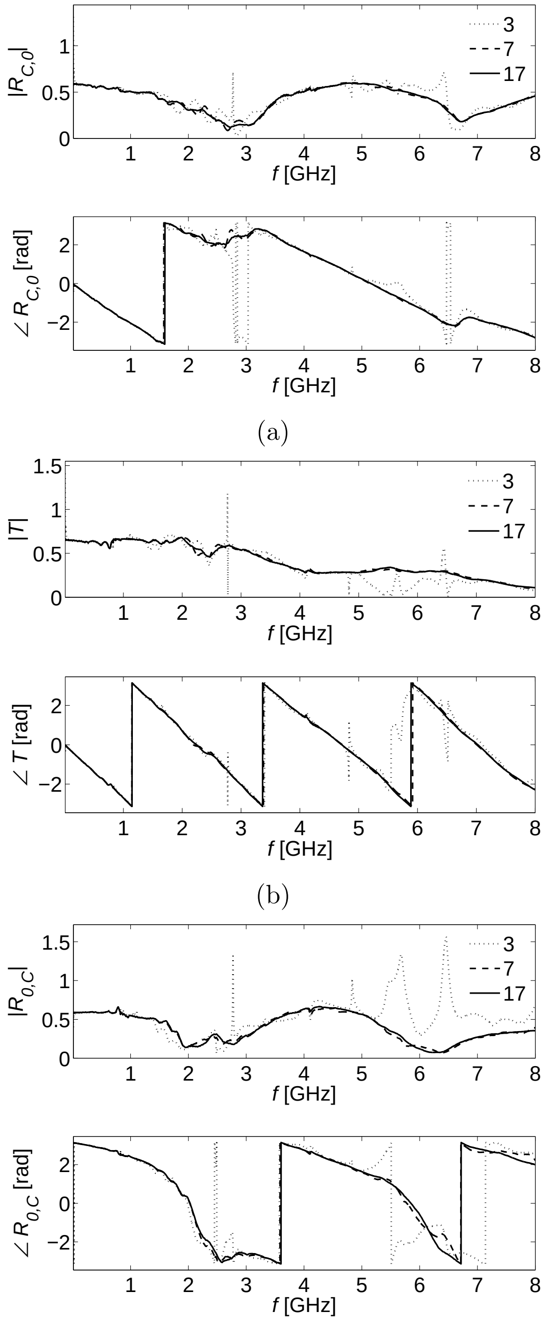

(a)

(b)

(c)

Figure 1.2: Frequency domain reflectometry (FDR) probe transfer functions reflection coefficients $R_{C,0}(\omega)$ (a) and $R_{0,C}(\omega)$ (c) and transmission coefficients $T(\omega)$ (b) determined throughout the entire frequency range (f) from 10 MHz to 8 GHz, depicted in amplitude (upper graphs) and phase (lower graphs), for three different number of measurements (three, seven, and 17) used to solve the systems of equations.

Over-determining the system of equations using at least seven or higher model configurations led to very similar values of the transfer functions over the whole frequency range, with smooth trends in terms of both amplitude and phase of the transfer functions, thereby denoting a good accuracy. For the analysis of the FDR data taken in salt water and humid sand (see the following section), the transfer functions determined with the maximal number of measurements (i.e., 17) were used, but, as it can be observed in Fig. 1.2, a number of seven measurements is already sufficient to obtain a high accuracy.

The analysis of these probe transfer functions permitted to determine in which frequency range the probe is the most efficient. In particular, high $R_{C,0}(\omega)$ values (e.g., > 0.5) indicate that, at these frequencies, most of the wave is reflected within the probe and is not transmitted to the ground. In contrast, high $T(\omega)$ values indicate that the probe is efficient to transmit waves into the ground. In particular, we can see in Fig. 1.2(b) that the probe efficiency is strongly decreasing above 2 GHz because of the low $T(\omega)$ values. $R_{0,C}(\omega)$ can be analyzed similarly to $R_{C,0}(\omega)$ and low $R_{0,C}(\omega)$ are observed for the same frequency values than for $R_{C,0}(\omega)$, namely, around 3 and 6.5 GHz. Once they are characterized, these probe transfer functions can be used to filter out the raw measured data $S_{11}(\omega)$ from all the FDR probe head effects and obtain the global reflection coefficient of the FDR rods medium only ($R_{0,N}(\omega)$), namely, the soil. It is worth noting that in practice, only three reference measurements are required to accurately calibrate the probe, provided it is sufficiently efficient in the frequency range of concern.

1.5.2 Inversion of FDR measurements in salt water

The validity of the probe calibration and of the inversion procedure was assessed by comparing measured, theoretically-predicted and inverted (fitted) signals, as well as the theoretical or laboratory-measured and inverted parameters (i.e., ε_r, σ_{fmin} and s) for the 10 measurements in salt water. The inversion was set in a large parameter space, namely, $2 < \varepsilon_r < 90$, $10^{-2} < \sigma_{fmin} < 10$ Sm^{-1} and $10^{-11} < s < 10^{-7}$ sSm^{-1} and more than 5400 iterations were performed. Salt concentrations were regularly increased from 0.154 gL^{-1} to 1.540 gL^{-1} by adding precise quantities of salt (NaCl) into demineralized water. The solution electrical conductivity, as well as the solution temperature, was measured by a WTW LF318 (WTW, Weilheim, Germany) conductivity meter. Bulk electrical conductivity measurements were then temperature-corrected in order to obtain the actual electrical conductivity at the solution temperature. According to the datasheet of the conductivity meter, measurements errors are 10^{-4} Sm^{-1} and 10^{-3} Sm^{-1} for conductivities, respectively, smaller and larger than 0.2 Sm^{-1}.

Figure 1.3 shows measured, predicted and inverted scatter functions $S_{11}(\omega)$ arising from the whole FDR probe, including the probe head, for a measurement in salt water with the lowest salt concentration (0.154 gL^{-1}) depicted in the frequency domain in amplitude and phase (Fig. 1.3(a)) and in the time domain (Fig. 1.3(b)). In laboratory conditions, measured scatter functions showed a good repeatability, with identical measured signals when repeating the measurement. The inverted parameters were used to compute the inverted global

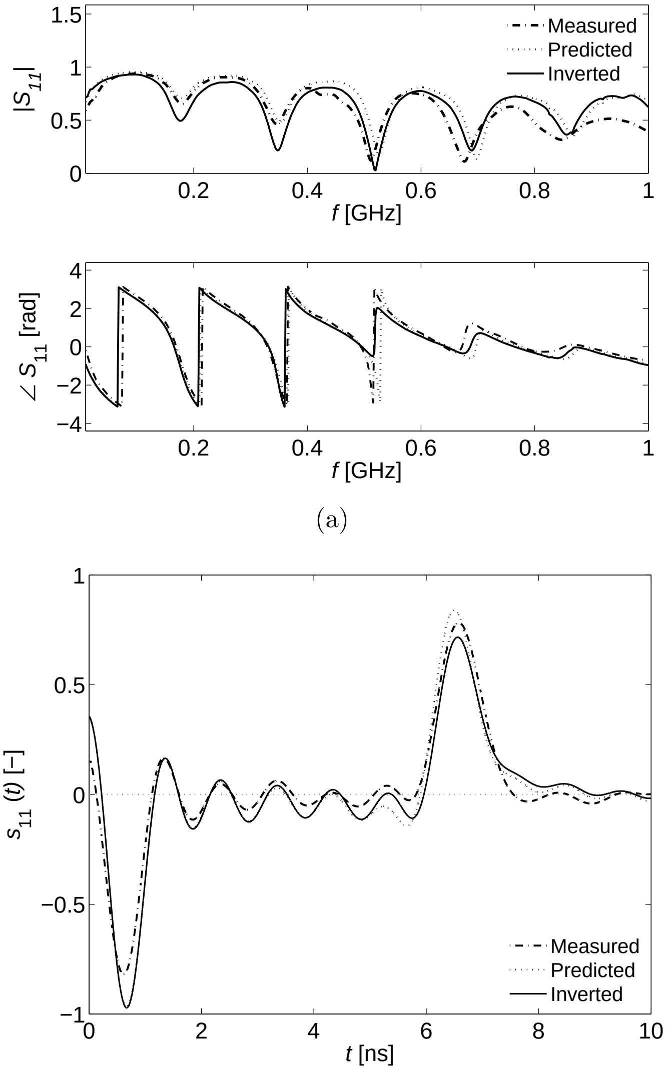

(a)

(b)

Figure 1.3: Measured, predicted and inverted scatter functions $S_{11}(\omega)$ depicted in the frequency (a) and time domains (b) for water with a salt concentration of 0.154 gL^{-1}.

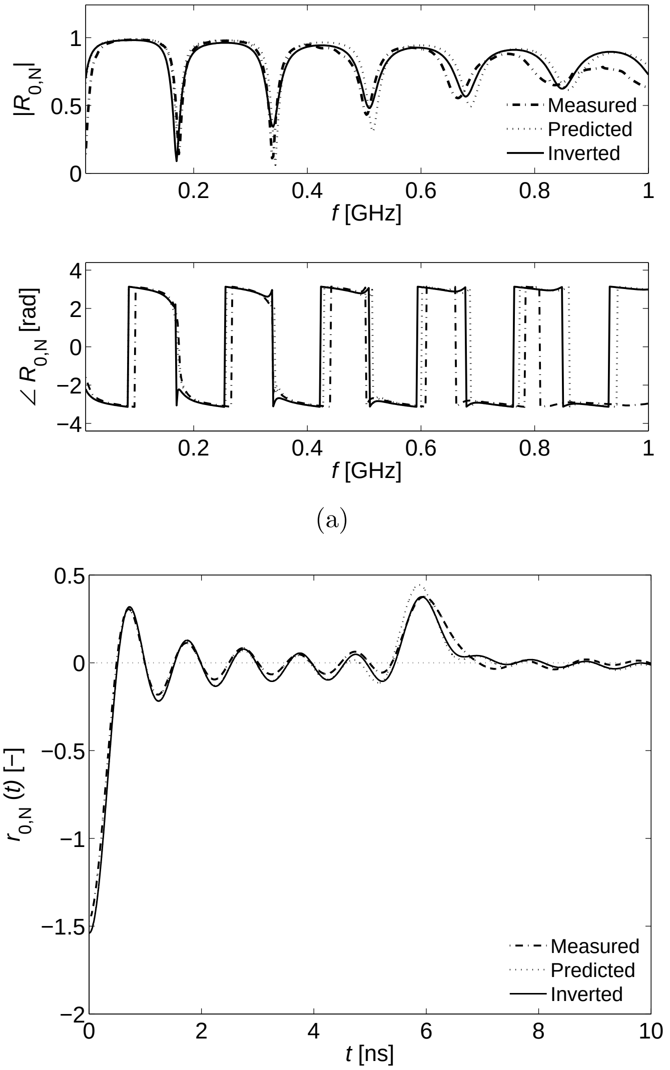

(a)

(b)

Figure 1.4: Measured, predicted and inverted global reflection coefficients $R_{0,N}(\omega)$ depicted in the frequency (a) and time domains (b) for water with a salt concentration of 0.154 gL^{-1}.

reflection coefficient, which was then translated backward in the inverted scatter function $S_{11}(\omega)$ using (1.4). The predicted scatter function was computed using the electromagnetic model and theoretical permittivity and conductivity values estimated by a formulation of the model of Debye for salt water from Meissner and Wentz (2004), using measured bulk electrical conductivity and temperature. This accurate model accounts for frequency- and temperature-dependence of the electrical parameters, but it is restricted to salt water only. Measurement errors of the bulk electrical conductivity ($\Delta\sigma = 0.0001$ Sm^{-1}) and of the solution temperature ($\Delta \mathrm{T} = 0.1^{\circ}\mathrm{C}$) do not have a visible impact on the predicted signal when propagating the errors to the predicted scatter function $S_{11}(\omega)$ (RMSE of 0.00110 in terms of amplitude of the scatter function in the frequency domain).

In the frequency domain, some discrepancies are observed between the measured and inverted or predicted signals, both in amplitude and phase, especially with increasing frequencies. These discrepancies may be attributed to a lower signal-to-noise ratio, as a result of the stronger attenuation of the waves due to increasing relaxation phenomena with frequency. In the time domain, the reflection at the beginning of the FDR rods is observed around 1 ns and the final reflection from the end of the probe after 6 ns. Arrival times of the reflection are identical between the measured, inverted and predicted signals, whereas there is a poorer agreement between the amplitudes of the reflection peaks. For the inverted signal, this indicates a high sensitivity of the model to the dielectric permittivity, that mainly governs the propagation time, rather than the electrical conductivity.

Figure 1.4 shows the corresponding measured, predicted and inverted global transfer coefficients $R_{0,N}(\omega)$ depicted in the frequency domain in amplitude and phase (Fig. 1.4(a)) and in the time domain (Fig. 1.4(b)) for the same salt water medium as shown in Fig. 1.3. In the frequency domain, discrepancies between the measured and inverted or predicted signals are smaller compared to Fig. 1.3(a), although increasing errors with frequency are still observed. For low frequencies (e.g., < 600 MHz), the inverted signal fits well the measured signal. In the time domain, the same agreements between the measured and inverted, as well as the predicted signals, are also observed. It is worth noting that the signal appears to be better modeled when expressed in terms of $R_{0,N}$ because it is referenced with respect to the fictive air layer, resulting in a larger contrast at the beginning of the FDR rods. In particular, the reflection of the end of the probe is relatively higher for the signal expressed in terms of S_{11} (Fig. 1.3(b)) when comparing with $R_{0,N}$ (Fig. 1.4(b)) because $R_{0,N}$ is computed assuming that less signal is transmitted in the FDR rods.

Corresponding to the case depicted in Fig. 1.4, the inverted parameters that were retrieved are $\varepsilon_r = 84.4$, $\sigma_{10MHz} = 0.0210$ Sm^{-1} and $s = 10^{-9.55}$ sSm^{-1}. The dielectric permittivity ε_r at the solution temperature ($13.5^{\circ}\mathrm{C}$) is expected to range from 82.2 to 82.6 in the limited frequency range of 10-1000 MHz (Meissner and Wentz, 2004), which is close to the inverted dielectric permittivity value. The slight overestimation of the water dielectric permittivity is expected to come from the fact that during the measurements with the probe in the water, some water wetted the inside of the probe head through the rods.

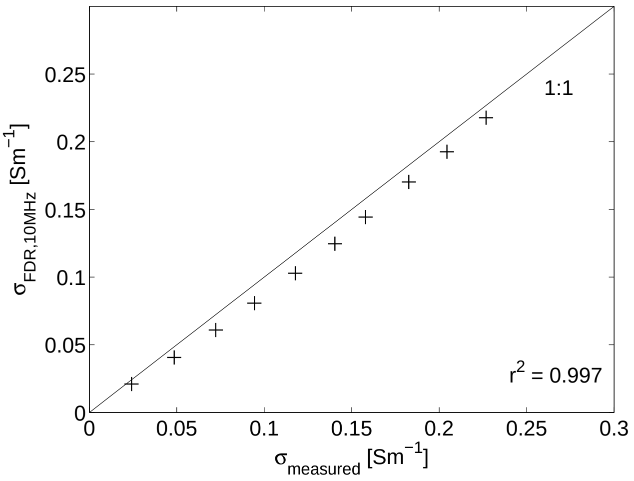

Figure 1.5: Inverted electrical conductivity (σ) at the minimal frequency (10 MHz) from frequency domain reflectometry (FDR) measurements as a function of the measured σ in the 10 different salt water solutions.

The measured solution bulk conductivity with the conductivity meter was, for that case, 0.0242 ± 0.0001 Sm^{-1}.

Figure 1.5 compares measured and inverted electrical conductivity values for the ten different salt water solutions. Inverted frequency-dependent electrical conductivities are chosen at the minimal frequency of 10 MHz. There is a good agreement between these two variables, with a coefficient of determination equal to 0.997. Inverted values are slightly underestimated compared to the measured electrical conductivities, but inverted values can be higher considering higher frequencies. The relation between the mass of added salt in the solution and the measured electrical conductivity appears to be linear in this range of salinity (not shown) and also well-determined, with a coefficient of determination of 0.999. Inverted dielectric permittivity values are very similar between the ten salt water solutions, ranging from 84.39 to 84.69. The good agreement of the measured or theoretical and inverted parameters, as well as the small discrepancies between theoretically-predicted, inverted and measured signals, demonstrate the accuracy of the electromagnetic model and probe transfer functions determination with respect to real measurements, as well as the well-posedness of the inverse problem.

1.5.3 Determination of the sand water content

The measured FDR signals from the 10 humid sand media were filtered for the probe effects using (1.5) and then inverted in the limited frequency range 10-1000 MHz to retrieve the soil dielectric permittivity and the frequency-dependent apparent electrical conductivity. The parameter space for the inversion was set as follows: $2 < \varepsilon_r < 90$, $10^{-4} < \sigma_{fmin} < 10^{-1}$ Sm^{-1} and

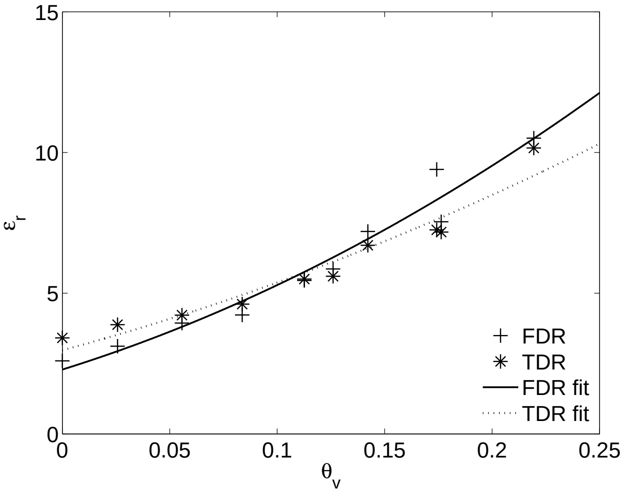

Figure 1.6: Relative dielectric permittivity (ε_r) estimated from time domain reflectometry (TDR) measurements and frequency domain reflectometry (FDR) inversions as a function of the sand water content (θ_v) measured by volumetric sampling. The model of Ledieu *et al.* (1986) was fitted over the TDR and FDR data.

$10^{-12} < s < 10^{-5}$ sSm^{-1}. The media were assumed to be homogeneous in the electromagnetic model ($N = 2$ in Fig. 1.1). Subsequently to the FDR measurements, volumetric samples of the humid sand were collected to determine the actual water content, using the oven-drying method at 105°C for at least 48h.

Figure 1.6 shows the relative dielectric permittivity estimated from TDR measurements and FDR inversions as a function of the sand water content measured by volumetric sampling. The model of Ledieu *et al.* (1986) (Eq. (1.17)) linking the volumetric water content and the dielectric permittivity was fitted on both TDR and FDR data. The root mean square error RMSE of the fits and the coefficient of determination r^2 between $\sqrt{\varepsilon_r}$ and θ_v are shown in Table 2.1.

Both TDR and FDR relationships show similar good agreements, with r^2 close to 1 and RMSE to 0.5 in terms of dielectric permittivity, corresponding to an error of less than 1 % in terms of volumetric water content. The differences between FDR and TDR estimates may originate from the different locations where the FDR and TDR probes were inserted, given the inherent heterogeneities in the sand water content and densities.

Figure 1.7 shows the frequency-dependent electrical conductivity $\sigma(f)$ inverted from FDR signals for the ten different sand water contents (depicted from WC1 to WC10 in Fig. 1.7(b)) as a function of the frequency range in which the data were inverted. Frequency-dependent electrical conductivity determined from a FDR measurement in demineralized water and the theoretical

Table 1.1: Root mean square error RMSE of the fits according to the model of Ledieu *et al.* (1986) and coefficient of determination r^2 between the square root of the relative dielectric permittivity $\sqrt{\varepsilon}_r$ and the volumetric water content θ_v for time domain reflectometry (TDR) and frequency domain reflectometry (FDR) measurements.

	$RMSE$	r^2
TDR	0.461	0.948
FDR	0.514	0.965

Debye model for pure water according to the parameterization of Meissner and Wentz (2004) are shown for comparison purposes.

The slopes of the linear frequency dependence for the different humid sands are different, ranging from $10^{-25.3}$ to $10^{-10.6}$ sSm^{-1}, for the lowest and highest sand water content, respectively. Not surprisingly, the apparent electrical conductivity increases with the sand water content, tending to the slope of demineralized water ($s = 10^{-9.59}$ sSm^{-1}). Nevertheless, the apparent frequency-dependent electrical conductivity of the most humid sand remains far from the frequency-dependent electrical conductivity of water because of the multiple composition of humid sand, which is a mix of air, water and soil particles. The assumption of the linearity of the frequency-dependence appears to be quite acceptable for pure water, with a line approaching the curved Debye model. It is worth noting that, at the lowest and highest frequencies, the inverted frequency-dependent electrical conductivities of demineralized water measurement correspond to the values calculated with the theoretical Debye model.

1.6 Conclusions

We developed a new FDR technique based on an electromagnetic model decoupling the FDR probe head from the measured medium using three frequency-dependent transfer functions. At least three laboratory measurements in perfectly known media and modeling of the global reflection coefficients in these configurations can be used to fully determine the probe transfer functions, owing to the decoupling of the FDR probe and the accurate electromagnetic modeling. The technique was validated with measurements in salt water media. Measured, inverted and theoretically-predicted signals in the frequency range in which the probe is efficient were in close agreement, thereby demonstrating the accuracy of the whole forward model and the well-posedness of the inverse problems dealt with.

A good agreement was also observed when comparing measured or theoretical and inverted parameters, i.e., the dielectric permittivities and electrical conductivities. Measurements in ten different humid sands were then conducted and the dielectric permittivities retrieved from FDR inversions were close to the values derived from classical TDR measurements and in a good agreement with volumetric water contents, with a coefficient of determination between $\sqrt{\varepsilon}$

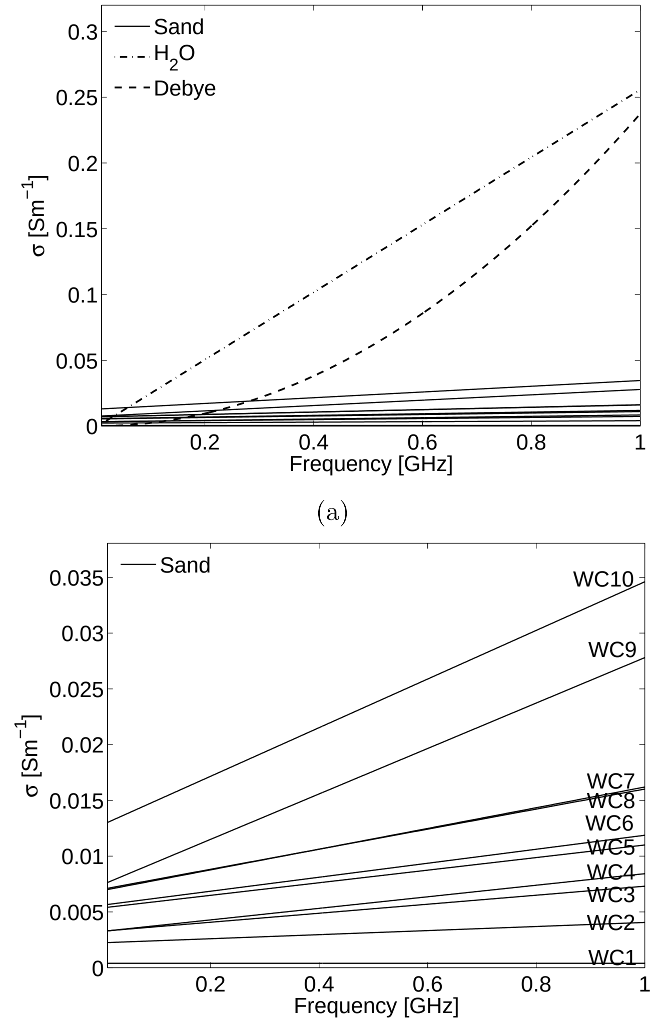

(a)

(b)

Figure 1.7: Frequency-dependent, apparent electrical conductivity (σ) retrieved from frequency domain reflectometry (FDR) inversions for sand media at 10 different water contents (WC) and for demineralized water depicted with theoretical values from the model of Debye (a); enlargement of the electrical conductivity of the sand media (b).

and θ of 0.948 and 0.965 for the TDR and FDR, respectively. Moreover, the frequency-dependent electrical conductivity could also be retrieved.

The proposed method appears promising for simple calibration of the FDR probe, for assessing the frequency dependence of the electrical properties and for inverting waveforms coming from multilayered media. Compared to previous studies, the proposed calibration method bypasses the determination of the cable and probe impedances. As such, the complete profile of soil electromagnetic properties along the FDR probe could be retrieved using a multi-layered model, depending on the information content in the data, as indeed, the inverse problem may be ill-posed. However, in practice, this may be limited by the narrow frequency bandwidth in which the probe is efficient, thereby limiting the information content in the FDR waveform. In that respect, the design and construction of an optimal probe is particularly important.

Chapter 2

Soil moisture estimation by ground penetrating radar in the presence of thin layers: Numerical and laboratory experiments*

2.1 Outline

We analyzed the effect of shallow thin layers on the estimation of surface soil moisture using full-waveform inversion of off-ground ground penetrating radar (GPR) data in numerical and laboratory experiments. Strong dielectric contrasts are expected to occur under fast wetting or drying weather conditions, thereby leading to constructive and destructive interferences with respect to the surface reflection in the presence of shallow thin layers. Soil moisture retrieval in layered soil conditions was poorly investigated in previous GPR studies while shallow soil layering is believed to be prevalent in the environment. First, synthetic GPR data were generated and subsequently inverted considering different thin-layer model configurations. The resulting inversion errors when neglecting the thin layer were quantified, and then, the possibility to reconstruct these layers was investigated. Second, laboratory experiments reproducing some of the numerical experiments configurations were conducted to assess the stability of the inverse solution with respect to actual measurement

---

*This chapter is adapted from:
Minet, J.; Lambot, S.; Slob, E. & Vanclooster, M. Soil surface water content estimation by full-waveform GPR signal inversion in the presence of thin layers, in *IEEE Transactions on Geoscience and Remote Sensing*, **2010**, 48, 1138 - 1150
Minet, J.; Patriarca, C.; Slob, E.; Vanclooster, M. & Lambot, S. Characterization of layered media using full-waveform inversion of proximal GPR data, *Proceedings of the URSI International Symposium on Electromagnetic Theory - EMTS2010*, **2010**.

and modeling errors. Results showed that neglecting shallow thin layers may lead to significant errors on the estimation of soil surface water content ($\Delta\theta >$ 0.03 m^3m^{-3}), depending on the contrast. In the laboratory, the proposed full-waveform method permitted to reconstruct thin layers with a high resolution up to 2 cm and to retrieve the soil surface water content with an RMSE less than 0.02 m^3m^{-3}, owing to the full-waveform inverse modeling. These results suggest that the proposed GPR approach is promising for surface soil moisture sensing for instances when soil layering is encountered.

2.2 Introduction

At the field scale, evaluating the soil moisture spatial variability is an important issue for many research and engineering applications (Western *et al.*, 2003). Usual soil moisture measurement techniques at the field scale are invasive methods, like gravimetric sampling, capacitance probe or time domain reflectometry (TDR). Although the TDR technology has been automated to some extent, the method remains problematic for mapping large areas due to the local measuring support of the TDR probe (Robinson *et al.*, 2003). On the other hand, airborne and spaceborne microwave remote sensing methods have been proven to be effective tools for estimating surface soil moisture over larger areas, with either passive radiometry or active radar instruments (Wagner *et al.*, 2007). However, microwave remote sensing techniques are limited by its large support scale, resulting in an unknown within-pixel heterogeneity and the usually poor agreement with calibrating and gravimetric sampling (Jackson *et al.*, 1996; Wagner *et al.*, 1999; Ceballos *et al.*, 2005; Famiglietti *et al.*, 2008). Hence, no absolute relation between the backscattered signals from synthetic aperture radar (SAR) and the soil moisture exist, necessitating site-specific calibrations (D'Urso and Minacapilli, 2006). In particular, remote sensing radar systems are highly affected by soil roughness, due to the relatively high frequencies used in SAR systems, such that many studies have also addressed that problem (Verhoest *et al.*, 2008). Radar sensing is also affected by high apparent electrical conductivity values when not taken into account (Lasne *et al.*, 2008).

To bridge the scale gap between remote sensing and small-scale soil moisture determination methods, noninvasive techniques are required to characterize soil moisture at the intermediate field scale and with a spatial resolution in the order of 1 m. In that respect, ground penetrating radar (GPR) techniques are specifically suited for field scale soil moisture characterization (Annan, 2002; Huisman *et al.*, 2003; Lambot *et al.*, 2008a). Several techniques were developed to infer the soil moisture from GPR measurements, but two approaches are commonly used: the direct ground wave propagation analysis (Huisman *et al.*, 2002a; Grote *et al.*, 2003; Galagedara *et al.*, 2005; Lunt *et al.*, 2005; Grote *et al.*, 2010) and the surface reflection coefficient methods (Chanzy *et al.*, 1996; Redman *et al.*, 2002; Serbin and Or, 2003, 2004). A more recent advance was developed by Lambot *et al.* (2004b) for the particular case of off-ground and zero-offset GPR. Specific inversion strategies were developed for the retrieval of surface soil dielectric permittivity and correlated water content (Lambot *et al.*, 2006b).

The soil surface is a particularly active layer in terms of water dynamics, as it is directly exposed to the varying atmospheric conditions, while the soil water dynamics in the subsurface is more stable. Similarly to soil temperature, soil moisture temporal variations are larger in surface than in subsurface (De Lannoy *et al.*, 2006). As a result, soil layering in terms of soil moisture may appear, either in wet soils subject to fast evaporation or dry soils subject to precipitation, because of physical decoupling between surface and subsurface soil moisture (Vereecken *et al.*, 2008). This may occur preferentially in coarse materials, but not limited to, whereas pedogenetic processes and agricultural practices can lead to vertically-varying soil moisture conditions, according to the different soil layer properties (Schaap *et al.*, 2003). When surface soil moisture is sensed by a radar wave (in remote sensing or GPR applications), shallow soil moisture layering gives rise to two limitations in soil moisture sensing. First, soil layers may cause destructive or constructive interferences in the backscattered radar signal (Lambot *et al.*, 2006b). Under critical cases, resulting soil moisture measurement can be drastically different from the two soil layers moisture as well as from their average. Second, remotely-sensed surface soil moisture may largely diverge from the whole soil moisture profile (Capehart and Carlson, 1997). While the root-zone soil moisture (0-30 cm) is important for most hydrological and environmental processes, remote sensing of soil moisture is restricted to the first centimeters of the soil surface.

The effect of thin layers has been addressed in a rather large number of studies in the area of remote sensing of soil moisture (Capehart and Carlson, 1997; Wagner *et al.*, 1999; Li and Islam, 2002; Ceballos *et al.*, 2005; Das and Mohanty, 2006) whereas few studies have addressed this issue in the field of GPR (van der Kruk, 2006; van der Kruk *et al.*, 2007; Strobbia and Cassiani, 2007; Kao *et al.*, 2007). Currently, due to the single-frequency remote sensing sensors, root-zone soil moisture can only be estimated through the fusion of remotely-sensed shallow soil moisture data into soil hydrodynamic models. However, this requires a strong knowledge of the soil hydraulic properties for the correct parameterization of the hydrodynamic model. Field or watershed scale hydraulic parameters are often derived from soil texture information using pedotransfer functions (Vereecken *et al.*, 1989), but the soil parameterization schemes remain inadequate due to their inability to incorporate the natural heterogeneity of soils and the lack of detailed soil property maps. However, in contrast to single-frequency sensors, ultra-wideband GPR provides depth-dependent information and has, thereby, the potential to reconstruct thin layers.

2.3 Objectives

In this chapter, we analyze the effect of thin layers on the retrieval of soil surface water content from zero-offset, normal incidence, and proximal GPR and we addressed the reconstruction of these layers by full-waveform inversion. Shallow soil layering may give rise to interferences in the backscattered GPR data that alter the inversion results. First, numerical experiments were performed for the following reasons: 1) to investigate the well-posedness of the inverse problem when thin layers are accounted for; 2) to quantify the errors resulting from the homogeneous medium assumption; and 3) to compare different inversion strategies to deal with the reconstruction of these thin layers. Then, laboratory experiments were conducted in order to corroborate the statements inferred from the synthetic experiments and analyze the stability of the inverse problem with respect to real measurement and modeling errors. GPR measurements were made above a two-layered medium set up in a sandbox with 50 different model configurations.

2.4 Materials and methods

2.4.1 Theory

GPR is based on the propagation of an electromagnetic wave into the ground, which is governed by its electromagnetic parameters, i.e., the dielectric permittivity ε, the electrical conductivity σ and the magnetic permeability μ . As the dielectric permittivity of water ($\varepsilon_w \approx 80$) is much larger than the one of the soil particles ($\varepsilon_s \approx 5$) and air ($\varepsilon_a = 1$), the GPR wave propagation in the soil is principally determined by its water content.

The GPR system that we used consists of a vector network analyzer (VNA) connected to an ultra-wideband monostatic (zero-offset transmitter and receiver) horn antenna placed off the ground. For this configuration, the following equation is applied to filter out the antenna effects (Lambot *et al.*, 2004b):

$$S_{11}(\omega) = H_i(\omega) + \frac{H(\omega)G_{xx}^{\uparrow}(\omega)}{1 - H_f(\omega)G_{xx}^{\uparrow}(\omega)} \tag{2.1}$$

where $S_{11}(\omega)$ is the quantity measured by the VNA, $H_i(\omega)$ is the antenna return loss, $H(\omega)$ is the antenna transmitting-receiving transfer function, $H_f(\omega)$ is the antenna feedback loss, $G_{xx}^{\uparrow}(\omega)$ is the transfer function of the air-subsurface system modeled as a multilayered medium, the so-called Green's function, and ω is the angular frequency. The Green's function represents an exact solution of the 3-D Maxwell's equations for electromagnetic wave propagation in multilayered media. The consideration of a 3-D model is essential to take into account spherical divergence (geometric spreading) in GPR wave propagation. Solutions of Maxwell's equations for wave propagation in 3-D multilayered media are well known (Michalski and Mosig, 1997). We derived this specific Green's function using a recursive scheme to compute the transverse electric and magnetic global reflection coefficients of the multilayered medium in the spectral domain (Slob and Fokkema, 2002; Lambot *et al.*, 2004b). The transformation back to the spatial domain is performed by evaluating numerically a semi-infinite, complex integral. A specific procedure was applied for a fast and accurate evaluation of that integral (Lambot *et al.*, 2007), which inherently contains singularities.

The electromagnetic properties (i.e., the dielectric permittivity and the electrical conductivity) of the multilayered medium are retrieved by a full-waveform inversion of the Green's function. This inversion can be done in the frequency domain, where the wave is actually modeled and measured, or in the time domain. For the time domain analysis, the generated and modeled frequency domain Green's functions are first transformed in the time domain using the inverse Fourier transform. The inverse problem is formulated in the least-squares sense and the objective function is accordingly defined as follows:

$$\phi(\mathbf{p}) = \left(\mathbf{g}_{\mathbf{xx}}^{\uparrow *} - \mathbf{g}_{\mathbf{xx}}^{\uparrow}\right)^{T} \left(\mathbf{g}_{\mathbf{xx}}^{\uparrow *} - \mathbf{g}_{\mathbf{xx}}^{\uparrow}\right) \tag{2.2}$$

where $\mathbf{g}_{\mathbf{xx}}^{\uparrow *}$ and $\mathbf{g}_{\mathbf{xx}}^{\uparrow}$ are, respectively, the generated and the modeled Green's function vectors (arranged versus frequency) and $\mathbf{p}$ is the vector of parameters to be estimated, i.e., electromagnetic properties and dimensions of the multilayered medium. This objective function is minimized by means of the global multilevel coordinate search algorithm (Huyer and Neumaier, 1999) combined sequentially with the classical Nelder-Mead simplex algorithm (Lagarias *et al.*, 1998). The reader is referred to the study by Lambot *et al.* (2004b, 2006b) for additional details on this model and the optimization procedure for GPR signal inversion.

2.4.2 Numerical experiments

The objective of these numerical experiments is to investigate and compare different inversion strategies for the estimation of thin layer properties and examine the well-posedness of the inverse problem. Synthetic radar datasets were generated assuming a two-layered model. Inversions were performed in both the frequency and time domains, assuming either the correct two-layered configuration or a simplified one-layered model. This resulted in four different inversion strategies.

The GPR frequency bandwidth used for these synthetic experiments ranges from 0.8 to 2.6 GHz, with a frequency step of 6 MHz. The antenna phase center (S) was situated at 0.5 m in air above the soil surface (see Fig. 2.1). Different thicknesses h_1 were considered for the top thin layer (0.005, 0.01, 0.02, 0.04 and 0.08 m, as used in Lambot *et al.* (2006b)), while the bottom layer was an infinite half-space. We chose 13 different volumetric water contents for each layer, evenly ranging from 0 to 0.36. This resulted in 845 two-layered model configurations (13 × 13 × 5).

The relations between the soil water content and its electromagnetic properties were described, respectively, by (1) the model of Ledieu *et al.* (1986) to derive the relative soil dielectric permittivity from water content (see Eq. (1.17)) with the parameters $a = 0.1264$ and $b = -0.1933$, and by (2) the model of Rhoades *et al.* (1976) to relate soil electrical conductivity σ to water content θ:

$$\sigma = (c\theta^2 + d\theta)\sigma_w + \sigma_s \tag{2.3}$$

where the parameters were set to $c = 1.85$, $d = 3.85 \times 10^{-2}$, $\sigma_w = 0.075$ Sm^{-1} and $\sigma_s = 5.89 \times 10^{-4}$ Sm^{-1}. These parameters were determined in the laboratory for that specific sand subject to different water contents and salinities in

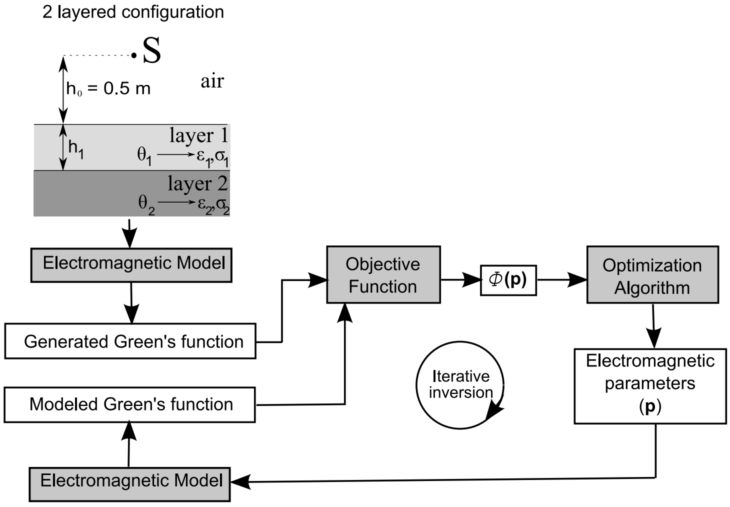

Figure 2.1: Model configuration used for the numerical experiments and inverse modeling flowchart.

Lambot *et al.* (2004b). Both dielectric permittivity and electrical conductivity are thus related to the soil water content by these specific relationships.

As the generated data are created with a two-layered model, the inversion procedure taking into account this layering with the two-layered model is naturally exact in contrast to the model with a one-layered configuration. However, the two-layered inversion may suffer from uniqueness and optimization problems. The inverse problem assuming a single layer is more simple, but modeling errors are then introduced. A one-layered model counts 3 parameters to invert (the electromagnetic parameters ε and σ and the antenna height h_0) while 5 parameters are inverted with the two-layered model (ε_1, σ_1, h_1, ε_2, σ_2), as the antenna height above the soil is assumed to be exactly known. The error in the estimation of a parameter is defined as the absolute value of the difference between the true parameter and the value obtained by inversion. The estimation errors are computed for each inverted parameter.

2.4.3 Laboratory experiments

The objective of the laboratory experiments was to analyze in realistic conditions the same configurations of layering as for the numerical experiments. Indeed, inverse modeling of actual data are expected to show the same divergences as a function of the different model configurations and inversion strategies, plus issues related to measurement and modeling errors. Modeling errors can be caused by the antenna calibration model, the assumption of a plane layered soil surface and by the fact that the models of Ledieu *et al.* (1986) and Rhoades *et al.* (1976) may not be the correct models to relate water content to the electric properties of the layers. A schematic representation and a picture of the laboratory experimental setup are depicted in Fig. 2.2(a) & (b), respectively. A square sandbox made of wood (with 1.50 m on each side and 0.50 m in height) was filled with two layers of sand subject to specific water contents. A perfect electrical conductor (PEC), namely, an aluminum sheet, was placed on the bottom of the sandbox in order to control the bottom boundary condition in the electromagnetic model. As a result, deeper laboratory materials (concrete with rebar) did not influence the measured backscattered GPR signal.

The water content in the sand layers was controlled by mixing calculated volumes of dry sand and demineralized water. Volumetric samples were then collected to determine the actual water content of the sand layers. The top thin layer (layer 1 in Fig. 2.2) was subject to ten different water contents, ranging from 0 to 0.270. Its thickness was set to 0.005, 0.01, 0.02, 0.04 and 0.08 m, respectively. The second layer (layer 2 in Fig. 2.2) was subject to a constant water content of about 0.064. Its thickness was kept constant and was equal to 0.32 m. The two sand layers were separated by a thin plastic sheet that had no influence on the propagation of the electromagnetic waves. The resulting total number of model configurations was then 50 (10 × 5). The radar antenna was at a fixed position above the sandbox, at about 30 cm above the sand surface depending on the thin-layer thickness.

We used an ultra-wideband stepped frequency continuous wave radar system using a vector network analyzer (VNA) (ZVRE, Rohde & Schwarz, Münich, Germany) combined with an off-ground monostatic horn antenna. The antenna system was a linear polarized double-ridged broadband horn (BBHA 9120 A, Schwarzbeck Mess-Elektronik, Schönau, Germany). Antenna dimensions are 22 cm in length and 14×24 cm^2 in aperture area, and the nominal frequency range is from 0.8 to 5 GHz. The antenna was connected to the reflection port of the VNA with a high-quality coaxial cable of 2.5 m length. We calibrated the VNA at the antenna feed point using a 50-Ω OSM calibration kit. The frequency-dependent complex ratio S_{11} between the returned and the emitted signal was measured sequentially at 301 stepped frequencies from 0.8 to 2.6 GHz, with a frequency step of 6 MHz. Measured signals from the laboratory (S_{11}) were first transformed in Green's functions using Eq. (2.1) and previously determined transfer functions (Lambot *et al.*, 2004a). Figure 2.3 presents the measured Green's functions in the time domain according to the 50 configurations. These measured Green's functions were then used for inverse modeling in order to retrieve the parameters of the two-layered medium.

Sampling for volumetric water content determination using the oven-drying method at 105°C for at least 48h was performed using different sampling volumes for the different thin-layer thicknesses. Laboratory-made metallic rings were used to collect the sand samples, with heights corresponding to the thin-layer thicknesses. The bulk density of the sand was found to be 1.39 g/cm^3. Five samples were taken for each mix of sand and water, accounting in total for 50 water content measurements.

The same models as the ones used in the numerical experiments (one- and two-layered models) were used for performing the inversions in both the frequency and time domains, except that the width of the second layer (h_2) was inverted in addition as the second layer is not a half-space medium anymore in

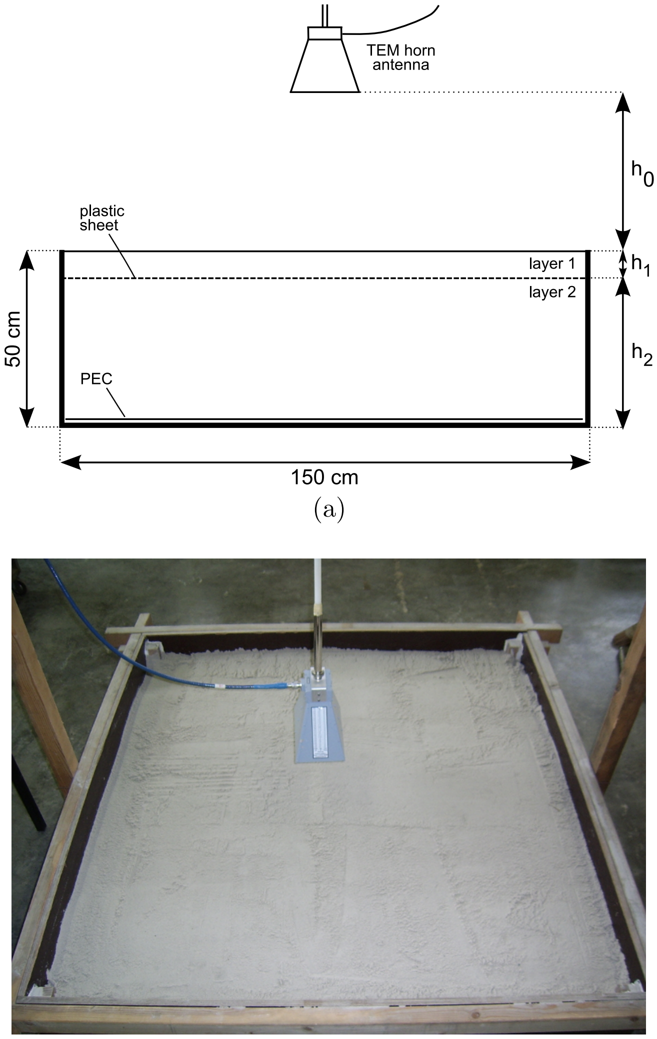

(a)

(b)

Figure 2.2: Schematic of the laboratory experimental setup showing the GPR horn antenna above the two-layered sandbox (a) and picture of the experimental setup viewed from the top (b).

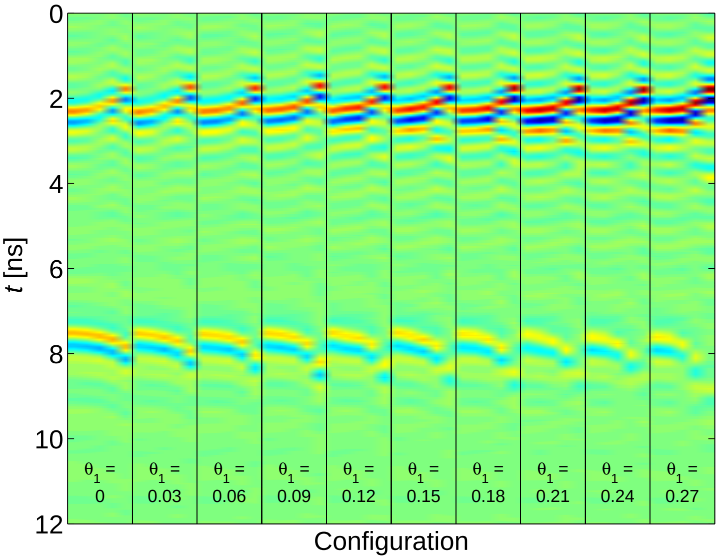

Figure 2.3: Time domain representation (b-scan) of the measured Green's functions for the 50 configurations in the laboratory experiments. Vertical lines delineate the configurations according to the 10 different first layer water content (θ_1). For each θ_1, five different first layer thicknesses were set.

the laboratory experiments. Furthermore, two other inversion scenarios were performed: 1) a two-layered model in the time domain ignoring the reflections from the PEC situated at the bottom of the sandbox (TIME 2L*), and 2) a one-layered model in the time domain with inversions focused on the surface reflection only (TIME L-M). In the TIME 2L* inversion scenario, the final reflection from the PEC is avoided by focusing on a time window defined between 0 and 5 ns, and hence, it is naturally not accounted for in the layered model. This simplified model permits a decrease in the number of unknowns in the inversion from seven to six (ε_1, σ_1, h_1, ε_2, σ_2 and h_0). In the TIME L-M inversion scenario, the GPR signal is reduced to the sand surface reflection in the time domain. In this case, the soil model reduces to a half-space and the number of parameters to estimate is two, i.e., the surface dielectric permittivity ε_1 and the antenna height h_0. This highly simplifies the inverse problem and inversions can be performed using local optimization, in our case with the Levenberg-Marquardt algorithm. This last inversion strategy has shown to be practical and suitable in different field conditions (Lambot *et al.*, 2008b).

In order to estimate the posterior distributions of the optimized parameters, the parameter space was also sampled by a Markov-Chain Monte-Carlo method using the Metropolis-Hastings algorithm implemented in the framework of the differential evolution adaptive metropolis (DREAM) algorithm (Vrugt *et al.*, 2009).

2.5 Results and discussion

2.5.1 Numerical experiments

Inversion with the correct two-layered model

Figure 2.4 shows the observed errors on inverted ε_1 with the correct two-layered model for the 845 considered model configurations, presented as a function of the water content of the two layers and the thickness of the thin layer. Although the model used for inverse modeling is the same as the one used for generating the synthetic radar data (i.e., a two-layered model), some discrepancies between the true and optimized parameters can be observed. For cases where there is no contrast between the two soil layers (i.e., homogeneous medium), the error is almost always null and, in all cases, negligible. For very thin layers (Fig. 2.4(a) and (b)), the amplitude of the error generally increases with the dielectric contrast between the two layers. For thicker layers, the error is more randomly distributed as a function of the contrast. In general, errors decrease with increasing top layer thickness. The statistical behavior of this error follows a strong negative exponential distribution (i.e., the mean error is 1.0059 while the median error is only 0.0107) with the majority of the errors that are null. The results for ε_2 are presented in Fig. 2.5. Again, the amplitude of the error increases with the contrast between the two layers, especially for thin layers. The errors in ε_2 are globally correlated with errors in ε_1 but they are larger than errors in ε_1.

The observed behaviors in the error can be partly attributed to the maximum resolution that can be theoretically achieved with the considered frequency range, namely, 0.8-2.6 GHz. The range resolution is usually assumed as one quarter of the average wavelength. In dielectric media, the wavelength is decreasing proportionally to the square root of the dielectric permittivity. Hence, the range resolution increases with water content. In our case, for an average relative dielectric permittivity of nine and for a central frequency of 1.8 GHz, the range resolution is found to be 1.4 cm. This corroborates the results in Fig. 2.4, as significant errors are mostly observed for thinner layers. It is worth noting that in a series of cases, the observed errors for sub-resolution characterization may be also negligible. For cases where the layer thickness is larger than the range resolution, still some errors can be observed. These errors are to be attributed to optimization issues, as the global minimum of the objective function (equal to zero) could not be reached by the optimization algorithm.

For instance, Fig. 2.6 represents the synthetic and fitted Green's functions, in both the frequency and time domains, for the largest error observed for ε_1 (for $h_1 = 0.01$ m, $\theta_1 = 0.36$, and $\theta_2 = 0$). Although the fit is relatively good, the error in the estimated parameter is quite large. It was not possible to find a better solution with the optimization algorithm, even subject to a relatively large number of iterations (> 10000). In the time domain, the reflections from the two layer interfaces cannot be clearly distinguished, as a result of the subresolution conditions. However, a slight misfit can still be observed beyond the main reflection peak.

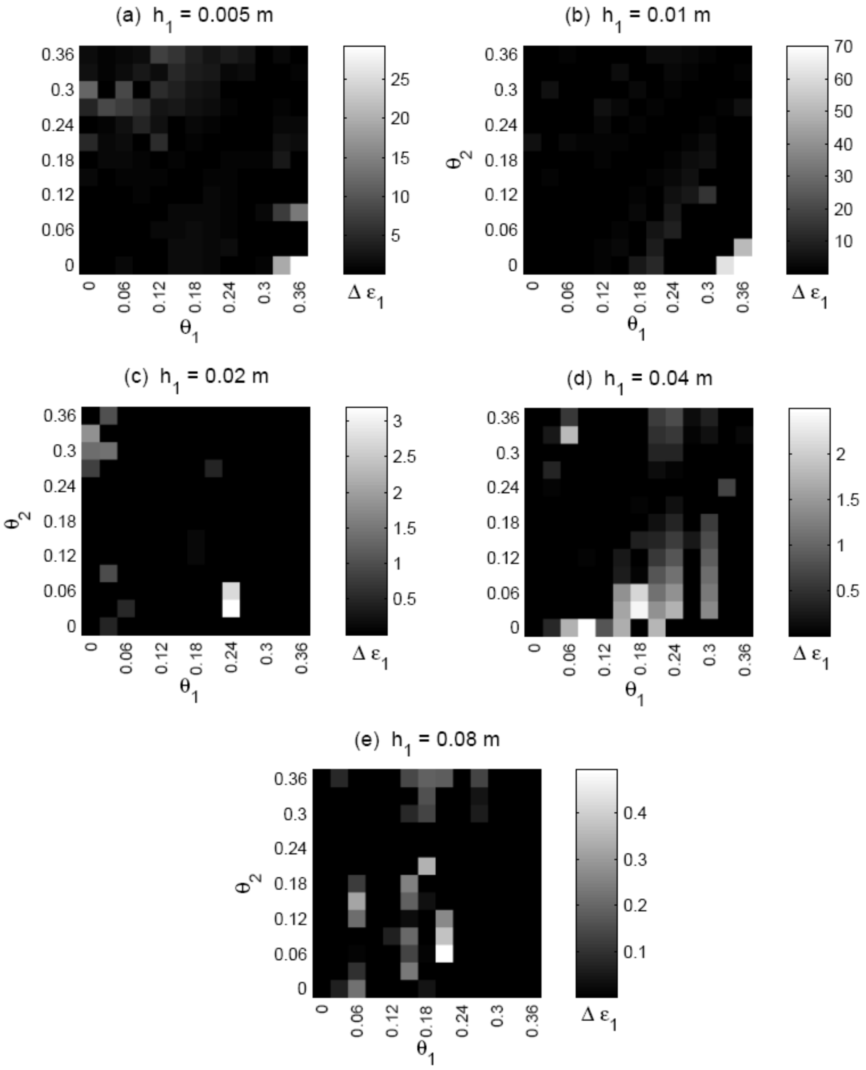

Figure 2.4: Error on the dielectric permittivity of the first layer $\Delta\varepsilon_1$ for each top layer thickness h_1, with inversions performed with the two-layered model in the frequency domain. Results from the numerical experiments.

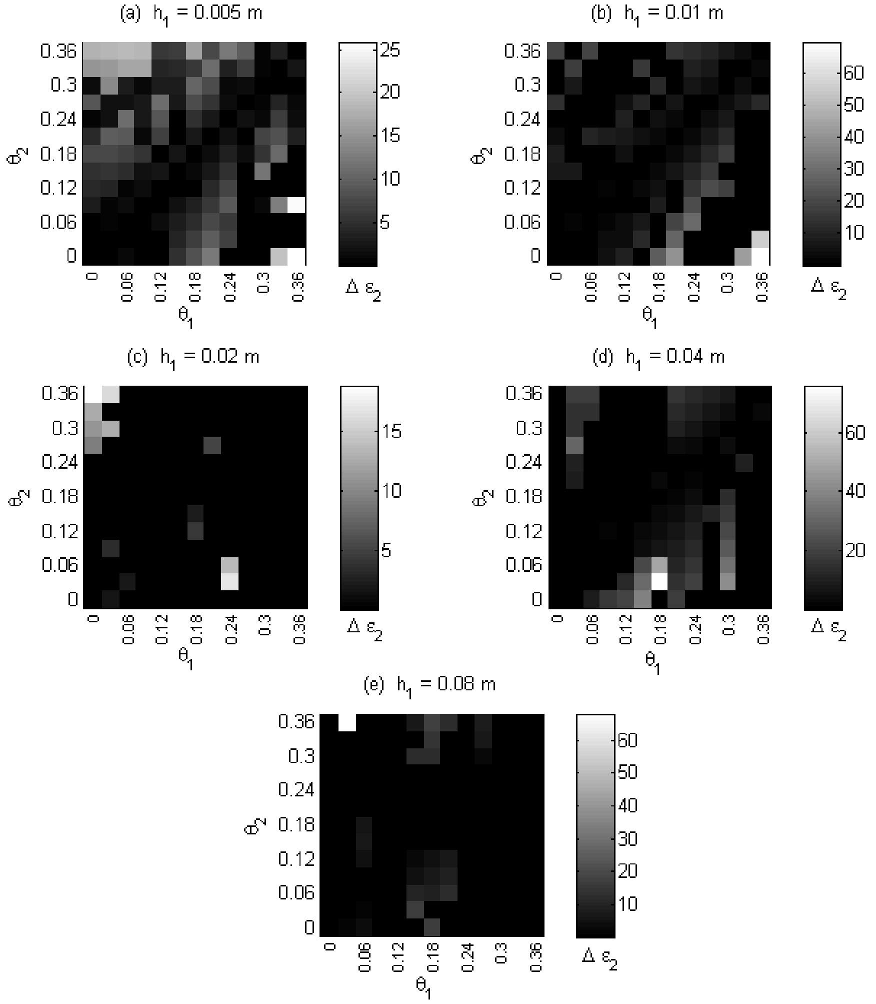

Figure 2.5: Error on the dielectric permittivity of the second layer $\Delta\varepsilon_2$ for each top layer thickness h_1, with inversions performed with the two-layered model in the frequency domain. Results from the numerical experiments.

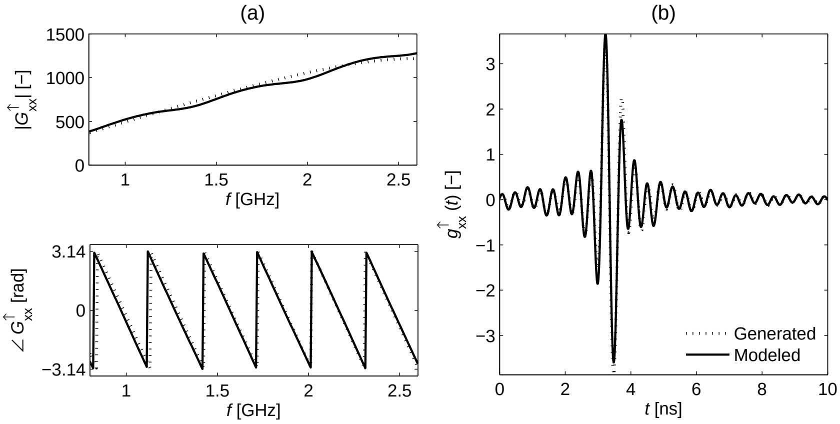

Figure 2.6: Generated and inverted Green's functions for a first layer water content of 0.36, a second layer water content of 0 and a first layer thickness of 0.01 m, depicted in frequency (a) and time domain (b). Results from the numerical experiments.

Figures 2.7 and 2.8 show 2-D slices of the 5-D objective function for a number of parameter pairs considering, respectively, a top thin layer of 1 cm (under range resolution) and 8 cm (above range resolution). In the case of the thinner layer (Fig. 2.7), the global minimum for the thin layer dielectric permittivity (ε_1) is well defined in all parameter planes. However, some correlation and weaker sensitivity can be observed in the $\varepsilon_1 - h_1$ plane (Fig. 2.7(c)), which is disadvantageous for its estimation. Accounting for the geometrical spreading of the wave and for the electrical losses due to the electrical conductivity is thus crucial in the model inversion, as these phenomena also depend of h_1, so that h_1 can be determined independently from ε_1.

The objective function topography with respect to the electrical conductivity for both layers is always flat, which denotes a poor sensitivity of the model to these parameters. It is also worth noting that the objective function topography is relatively complex, including oscillations and local minima. In the 5-D objective function, this is therefore expected to strongly affect the optimization procedure. In Fig. 2.8, we observe that, compared to the 1-cm layer case, the global minimum of the objective function is better defined with increased sensitivity of the model to all parameters (except for σ_1 and σ_2). This was expected as the radar data contain sufficient information to ensure a unique estimate of the layer parameters.

One-layer model inversions and effect of the contrast

Fig. 2.9 shows the error in the estimated dielectric permittivity of the top layer ($\Delta\varepsilon_1$) with respect to the dielectric contrast between the two layers, expressed in terms of water content contrast. Results are presented for both inversion strategies in the frequency domain, assuming the correct two-layered model

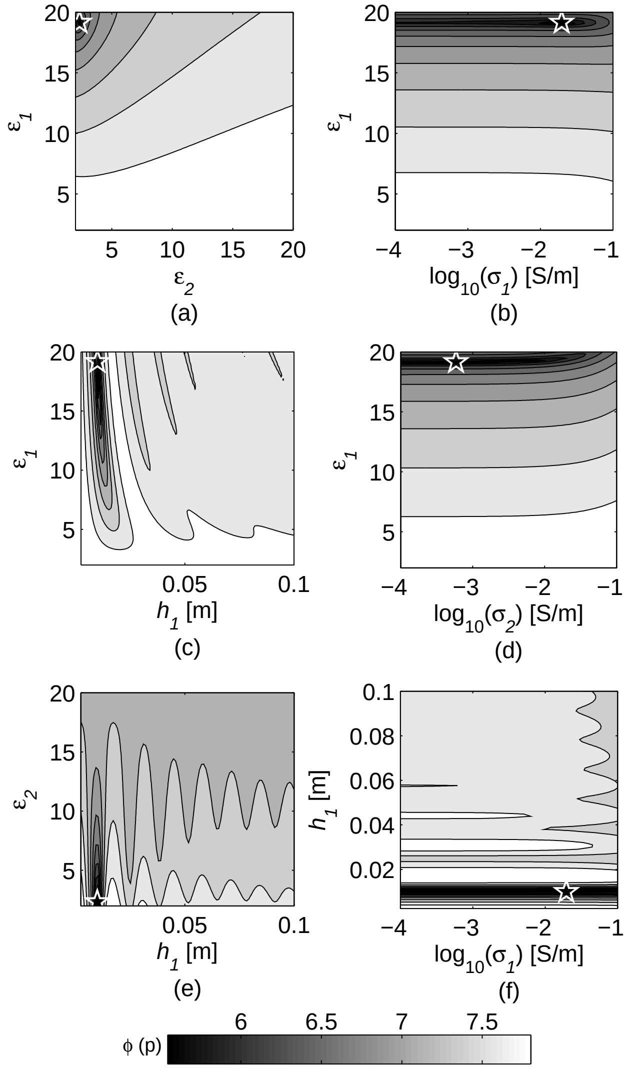

Figure 2.7: Response surfaces of the objective function logarithm $\log_{10}(\phi)$ in the (a) ε_1-ε_2, (b) ε_1-$\log_{10}(\sigma_1)$, (c) ε_1-h_1, (d) ε_1-$\log_{10}(\sigma_2)$, (e) ε_2-h_1 and (f) h_1-$\log_{10}(\sigma_1)$ parameter planes. These objective functions are plotted for the particular case depicted in Fig. 2.6, i.e., $h_1 = 0.01$ m, $\theta_1 = 0.36$, and $\theta_2 = 0$. True parameter values are represented by the white star marker. Results from the numerical experiments.

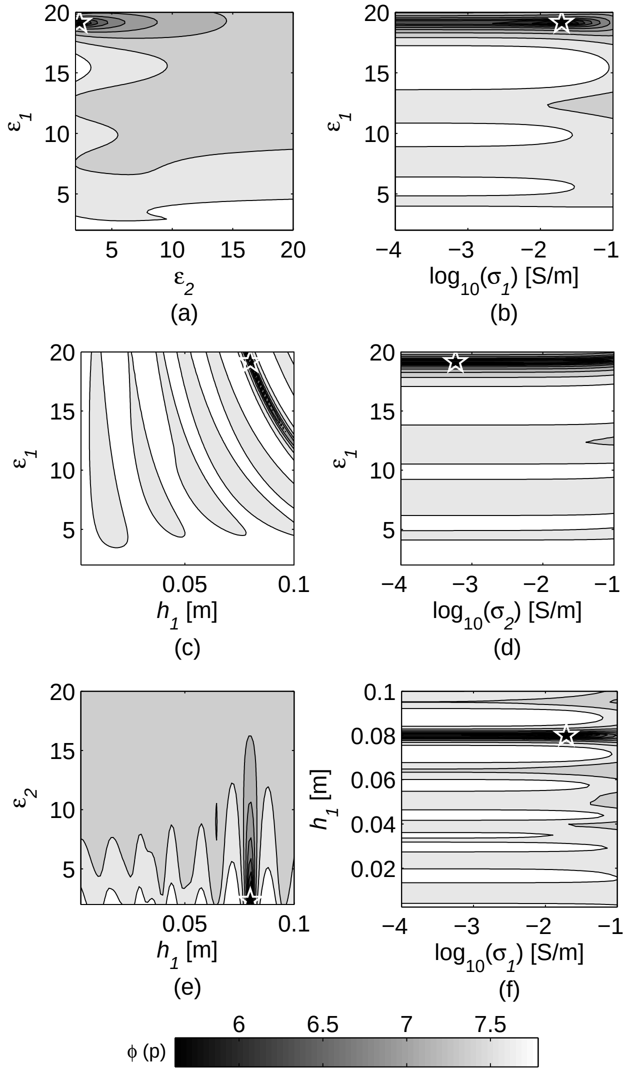

Figure 2.8: Response surfaces of the objective function logarithm $\log_{10}(\phi)$ in the (a) ε_1-ε_2, (b) ε_1-$\log_{10}(\sigma_1)$, (c) ε_1-h_1, (d) ε_1-$\log_{10}(\sigma_2)$, (e) ε_2-h_1 and (f) h_1-$\log_{10}(\sigma_1)$ parameter planes. These objective functions are plotted for the case where $h_1 = 0.08$ m, $\theta_1 = 0.36$, and $\theta_2 = 0$. True parameter values are represented by the white star marker. Results from the numerical experiments.

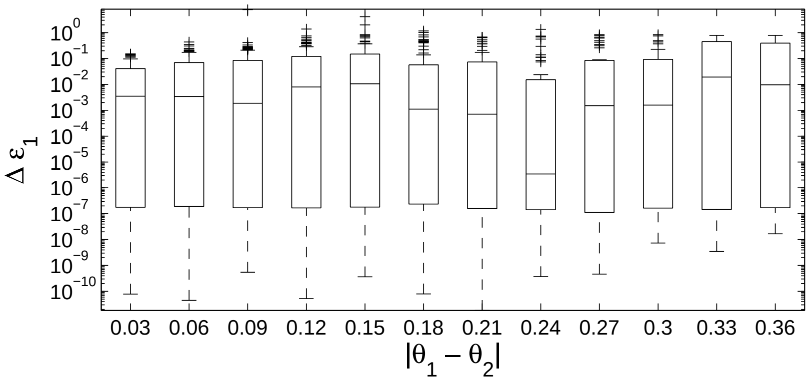

(a)

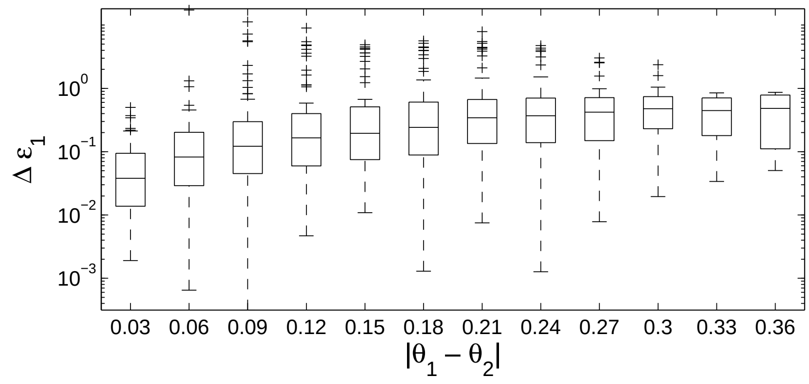

(b)

Figure 2.9: Error distribution of the dielectric permittivity of the top layer, as a function of the contrast in water content between the layers. The box extent shows interquartile range (i.e., the range between the first and the third quartiles), while the median of the error distribution is represented by the horizontal line that cuts the box. Whiskers length is 1.5 times the vertical length of the boxes. Outlier error values are displayed as crosses outside of the whiskers. Comparison between inversions performed with the two-layered (a) and the one-layered (b) models in the frequency domain. Results from the numerical experiments.

and the simplified one-layered model, respectively. Errors for null contrast $|\theta_1 - theta_2 = 0|$ are not presented in this graph as they are negligible.

For the two-layered model [Fig. 2.9(a)], there is no clear relationship between the contrast and the error on the dielectric permittivity. We can observe the presence of numerous outliers with high error values that are out of the whisker ranges. These outliers are expected to originate from nonconvergence of the optimization algorithm.

For the one-layered model [Fig. 2.9(b)], a positive relationship between the median values of the errors on ε_1 and the contrast can be observed. In that respect, it is worth noting that the errors are shown on a logarithmic scale and, therefore, the observed trend is significant, in particular for lower contrasts. As expected, the errors for the one-layered model are larger compared to the exact model inversion (modeling errors are introduced). Large contrasts between the layers lead to significant errors as a result of constructive and destructive interferences in subresolution conditions (Lambot *et al.*, 2006b) [e.g., the two reflection peaks in the time domain cannot be distinguished in Fig. 4(b)]. In case of inversion with the exact model configuration, these interferences are inherently properly accounted for. When the top layer is thick enough compared to the wavelength, the reflections at the interfaces are well separated in time and, as shown by Lambot *et al.* (2006b), the one-layered model performs well for estimating the surface dielectric permittivity.

Comparison between model inversion routines

Table 2.1 shows the number of convergent configurations for both time and frequency domains and for the one-layered and the two-layered inversion models. Values number the convergent cases among the 845 model configurations and percentages refer to the proportions with respect to the total. A case is counted as convergent according to the error on the dielectric permittivity of the first layer and on the first layer thickness, as classified in Table 2.1. This last parameter can obviously only be determined with the inversions performed with the two-layered model.

The largest convergence rate is encountered with the inversion performed in the frequency domain for the two-layered model. The one-layered model clearly shows less convergent cases than the two-layered model. This is obvious since the one-layered model does not take into account the presence of electromagnetic contrast between the layers. All the same, inversions with the one-layered model (three parameters) are about 6 times faster in terms of computation time compared to the two-layered model inversions (five parameters). Comparing time- and frequency-domain analysis, for the one-layered model, better results are obtained in the time domain than in the frequency domain, while it is not the case with the two-layered model. As time- and frequency-domain data are equivalent in terms of information content, these differences are to be attributed to the different model sensitivities with respect to the surface dielectric permittivity. Indeed, the transformation of the frequency domain data to the time domain alters the shape of the objective function and different global minima may be found.

Table 2.1: Number of convergent configurations for time and frequency domains and for the one-layered and the two-layered inversion models in the numerical experiments.

	Error on surface dielectric permittivity	
	$\Delta\varepsilon_1 \leq 0.1$	$\Delta\varepsilon_1 \leq 0.5$
Frequency domain		
1-layer	104 (12.3%)	268 (31.7%)
2-layer	485 (57.4%)	624 (73.8%)
Time domain		
1-layer	150 (17.7%)	324 (38.3%)
2-layer	342 (40.5%)	426 (50.4%)
	Error on the first layer thickness	
	$\Delta h_1 \leq 0.005$ m	$\Delta h_1 \leq 0.01$ m
Frequency domain (2-layer)	522 (61.8%)	646(76.4%)
Time domain (2-layer)	352 (41.6%)	383 (45.3%)
	$\Delta\varepsilon_1$ & Δh_1	
	$\Delta\varepsilon_1 \leq 0.1$ & $\Delta h_1 \leq 0.005$ m	$\Delta\varepsilon_1 \leq 0.5$ & $\Delta h_1 \leq 0.01$ m
Frequency domain (2-layer)	403 (47.7%)	535 (63.3%)
Time domain (2-layer)	280 (33.1%)	314 (37.1%)

Hence, this results in different shapes for the objective function topography, with more or less well-defined global minima. Differences may also partly originate from the relation between a specific objective function topography and the used optimization algorithm (GMCS-NMS), for which the same parametrization among the scenarios was kept.

2.5.2 Laboratory experiments

Comparison with ground-truth measurements

Figure 2.10 shows the soil surface relative dielectric permittivity estimated from GPR data inversion as a function of the ground-truth soil volumetric water content for six different inversion scenarios. The symbols discriminate the values according to the five top layer thicknesses that were set in the sandbox for each water content. The dotted vertical line at $\theta_v = 0.064$ indicates the soil water content of the bottom layer that was determined by inverse modeling of the measured GPR signal above the bottom layer without the top thin layer. In that case, the inverse problem is expected to result in accurate estimates (Lambot *et al.*, 2004b). For each scenario, the relationship between ε_{GPR} and θ_v is fitted assuming the model of Ledieu *et al.* (1986) (Eq. (1.17)).

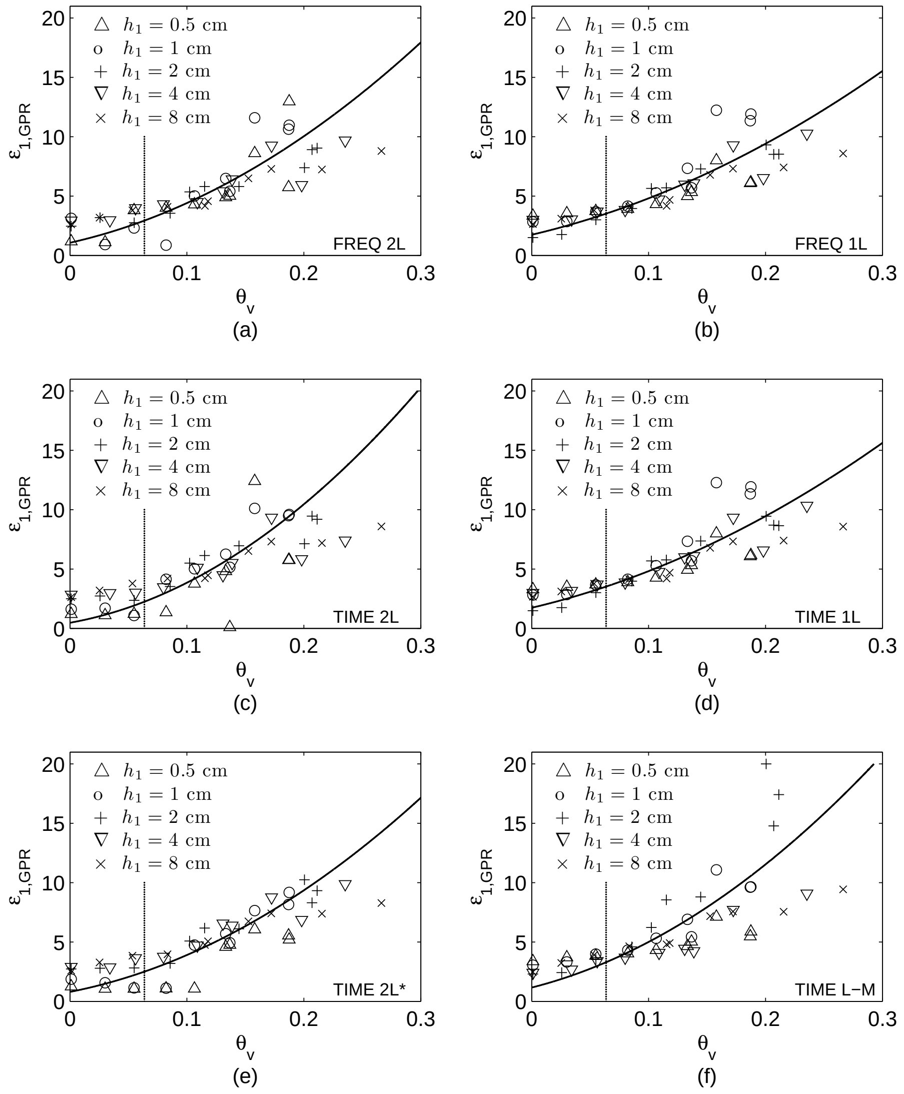

Figure 2.10: Soil surface relative dielectric permittivity estimated from GPR data inversion ($\varepsilon_{1,GPR}$) as a function of soil volumetric water content θ_v. Dielectric permittivities are depicted with different symbols according to the top layer thickness. The model of Ledieu *et al.* (1986) is fitted on the observed data (solid line). The dotted vertical line at value $\theta_v = 0.064$ indicates the soil water content of the second layer (constant for all configurations). (a) Two-layered inversion in the frequency domain. (b) One-layered inversion in the frequency domain. (c) Two-layered inversion in the time domain. (d) One-layered inversion in the time domain. (e) Two-layered inversion in the time domain assuming no PEC as lower-halfspace. (f) Inversion in the time domain by focusing on the surface reflection only (Lambot *et al.*, 2006b).

Table 2.2: Statistics on the comparison between ground measurements of volumetric water content and GPR-measured dielectric permittivities.

	a	b	$RMSE$	r^2
Frequency domain				
2-layer	0.094	-0.097	1.912	0.714
1-layer	0.114	-0.151	1.542	0.780
Time domain				
2-layer	0.079	-0.054	2.479	0.579
1-layer	0.114	-0.150	1.548	0.781
Time 2-layer*	0.092	-0.082	1.651	0.699
Time L-M	0.086	-0.093	2.682	0.665

The relationships between the first-layer dielectric permittivities and water content are quite well defined and consistent for all scenarios. In general, the fits are relatively good, except for higher water contents. It is worth noting that the measured water contents are expected to be also subject to significant uncertainties, due to the following: 1) the difficulty to properly sample so thin layers with a loose material and 2) the sampling scale (5-10 cm^2), which is different from the GPR characterization scale (order of 2500 cm^2), and this is in relation to the inherent heterogeneity. The mean confidence interval at 95%, calculated for each mix of humid sand, is equal to 0.010. Outlier permittivity values can be observed and are either very low [FREQ 2L Fig. 2.10(a), TIME 2L Fig. 2.10(c) and TIME 2L* Fig. 2.10(e)] or very high [TIME L-M Fig. 2.10(f)] compared to expected values from the fitted model of Ledieu *et al.* (1986). For overestimated values, their origin may be theoretically twofold (Lambot *et al.*, 2006b). First, they can result from a too high electrical conductivity, as this parameter is neglected in the TIME L-M inversion. Second, they can originate from constructive interferences in presence of thin layers in the near surface. In our case, as we observe that these discrepancies occur only for thin layers (especially 2 cm), they are believed to come from constructive interferences. In addition, the electrical conductivity is expected to be low for a sand wetted with demineralized water.

It is worth noting that the values obtained with the largest layer thickness (h_1 = 8 cm) are very similar among the inversion scenarios. Indeed, with such layer thickness, the reflection from the second layer interface does not affect the first reflection within the given range resolution. These results for the thicker layer are therefore expected to be the most accurate.

Table 2.2 shows parameters a and b of the model of Ledieu *et al.* (1986), the root mean square error (RMSE) between the fitted and measured dielectric permittivities, and the coefficient of determination r^2 between θ_v and $\sqrt{\varepsilon_{GPR}}$ for the corresponding six scenarios. Except for the TIME L-M scenario, the one-layered models show the lowest RMSE and largest coefficients of determination r^2. In general, better results are obtained with the one-layered model as the dimensionality of the inverse problem is lower. Similarly, the TIME 2L* scenario also presents relatively low RMSE as, in that case, only six parameters are to be inverted for (see also Fig. 2.10(e)). For scenario TIME L-M, a large RMSE and a low r^2 are obtained, arising from the presence of numerous outliers. These outliers come from low model adequacy, as it does not account for the constructive and destructive interferences produced by the two interfaces.

The two-layered models show intermediate performances in terms of RMSE and r^2, as a trade-off between model adequacy and inverse problem complexity. A smart parameterization of the inverse algorithm is required because of the high non-linearity of the model to its parameters. In that way, reducing the number of parameters to optimize considerably makes the inverse problem easier. For instance, the best performance of the model TIME 2L* compared to FREQ 2L and TIME 2L comes simultaneously from the limited number of parameters (passing from seven to six) and high model adequacy.

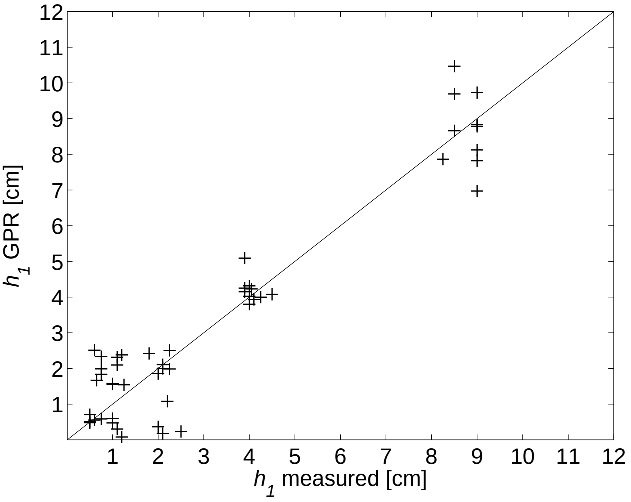

Figure 2.11: Comparison between first layer thickness measured in the sandbox and derived from GPR signal inversion using the TIME 2L* scenario.

Figure 2.11 shows the GPR-derived top layer thickness (h_1) as a function of the real thickness measured using a millimetric ruler. Inversions were performed with the TIME 2L* scenario, which produces the best results. The observed errors are relatively small, ranging from a few millimeters up to two centimeters. The most accurate estimations are obtained for the 4-cm-thick layer. For thicknesses lower than 2 cm, discrimination between the two interfaces cannot always be achieved, because, in that case, the range resolution limit is reached. As it was shown in the numerical experiments, this range resolution is about 1.5 cm for a center frequency of 1.7 GHz and a dielectric permittivity of nine. For larger thicknesses, the larger errors are to be attributed to the negative correlation between the layer thickness and its dielectric permittivity (see Fig. 2.8(c) & 2.12(c)).

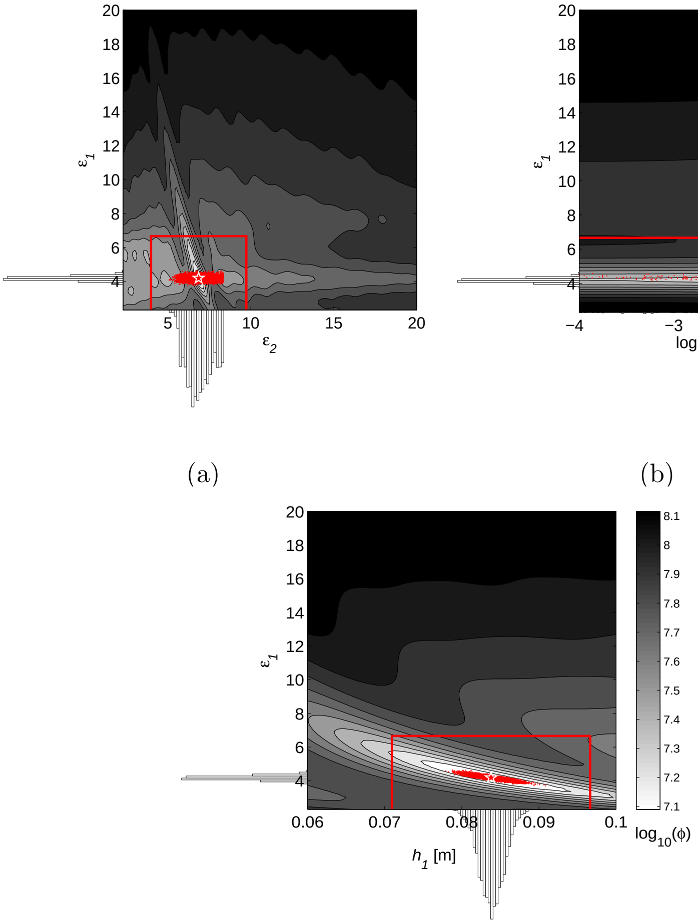

(a) (b)

(c)

Figure 2.12: Response surfaces of the logarithm of the objective function in the ε_1-ε_2 (a), ε_1-σ_1 (b) and ε_1-h_1 (c) parameter planes for a GPR laboratory measurements inversion (FREQ 2L scenario) where θ_v = 0.115 and h_1 = 8 cm. The unique value retrieved by the GMCS-NMS inversion is depicted with a star. Points of the parameter space sampled by the DREAM algorithm are projected (in red) over the response surfaces. Histograms of the posterior distributions are drawn along the axis of the parameters. Confidence intervals using a linear approximation of the slope of the objective functions are drawn in red rectangles.

Response surfaces

Response surfaces of the objective functions for a laboratory measurement (θ_v = 0.115 and h_1 = 8 cm) inverted with the FREQ 2L scenario are depicted in Fig. 2.12 in the ε_1-ε_2, ε_1-σ_1 and ε_1-h_1 parameter planes (other parameter values were fixed at their optimized values). Similar response surfaces were obtained when compared with the numerical experiment results (Figs. 2.7 & 2.8), especially for the ε_1-σ_1 parameter plane. The response surface of the ε_1-ε_2 parameter plane (Fig. 2.12(a)) shows some local minima, pointing out the need of a global search optimization algorithm to find the global minimum. It is worth remarking that, in the presence of measurements and modeling errors due to the real conditions, the response surface becomes flatter, as it can be noticed for the ε_1-h_1 parameter plane in Figs. 2.8(c) & 2.12(c).

Markov-Chain Monte-Carlo sampling with the DREAM algorithm led to the sampling of more than 400,000 sets of parameter values that represent probable solutions of the inverse problem. These points generally match the locations of the parameter space where objective function values are low, as in Fig. 2.12(b) and (c), whereas the points in Fig. 2.12(a) do not match exactly the minimum valley along ε_1. Confidence intervals were also drawn on the response surfaces using a linear approximation of the objective function in the proximity of the global minimum (see chapter 4, Inversion uncertainties, for a description of the method). This method resulted in an overestimation of the parameter intervals because of the complexity of the inverse problem. It is worth mentioning that the response surface planes are cut in the 7-dimensions parameter space at the optimized values, which may not be the exact values. Therefore, the topography of the objective function depicted in the ε_1-ε_2 plane may be incorrect, leading to the observed mismatch with the points sampled by the DREAM algorithm. Hence, the Markov-Chain Monte-Carlo sampling permits to overcome the difficulty of drawing objective functions in a multi-dimension parameter space. Histograms of the posterior distributions of the parameters were derived from the points sampled by the DREAM algorithm, resulting in an uncertainty assessment of each parameter. In particular, it can be observed that ε_2 is less sensitive than ε_1, as the cloud of points is more spread along ε_2 than ε_1. The poor sensitivity of σ_1 is well represented, with sampling points covering almost the entire parameter range.

Effect of the contrast

As it was already observed in the numerical experiments, high contrasts between the two soil layers lead, in general, to larger errors in the estimation of the surface dielectric permittivity with one-layered models. In Fig. 2.10, the dotted vertical lines correspond to the water content of the bottom layer, which is 0.064, and therefore, at this line, the contrast between the two layers is zero. Accordingly, we clearly see that, for this water content, the dispersion of the dielectric permittivities around the model of Ledieu *et al.* (1986) for the one-layered models is minimal. Indeed, the two-layered configuration then reduces to a one-layered configuration. We can also observe that, for the zero contrast, inversion results are better for the one-layered inversion, because of the lower dimensionality of the inverse problem. When the contrast between the two layers increases, the inadequacy between the one-layered model and the reality (two layers) increases, which results in proportionally larger errors.

For the two-layered inversions, in general, error also increases with the contrast. As in that case the forward model is correct, these discrepancies are to be attributed either to optimization issues or a badly defined global minimum of the objective function. As this was not observed for the numerical experiments, we believe that the problem mainly originates from the objective function topography, which inherently becomes flatter when measurement errors are present.

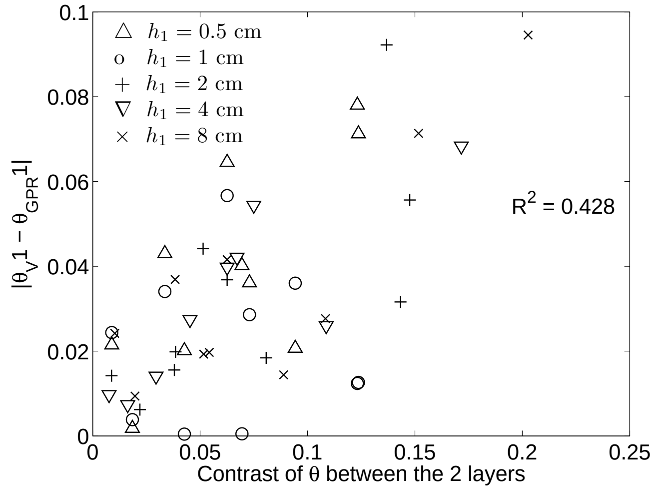

Figure 2.13: Error between the ground measurements and GPR-derived soil surface water content as a function of the contrast between the two layers for TIME L-M inversion scenario. Coefficient of determination r^2 is depicted in the upper-left corner.

Figure 2.13 shows the absolute value of the difference between the measured and the fitted top layer water content as a function of the contrast between the layers for the TIME L-M inversion scenario. This figure emphasizes the positive correlation between the contrast and the error on the GPR-derived soil properties, as already observed in Fig. 2.10. It is important to mention here that this inversion strategy (i.e., a time domain inversion focusing on the surface reflection only) appears to be very robust in general when dealing with field data (Weihermüller *et al.*, 2007; Lambot *et al.*, 2008b). In that respect, these laboratory experiments show that one-layered inversions even perform relatively well in the presence of thin layers with low contrasts. For high contrasts, however, accounting for thin layers is necessary.

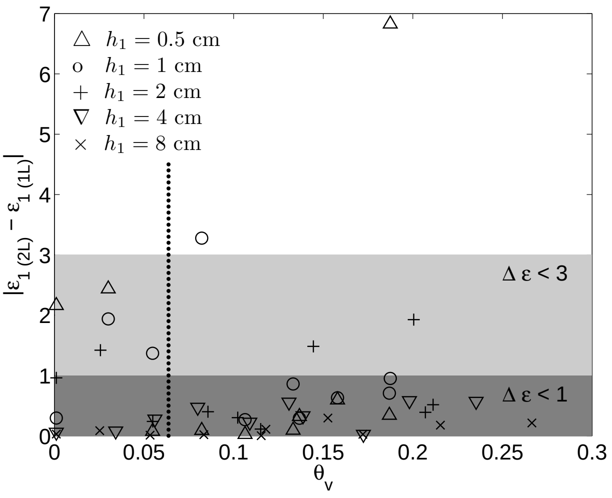

Figure 2.14: Absolute difference in the top-layer dielectric permittivities between one- and two-layered models in frequency domain as a function of the top-layer volumetric water content. Dielectric permittivities are depicted with different symbols according to the first-layer widths. The dotted vertical line at value $\theta_v = 0.064$ indicates the soil water content of the second layer.

Comparison between one- and two-layered models for estimating the surface dielectric permittivity

Figure 2.14 shows the absolute difference in dielectric permittivities of the top layer between the one- and two-layered inversions, as a function of the ground-truth top-layer water content. This figure allows the evaluation of the resulting error when a one-layered model is assumed for a two-layered medium. Gray areas in the graph delineate two dielectric permittivity error thresholds, namely, $\Delta\varepsilon_1 \leq 1$ and $\Delta\varepsilon_1 \leq 3$. Dielectric permittivities are depicted with different symbols according to the first-layer thickness.

All the values that are above the two thresholds pertain to configurations with small layer thicknesses, i.e., $h_1 = 0.5$ cm, $h_1 = 1$ cm and, to a lesser extent, $h_1 = 2$ cm. On the other side, configurations whose first-layer thickness are $h_1 = 8$ cm systematically lead to low differences (i.e., very close dielectric permittivity estimations are obtained with the two model configurations). As expected, this shows that a top layer thick enough compared to the wavelength can be characterized from the surface reflection only. It also appears that errors sightly increase with higher water contents, denoting the dielectric contrast effect.

Effect of the frequency bandwidth sampling

Information content in the radar data increases with increasing bandwidth. An important asset of using VNA technology is that the bandwidth is fully controllable and, in particular, ultrawideband GPR can be set up. The only limitation is the operating frequency range of the antenna. However, in some cases, other factors may also affect the utilizable bandwidth. In our case, in the laboratory conditions, lower frequencies were subject to ambiguous reflections from extraneous objects present in the laboratory, given the limited size of the sandbox. Measurements for higher frequencies were also influenced to some extent by the inherent heterogeneities present in the sandbox, including slight surface roughness. For instance, Fig. 2.15 shows that the GPR measured signal becomes of poorer quality for the lowest and highest frequencies of the 0.8-2.6 GHz bandwidth we used, and in particular below 1 GHz and above 2 GHz. The correct two-layered model used for the inversion could reproduce remarkably well the measured signal in both the frequency and time domains.

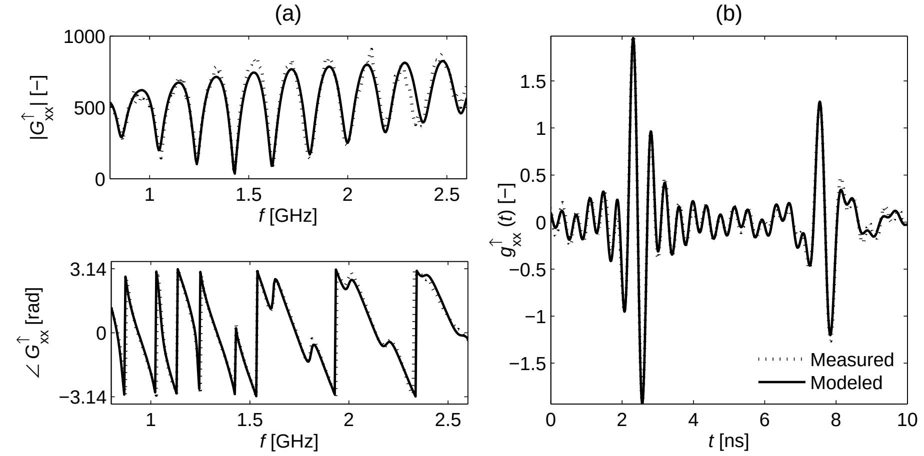

Figure 2.15: Measured and modeled Green's functions on the frequency bandwidth from 0.8 to 2.6 GHz, depicted (a) in the frequency and (b) time domain.

In order to determine the optimal frequency bandwidth for the top layer dielectric permittivity estimation, we performed inversions in different limited frequency ranges selected from the full range, and we assumed the correct two-layered model (FREQ 2L). Fig. 2.16 presents boxplots of the errors in the top-layer water content estimation for inversions performed in eight different frequency ranges. The errors are defined as the bias between the GPR soil water content derived from the dielectric permittivities using the model of Ledieu *et al.* (1986) with a given parametrization and the soil water content determined by volumetric sampling. Start frequencies were set to either 0.8 or 1 GHz and stop frequencies to 2, 2.2, 2.4 or 2.6 GHz, respectively.

Clearly, the full frequency bandwidth leads to the best estimations for the sand water content. Narrower bands lead, in particular, to outliers with significant errors. Reducing the frequency bandwidth is clearly contraindicated for estimating the soil parameters in the presence of thin layers. For layers that are thick compared to the wavelength, a bandwidth as small as 0.4 GHz still leads to accurate results (Lambot *et al.*, 2005). Although the radar data for

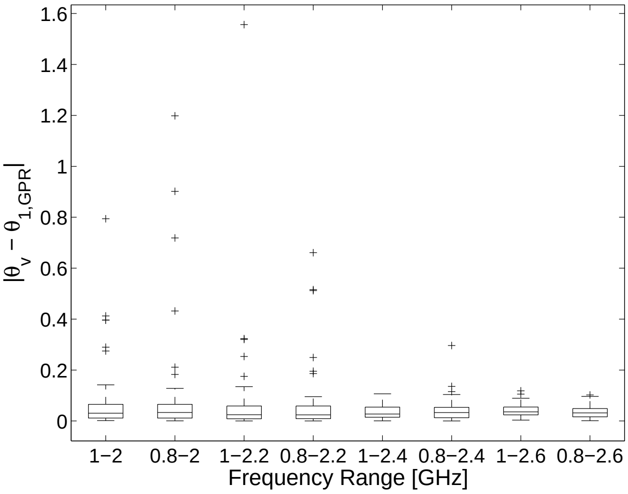

Figure 2.16: Error boxplots between the GPR-derived and the sampled volumetric soil water content of the top layer, for inversions with different frequency bandwidths. The box extent shows interquartile range (i.e., the range between the first and the third quartiles), while the median of the error distribution is represented by the horizontal line that cuts the box. Whiskers length is 1.5 times the vertical length of the boxes. Outlier error values are displayed as crosses outside of the whiskers.

frequencies between 0.8 GHz and 1 GHz are contaminated by some noise, inversions without these frequencies do not lead to significantly different results. A large bandwidth is important for thin-layer retrieval because, in the frequency domain, thin layers lead to oscillations of the amplitude of the Green's function with a large period. This period is inversely proportional to the electric thickness of the layer. It is worth noting that the problem is similar in the time domain where the limitation of the bandwidth results in less well-defined reflection (the bandwidth defines range resolution). For instance, with remote SAR acquisition, it is well known that using various frequencies enhances the extraction of information for the retrieval of soil surface moisture (D'Urso and Minacapilli, 2006). Moreover, D'Urso and Minacapilli (2006) have shown that relatively low frequencies (L-band, 1.6 GHz) lead to better results, mainly due to the lower sensitivity to soil surface roughness and vegetation compared to higher frequencies.

2.6 Conclusions

We performed numerical and laboratory experiments to evaluate the effect of shallow thin layers on the retrieval of soil electromagnetic properties by full-waveform inversion of GPR data. Shallow soil layering may occur in various conditions in natural conditions and alter the backscattered GPR data. First, inversions of numerical data, assuming the correct model configuration (two-layered), showed some discrepancies between true and inverted dielectric permittivities. This was attributed to the complexity of the inverse problem (five parameters to be retrieved) and the not well-defined global minimum of the objective function for subresolution layer thicknesses. We also showed that the errors increase, as expected, with the use of a simplified one-layered model (i.e., when the true two-layered medium is not taken into account). However, provided limited contrast between the two layers, such approach remains robust owing to the low dimensionality of the inverse problem (three parameters). For relatively large contrasts (e.g., > 0.10 in terms of water content), significant errors arise with the simplified model (> 0.10 in terms of water content).

For the laboratory experiments, a good agreement was obtained between volumetric water content determined by sampling and GPR-derived dielectric permittivity. The same limitations as for the numerical experiments were observed. In addition, part of the observed discrepancies was attributed to the inherent variability of the water content within the sand layers with respect to the different measurement support, making the water content measurements not fully reliable in comparing the larger-scale GPR measurements. Retrieval of the thin-layer thickness led to relatively small errors, ranging from a few millimeters up to a maximum of two centimeters (corresponding to the range resolution). Markov-Chain Monte-Carlo sampling permitted to assess the posterior distribution of the optimized parameters in the GPR data inversion.

The benefit of these experiments and analysis is that it shows both the theoretical and practical limits in terms of thin layers reconstruction using zero-offset, off-ground GPR. These results also apply to other radar remote sensing, but considering a much larger bandwidth. When shallow soil layering conditions are to be encountered, two-layered inversions would be preferred if there is a large contrast between soil layers. One-layered inversions can deal with shallow layering for low contrast conditions. The proposed methods appear to be promising for surface soil moisture estimation in layered soil moisture conditions and for reconstructing these layers.

Chapter 3

Soil moisture mapping by ground penetrating radar in profile conditions: Numerical and field experiments*

3.1 Outline

Full-waveform inversions were applied to retrieve surface, two-layered and continuous soil moisture profiles from ground penetrating radar (GPR) data acquired in an 11-ha agricultural field situated in the loess belt area in central Belgium. The radar system consisted of a vector network analyzer combined with an off-ground horn antenna operating in the frequency range 200-2000 MHz. The GPR system was computer controlled and synchronized with a differential GPS for real-time data acquisition. Several inversion strategies were also tested using numerical experiments, which in particular demonstrated the potentiality to reconstruct simplified two-layered configurations from more complex, continuous dielectric profiles as prevalent in the environment. The surface soil moisture map obtained assuming a one-layered model showed a global moisture pattern mainly explained by the topography while local moisture patterns indicated a line effect. Two-layered and profile inversions provided consistent estimates with respect to each other and field observations, showing significant moisture increases with depth. However, some discrepancies were observed between the measured and modeled GPR data in the higher frequency ranges,

---

[*] This chapter is adapted from:
Minet, J.; Wahyudi, A.; Bogaert, P.; Vanclooster, M. & Lambot, S. Mapping shallow soil moisture profiles at the field scale using full-waveform inversion of ground penetrating radar data, in *Geoderma*, **2011**, 161, 225-237.

mainly due to surface roughness effects which were not accounted for. The proposed GPR method and inversion strategies showed great promise for high-resolution mapping of soil moisture at the field scale and for reconstructing continuous or layered soil moisture profiles.

3.2 Introduction

Soil moisture dynamics is a key component in many researches and applications like precision agriculture, hydrological studies, meteorological and climatological modeling and other environmental studies. In hydrology, soil moisture is a highly sensitive state-variable in runoff, solute transport, evaporation and erosion processes, as it governs the partitioning between runoff and infiltration, and reducing its uncertainty largely improves modeling precision (Zehe *et al.*, 2005). In global circulation models, soil moisture largely controls the energy fluxes between the land surface and the atmosphere (Schumann *et al.*, 2009).

Recent developments in microwave remote sensing of surface soil moisture bring increasing opportunities for extensive soil moisture characterization at different spatial and temporal scales, as new remote sensing data products (e.g., from SMOS and SMAP) become available (Wagner *et al.*, 2007). Nevertheless, a poor agreement still exists between remote sensing derived soil moisture and ground-truth measurements (i.e., gravimetric sampling, time domain reflectometry measurements). Ground-based soil moisture measurement techniques may fail to match the remote sensing retrievals as a result of the different support scales of the techniques, particularly with respect to the depth of characterization, as it was stated by Stevens *et al.* (2008). In addition, the inherent large spatial variability of soil moisture within a remote sensing pixel implies that a large number of ground measurements must be collected to adequately compare the data. Hence, no absolute relation between the backscattered signals from remote sensing sensors and the surface soil moisture exists, necessitating site-specific calibrations (D'Urso and Minacapilli, 2006; Verhoest *et al.*, 2008).

Furthermore, the value of remotely-sensed surface soil moisture may be limited by a lack of correlation between surface and subsurface soil moisture (Vereecken *et al.*, 2008). As it is directly exposed to atmospheric forcing, surface soil moisture dynamics is a lot more active than subsurface soil moisture (see chapter 2) . Surface soil moisture may therefore fail to reflect the soil moisture conditions in the subsurface that are actually of interest for a lot of processes (Capehart and Carlson, 1997). Some studies have addressed this issue in remote sensing acquisition, using transfer functions based on statistical relationships or physically-based hydrodynamic models to relate the soil moisture profile to the remotely-sensed surface soil moisture (Wagner *et al.*, 1999; Ceballos *et al.*, 2005). Nevertheless, soil moisture profile information cannot be inherently inferred from the single-frequency satellite sensors.

In that respect, ground penetrating radar (GPR) has shown further potentialities to increase the extraction of information about surface and subsurface soil moisture (Huisman *et al.*, 2003; Galagedara *et al.*, 2005; Serbin and Or, 2005; Lunt *et al.*, 2005; Doolittle *et al.*, 2006; Lambot *et al.*, 2008a). Characterization of soil moisture in multilayered media using inversion of GPR data was performed by Lambot *et al.* (2004b), van der Kruk (2006) and Strobbia and Cassiani (2007). In particular, borehole GPR applications can accurately reconstruct 2-D images (tomograms) of the complete soil moisture profile between borehole locations (Binley *et al.*, 2001; Looms *et al.*, 2008), but these techniques remain limited at small-scale (a few meters) studies, as it requires the installation of vertical wells into the soil. Hence, although they showed a good accuracy, these techniques remain largely cumbersome and time-consuming, hampering for the mapping of large areas. Surface soil moisture determination by the surface reflection coefficient method, using off-ground GPR antennas, have shown a potential for proximal soil moisture sensing at a much larger scale compared to the borehole methods (Redman *et al.*, 2002; Serbin and Or, 2003, 2005). However, this method still remains unused in real field applications due to several practical and theoretical limitations. A more practical and accurate GPR approach for mapping surface soil moisture at the field scale is the one developed by Lambot *et al.* (2004b), which is based on off-ground, zero-offset GPR and full waveform inverse modeling. Owing to an accurate radar model that accounts for three dimensional wave propagation, antenna effects and antenna-soil interactions, information retrieval from the radar data is inherently maximized in terms of quantity and accuracy. Specific inversion strategies have been developed for the retrieval of soil surface dielectric permittivity and correlated water content (Lambot *et al.*, 2006b) and have been applied to field data (Lambot *et al.*, 2008b). The main advantages of this advanced GPR approach are: (1) the off-ground configuration allowing for a high-resolution on-the-go mapping of soil moisture at the field scale and (2) the full-waveform inversion and the exactness of the modeling approach that permit to investigate vertically-varying moisture profiles.

3.3 Objectives

In this chapter, we propose to investigate the retrieval of soil moisture vertical profiles by full-waveform inversion of GPR data acquired in an 11-ha agricultural field. This chapter attempts to apply to field conditions the two-layered modeling approach presented in chapter 2 and a continuously-variable profile model as studied in laboratory by Lambot *et al.* (2004a). The field was situated in the loess belt region in central Belgium (Walhain), consisting mainly of loamy soils. Soil moisture conditions were described by three models, i.e., a one-layered, a two-layered and a continuously-variable profile model. Numerical experiments are first presented, that evaluate GPR inversions assuming the two-layered soil model facing continuous soil moisture profile conditions. Then, GPR inversions of the field data were performed with the three models, the two-layered and profile inversions being limited to some parts of the field where specific profile conditions were observed. The surface soil moisture map from the one-layered inversion is presented and interpreted in the light of in-situ observations. Soil moisture maps from two-layered and profile inversions are compared, as well as soil moisture profiles. Finally, the errors of the approach with respect to the field conditions are discussed.

3.4 GPR forward and inverse modeling

3.4.1 GPR system modeling

Following Lambot *et al.* (2004b, 2006b), the GPR system was set up with a vector network analyzer (VNA) connected to an ultra-wideband monostatic horn antenna situated off the ground. The VNA emulates a stepped-frequency continuous wave radar, that is, the GPR measurements are performed in the frequency domain. For this configuration, all antenna effects can be filtered out using Eq. (2.1) where the GPR antenna is modeled as a linear system by three frequency-dependent antenna transfer functions. A specific calibration of the radar antenna permits to determine the transfer functions and thus to obtain the soil response (i.e., the Green's function $G_{xx}^{\uparrow}(\omega)$) from the raw measurements $S_{11}(\omega)$ (Jadoon *et al.*, 2010b). The reader is referred to Lambot *et al.* (2004b) and chapter 2 for further details about the antenna calibration and electromagnetic model.

The electromagnetic model calculating the Green's function simulates the response of the soil illuminated by the GPR antenna, depending on the soil electromagnetic properties. The soil can be discretized in multiple layers with homogeneous electromagnetic properties, i.e., the dielectric permittivity ε, the electrical conductivity σ and the thickness of each layer h. A continuously variable medium can be modeled using layer thicknesses that are smaller than one tenth the wavelength (subresolution conditions).

The petrophysical relationships between the soil moisture and its electromagnetic properties are described, respectively, by 1) the model of Ledieu *et al.* (1986) (Eq. (1.17)) to derive the volumetric soil moisture θ from the relative dielectric permittivity ε and by 2) the model of Rhoades *et al.* (1976) (Eq. (2.3)) to relate the soil electrical conductivity σ to the soil moisture, as presented in chapter 2. Both dielectric permittivity and electrical conductivity are thus related to the soil moisture by these specific relationships throughout all this chapter. The petrophysical relationship of Ledieu *et al.* (1986) was chosen for its simplicity in the development of Eq. (3.2). It is worth noting that the soil specific parameters in equations (1.17) and (2.3) may actually vary within the field depending on soil texture and structure variations. However, the $\theta - \varepsilon$ relationship variation is expected to be relatively small due to the very strong correlation between these two variables and, as discussed below, σ has a small effect on the estimation of the soil surface dielectric permittivity. The assumptions made for these petrophysical relationships are therefore expected not to affect our results.

3.4.2 Inversion of GPR data

The parameters of the multilayered medium investigated by the GPR are retrieved by a full-waveform inversion of the filtered radar signal, i.e., the Green's function. This inversion is done in the frequency domain, where the wave is actually modeled. The inverse problem is formulated in the least-squares sense according to Eq. (2.2). Optimization is performed using a local search algorithm (i.e., the Levenberg-Marquardt (L-M) algorithm) for the simplest models with few parameters to invert for and a combination of global and local optimization (i.e., the Global Multilevel Coordinate Search (GMCS) and the Nelder-Mead Simplex (NMS) algorithms) for the more complex models.

In this study, the electrical conductivity of the soil is not optimized but is directly derived from the dielectric permittivity using equations (1.17) and (2.3). The electromagnetic model is mostly insensitive to the electrical conductivity in this frequency range, as it was shown by Lambot *et al.* (2006b) (negligible effects for $\sigma < 0.01$ S/m). The optimization of the electrical conductivity would therefore uselessly make the inverse problems more complex because of the larger number of parameters to optimize, leading to more CPU time requirement and to non-uniqueness issues (especially due to insensitivity) in the inverse problem.

3.4.3 Multilayered medium models

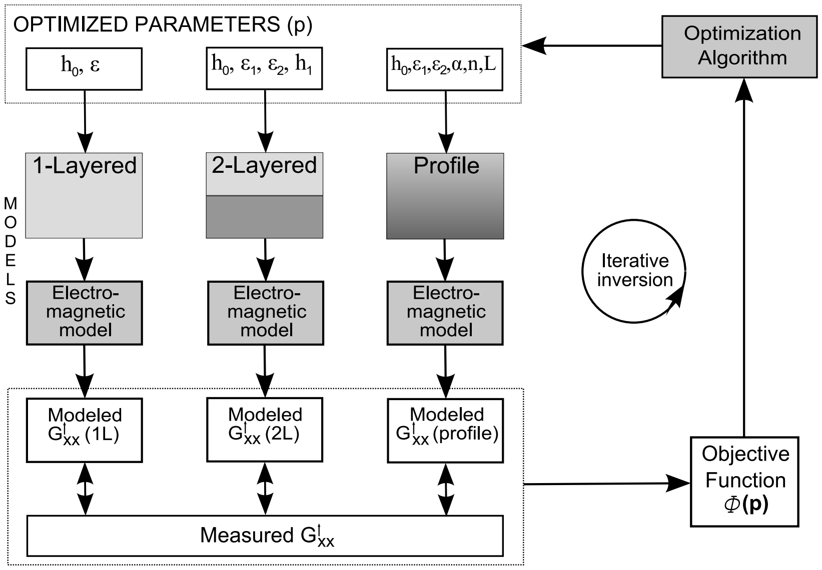

Figure 3.1: Flowchart of the inversion of the Green's function $\mathbf{G}_{\mathbf{xx}}^{\uparrow}$ with the three different multilayered soil moisture models, that are, the one-layered, two-layered and profile models.

In this chapter, the soil is modeled using three types of multilayered media. Inversion of the GPR signals using the three different types of model permits to get different soil moisture descriptions. Figure 3.1 shows the inversion flowchart for the three different multilayered models.

One-layered model

The one-layered model is the most simplified one as it assumes an homogeneous half-space for the soil, below the air layer. Only two parameters are considered in the inversion, i.e., the soil dielectric permittivity ε and the antenna height above the soil h_0, as the electromagnetic properties of the air layer are known ($\varepsilon_a = 1$ and $\sigma_a = 0$ S/m). This robust inversion procedure was used for soil moisture retrieval from GPR data in field conditions in Weihermüller *et al.* (2007); Lambot *et al.* (2008b) and in chapter 2 with laboratory measurements (FREQ 1L scenario).

Two-layered model

The two-layered model assumes a two-layered soil with a top soil layer (1^{st} layer) above an half-space medium (2^{nd} layer), in addition to the air layer. This model permits to assess two different homogeneous soil dielectric permittivity values ε_1 and ε_2, the thickness of the top layer h_1 and the antenna height h_0. For small top layer thicknesses, constructive and destructive interferences in the GPR signal may occur, resulting in a less sensitivity of the model to its parameters (see chapter 2). The method was validated in laboratory conditions against real measurements for these critical cases in Lambot *et al.* (2006b) and in chapter 2 (FREQ 2L scenario).

Profile model

The profile model assumes a soil where the soil moisture can vary continuously with depth, according to a hydrostatically coherent soil moisture profile. We chose to simulate sigmoidal soil moisture profiles with the model of van Genuchten (1980), which describes the water retention curve between two extreme soil moisture values at the top and the bottom of the profile (hydrostatic equilibrium). The model of van Genuchten was chosen for its expected relevance for most natural soil moisture profiles, although alternative profile models could be chosen. The model of van Genuchten giving the water retention curve as a function of the depth z taken positively downwards is given below:

$$\theta(z) = \begin{cases} \theta_1 + (\theta_2 - \theta_1)(1 + |\alpha(L - z)|^n)^{-m} & \text{for } z < L \\ \theta_2 & \text{for } z \geq L \end{cases} \tag{3.1}$$

where θ is the volumetric soil moisture, θ_1 and θ_2 are the top and bottom soil moisture respectively, L is the depth in which the profile is developed, α and n are curve shape parameters, and $m = 1 - 1/n$ is restricted by Mualem's condition with $n > 1$.

The soil moisture profiles must be transformed to permittivity profiles for the need of the electromagnetic model. Introducing (1.17) into (3.1) leads to the equation describing the soil dielectric profiles as a function of the depth z (Lambot *et al.*, 2004a):

$$\varepsilon(z) = \begin{cases} [\sqrt{\varepsilon_1} + (\sqrt{\varepsilon_2} - \sqrt{\varepsilon_1})(1 + [\alpha(L - z)]^n)^{-m}]^2 & \text{for } z < L \\ \varepsilon_2 & \text{for } z \geq L \end{cases} \tag{3.2}$$

where ε_1 and ε_2 are, respectively, the dielectric permittivity of the soil surface and of the soil at the depth $z = L$.

The dielectric profiles are discretized into 1 mm thick soil layers, resulting in maximum 250 layers in the electromagnetic model, as the depth of the profile L is bounded to 0.25 m in the optimization. This high resolution permits to emulate the continuity of the profile for the computation of the Green's function as the layer thickness (1 mm) is far below the wavelength of the GPR signal. It is worth noting that the coupling of the van Genuchten's model to the electromagnetic model considerably decreases the number of unknowns in the optimization (from maximum 2×250 to 6 unknowns), the GPR inversion being constrained by the van Genuchten's model. The optimized parameters in the inversion are the van Genuchten parameters α, n, θ_1, θ_2 and L and the antenna height h_0. This approach was validated with numerical and laboratory experiments in Lambot *et al.* (2004a).

3.5 Numerical experiments

3.5.1 Model configurations

The numerical experiments aim to reproduce the real medium that was investigated with the GPR in field conditions and that is expected to be a continuous (and hydrostatically coherent to some extent in this case) soil moisture profile. Synthetic Green's functions were generated using the profile model, using dielectric profiles that were computed by the van Genuchten model. Different configurations of soil dielectric profiles were investigated, with α ranging from 16 m^{-1} to 30 m^{-1} and n from 6 to 20 by a step of 2, resulting in total in 120 configurations. The other parameters of Eq. (3.2) were fixed at $\varepsilon_1 = 3.12$ and $\varepsilon_2 = 12.30$, corresponding to soil moisture values of $\theta_1 = 0.03$ and $\theta_2 = 0.25$, respectively, and $L = 0.10$ m. The profile was discretized into 100 soil layers of 1 mm thickness for generating the Green's functions using the multilayered electromagnetic model. Green's functions were computed in a wide frequency bandwidth, from 200 to 2000 MHz, with a frequency step of 6 MHz.

Then, synthetic Green's functions generated with the profile model were inverted with the two-layered model within the same frequency range, considering the optimization of the first (ε_1) and second layer (ε_2) dielectric permittivities and of the first layer thickness (h_1). The objective of the numerical experiments was to assess the reliability of the simplified two-layered model facing a continuous dielectric profile. Using a simplified model in practice is beneficial in terms of uniqueness and computing resources. Indeed, the calculation time of the Green's function is almost proportional to the number of layers in the model.

3.5.2 Numerical results

Soil moisture profile retrieval with the two-layered inversion

Figure 3.2 shows the soil moisture profiles used for generating the Green's functions and the two-layered discontinuous profiles retrieved by two-layered model inversions, for four different configurations. The parameters of the model

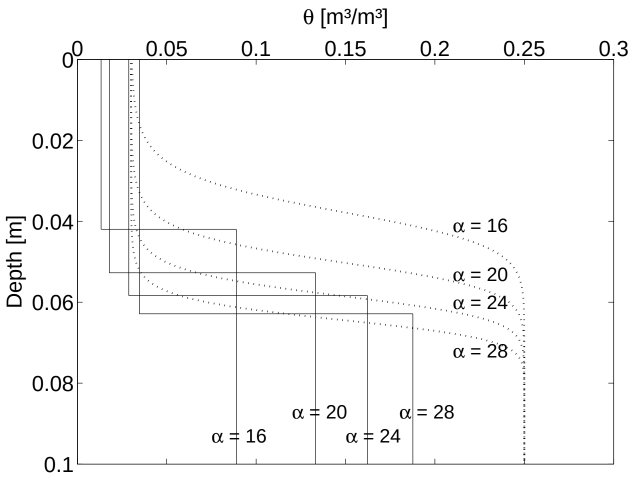

Figure 3.2: Numerically generated soil moisture profiles with the van Genuchten model (dotted lines) and two-layered profile (plain lines) retrieved by inversion using the two-layered model, for four different van Genuchten parametrizations ($n = 14$ and $\alpha = 16$, 20, 24 and 28 m^{-1}). Results from the numerical experiments.

of van Genuchten for the configurations shown here are $n = 14$ and $\alpha = 16$, 20, 24 and 28 m^{-1}, respectively. It is worth mentioning that inversions performed with the same profile model as the one used for generating the synthetic Green's functions led to exactly the same parameter values (and thus the same moisture profiles) than the values used for generating the data.

The general trend of the profile, that is, the soil moisture increases with depth ($\theta_1 < \theta_2$), is always respected in the two-layered profile and can be observed for all the 120 configurations (not shown). The first layer soil moisture values retrieved by two-layered inversions θ_1 are very close to the top soil moisture from the profile model. However, the second layer soil moisture values θ_2 are underestimated compared to the soil moisture at the bottom of the profile, especially for configurations where $\alpha = 16$ and 20 m^{-1}. This poorer performance of the two-layered inversion in the retrieval of the second layer soil moisture compared to the first layer soil moisture is to be attributed to the lower information content in the GPR waves reflection from deeper soil layers. Although there is a larger dielectric contrast between the two extreme soil permittivity values ($\Delta\varepsilon_{1,2} = 9.18$) than between the air and the soil surface values ($\Delta\varepsilon_{air,1} = 2.12$), the smooth continuously-varying interface between the two extreme soil permittivities leads to a less well-defined wave reflection than the clear-cut interface between the air and soil surface, especially for low α. Hence, for configurations where the profile is more abrupt (e.g., $\alpha = 28$ m^{-1}), the retrieved second layer soil moisture is better matching the bottom soil moisture of the continuous profile. In addition, GPR waves are attenuated while penetrating deeper into the soil because of the electrical losses due to the non-null electrical conductivity. Even though this is accounted for in the electromagnetic model, it reduces the information content in the soil subsurface waves reflections. These two reasons result in a less sensitivity of the two-layered model to the parameters of the second layer. A better confidence for the first layer soil moisture compared to the second layer soil moisture can then be expected when using a two-layered model facing a continuously-varying soil moisture profile, especially for smooth profiles. This poorer sensitivity of the second layer soil moisture was also observed in chapter 2 (Fig. 2.12(a)) for a two-layered configuration.

Comparison of interfaces depth between two-layered and profile inversions

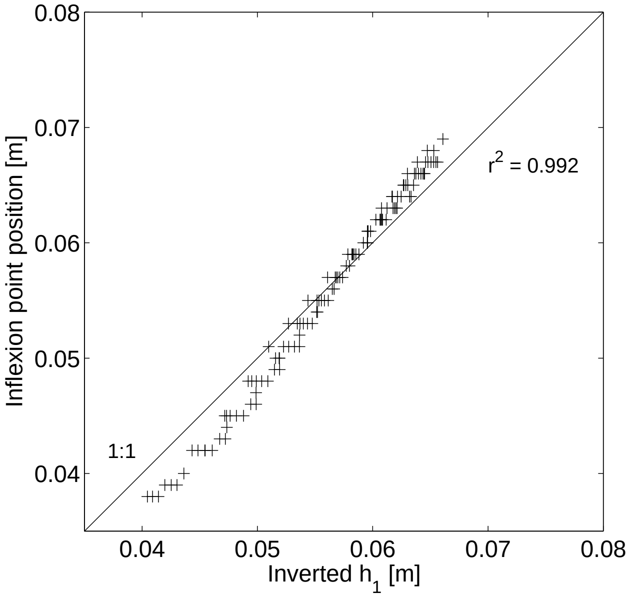

Figure 3.3: Comparison between the first layer thickness h_1 retrieved by inversion using the two-layered model and the position of the inflexion point z_i of the generated soil moisture profile. Results from the numerical experiments.

For the four configurations shown in Fig. 3.2, the inverted first layer thickness h_1 retrieved by the two-layered inversion seems to match the depth at which the generated soil moisture profile is abruptly increasing (inflexion point). Figure 3.3 compares, for all the configurations, the first layer thickness h_1, that is, the depth of the interface between the two layers, and the position of the inflexion point of the van Genuchten soil moisture profiles z_i, determined by solving $\frac{\delta^2\theta(z_i)}{\delta\ z^2} = 0$. There is a very good agreement between these two variables, with a coefficient of determination of $r^2 = 0.992$. Maximum difference between the two variables is about 4 mm, which is very accurate knowing that the numerical resolution of the profile (i.e., the size of the layers) is 1 mm and that the GPR resolution (one tenth the wavelength) is equal to 8 mm for a dielectric permittivity of 3.2 and for the highest frequency (2000 MHz). The use of a two-layered model to reconstruct continuously-varying profiles shows therefore a great potential to retrieve the depth of the interface between two extreme soil moisture values, as well as the surface soil moisture.

3.6 GPR Field Measurements

3.6.1 Materials and methods

Study site and weather conditions

The 11-ha cultivated field that was mapped with the GPR is located in the loess belt area near the locality of Walhain in the center of Belgium (Long. 4°41'8"E, Lat. 50°35'59"N) (see Fig. 3.4). Soil type is uniformly a silt loam, with a gentle topography ranging from 153 to 161 m a.s.l and slope lower than 7%. The campaign took place at the end of the winter on the 23^{th} of March 2009, while the field was covered by winter barley with a canopy height less than five cm. Soil was relatively dry as no rainfall were recorded for eight days according to a weather station located at around ten km from the field*.

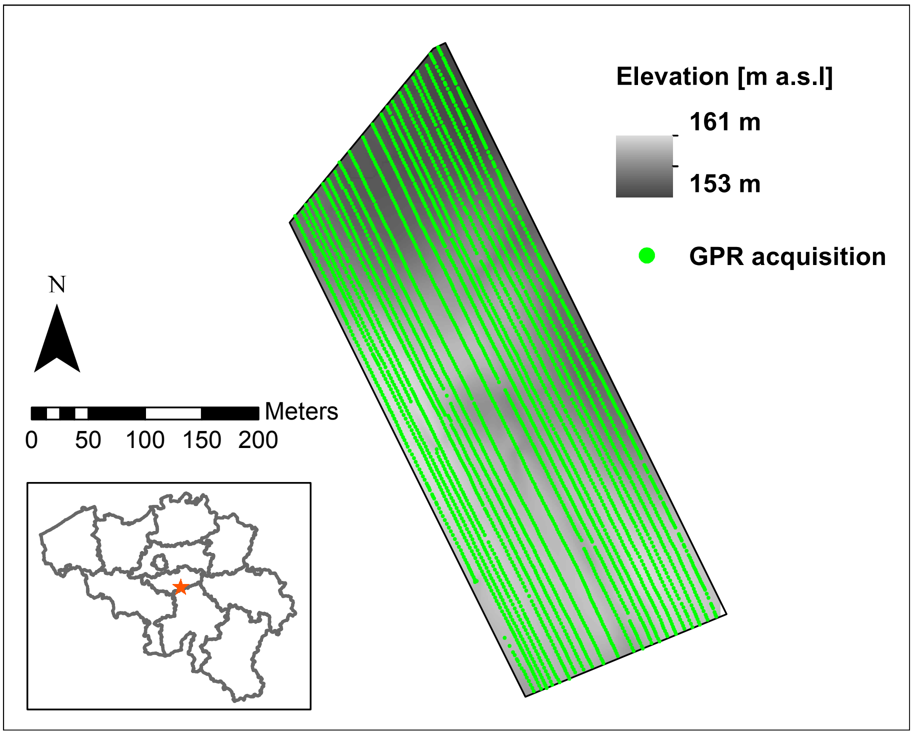

Figure 3.4: Study site for the GPR acquisitions near Walhain, Belgium. The 3741 GPR measurements are depicted over the field.

---

[*] ASTR-UCL Weather Station http://www.climate.be/wview/

The soil moisture was suspected to increase with depth, as we observed in-situ a dry superficial soil layer above a wetter subsurface soil. An abrupt profile or two-layered conditions were thus supposed to be encountered. Soil moisture volumetric sampling could not be performed to assess actual soil layering as the dry superficial layer was very thin (<5 cm). In addition, comparison of GPR-derived soil moisture with volumetric ground sampling measurements is expected to be cumbersome and suspicious due to the inherent high spatial variability of soil moisture both vertically and horizontally, to the different support scales of the measurement techniques and to the uncertain petrophysical relationship that is used to convert the dielectric permittivity into volumetric water content. Therefore, we decided not to take soil samples for this study.

GPR platform

Figure 3.5: All-terrain vehicle holding the GPR system constituted of a horn antenna linked to a vector network analyzer, the DGPS device and the PC. Picture taken on the 23^{th} of March 2009 in a barley field near Walhain, Belgium.

The GPR system was set up by combining a vector network analyzer (VNA) (ZVL, Rohde & Schwarz, Münich, Germany) with a linear polarized double-ridged broadband horn antenna (BBHA 9120 F, Schwarzbeck Mess-Elektronik, Schönau, Germany). Antenna dimensions are 95 cm in length and 68 × 96 cm^2 in aperture area and the nominal frequency range is from 0.2 to 2 GHz. The antenna was connected to the reflection port of the VNA with a high quality N type 50-Ω coaxial cable of 2.5 m length. We calibrated the VNA three times during the field acquisition at the connection point at the end of the cable before the antenna feed point using a 50-Ω OSM calibration kit. The stability of the OSM calibration in field conditions was verified, as no differences in

Table 3.1: Summary of the inversions of GPR field data for the three models.

	Number of points	Inverted parameters	Number of soil layers	
1-layered	3741	h_0, ε	1	
2-layered	300	h_0, ε_1, ε_2, h_1	2	
Profile	300	h_0, ε_1, ε_2, α, n, L	1-250	
	Frequency range [MHz]	Optimization algorithms	Number of iterations	CPU time[1]
1-layered	200 - 800	L-M	∼20	1
2-layered	200 - 1600	GMCS-NMS	6400	170
Profile	200 - 1600	GMCS-NMS	14400	12000

[1] CPU time is the relative time of computation for one GPR inversion compared to the one-layered inversion.

GPR data quality was observed before and after the calibrations during the acquisition. The frequency-dependent complex ratio S_{11} between the returned and the emitted signal was measured sequentially at 301 stepped frequencies from 200 to 2000 MHz, with a frequency step of 6 MHz.

The GPR system was mounted on an all-terrain vehicle (ATV) to allow for fast data acquisition. Figure 3.5 shows a picture of the ATV that we used for acquiring the data. The GPR was automatically controlled by a PC and combined with an accurate differential global positioning system device (DGPS) (Leica GPS1200, Leica Geosystems) for the georeferencing of the measured points, with a precision of about 3 cm. Real-time GPR measurements were performed at a regular distance spacing of two meters in the same track, according to the DGPS position. The ATV was driven along 22 parallel tracks with a distance spacing between the tracks of about ten meters. The GPR antenna footprint where soil moisture is measured has a diameter of about 1.5 m. In total, 3741 GPR measurements were taken across the field in 3h48, with a driving speed of about 5-10 km/h. As a GPR measurement takes about 1 ms, the GPR data acquisition is considered as instantaneous at the speed of the acquisition, allowing for a continuous acquisition without stop-and-go of the platform.

GPR field data inversions

The raw measured signals $S_{11}(\omega)$ were first filtered from the antenna effects using Eq. (2.1) to obtain the Green's functions $G^{\uparrow}_{xx}(\omega)$ from the soil. Inversions of the $G^{\uparrow}_{xx}(\omega)$ were conducted with the three different models described above, namely, the one-layered, the two-layered and the profile models. For the simplified one-layered model, GPR data were selected within the frequency range from 200 to 800 MHz, as noise in the signal appears at frequencies higher than 800 MHz. Noise arises at high frequencies due to interferences caused by the soil roughness and the presence of vegetation. For roughness larger than one tenth the GPR wavelength, constructive and destructive interferences may affect the GPR signal. Therefore, rejection of high frequencies (i.e., small wavelengths) permits to avoid interference problems, although it results in a poorer wave resolution for detecting small layers.

For the two-layered and the profile models, a more extended frequency range from 200 to 1600 MHz is necessary to get more information about the layered or profile structure. According to visual in-situ observations, we selected 300 points where an abrupt soil moisture profile was expected to be encountered. Only these selected points were thus inverted considering two-layered and profile models. Inversions were set in a large parameter space, namely, $0 \leq \varepsilon_1 \leq 25$, $0 \leq \varepsilon_2 \leq 25$, $1.45 \leq h_0 \leq 1.75$ m and $0 \leq h_1 \leq 0.25$ m for the two-layered inversions and $1 \leq \alpha \leq 75$ m^{-1}, $1 \leq n \leq 75$, $0 \leq \varepsilon_1 \leq 12$, $0 \leq \varepsilon_2 \leq 25$, $1.45 \leq h_0 \leq 1.75$ m and $0 \leq L \leq 0.25$ m for the profile inversions. Table 3.1 summarizes the status of the three inversions performed on the GPR field data.

3.6.2 Field measurements results

Map of surface soil moisture from the one-layered model inversion

Figure 3.6 shows the soil moisture point-data retrieved by one-layered model inversions of the 3741 points that were measured during the GPR field acquisition campaign. Inverted dielectric permittivities were translated into soil moisture values using Eq. (1.17). Size of the symbols are varying according to a weight function based on the root mean square error (RMSE) between the amplitude of measured and modeled (inverted) Green's functions ($Weight = max(RMSE) - RMSE$). The RMSE is an indicator of the uncertainty associated with the inversion of the measured signal. It is worth noting that symbols appear two or three times larger on the map than the real antenna footprint size ($\sim$2m^2). Topography is depicted with black contour lines with a contour interval of 1 m. The red polygon located in the driest part of the map delineates the 300 manually selected points for the two-layered and profile inversions.

The mean volumetric soil moisture is equal to 0.108 and its standard deviation is 0.0401. These values are similar to the ones observed in previous studies for the same extent and similar support depth (e.g., Famiglietti *et al.* (2008)). It is worth mentioning that the 300 selected points for the two-layered and profile inversions are affected by a large uncertainty (i.e., smaller points on the map), due to their large RMSE between measured and inverted signals. These large RMSE values indicate that one-layered model fails to adequately reproduce the Green's functions at these points because of the non-uniform moisture conditions.

At the global pattern scale, soil moisture is mainly explained by topography. A wet area can be observed in the North of the field, where a thalweg flows in the North-North-East direction. Another wet area can be observed in the South-West part of the field, which is characterized by a flat area. Hilltops are mainly dry, like in the South-East corner and around the zone delineated by the red polygon.

A close examination of the map reveals that the spatial local pattern of soil moisture exhibits a clear line effect. This line effect is translated by a high

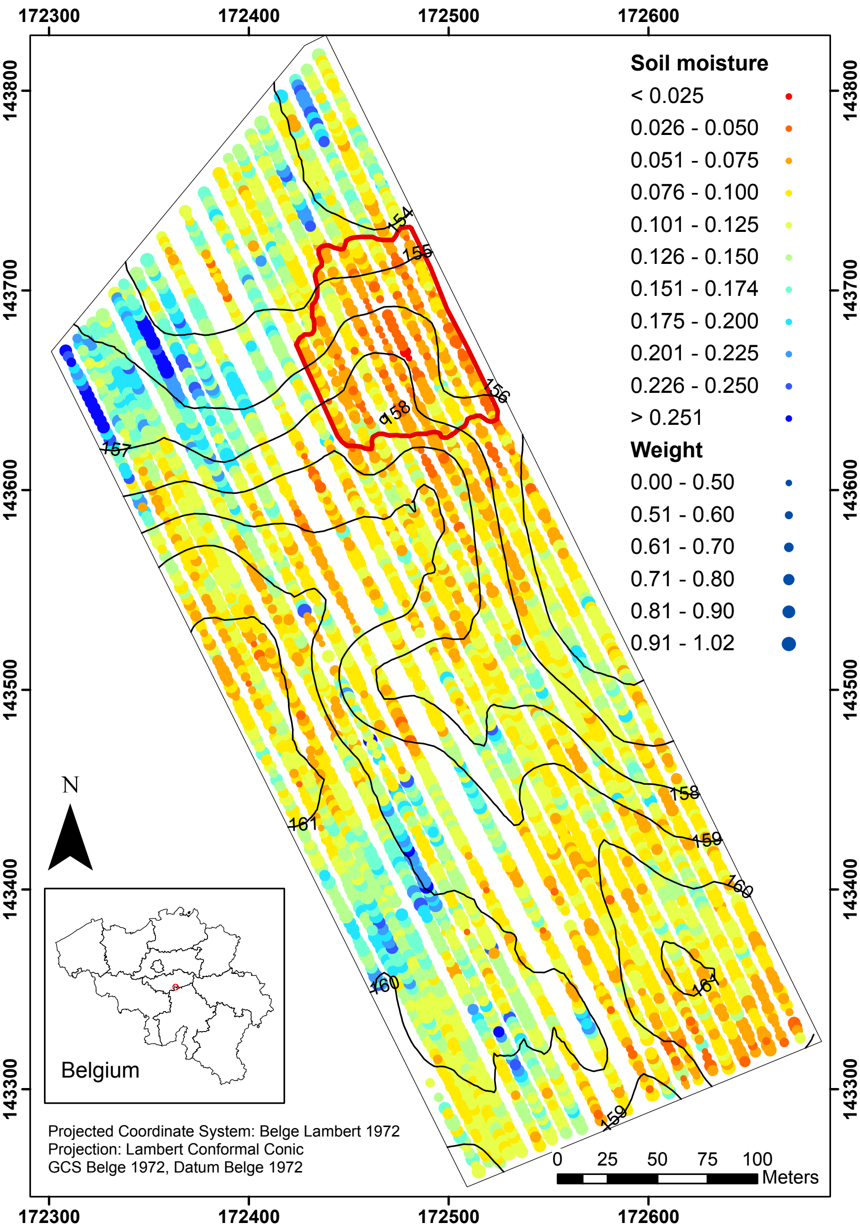

Figure 3.6: Soil moisture map retrieved by one-layered model inversions from the field acquisition near Walhain on the 23rd of March 2009. Size of the symbols are inversely related to their uncertainty by the weight function, which is, $Weight = max(RMSE) - RMSE$.

spatial continuity for data retrieved along the sampling line, whereas at the same time there is an abrupt change in soil moisture when moving to adjacent lines. This effect is clearly visible e.g., in the North-West corner of the field, where there are adjacent segments of high or low water contents.

Investigating the variogram by separating its estimates along the lines and perpendicular to the lines clearly confirms this effect (Fig. 3.7). The variogram estimated along the lines shows smoothly increasing variance with distance, with a moderate nugget effect accounting for about 25% of the sampling variance, thus emphasizing the rather progressive changes of water content, with correlated values up to about 130 m. This nugget effect may originate from either the small-scale variability of soil moisture or from errors in the GPR sensing of soil moisture (see the last section of the field measurements results). It is believed that the spatial variability of soil moisture at the resolution scale (2 meters along the acquisition lines) may be large enough to explain this relatively high nugget effect. In contrast, the variogram perpendicular to the lines is offset by a value that corresponds to the additional nugget effect induced by the between-lines variability, which tends to mask the global pattern of volumetric soil moisture. It can presumably be assumed that the line effect is the result of the dragging line laid by ploughing or fertilizer spreading machine, as the machine causes compaction layer along the track of the wheels. This could also originate from the surface soil roughness that is mainly dependent on the soil tillage conditions, such as the tractor velocity and the depth of the plough that may change from line to line. A more detailed discussion about this line effect is presented in chapter 5, Line effect.

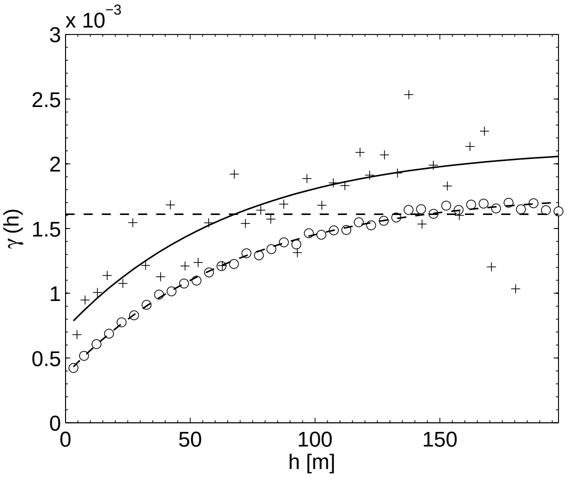

Figure 3.7: Variogram for soil moisture computed on the whole field with a class distance from 0 to 200 m by a step of 5 m. Variogram along and perpendicular to the sampling line is denoted by circle and plus symbols, respectively. Exponential models are fitted for both variograms. The sampling variance is indicated by the horizontal dashed line.

Though these findings are not completely validated yet, further application such as mapping continuous soil moisture content could require some subsequent work in order to remove the line effect and improves the estimation and mapping of the moisture content in the field.

Maps of surface and subsurface soil moisture from two-layered and profile inversions

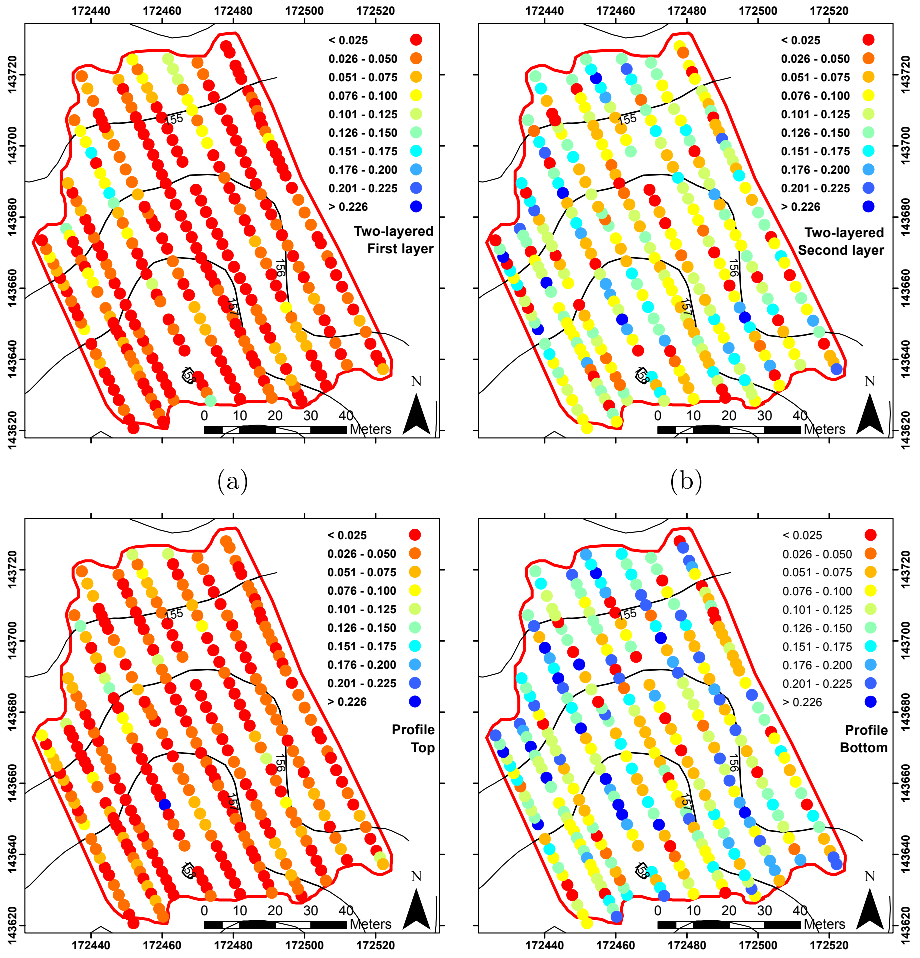

(a) (b)

(c) (d)

Figure 3.8: Soil moisture maps from two-layered model inversions for the first layer (a) and the second layer (b) and from the profile model inversions for the top (c) and the bottom (d) of the profile for the 300 points outlined with the red polygon in Fig. 3.6.

Figure 3.8 shows the first layer (a) and second layer (b) soil moisture maps from two-layered inversions and the top (c) and bottom (d) soil moisture maps from profile inversions, for the 300 selected points. Soil moisture values are depicted with the same color range from 0 to 0.25 in the four maps. In addition, Table 3.2 summarizes the soil moisture data from the one-, two-layered and profile model inversions for the 300 selected points. Variograms for soil moisture from the two-layered and profile model inversions are depicted in Fig. 3.9 and the parameters of the variograms are presented in the last three columns of Table 3.2.

Considering two-layered model inversions, first layer soil moisture values (Fig. 3.8(a)) are very low, indicating a completely dry soil at the wilting point, as it was visually observed in the field. Soil moisture is spatially structured (see the variogram in Fig. 3.9(a)) with a smaller range than the one observed in Fig. 3.7. Second layer soil moisture map (Fig. 3.8(b)) shows globally higher values and almost no spatial structure, with a nugget effect close to the total variance (Fig. 3.9(b)). This high nugget effect could originate from higher errors in the GPR sensing for second-layer soil moisture, with respect to the lower sensitivity of the two-layered model to the second layer dielectric permittivity, as it was already explained in the numerical experiments. The optimized first layer thickness (not shown) varies from 2 to 20 cm, although most of the values are around 3 cm (71.3 % of the points show first layer thickness values between 2 and 4 cm).

Soil moisture maps from the profile inversions show similar patterns than the maps from the two-layered inversions, particularly when comparing first layer values and values at the top of the profile (Fig. 3.8(a) and (c)), that yield the same mean soil moisture (Table 6.2) and similar variograms (Fig. 3.9(a) and (c)). However, these two soil moisture variables are poorly correlated ($r = 0.365$) and the RMSE ($RMSE = 0.064$) between these soil moisture values indicates that some outliers are affecting this correlation. It is worth pointing out that, whereas the overall patterns seem similar, particular points may drastically deviate when comparing two-layered and profile model inversions. These deviations may be simply explained by the different first layer thicknesses that are retrieved in the two-layered and profile model inversions. Soil moisture values at the bottom of the profile (Fig. 3.8(d)) are higher than the second layer values (Fig. 3.8(b)) in the two-layered inversions, probably because of the deeper characterization of the soil moisture with the profile inversion. Again, these two variables are poorly correlated ($r = 0.356$) with a large RMSE ($RMSE = 0.077$) between them. Although the nugget effect remains important, the variogram for the soil moisture values at the bottom of the profile (Fig. 3.9 (d)) shows a better spatial coherence than its counterpart for the two-layered model.

From field visual observations, it is expected that soil moisture was increasing with depth, with the presence of a shallow dry crust of soil. For the two-layered model inversions results, first layer soil moisture values $\theta_1(2L)$ are smaller than second layer soil moisture values $\theta_2(2L)$ in 265 (88.3%) points. Moreover, comparing with one-layered model inversions, the condition $\theta_1(2L) < \theta(1L) < \theta_2(2L)$, where $\theta(1L)$ is the value retrieved by the one-layered inversion, is observed in 204 (68.0%) points. Regarding the profile model inversions, top soil moisture values $\theta_1(\text{profile})$ are smaller than bottom soil moisture val-

Table 3.2: Statistics of GPR-derived soil moisture from the one-, two-layered and profile inversions for the 300 selected points. The mean (μ) and the standard deviation (σ) of soil moisture and three variogram parameters (Nugget effect, Sill and Range) are presented.

		μ	σ	Nug. effect	Sill	Range [m]
1-Layered	θ	0.074	0.031	2.45e-4	7.55e-4	24.6
2-Layered	θ_1	0.030	0.034	4.61e-4	7.21e-4	15.9
	θ_2	0.100	0.056	2.62e-3	4.90e-4	10.5
Profile	θ_1	0.030	0.032	7.90e-4	2.35e-4	12.8
	θ_2	0.124	0.071	2.92e-3	2.20e-3	11.8

ues θ_2(profile) in 280 (93.3%) points, while the condition θ_1(profile)$< \theta(1L) <$ θ_2(profile) is observed in 221 (73.7%) points. The profile coherence is therefore more widely observed with the profile model than with the two-layered model inversions.

Regarding these 300 points only, the one-layered model inversions lead to intermediate values between surface and subsurface soil moisture values (Table 6.2). The pattern of the one-layered soil moisture (see Fig. 3.6) seems more spatially coherent, with a corresponding smaller nugget effect, which is two to three times smaller than the nugget effect observed for θ_1 and ten times smaller than the nugget effect observed for θ_2. This larger nugget effect with the two-layered and profile model inversions may originate: 1) from the fact that the first layer thickness is actually varying from point to point and; 2) from inverse modeling difficulties in these complex models.

Comparison of soil moisture profile between inversion models

Figure 3.10 presents soil moisture profiles retrieved from the two-layered and profile inversions and a unique soil moisture value retrieved from the one-layered inversion, for two GPR measured points. Both inversions with the two-layered and profile models at these two points show an increase of the soil moisture with depth. The top and bottom soil moisture values from the continuous profile inversions are very close, respectively, to the first and second layer soil moisture values from the two-layered inversions. In Fig. 3.10(b), the continuous profile inversion leads to an abrupt soil moisture profile sharply following the discontinuous two-layered dielectric profile. It is worth mentioning that a majority of measured points shows a similar behavior, with soil moisture profiles that are identical between two-layered and profile inversions.

The abrupt soil moisture profiles retrieved by the profile inversion could originate from a lack of resolution of the GPR. Considering a dielectric permittivity of 5.5 (i.e., corresponding to the first layer soil moisture of 0.103), the GPR resolution at the maximal frequency of 1600 MHz is equal to 0.020 m. Thus, inversions may be insensitive to continuous variations occurring within a very thin layer. This can also indicate real abrupt soil moisture profile condi-

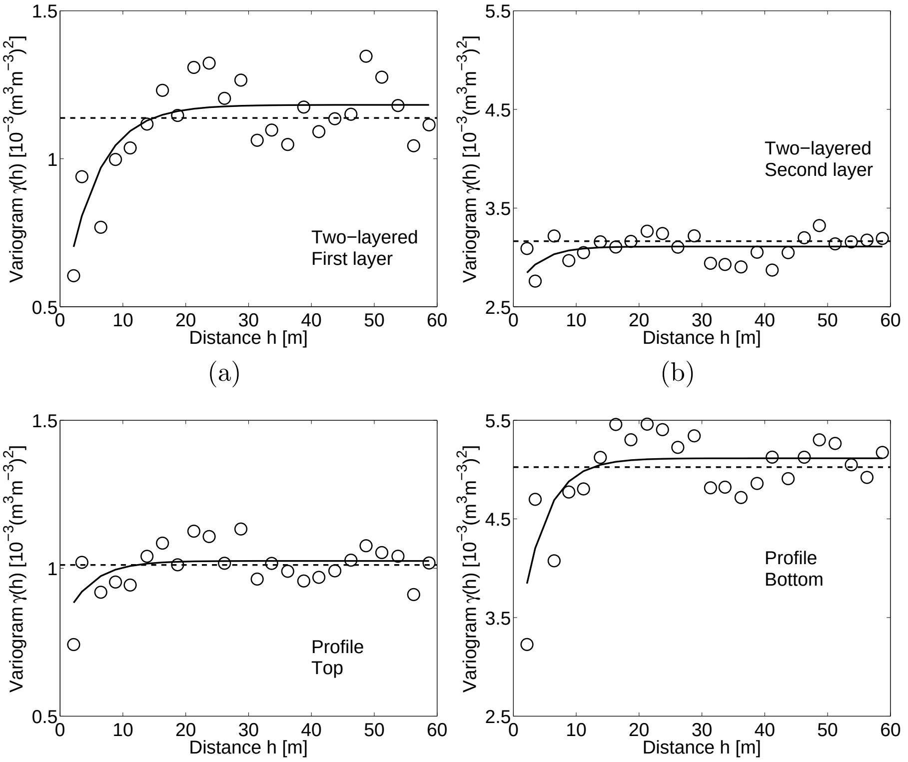

(a) (b)

(c) (d)

Figure 3.9: Variograms for soil moisture computed on the 300 selected points for the first layer (a) and the second layer (b) from the two-layered model inversions and for the top (c) and the bottom (d) from the profile model inversions. Exponential models are fitted for all variograms. The total variance is indicated by the horizontal dashed line.

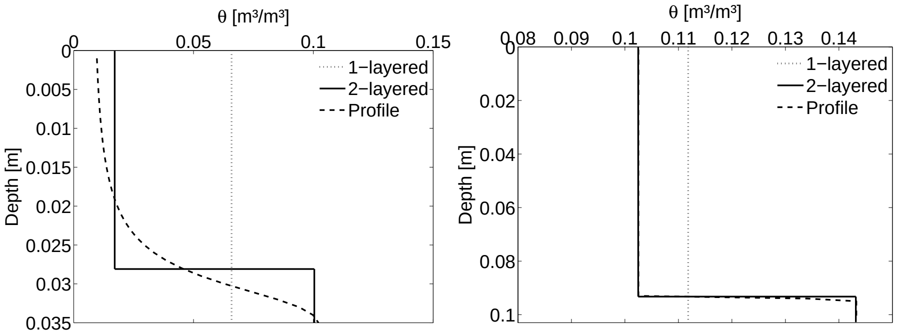

(a) (b)

Figure 3.10: Soil moisture profiles retrieved from the two-layered inversion and the model inversion and unique soil moisture value retrieved from the one-layered model inversion for two GPR measured points ((a) and (b)).

tions, resulting from a physical decoupling (strong pressure head gradient due to surface evaporation) of the soil water between the soil surface and subsurface.

Comparison of interfaces depth retrieval between two-layered and profile inversions

For the two points depicted in Fig. 3.10, positions of the interfaces retrieved by the two-layered model inversions correspond quite well to the positions of the inflexion point of the continuous profile inversion, indicating that both models retrieve the same depth where the soil moisture is supposed to increase rapidly.

However, for all the 300 selected points, two-layered and profile inversions locate the interfaces at the same depth with a tolerance of ±4 mm for 144 (48.0%) points only, contrarily to the very good agreement that was observed in the numerical experiments with the same tolerance (Fig. 3.3). This poorer performance with some field data are to be attributed to the lowest maximum frequency of the GPR signal (1600 MHz instead of 2000 MHz), to the measurement noise arising with real data, and to model inadequacies with respect to the actual conditions that may not be adequately modeled with either a two-layered or a coherent soil moisture profile.

Comparison between measured and modeled Green's functions

Figure 3.11 shows measured and modeled Green's functions $G^{\uparrow}_{xx}(\omega)$ with the one-layered model, the two-layered model and the profile model, in frequency and time domains. The GPR measurement presented here corresponds to the point whose inverted profiles are depicted in Fig. 3.10(b). Time domain representation of the Green's functions is achieved by applying an inverse Fourier transform to the frequency domain signal. As frequency bandwidths are different between the one-layered model (200-800 MHz) and the two other model (200-1600 MHz) inversions, the time domain representations must be separated.

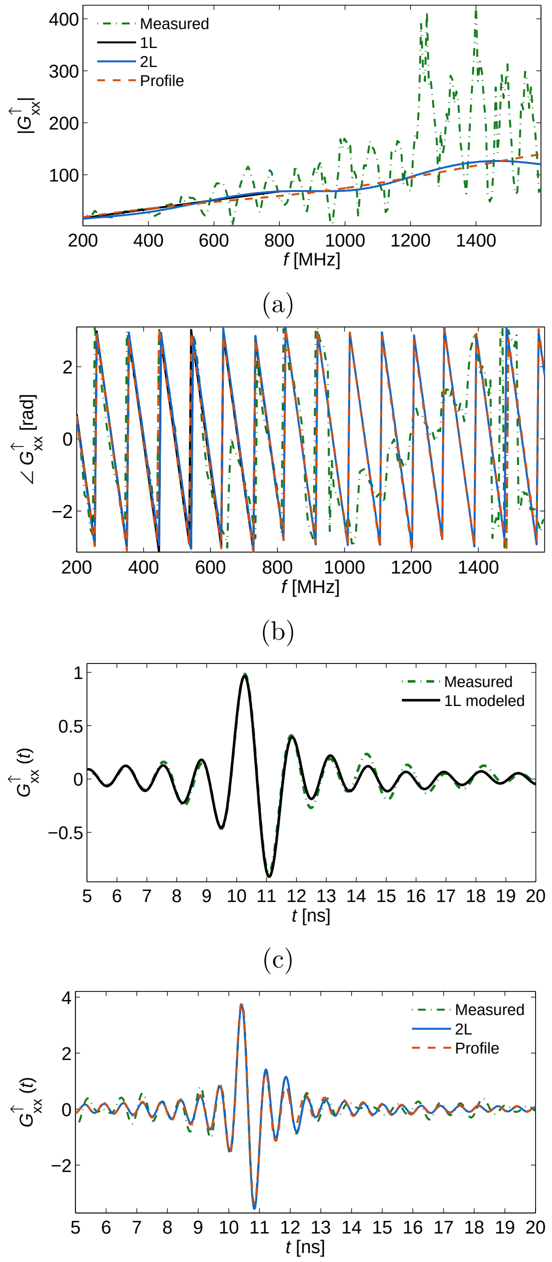

(a)

(b)

(c)

(d)

Figure 3.11: Measured and modeled Green's functions in the frequency domain depicted in amplitude (a) and phase (b) and in time domain for the one-layered model (c) and for the two others models (d). The one-layered modeled Green's function is defined on the frequency range from 200 to 800 MHz. Two-layered and profile modeled Green's functions are defined on the frequency range from 200 to 1600 MHz.

In the frequency domain, discrepancies between measured and modeled signals appear very large, both in amplitude and in phase of the signal, especially at high frequencies above 1200 MHz. A regular oscillation of the measured signal with a small frequency period can be observed in the amplitude from 600 MHz, but this oscillation could not be modeled. This oscillation may correspond actually to a far-field reflector situated in the subsurface, that the two-layered or the profile models cannot reproduce because the maximum depth at which a reflector can be found for these models is bounded at 0.25 m.

As the noise appears to increase with frequency, i.e., with small wavelengths, this could also originate from surface soil roughness interferences, which produce scattering in the reflected signal. Nevertheless, such discrepancies between measured and modeled signals are not observed in the time domain representation, both for one-layered (Fig. 3.11(c)) and two-layered or profile models (Fig. 3.11(d)). The misfits between the measured and the modeled time domain GPR signals were assessed by the RMSE between these two signals in the 5-20 ns time window. The case depicted in Fig. 3.11(d) exhibits a RMSE of 0.175 and 0.186 for the two-layered and the profile modeled signals, respectively. The mean of the RMSE for the 300 points are 0.160 and 0.203, for the two-layered and the profile modeled signals, respectively. Similar agreements between measured and modeled GPR signals in the time domain can thus be observed for other points. Even though the inversion is performed in the frequency domain, the good agreement between measured and modeled signals in the time domain indicates that the models used for simulating the Green's functions can adequately reproduce the GPR signal in the soil up to 0.25 m in depth.

As the first layer thickness that is to be retrieved is small, it corresponds in the frequency domain to a large oscillation, whose period is covering around 600 MHz (e.g., local maxima of the amplitude in the frequency domain can be observed around 800 and 1400 MHz for the two-layered modeled signal). This oscillation indicates the presence of vertically-varying soil moisture, that can thus be detected owing to the large frequency bandwidth of the data. As a result, a large frequency bandwidth (i.e., 1400 MHz) is required to model such small layers or profiles with two-layered and profile models. The use of these models on a limited frequency bandwidth as the one-layered model inversion would hamper the retrieval of the layering conditions.

In the time domain, the air-soil surface reflection peak is centered at 10.5 ns and is highly visible in both Fig. 3.11 (c) and (d). The signals oscillations are larger in Fig. 3.11 (c) than in Fig. 3.11 (d) because of the lowest frequencies (200 to 800 MHz) used in the one-layered inversion. The second reflection peak, i.e., between the two soil layers, can be detected around 12 ns. It remarkably well corresponds to the travel time in the first layer computed knowing the inverted parameters of the first layer with the two-layered model. For this point, the first layer thickness being around 0.1 m and the permittivity around 5 (see Fig. 3.10 (b)), the travel time in the first layer is equal to 1.5 ns, which is corresponding to the position in time after the surface reflection peak.

3.6.3 Error sources in field acquisition

In this section, we discuss the sources of errors that are affecting the soil moisture values from the GPR acquisitions in field conditions. In laboratory conditions, with a critical two-layered medium, Minet *et al.* (2010a) (chapter 2) found a RMSE of about 0.02 in terms of volumetric water content when comparing laboratory-measured soil water content and GPR-inverted dielectric permittivities using a similar GPR setup. In field conditions, using the same GPR antenna and setup, Jadoon *et al.* (2010a) obtained a RMSE of 0.025 in terms of volumetric water content between TDR and GPR estimates.

Potential error sources in field conditions are model inadequacies and the use of the petrophysical relationship to translate the permittivities into soil moisture. Model inadequacies refer to the mismatch between the real soil structure and the way it is represented in the electromagnetic model. In this study, the soil is modeled as a multilayered medium of homogeneous soil layers. Lateral variability in the soil properties within the antenna footprint may therefore lead to a disagreement between the inverted and the footprint-averaged dielectric permittivities. The non-optimization of the electrical conductivity and the problem of soil roughness are other model inadequacies.

Soil electrical conductivity

In this chapter, the electrical conductivity was not optimized in order to reduce the inversion complexity and because it is assumed that the electromagnetic model is mostly insensitive to the electrical conductivity. Nevertheless, inversions with the optimization of the electrical conductivity were tested for the one-layered model only in order to evaluate the effect of neglecting the electrical conductivity optimization on the dielectric permittivity estimation.

Compared to the initial inversions, the dielectric permittivities from the inversions optimizing the electrical conductivity were slightly underestimated with a mean difference of 0.536 and a RMSE of 0.695 in terms of permittivity, corresponding to a water content difference of about 0.01 or 0.015, whereas the overall pattern of soil moisture remained unchanged. Therefore, neglecting the electrical conductivity in the optimization did not significantly impact on the permittivity estimation for the one-layered model. Similar impacts are to be expected for the two-layered and the profile model inversions.

Soil roughness

Soil roughness may affect the GPR signal for roughness heights larger than the tenth of the radar wavelength. At the minimal frequency of 200 MHz and considering the dielectric permittivities of the one-layered inversion, 91 % of the points are characterized by a wavelength larger than 50 cm, corresponding to an amplitude roughness threshold of 5 cm. However, considering larger frequencies, the free space wavelength of the radar waves is diminishing and roughness may affect the surface reflection by scattering. The effect of soil roughness on the GPR signal with increasing frequencies may be observed in Fig. 3.11(a), mainly above 800 MHz.

The effect of soil surface roughness on the GPR signal using a similar GPR setup was investigated in laboratory conditions in Lambot *et al.* (2006a). In that study, GPR signals were acquired in the 1-3 GHz frequency range. The largest roughness that was set had a standard deviation of 0.72 cm and an average maximal amplitude of 3.8 cm. There was a very slight effect of the roughness on the GPR signals in the 1-1.5 GHz frequency range. Regarding the GPR inversion, there was an overestimation of the GPR-derived permittivities of about 1 (in terms of absolute value) for an average maximal amplitude of one quarter the wavelength. Furthermore, the errors in the inverted parameters seemed to increase regularly with the roughness, so it may be expected that, to some extent, the response of the GPR inversion to larger roughnesses is proportional.

In our case, the field roughness is expected to be larger than the roughness investigated in that study (up to five times larger). However, the frequencies used are much lower than the ones considered in that study (0.2-0.8 GHz for the one-layered inversions instead of 1-3 GHz). Still, from that laboratory experiment results, we can expect an error of 1 in terms of absolute permittivity (that is, about 0.02 in terms of soil moisture) for roughness equal to one quarter the wavelength, which may be the most widely encountered situation during the field acquisition.

Use of the petrophysical relationship

In this chapter, the petrophysical relationship of Ledieu *et al.* (1986) (see Eq.(1.17)) is used to translate the GPR-derived dielectric permittivity into volumetric soil moisture. The use of another petrophysical relationship may however lead to different soil moisture results. A review on the use of numerous petrophysical relationships for linking GPR-derived permittivity and soil moisture can be found in Steelman and Endres (2010). In that study, using seven different Topp's like empirical relationships (i.e., with different parameterizations), the RMSE between GPR-derived permittivities and measured soil moisture ranged from 0.048 to 0.080 in terms of absolute soil moisture. The change in soil moisture caused by using different petrophysical relationships was thus around 0.03, which is lower than the smallest RMSE compared to soil sampling measurements. The error in soil moisture due to the petrophysical relationship choice can therefore be expected to be lower than the error when fitting a petrophysical model on field data. More complex models such as volumetric mixing formulae (e.g., the Complex Refractive Index) may reduce fitting errors, but they require highly spatially-variable field data, such as porosity and textural information, which is beyond the scope of this study. It is worth noting that the petrophysical relationship is actually expected to vary within a field because of soil properties variability.

In order to evaluate the influence of the choice of the petrophysical relationship, the differences in soil moisture estimated from the Ledieu relationship and the widely-used relationship of Topp *et al.* (1980) were computed and appeared negligible regarding other sources of errors in field conditions. The mean error and the root mean square error in volumetric soil moisture were equal to 0.0124 and 0.0133 m^3m^{-3}, respectively, with an overestimation for the Ledieu relationship. Nevertheless, this is not meaning that the errors due to the petrophysical transformation are negligible per se, but merely that the choice of another spatially-constant petrophysical relationship does not have a large impact on the soil moisture patterns presented in this study.

3.7 Conclusions

We analyzed GPR data inversion strategies using three models, i.e., a one-layered, a two-layered and a continuously-variable profile model for soil moisture retrieval in the field facing non-uniform conditions of soil moisture with depth. Numerical experiments showed that two-layered inversions permit to retrieve coherent soil moisture profiles, especially for the depth of the interface and for surface soil moisture, although more uncertainties were attributed to the lower layer soil moisture, because of the smoothly varying interface.

A high-resolution GPR survey, including 3741 records over an 11-ha agricultural field, was conducted and data were analyzed using the three inversion strategies tested for the numerical experiments. One-layered inversions led to a consistent surface soil moisture map, with a global soil moisture pattern mainly explained by the topography whereas local patterns indicated a line effect presumably caused by the ploughing lines. Surface and subsurface soil moisture maps from two-layered and profile inversions showed in general similar values and coherent soil moisture profile with respect to terrain observations, that is, soil moisture increases with depth. Further terrain evidences are needed to fully validate the technique, although the ground-truthing of soil moisture profiles remains complicated to perform at the field scale.

The off-ground GPR system appears as a promising proximal soil sensing tool for high-resolution and soil moisture mapping at the field scale and for soil moisture profile retrieval, when profiles conditions are encountered. It could be used for the validation of microwave remote sensing data products by ground-based surveys or the improvement of hydrological modeling at the field or subcatchment scale, especially when it is relevant to differentiate between the surface and subsurface soil moisture. Other naturally-layered media could be investigated, such as frozen soil layers in freezing or thawing conditions. In particular, the propagation of the GPR waves in frozen soils is alleviated and larger characterization depths could be reached.

Chapter 4

Validation of ground penetrating radar full-waveform inversion for field scale soil moisture mapping*

4.1 Outline

Ground penetrating radar (GPR) is an efficient method for soil moisture mapping at the field scale, bridging the scale gap between small-scale invasive sensors and large-scale remote sensing instruments. Nevertheless, commonly-used GPR approaches for soil moisture characterization suffer from several limitations and the determination of the uncertainties in GPR soil moisture sensing has been poorly addressed. Herein, we used an advanced proximal GPR method based on full-waveform inversion of ultra-wideband radar data for mapping soil moisture and uncertainties in the soil moisture maps were evaluated by three different methods. First, GPR-derived soil moisture uncertainties were computed from the GPR data inversion, according to measurements and modeling errors and to the sensitivity of the electromagnetic model to soil moisture. Second, the repeatability of the soil moisture mapping was evaluated. Third, GPR-derived soil moisture was compared with ground-truth measurements (soil core sampling). The proposed GPR method appeared to be highly precise and accurate, with spatially averaged GPR inversion uncertainty of 0.0039 m^3m^{-3}, a repetition uncertainty of 0.0169 m^3m^{-3} and an uncertainty of 0.0233 m^3m^{-3}

---

*This chapter is adapted from:
Minet, J.; Bogaert, P.; Vanclooster, M. & Lambot, S. Validation of ground penetrating radar full-waveform inversion for field scale soil moisture mapping, in *Journal of Hydrology*, **2011**, submitted.

when compared with ground-truth measurements. These uncertainties were mapped and appeared to be related to some local model inadequacies and to small-scale variability of soil moisture. The three methods permitted to discriminate the sources of errors in the GPR sensing of soil moisture and the interpolation was found to be the determinant source of the observed uncertainties in a soil moisture mapping framework. The proposed GPR method was proven to be largely reliable in terms of accuracy and precision and appeared to be highly efficient for soil moisture mapping at the field scale.

4.2 Introduction

The importance of accurate soil moisture characterization at various temporal and spatial scales for hydrologic, climatic and agriculture applications has boosted the development of different soil moisture sensing techniques. Among the soil moisture measurements techniques, invasive sensors such as time domain reflectometry (TDR) and capacitance probes still suffer from their small sampling volume ($\sim$ dm) that can be hardly compared with the larger footprint of the remote sensing instrument ($\sim$ 10 m), given the inherent high spatial variability of soil moisture at the radar footprint scale. With an intermediate support scale ($\sim$ m), ground penetrating radar (GPR) for soil moisture sensing may bridge the scale gap between invasive sensors and remote sensing instruments. A review about recent GPR developments can be found in Slob *et al.* (2010) while a complete review of GPR applications for soil moisture sensing was given in Huisman *et al.* (2003).

Off-ground (i.e., proximal or air-launched) GPR systems offer particularly promising perspectives in terms of proximal soil sensing, as antennas can be rapidly moved over the soil surface when mounted on mobile platforms. Using an approach similar to satellite remote sensing of soil moisture, the retrieval of soil moisture using off-ground GPR is based on the measurement of the soil surface reflection. Few studies have applied such an off-ground GPR approach for soil moisture sensing in field conditions (Chanzy *et al.*, 1996; Redman *et al.*, 2002; Serbin and Or, 2003, 2005). Based on a full-waveform inversion of the GPR data and an accurate GPR system modeling, the off-ground GPR system developed by Lambot *et al.* (2004b, 2006b) has shown excellent potentialities for surface soil moisture sensing and mapping in field conditions (Weihermüller *et al.*, 2007; Lambot *et al.*, 2008b; Jadoon *et al.*, 2010a; Jonard *et al.*, 2010; Minet *et al.*, 2011). The method relies on an accurate radar model that, in particular, accounts for the antenna and antenna-soils interactions.

The validation of the GPR technology for soil moisture retrieval implies a comprehensive assessment of the uncertainties in retrieval methods. The methods for assessing the uncertainties vary greatly in the literature, furthermore depending on the GPR system. Most of the studies attempted to calibrate or validate GPR measurements by comparing the GPR estimates with another measurement technique assumed to be the ground-truth (mainly TDR or soil sampling). Using the ground-wave technique, Huisman *et al.* (2001) compared GPR and TDR estimates of soil moisture with gravimetric sampling measurements and found similar root mean square error (RMSE) around 0.03 m^3m^{-3}.

The sources of errors were also identified and the dominant error was attributed to the petrophysical relationship. In controlled laboratory conditions, Lambot *et al.* (2004b) found a very low RMSE of 0.0066 m^3m^{-3} between water content from sampling measurements and off-ground GPR using a linear approximation of the frequency-dependent effective electrical conductivity. However, in field conditions and using the same off-ground GPR, Jadoon *et al.* (2010a) found a RMSE of 0.025 m^3m^{-3} between TDR and GPR estimates. The errors were mainly attributed to the different support scales of the instruments with respect to the small-scale within-field variability. As well as for remote sensing, the different support scales and the large vertical and lateral variations of soil moisture in real conditions may actually preclude the use of small-scale ground-truthing to fully validate the GPR sensors for soil moisture.

In that respect, Jacob and Hermance (2004) assessed the repeatability of GPR common mid-point (CMP) measurements using information from the same CMP measurements and from several independent CMP measurements performed at the same location. Using a cross-borehole GPR, Alumbaugh *et al.* (2002) obtained a RMSE in volumetric soil moisture of 0.005 m^3m^{-3} between repeated measurements. Recently, Bikowski *et al.* (2010) and Minet *et al.* (2010b) (chapter assessed the posterior distributions of GPR-derived soil properties by a Markov Chain Monte Carlo technique in GPR inversion frameworks. This permitted to quantify confidence intervals around the inverted parameters by accounting for errors associated with the GPR data processing.

4.3 Objectives

In this chapter, we propose to comprehensively evaluate the reliability of the GPR system developed by Lambot *et al.* (2004b) and exposed in the previous chapters for surface soil moisture mapping in field conditions and to quantify the soil moisture uncertainties. A mobile proximal GPR, as used in chapter 3, was conducted over a 2.5 ha agricultural field to map the soil moisture at high spatial resolution. One-layered model inversions in the time domain focused on the surface reflection only are considered in this chapter. We evaluated the reliability of the GPR technique by three independent uncertainty assessment methods. First, soil moisture uncertainties were derived from the inversion of the GPR data for each point by the computation of modeling error and soil moisture sensitivity. Second, three repetitions of the acquisition were performed, in order to assess the repeatability of the technique, by comparison with the spatial interpolation uncertainties. Third, soil moisture core sampling were performed in order to compare the GPR estimates with reference soil moisture measurements, allowing for the evaluation of the petrophysical model. These three independent soil moisture uncertainty assessment methods were compared and the different sources of errors were identified.

4.4 Materials and Methods

4.4.1 Study site

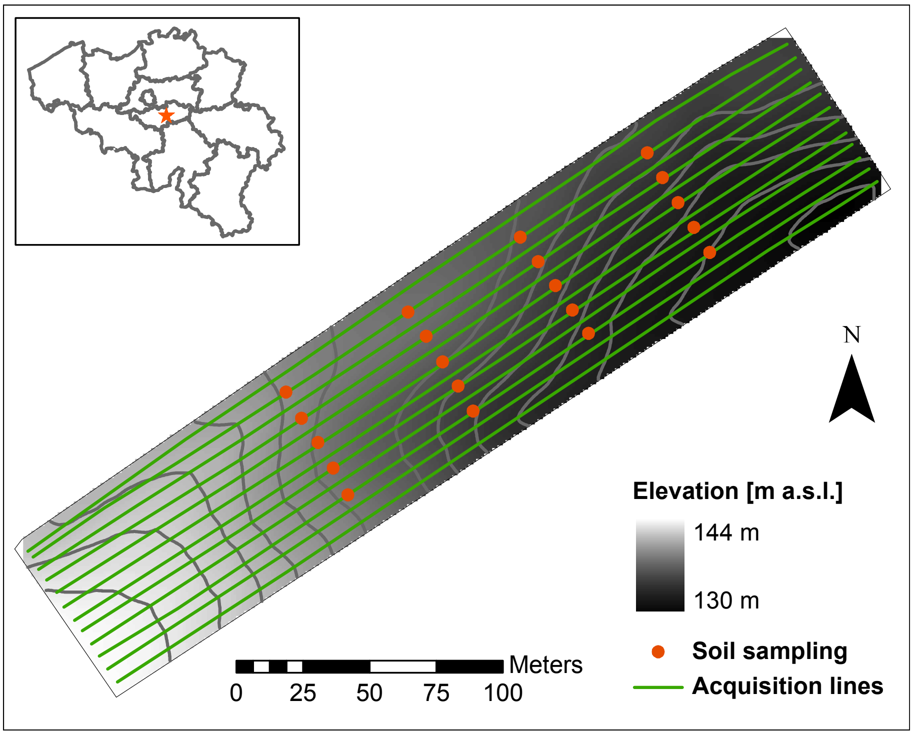

Figure 4.1: Study site of Burnia near Louvain-la-Neuve, Belgium. The GPR acquisition was performed along 12 parallel lines. Soil core sampling was performed in 20 locations.

We surveyed a 2.5-ha agricultural field situated in the loess belt area in the center of Belgium (Long. 4°41'8"E, Lat. 50°35'59"N) (Fig. 4.1). The soil type is uniformly a silt loam and elevation ranges from 130 to 144 m a.s.l. According to the national Belgian soil database (Aardewerk, Van Orshoven and Vandenbroucke (1993)), particles fraction are 4 % of sand, 82 % of silt and 14 % of clay for a soil sampling point situated at 500 m from the field. The GPR acquisition took place at the end of the winter on the 18^{th} of March 2010 in moderately wet conditions. According to a rain gauge station situated 2 km apart from the field, no rainfall were recorded for 11 days, but evaporation was limited due to low temperatures (3 °C on average for the 11 previous days). The field was covered by low-grown winter wheat (canopy height lesser than 5 cm). Surface roughness was low (amplitude around 5 cm) as the field was finely ploughed for wheat sowing four months before the campaign while rainfalls have flattened the soil surface during the winter.

4.4.2 Soil moisture sensing by ground penetrating radar

GPR setup

Figure 4.2: All-terrain vehicle holding the GPR system constituted of a horn antenna linked to a vector network analyzer, the DGPS device, an EM38 sensor and the PC. Picture taken on the 15^{th} of March 2010 in a Burnia near Louvain-la-Neuve, Belgium.

For field acquisition, the GPR system was mounted on an all-terrain vehicle (ATV), as widely described in chapter 3, GPR platform. Figure 4.2 presents a detailed picture of the ATV with the GPR system. The GPR setup was identical as presented in chapter 3, that was, an ultra-wideband horn antenna operating in the 200-2000 MHz was used. The ATV followed 12 parallel tracks with a spacing of 5 m between the acquisition tracks (see Fig. 4.1) and a driving speed of about 5 km/h. The GPR antenna footprint where soil moisture is measured has a diameter of about 1.5 m and a sampling depth around 5 cm. Three repetitions of the acquisition were performed within 3h, accounting in total for 4600 measured points. The purpose of the repetitions were to evaluate the repeatability of the overall GPR technique in field conditions, including the interpolation effect, knowing that the measured points were not taken exactly at the same locations for each repetition but at least were along the same tracks.

GPR data inversions for surface soil moisture

Surface soil moisture was retrieved using full-waveform inversion of GPR data focused on the surface reflection. The raw measured GPR data in the frequency domain were first filtered out from the antenna effects using the antenna transfer functions in order to obtain the GPR response from the soil only, namely, the Green's function, as presented in Fig. 4.3 for an arbitrary GPR measurement. In this chapter, the soil is considered as a homogeneous medium within the GPR antenna footprint (i.e., a one-layered configuration as presented in chapter 3). The frequency-dependent GPR data from field measurements were selected from 200 to 800 MHz as the highest frequencies were affected by measurements noise arising because of soil roughness scattering (Lambot *et al.*, 2006a) (see Fig. 4.3 (a)). In order to identify the shallow surface soil dielectric permittivity, the GPR data were selected on a time window focused on the soil surface reflection peak, after transformation of GPR data from the frequency to the time domain using the inverse Fourier transform (i.e., the TIME L-M scenario in chapter 2). The soil surface reflection peak can be easily detected as it corresponds to the largest oscillation in the time domain GPR waveform, as delineated in Fig. 4.3 (b). This time-windowing permitted to identify the surface soil dielectric permittivity and correlated soil moisture from the shallow soil layer (Lambot *et al.*, 2006b; Minet *et al.*, 2011).

Two parameters were optimized in the GPR inversion, namely, the surface soil dielectric permittivity ε and the GPR antenna height h_0. The inverse problem was formulated in the least-squares sense and the objective function was accordingly defined as:

$$\phi(\mathbf{b}) = \sqrt{\frac{\mathbf{e}(\mathbf{b})^T \mathbf{e}(\mathbf{b})}{n-p}} \tag{4.1}$$

with n being the length of the time domain vector, p the number of parameters, and the error function $\mathbf{e}(\mathbf{b})$ defined as the difference between the measured and modeled Green's functions in the time domain with:

$$\mathbf{e}(\mathbf{b}) = \mathbf{g}^{\uparrow *}_{\mathbf{xx}}(t) - \mathbf{g}^{\uparrow}_{\mathbf{xx}}(\mathbf{b}, t) \tag{4.2}$$

where $\mathbf{g}^{\uparrow *}_{\mathbf{xx}}(t)$ and $\mathbf{g}^{\uparrow}_{\mathbf{xx}}(\mathbf{b}, t)$ being, respectively, the measured and modeled Green's functions in the time domain (n $\times$ 1) focused on the surface reflection, and $\mathbf{b}$ (p $\times$ 1) the parameter vector of the inverse problems ($\mathbf{b} = [\varepsilon, h_0]$).

The inverse problem thus consists of finding the minimum of this objective function by optimizing the parameter values. Optimization was performed using a local search algorithm (i.e., the Levenberg-Marquardt algorithm (Marquardt, 1963)). The initial guess for the dielectric permittivity was arbitrarily chosen as $\varepsilon = 10$ as this was a mean expected value for this parameter (corresponding to a volumetric soil moisture $\theta \approx 0.20$ m^{3}m^{-3}). The initial guess for the GPR antenna height h_0 was computed for each measured Green's function $\mathbf{g}^{\uparrow *}_{\mathbf{xx}}(t)$ in the time domain using the arrival time of the soil surface reflection peak.

For electrical conductivity lower than 0.01 S/m, Lambot *et al.* (2006b) demonstrated that the electromagnetic model was insensitive to the electrical

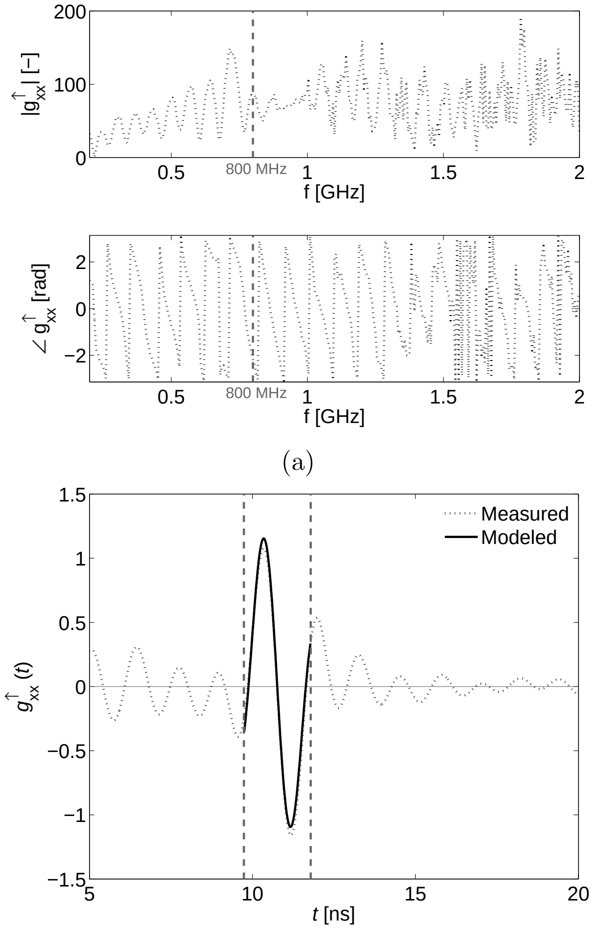

(a)

(b)

Figure 4.3: Measured and modeled Green's function depicted in the frequency domain in amplitude and phase (a) and in time domain (b). The time-window corresponding to the surface reflection is delineated in (b).

conductivity in a similar frequency range. Therefore, this parameter could be neglected in the optimization and was set to zero in the electromagnetic model. This assumption was nevertheless verified by performing inversions accounting for the optimization of the electrical conductivity, i.e., with $\mathbf{b} = [\varepsilon, h_0, \sigma]$

We used two petrophysical models for relating GPR-derived dielectric permittivity ε to volumetric soil moisture values θ. The first model was the widely-used relationship of Topp *et al.* (1980) with the classical parameterization (Eq. (1.16)). The Topp's relationship was used to translate the permittivity retrieved by the GPR data inversions into soil moisture. However, the second model, i.e., the model of Ledieu *et al.* (1986), was used for fitting the GPR-derived permittivity and volumetric soil moisture from soil sampling measurements (Eq. (1.17)). This model assumes a linear relationship between $\sqrt{\varepsilon}$ and θ and appeared to be more robust for fitting the petrophysical relationship over a limited range of soil moisture conditions in this study.

Soil moisture interpolation

Soil moisture maps were produced by the interpolation of point measurements using ordinary kriging. To deal with the uneven disposition of the points in space (i.e., globally a 2 m spacing along the acquisition line and a 5 m spacing between lines), a rectangular neighborhood window was chosen such that the same numbers of points were taken in the perpendicular and parallel direction with respect to the acquisition lines direction. This permitted to prevent acquisition line effects to appear in the interpolated maps. Unidirectional variograms estimates were computed along (parallel) and perpendicular to the acquisition lines with a class distance from 0 to 150 m and from 0 to 60 m by a step of 5 m for the parallel and perpendicular variograms, respectively, according to the dimensions of the field. The parallel variogram was used for interpolating the point-data after fitting an exponential model accounting for a nugget effect, because this variogram reflects the natural spatial correlation of soil moisture independently of the line effect. The exponential model appeared to be the best model for fitting the parallel variograms estimates. Interpolated soil moisture values were computed as linear combinations of the values of neighboring points according to the ordinary kriging method.

4.4.3 Uncertainties assessment

Each of the previously exposed steps (i.e., GPR measurements, inversions and interpolation) introduces uncertainties in the final soil moisture maps. In this study, we assess the soil moisture uncertainties by three independent ways:

1. by computing GPR inversion uncertainties according to the modeling error and the model sensitivity to soil moisture;
2. by repeating the acquisition for assessing the repeatability of the sensing and mapping of soil moisture;
3. by comparing with ground-truth measurements of soil moisture (soil core sampling).

Inversion uncertainties

The GPR data inversion consists in finding the optimal set of parameter values that minimizes the objective function (Eq. (4.1)). The uncertainties of inverted parameters can be quantified from the value of the objective function at its minimum (measurement and modeling errors) and from its curvature around the minimum (model sensitivity), accounting for GPR measurement and modeling errors. According to Kool and Parker (1988), inverted dielectric permittivity uncertainty $\sigma_{\varepsilon,GPR}$ were determined by the square root of the diagonal element of the parameter variance-covariance matrix $\mathbf{C}$ (p × p) corresponding to the dielectric permittivity:

$$\sigma_{\varepsilon,GPR} = \sqrt{\mathbf{C}_\varepsilon} \tag{4.3}$$

with the matrix $\mathbf{C}$ being given by:

$$\mathbf{C} = \frac{\mathbf{e}^{*T}\mathbf{e}^{*}}{n-p}(\mathbf{J}^T\mathbf{J})^{-1} \tag{4.4}$$

where $\mathbf{J}$ is the Jacobian (or sensitivity) matrix (n × p) and $\mathbf{e}^* = \mathbf{e}(\mathbf{b}^*)$, the error vector at the minimum of the objective function (see Eq. (4.2)). The elements (i,j) of the Jacobian matrix are the partial derivatives of the error function $\mathbf{e}(\mathbf{b})$ with respect to the optimized parameters values $\mathbf{b}^*$ for each data i and parameter j with:

$$J_{i,j} = \frac{\delta \mathbf{e_i}}{\delta b_j^*} \tag{4.5}$$

The Jacobian matrix thus reflects the way the model is sensitive to a small parameter change. In practice, the partial derivatives $\frac{\delta \mathbf{e_i}}{\delta b_j^*}$ of the Jacobian matrix were approximated by finite differences, assuming a change in the parameter value of 1 %. The uncertainty in dielectric permittivity $\sigma_{\varepsilon,GPR}$ was translated in uncertainty in soil moisture $\sigma_{\theta,GPR}$ using propagation of error theory:

$$\sigma_{\theta,GPR} = \frac{\delta\theta(\varepsilon)}{\delta\varepsilon}\sigma_{\varepsilon,GPR} \tag{4.6}$$

where $\theta(\varepsilon)$ is the relationship of Topp *et al.* (1980) (Eq.(1.16)).

The parameter uncertainty can be seen as the combination of two contributions, that are the modeling error and the parameter insensitivity. The modeling error (or error of fit) is the value of the objective function at its minimum, i.e., the value of the objective function for the optimized parameters ($\phi(\mathbf{b}^*)$). The parameter sensitivity is related to the Jacobian matrix, as it expresses the curvature of the objective function in the vicinity of the minimum for a small change in the optimized parameter value. Therefore, the parameter uncertainty is large for a high modeling error and a low parameter sensitivity.

This method assumes that the model is linear in its parameters in the vicinity of the minimum and that measurement errors are normally distributed and independent of time and space. Although the electromagnetic model is not linear over the full physically-sound parameter range, this assumption may be reasonable when considering a small parameter range. This assumption was successfully verified by performing Markov-Chain Monte-Carlo sampling of the parameter space around the minimum of the objective function using the Metropolis-Hastings algorithm implemented in the differential evolution adaptive metropolis (DREAM) algorithm (Vrugt *et al.*, 2009). For nonlinear problems, this algorithm can efficiently draw the complete posterior parameter distributions.

Repetition uncertainties

The three repetitions were compared one by one by mapping the difference of the interpolated soil moisture values $\Delta\theta$. The comparison had to be done based on interpolated values because the GPR measurements could not be taken strictly at the same locations, although the same acquisition tracks were followed for each repetition. The global repetition error was computed as the root mean square of the differences between the repetitions (RMSE$_{rep}$).

Moreover, in order to truly compare the repetitions, the effect of the interpolation (kriging) was taken into account for comparing the maps of the difference between these repetitions. If the soil moisture is assumed as time-invariant for all repetitions, the part of the repetition uncertainty that is due to the interpolation of two datasets with different point locations can be assessed by the variance of the difference in the interpolated values $\sigma^2_{\Delta\theta}$, which was estimated in each point of the interpolated space x_0 as:

$$\sigma^2_{\Delta\theta}(x_0) = \sigma^2_{\theta_1}(x_0) + \sigma^2_{\theta_2}(x_0) - 2\mathbf{w}^{\mathbf{T}}_{\theta_1}\mathbf{K}_{\theta_1,\theta_2}\mathbf{w}_{\theta_2} \tag{4.7}$$

where $\sigma^2_{\theta_1}(x_0)$ and $\sigma^2_{\theta_2}(x_0)$ are the variance of the kriging predictor for the first and second repetitions, respectively, $\mathbf{w}_{\theta_1}$ and $\mathbf{w}_{\theta_2}$ are the weights of the kriging predictor for the first and second repetitions (i.e., the solution of the kriging system), respectively, and $\mathbf{K}_{\theta_1,\theta_2}$ is the covariance matrix between the points of the first and second repetitions. This variance $\sigma^2_{\Delta\theta}$ is the uncertainty on the predicted value given the fact that two sets of sampling locations are used for estimating soil moisture at the same location x_0. For each interpolated point, this variance depends only on the relative locations of the measured points of both repetitions, meaning that a null variance would be obtained if the points of two repetitions were exactly located at the same locations.

A standardized difference of the interpolated soil moisture $\Delta\theta^*$ can be computed by:

$$\Delta\theta^* = \frac{\Delta\theta}{\sqrt{\sigma^2_{\Delta\theta}}} \tag{4.8}$$

where $\Delta\theta^*$ is following the standard normal distribution (∼N(0,1)). By computing this standardized variable, the significance of the observed difference in interpolated soil moisture can easily be computed and errors can be compared over space independently of the interpolation effect.

Comparison with soil sampling measurements

In order to validate the accuracy of the GPR soil moisture measurements, surface soil moisture was independently measured by volumetric soil core sampling in the top 5 cm at 20 regularly spaced locations (see Fig. 4.1). Soil samples were oven-dried at 105°C for at least 48h and the dry and wet weights were measured, in order to determine the volumetric moisture. The volumetric soil moisture of the soil samples was then compared with the interpolated value of the GPR-derived dielectric permittivity using the three repetitions for the interpolation at the locations of the soil core sampling.

4.5 Results

4.5.1 Surface soil moisture maps

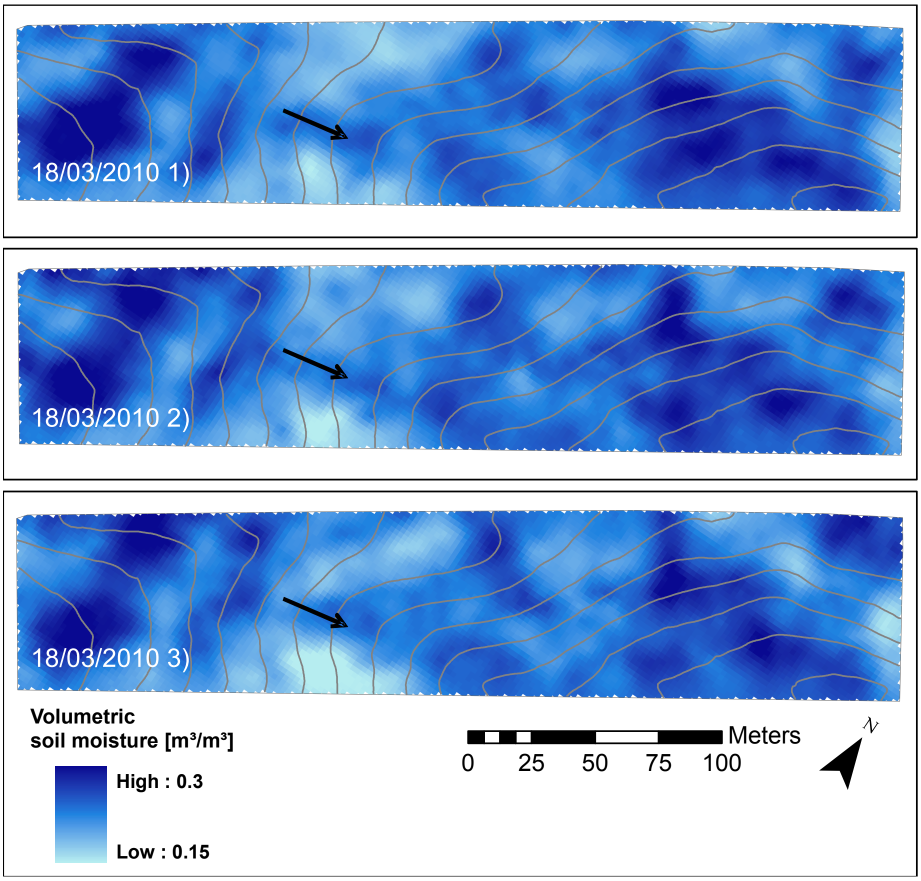

Figure 4.4: Soil moisture maps for the three acquisitions. Topographic contour lines with an interdistance of one meter are depicted in grey lines. The black arrows indicate the location and the direction of the slope of the main thalweg in the field.

Figure 4.4 presents the interpolated soil moisture maps from the three GPR acquisitions. Soil moisture pattern was driven by topography, as the soil and vegetation conditions were rather homogeneous. High soil moisture values were

Table 4.1: Statistics of GPR-derived volumetric soil moisture [m^3m^{-3}] (non-interpolated values)

Repetition	μ_θ	median$_\theta$	σ_θ	θ_{min}	θ_{max}
1	0.234	0.227	0.063	0.053	0.445
2	0.236	0.232	0.061	0.054	0.456
3	0.233	0.230	0.063	0.051	0.436

encountered in the lowest and highest elevated parts of the field, respectively, at the right and left of the figure, where the field is actually quite flat. The center of the thalweg, indicated with an arrow on the maps, appeared wetter than its surroundings. The field-average soil moisture was equal to about 0.23 m^3m^{-3} with a standard deviation of 0.06 m^3m^{-3}, with very similar values between the three repetitions (see Table 4.1). When optimizing the electrical conductivity in the GPR inversions, negligible impact was observed on the optimization of the permittivity ε (mean absolute error of 0.059 in terms of ε comparing to GPR inversions without the optimization of the electrical conductivity).

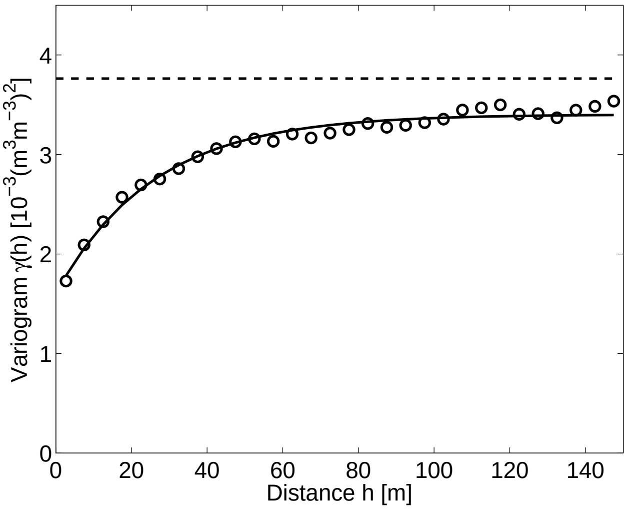

Figure 4.5: Variogram for soil moisture computed along the acquisition lines for the three repetitions. An exponential model is fitted on the variogram estimates. The sampling variance is indicated by the horizontal dashed line.

The observed soil moisture exhibited a very similar spatial correlation between the three repetitions, so that a unique variogram was used for interpolating the soil moisture point measurements (Fig. 4.5). An exponential model was fitted over the variogram estimates (nugget = 1.60 10^{-3} $(m^3m^{-3})^2$, partial sill = 1.80 10^{-3} $(m^3m^{-3})^2$, range = 77 m).

4.5.2 Inversion uncertainties

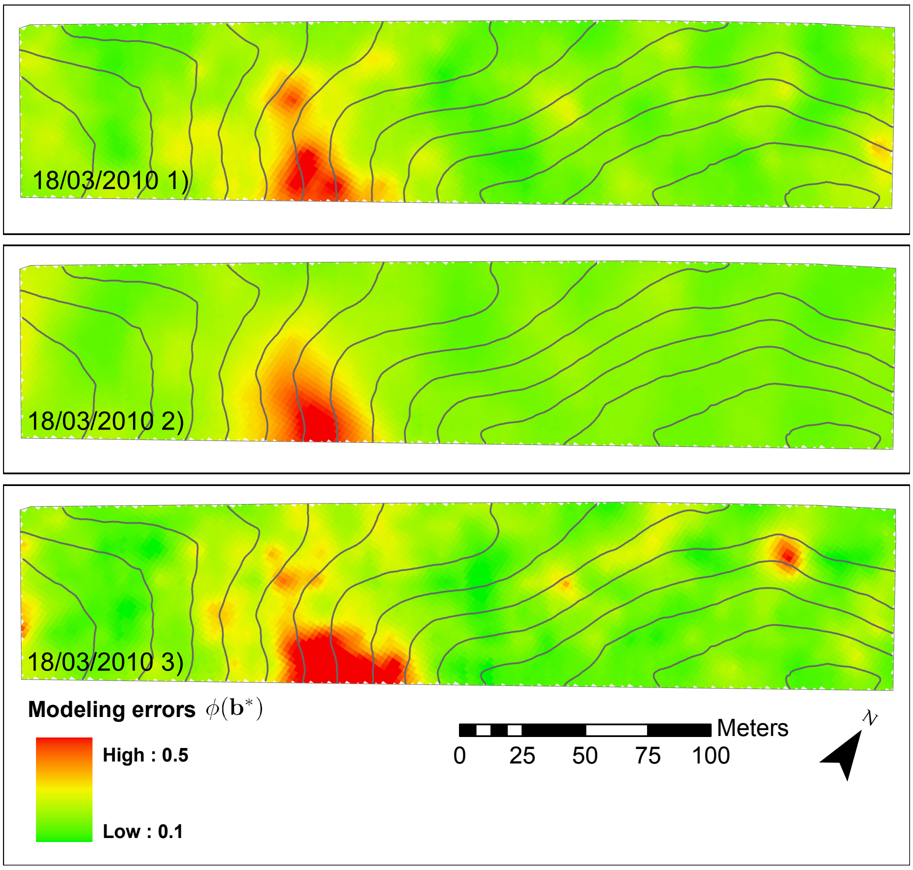

Figure 4.6: Maps of the interpolated modeling error $\phi(\mathbf{b}^*)$. Topographic contour lines with an interdistance of one meter are depicted in grey lines.

Inverted parameter uncertainties are affected by measurement and modeling errors and are decreasing with model sensitivity to the parameters (see Eq. (4.4)). Figure 4.6 shows the maps of the interpolated modeling error for the three repetitions. The modeling errors appeared to be spatially and temporally correlated. The spatial correlation was moderate, with nugget/sill ratios of 0.66, 0.66 and 0.49, for the three repetitions, respectively. However, the coefficients of correlation between the three repetitions ranged from 0.81 to 0.87, indicating large temporal correlations, as it could be expected from a visual comparison of the three maps. In particular, a patch of the field, situated in the middle left along the bottom limit of the field, was affected by a very high modeling error compared to the rest of the field. Furthermore, the location and the shape of the patch remained identical between the three repetitions.

Figure 4.7 presents the observed model sensitivity to the permittivity, i.e., the sum of the elements of the Jacobian matrix for the permittivity, as a func-

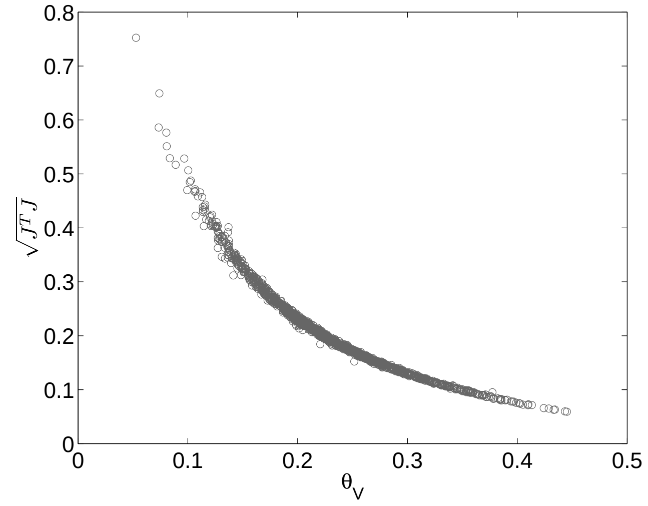

Figure 4.7: Observed sensitivity of the electromagnetic model, expressed by the sum of the elements of the Jacobian matrix for the permittivity, as a function of inverted soil moisture.

tion of inverted soil moisture for the first repetition. The sensitivity of the electromagnetic model to the dielectric permittivity was decreasing with increasing soil moisture. It indicated that for high soil moisture, a large variation of soil moisture results in a small variation of the model response. It is worth mentioning that the sensitivity is presented here as a function of soil moisture, instead of soil dielectric permittivity. Nevertheless, the relationship between dielectric permittivities and model sensitivity appeared similar, although more curved.

Figure 4.8 presents the maps of the interpolated soil moisture uncertainty $\sigma_{\theta,GPR}$ for the three repetitions. The soil moisture uncertainties appeared very small, with a mean equal to 0.0039 m^3m^{-3} for the three repetitions. As well as for the modeling error maps (Fig. 4.6), soil moisture uncertainties appeared temporally and spatially correlated. The $\sigma_{\theta,GPR}$ pattern (Fig. 4.8) resulted from the combination of the modeling errors (Fig. 4.6) and the soil moisture sensitivity, which is inversely related to the soil moisture pattern (Fig. 4.4). As the relationship between soil moisture and model sensitivity to the permittivity is clearly defined (see Fig. 4.7), the soil moisture uncertainty maps is inversely related with the soil moisture pattern, with a coefficient of correlation of 0.403 between θ and $\sigma_{\theta,GPR}$ for the non-interpolated values. When optimizing the electrical conductivity in the GPR inversions, the uncertainties in ε were poorly affected (mean absolute error of 0.038 in terms of ε). The uncertainties in electrical conductivity were however abnormally high with values outside of the realistic physical range for soils, as a result of the poor sensitivity of this parameter to the model in that frequency range and for low conductive conditions.

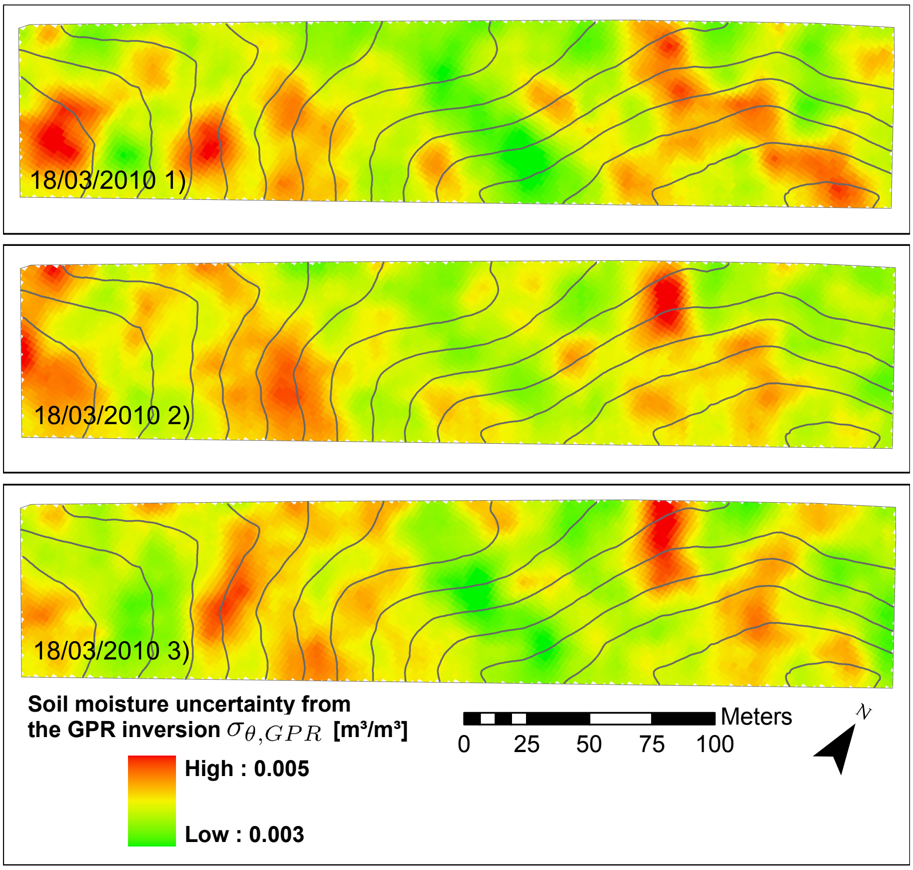

Figure 4.8: Maps of the soil moisture uncertainty $\sigma_{\theta,GPR}$ [$\mathrm{m^3m^{-3}}$] computed using Eqs (4.3) to (4.6). Topographic contour lines with an interdistance of one meter are depicted in grey lines.

The assumption of linearity of the electromagnetic model to its parameters was asserted by performing Markov-Chain Monte-Carlo sampling of the parameter space. The standard deviations of the complete posterior distributions of the optimized parameter and the uncertainties computed using the method of Kool and Parker (1988) appeared remarkably similar (results not shown). The use of a Markov-Chain Monte-Carlo sampling is therefore unnecessary, knowing that it requires about 1000 times more computation time.

4.5.3 Repetition uncertainties

The interpolated soil moisture maps (Fig. 4.4) showed very similar patterns when comparing the three repetitions, with coefficients of correlation of 0.87 between the first and second repetitions, 0.88 between the second and third repetitions and 0.81 between the first and third repetitions. Figure 4.9 shows the repetition uncertainty maps (i.e, the difference in interpolated soil moisture of each repetition to each other $\Delta\theta$) between the three repetitions. The global repetition errors RMSE$_{rep}$ were found to be equal to 0.0164, 0.0156 and 0.0186 $\mathrm{m^3m^{-3}}$ for the three maps, respectively. The repetition uncertainty patterns were poorly spatially correlated, although some parts of the field exhibited small patches of similar repetition uncertainties. Some similitude could be observed with the modeling error maps (Fig. 4.6). In particular, the patch of high modeling error in the middle left along the bottom limit of the field corresponded here to larger repetition errors than the rest of the field.

A part of the observed differences $\Delta\theta$ can be attributed to the effect of the interpolation, knowing that different sets of measurements were used for interpolating at same locations. The field-averaged deviations of the difference between the repetitions $\sigma_{\Delta\theta}$ computed by Eq. (4.7) were found to be equal to 0.0143, 0.0141 and 0.0143 $\mathrm{m^3m^{-3}}$ for the three maps shown in Fig. 4.9, respectively, denoting that the interpolation effect accounted for a large part in the observed discrepancies between repetitions. The zones delineated in Fig. 4.9 with black lines highlight the places where the standardized difference of the interpolated soil moisture $\Delta\theta^*$ (see Eq. (4.8)) is outside of the range [-2, 2], i.e., the zones where the two repetitions of the acquisition resulted in different soil moisture estimates at 95 % of confidence level, independently of the interpolation effect. These zones were rather small and appeared randomly located in the field. Finally, it is worth noting that the difference between the first and third repetition was larger than between the other repetitions, i.e., the RMSE$_{rep1,3}$ was the largest and the zones of different soil moisture estimates were the most extended. This could indicate a real change in soil moisture as the elapsed time between the first and third repetitions was the largest (two hours instead of one hour), although this could not be demonstrated.

4.5.4 Comparison with soil sampling measurements

Figure 4.10 presents the comparison between interpolated GPR-derived soil dielectric permittivity ε_{GPR} using the three repetitions and volumetric soil moisture θ_V from the soil sampling measurements. A simple petrophysical

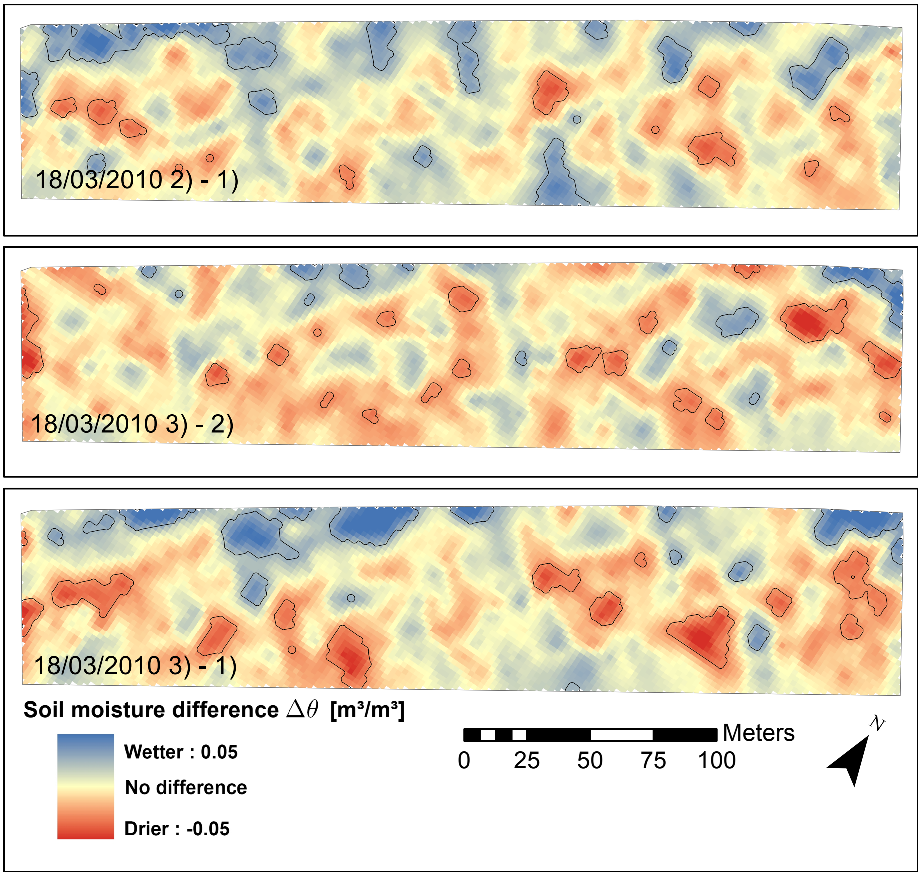

Figure 4.9: Maps of the repetition uncertainties for the three acquisitions. The repetition uncertainty is computed as the difference between the interpolated values of each repetitions. The black lines delineated the zones where the two repetitions of the acquisition resulted in different soil moisture estimates, at 95 % of confidence.

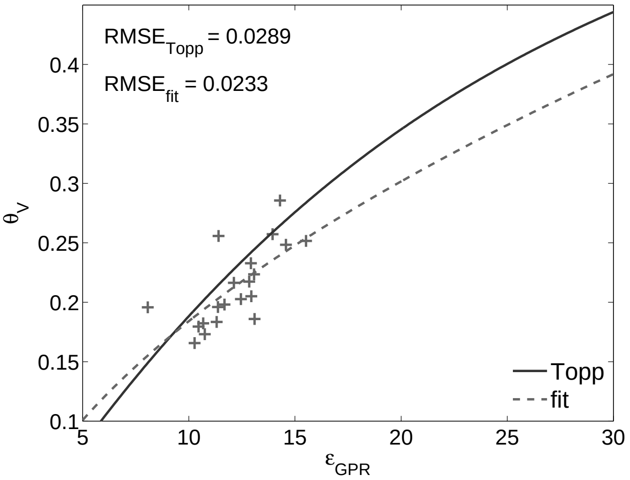

Figure 4.10: Comparison between interpolated GPR-derived soil dielectric permittivity ε_{GPR} and volumetric sampling soil moisture θ_V.

(Ledieu *et al.*, 1986) (Eq. (1.17)) was fitted over the data and the standard relationship of Topp *et al.* (1980) (Eq. (1.16)) was also drawn for comparison. There was a good agreement between the soil permittivity and moisture, with a RMSE$_{fit}$ of 0.0233 m^{3}m^{-3} when fitting the Ledieu's model, as well as when comparing with the Topp's relationship (RMSE$_{Topp}$ = 0.0289 m^{3}m^{-3}). The Topp's and fitted relationships were therefore in good agreement, except for high soil moisture. When considering the three repetitions for interpolating the GPR-derived permittivity separately, RMSE$_{fit}$ were equal to 0.0222, 0.0216 and 0.0259 m^{3}m^{-3} for the three repetitions, respectively (Table 4.2).

4.6 Discussions

4.6.1 Inversion uncertainties

The GPR-derived soil moisture uncertainties thus resulted from the combination of the modeling error and the soil moisture sensitivity. The decreasing model sensitivity with increasing soil moisture is related to the non-linearity of the Fresnel reflection coefficient function with the soil dielectric permittivity for an air/soil interface. The non-linearity of the petrophysical model relating the soil permittivity to the soil moisture reduces the degree of this non-linearity, but not to a sufficient extent. However, it is worth noting that for TDR and GPR methods that are based on the determination of the travel time of the wave propagation rather than on the surface reflection coefficient, the relationship between the soil moisture and the travel time is linear, assuming a Ledieu's like petrophysical relationship (Herkelrath *et al.*, 1991; Huisman *et al.*, 2001).

Non-null modeling errors indicated model inadequacies, i.e., the soil differed from the homogeneous medium it was supposed to be. The large spatial and temporal correlation and the similar patterns observed in the modeling error maps (Fig. 4.6) and, to a lesser extent, in the other uncertainty maps (Fig. 4.8 and 4.9), denoted that model inadequacies were probably related to local soil conditions, especially because modeling errors appeared to be spatially correlated when considering adjacent acquisition tracks. The model inadequacies caused a large modeling error (Fig. 4.6), that, in turn may impair the capacity of the GPR to sense the same soil moisture at each repetition (Fig. 4.9). As the errors appeared strongly dependent on local conditions rather than being randomly distributed or time-dependent, this therefore discarded the hypothesis of errors caused by a sensor drift, vibrations of the platform, or any measurement problems that are not linked to local soil conditions.

High electrical conductivity, surface soil roughness and within-support heterogeneities were identified as the hypothetic model inadequacies and were discussed below. First, highly conductive soils conditions may have impacted on the retrieval of the dielectric permittivity in the GPR inversion if not well accounted for (Giroux and Chouteau, 2010). Nevertheless, in our study, optimizing the electrical conductivity in the GPR inversions did not impact on the retrieval of dielectric permittivities nor on the inversion uncertainties of dielectric permittivities. The huge uncertainties in electrical conductivity denoted a complete insensitivity of this parameter to the electromagnetic model, as already observed in Lambot *et al.* (2006b) for conductivity values lower than 0.01 S/m, using the same GPR system and a similar frequency bandwidth (i.e., 100-900 MHz). As a result, GPR inversions neglecting the optimization of the electrical conductivity were used in this study.

Second, large surface soil roughness may have impacted on the reflection of the GPR wave by causing interferences. Using the same GPR setup, the effect of surface roughness on the retrieval of the dielectric permittivity was analyzed in laboratory in Lambot *et al.* (2006a) and widely discussed in case of field acquisition in chapter 3. Owing to the relatively low-frequency range used in the GPR inversion, surface soil roughness may significantly impact only for roughness larger than 5 cm. From visual field observation, we can state that such rough conditions were not widely encountered.

Lastly, lateral and vertical soil moisture heterogeneities within the GPR antenna footprint, which is assumed to be an homogeneous medium, could be an important cause of model inadequacy. The effect of vertically-varying soil moisture was investigated through numerical and laboratory experiments in chapter 2 (Minet *et al.*, 2010a) and in field conditions in chapter 3 (Minet *et al.*, 2011). In the presence of a shallow soil layer of a different moisture content than the sublayer, a RMSE of 0.05 m^3m^{-3} in the soil moisture estimation was obtained (Minet *et al.*, 2010a, laboratory experiment). For small contrast between the layers (< 0.05), the error was nevertheless negligible. The presence of a vertically-varying soil moisture profile can be detected in measured Green's functions over a large frequency bandwidth. Nevertheless, in this study, such conditions could not be revealed through an analysis of the Green's functions, as it could have done in chapter 3. The absence of observed profile conditions in the GPR data could originate from a poorly developed soil moisture profile (i.e., small contrast between surface and subsurface) or from a profile that is too deep to be sensed, with respect to the relatively small penetration depth of the GPR. In addition, no differences in the shape of the measured Green's functions could be observed when comparing GPR data from the zones where low and high uncertainties were identified with the different methods. This did not support the use of multi-layered medium inversions, as it would furthermore increase the inversion uncertainties for the optimized parameters.

4.6.2 Repetition uncertainties

A large part of the repetition uncertainties was explained by interpolation effects, given that different point measurements were used for each repetition. This could be related to the small-scale spatial variability of soil moisture and the relatively large nugget effect observed in the variogram. It is worth mentioning that this variance of the difference increases with the spacing between point measurements of two repetitions.

The residual repetition uncertainties that were not explained by the interpolation process may indicate either a real change in soil moisture or a different sensing of soil moisture by the GPR. The slightly larger difference between the first and third repetitions seemed to indicate a real change that could originate from surface evaporation or a slight soil compaction caused by the ATV, although these processes could not be explicitly proved.

Using cross-boreholes GPR measurements, Alumbaugh *et al.* (2002) found a repeatability error of 0.54 ns in the ground wave velocity, corresponding to a soil moisture error of about 0.005 m^3m^{-3}. Errors were increasing with soil moisture and were attributed to instrument instability. When comparing repeated CMP surface measurements, Jacob and Hermance (2004) found a precision of 0.7 ns in the two-way travel time. Huisman and Bouten (2003) reached a repeatability of 0.003 m^3m^{-3} when using single trace analysis of GPR ground wave data for soil moisture determination. In these studies, no uncertainties due to the interpolation and small-scale variability were taking part, which are however determinant for the repetitions uncertainties in our study.

4.6.3 Comparison with soil sampling measurements

The high accuracy of the GPR method for soil moisture sensing was established from the comparison with soil sampling measurements. The use of the Topp's relationship was also validated. However, the small range of permittivity values did not permit to verify this agreement over the full physical range of soil moisture. The observed discrepancies can be attributed to the different support scales and depths of characterization of the techniques, with respect to the important small-scale variability of soil moisture. Spatially-varying soil properties makes the use of a unique petrophysical model for the whole field questionable as well. In addition, soil moisture values from the soil sampling points were compared with interpolated dielectric permittivity, as both measurements were not taken exactly at the same locations, at least in the same acquisition line. Therefore, interpolation uncertainties can explain a large part of the observed discrepancies. Lastly, soil moisture values from sampling measurements can be affected by measurements errors as well.

The comparison of the GPR estimates with soil sampling measurements or other invasive measurements in field conditions is actually problematic because of the different support scales of the techniques. Using the same off-ground GPR in field conditions, Jadoon *et al.* (2010a) found a RMSE of 0.025 m^3m^{-3} between TDR and GPR estimates, but a soil moisture variability of 0.02 to 0.07 m^3m^{-3} was measured by TDR within each GPR footprint. Therefore, knowing this important submetric variability, it is problematic to compare a soil core sample (3 cm diameter) with the GPR antenna footprint (∼1.5 m diameter). With respect to the depths of penetration, Jadoon *et al.* (2010a) found that the GPR waves may sense the soil moisture up to 4 cm depth (which was close to the sampling depth of the core (5 cm)) but it is worth noting that this depth actually varies depending on the soil moisture itself.

Considering the whole field, the use of a unique petrophysical relationship may be affected by some limitations as this relationship may depend on the specific local soil conditions (e.g., soil texture, porosity). In addition, the use of different petrophysical models, even when calibrated with field data, can result in differences in terms of volumetric soil moisture up to 0.10 m^3m^{-3} (Sambuelli, 2009; Steelman and Endres, 2010). Despite these important limitations, the comparison with soil sampling measurements is still the only method for quantifying the accuracy of the GPR method, in addition to its precision. Nevertheless, larger variations of soil moisture from dry to wet states would be required for a stronger calibration of the petrophysical relationship.

4.6.4 Comparison of the uncertainties

Table 4.2: Summary of the soil moisture uncertainties [m^3m^{-3}] determined by the different methods

	GPR inversion uncertainties ($\sigma_{\theta,GPR}$)	Comparison with soil sampling (RMSE$_{fit}$)
Repetition 1	0.00392	0.0222
Repetition 2	0.00398	0.0216
Repetition 3	0.00394	0.0259
All	0.0039	0.0233
	Repetition uncertainties (RMSE$_{rep}$)	Deviation of the difference ($\sigma_{\Delta\theta}$)
Repetition 1 vs 2	0.0164	0.0143
Repetition 2 vs 3	0.0156	0.0141
Repetition 1 vs 3	0.0186	0.0143
All	0.0169	0.0142

In this section, we discuss the global soil moisture uncertainties quantified by the different methods and averaged over the whole field (Table 4.2). The two first uncertainties assessment methods, i.e., inversion and repetition uncertainties, evaluated the precision of the GPR technique while the comparison with ground-truth of soil moisture also evaluated its accuracy. The lowest uncertainties were the GPR inversion uncertainties $\sigma_{\theta,GPR}$, which were derived from GPR inversions only, i.e., without influence of the interpolation effects. It is however unknown to what extent this represented the total uncertainty associated with a GPR measurement.

The global repetition errors RMSE_{rep} could be assumed to result from the combination of the point measurement uncertainty and the uncertainty associated with the interpolation. It can be noticed that, globally, the values of the square of RMSE_{rep} appeared to be close to the sum of the mean GPR inversion uncertainties $\sigma^2_{\theta,GPR}$ and of the variance of the difference in the interpolated values $\sigma^2_{\Delta\theta}$, this latter accounting for the major part of the repetition error. Nevertheless, locally, the repetition uncertainty could not be seen as simply the sum of $\sigma^2_{\theta,GPR}$ and $\sigma^2_{\Delta\theta}$, as it can be verified by a close examination of Figs. 4.8 and 4.9. In addition, repetition uncertainties might be also influenced by a real change of soil moisture, which could not be quantified given its expected minor changes.

The largest uncertainty was found when comparing the interpolated GPR-derived permittivity to the soil moisture sampling measurements (Fig. 4.10), as this inherently combined the uncertainty from the GPR measurement and inversion, the interpolation of soil moisture and the reliability of the petrophysical relationship θ-ε. Nevertheless, these uncertainties remained weak as compared to previous studies and with respect to the range of soil moisture measured in the field ($\sim$0.15 $\mathrm{m^3m^{-3}}$).

The nugget effect, corresponding to a deviation of 0.0400 $\mathrm{m^3m^{-3}}$, was assumed to reflect the combined effect of the small-scale variability of soil moisture and the measurement uncertainty. However, this nugget effect appeared to be larger than the uncertainties in soil moisture determined in this study. This is an important finding with respect to the sampling strategies when measuring soil moisture with the proposed GPR method. It is believed that this nugget effect may reflect the unrevealed spatial variability of soil moisture between two measurements (i.e., with a spacing of 2 to 5 m). It is particularly encouraging that the uncertainty in soil moisture measured by GPR appeared lower than the soil moisture variability at the support and resolution scales of the GPR acquisition.

4.7 Conclusions

In this chapter, we evaluated the uncertainties in surface soil moisture sensing and mapping of a 2,5 ha agricultural field by full-waveform inversion of GPR data in a comprehensive manner by three independent uncertainty assessment methods.

1. The global uncertainty from the GPR inversion, that is, the point measurement uncertainty, was very low, i.e, 0.0039 $\mathrm{m^3m^{-3}}$ in terms of standard deviation. Locally, this uncertainty was large for high soil moisture values (lower sensitivity) and for high modeling errors.

2. The global repetition error was found to be equal to 0.0169 m^3m^{-3} and was largely attributed to the interpolation effect.
3. The accuracy of the GPR method was evaluated by the comparison with soil sampling measurements (ground-truth) and resulted in a RMSE of 0.0233 m^3m^{-3}, mainly due to the different support scales of the techniques.

The soil moisture sensing by the GPR system thus appeared to be very precise, repeatable and in a good agreement with ground-truthing. The three independent uncertainty assessment methods permitted to investigate the different sources of errors in soil moisture mapping and the interpolation appeared to be an important source of uncertainty. Furthermore, the uncertainties were mapped and local spots of high uncertainty were discussed. The temporal and spatial correlation of the uncertainties seemed to indicate that a part of the uncertainties originated from local model inadequacies, but these latter could not be clearly identified nor accounted for. The evaluated GPR method for soil moisture sensing and mapping shows very promising potentialities for measuring the soil moisture at an intermediate scale between the remote sensing platforms and invasive sensors.

Chapter 5

Temporal stability of soil moisture patterns measured by a proximal ground penetrating radar in an agricultural field[*]

5.1 Outline

We analyzed the temporal stability of spatiotemporal soil moisture patterns acquired using a proximal ground penetrating radar in a 2.5 ha agricultural field at five different dates. Accurate surface soil moisture estimates were retrieved using full-waveform inversion of ultra-wideband GPR data in the time domain focused on soil surface reflection. The GPR system was mounted on a mobile platform, allowing for real-time acquisition with a high resolution (2-5 meters). The spatiotemporal soil moisture patterns were in accordance with meteorological data and soil moisture measurements from soil core sampling. Observed soil moisture patterns could be mainly related to topography, denoting the redistribution of surface water in the field. Time-stable areas showing the field-average moisture could be revealed by two methods: 1) by the spatial intersection of the zones showing the field-average and 2) by the computation of the mean and variance of the relative differences of soil moisture to the field-average. Intersection of areas showing the field-average within a tolerance of 0.02 m^3m^{-3} covered 5 % of the field area, whereas locations where the mean relative difference was below 0.02 m^3m^{-3} extended up to 10 % of the field area.

---

[*] This chapter is adapted from:
Minet, J.; Vanclooster, M. & Lambot, S. Temporal stability of soil moisture patterns measured by a proximal ground penetrating radar in an agricultural field, in *Water Resources Research*, **2011**, to be submitted.

Compared to point soil moisture measurements techniques, the proposed GPR method allowed to acquire soil moisture patterns and investigate their temporal stability at an unprecedented spatial resolution. Future acquisitions over a larger time period would permit to assert the robustness of the time-stable areas.

5.2 Introduction

Following the huge development in soil moisture sensing techniques, soil moisture patterns have been widely investigated in numerous studies at various spatial and temporal scales. At the field scale, soil moisture patterns are mostly controlled by topography, soil type and land cover, whereas climate influences soil moisture patterns at much larger scales, i.e., for extents exceeding the precipitation correlation length. Soil moisture patterns were related to topographic attributes in many studies (e.g., Hawley *et al.*, 1983; Güntner *et al.*, 2004; Sørensen *et al.*, 2006; Western *et al.*, 1999). In that respect, soil moisture appeared to be well explained by the so-called topographic wetness index (TWI) that was developed by Beven and Kirkby (1979), especially in wet conditions and in the presence of a steep topography. Soil type and land cover heterogeneities were explaining soil moisture patterns particularly in semi-arid regions (Castillo *et al.*, 2003) and, not surprisingly, in case of flat topography (Hupet *et al.*, 2002). While topography tends to organize soil moisture spatial variability in structured patterns at the field and catchment scales, soil type and land cover are often local controls, leading to random patterns (Grayson *et al.*, 1997; Western *et al.*, 1999).

The relationship between spatial average and variability (i.e., the standard deviation) of soil moisture has been particularly studied for a wide variety of soil types, topography and extent scales. Reviews about these relationships are given in Famiglietti *et al.* (2008); Vereecken *et al.* (2007) and Western *et al.* (2003). Knowing the spatial variability of soil moisture within a certain extent permits to determine the minimal number of sampling needed to capture the field-average or to determine the level of accuracy of a sampling scheme (Brocca *et al.*, 2007; Hupet *et al.*, 2002). It could be also used for downscaling of large scale remotely-sensed soil moisture estimates. It is generally assumed that this relationship has a bell-curve shape (Western *et al.*, 2003), that is, the spatial variability of soil moisture increases from very dry to wet conditions, reaches a maximal value at an intermediate soil moisture and then decreases again with further wetting until saturation. The low soil moisture variability under extreme states of dryness and wetness was explained by the bounded behavior of the soil moisture at the wilting point and saturation conditions, respectively. As soil moisture is bounded by these values, very dry and very wet conditions result in more uniform soil moisture patterns. However, some studies perceived only a part of this behavior, reporting an increase of soil moisture variability with increasing soil moisture (De Lannoy *et al.*, 2006; Famiglietti *et al.*, 1998).

Vachaud *et al.* (1985) first introduced the concept of temporal stability of soil moisture, stating that spatial patterns of soil moisture might be time-invariant. The investigation of the temporal stability of soil moisture patterns has then received a specific attention in numerous experimental soil moisture field studies (Jacobs *et al.*, 2004; Grayson and Western, 1998; Guber *et al.*, 2008; Hu *et al.*, 2010). Although temporal stability studies have mainly focused on the retrieval of time-stable locations showing the field-average, time-stability of the whole soil moisture pattern is also deserving for many applications. Knowing the temporal stability of soil moisture patterns is useful to choose locations for the installation of grounded sensors or for soil sampling measurements, whether the time-stable locations exhibit field-average or extremes soil moisture values. More generally, knowing the temporal stability of soil moisture patterns can help for downscaling of large scale remotely-sensed soil moisture data, inform about the high-resolution soil properties and support hydrological modeling at the field scale. The concept of temporal stability implies that soil moisture might be mostly locally determined by soil or topographic attributes that are time-invariant. In that respect, Grayson and Western (1998) showed that time-stable locations representing the field-average were located in mid-slopes areas, which was further confirmed in the works of Brocca *et al.* (2009); Jacobs *et al.* (2004); Mohanty and Skaggs (2001). On the other hand, soil properties showing time-stability appeared to be site-specific and no general rule about soil properties that showed temporal stability could be drawn. Indeed, while Jacobs *et al.* (2004) observed that sampling points with moderate or moderately high clay content tended to have more temporal stability, Mohanty and Skaggs (2001) noticed that sandy loams showed more temporal stability than silt loams. The importance of influencing factors such as topography, soil properties and other factors for spatial patterns and temporal stability of soil moisture is actually dependent on the relative dominance of these factors for a particular landscape.

So far, the majority of the studies that have investigated the temporal stability of soil moisture patterns were built on soil moisture datasets acquired with small-scale invasive sensors (e.g., time domain reflectometry (TDR), capacitance probes, neutron probes or gravimetric sampling). These datasets are characterized by point measurements (small support scale) separated by large spacings over relatively small extents (field scale). On the other hand, remote sensing can provide soil moisture data over large extents but with a spatial resolution that is too large for field-scale studies. Proximal soil moisture sensing techniques, such as ground penetrating radar (GPR), permit to perform high spatial resolution measurements at the field scale and to bridge the scale gap in terms of spatial resolution and support scale between invasive and remote sensors. In particular, the off-ground GPR developed by Lambot *et al.* (2004b, 2006b) has shown great potential for rapid soil moisture sensing and was applied for proximal soil moisture mapping in Weihermüller *et al.* (2007); Lambot *et al.* (2008b); Jadoon *et al.* (2010a); Jonard *et al.* (2010) and Minet *et al.* (2011, submitted).

5.3 Objectives

In this study, we propose to use a large soil moisture dataset acquired with a proximal GPR to investigate the spatiotemporal patterns of surface soil moisture and their temporal stability. Soil moisture was acquired in a 2.5 ha bare field at five dates in spring 2010 in Belgium. Soil moisture patterns and their evolution over time were investigated through a geostatistical analysis. The temporal stability of the field-average moisture values was then analyzed by two methods: 1) by the spatial intersection of the zones showing the field-average and 2) by the computation of indicators based on the relative differences of soil moisture to the spatial-average (Vachaud *et al.*, 1985).

5.4 Materials and Methods

5.4.1 Study site

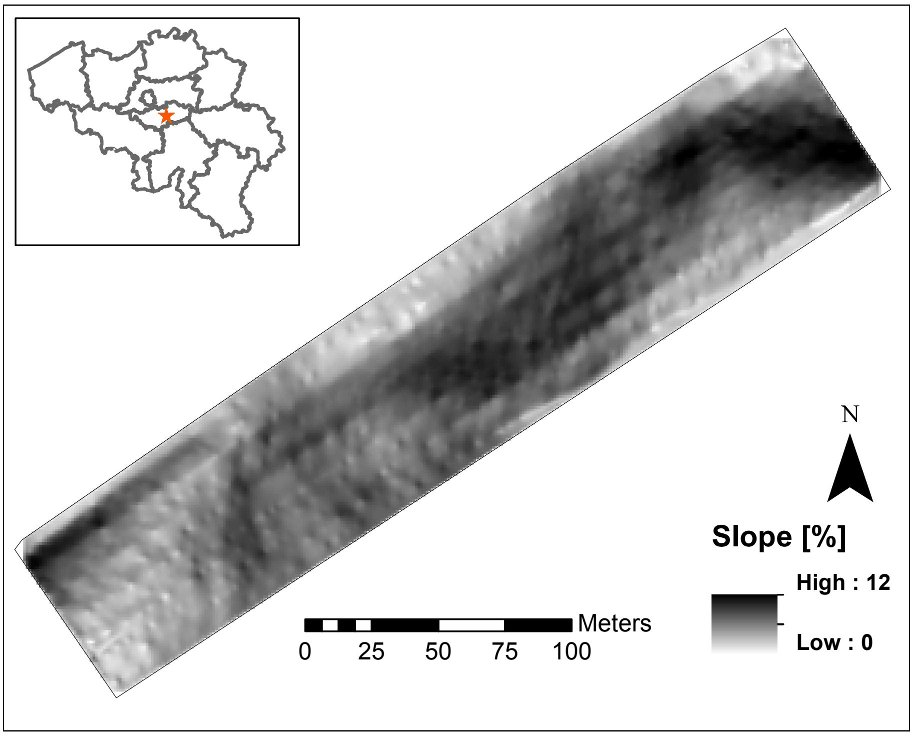

Figure 5.1: Study site of Burnia near Louvain-la-Neuve, Belgium. The slope is expressed in percents.

We surveyed a 2.5-ha agricultural field situated in the loess belt area in the center of Belgium (Long. 4°41'8"E, Lat. 50°35'59"N) (see chapter 4, Fig. 4.1). Figure 5.1 presents a map of the slope for that field. The GPR acquisitions were performed at the end of the winter at five different dates from 15 March to 06 April 2010. The field was covered by low-grown winter wheat (canopy height less than 5 cm) and surface roughness was low (amplitude around 5 cm). Meteorological data such as air temperature and precipitation were recorded with an hourly time step in a meteorological station situated at 2 km from the field (Fig. 5.2). Dry conditions characterized the first three dates of the acquisition while the two last surveys endured large antecedent rainfalls (Table 5.1).

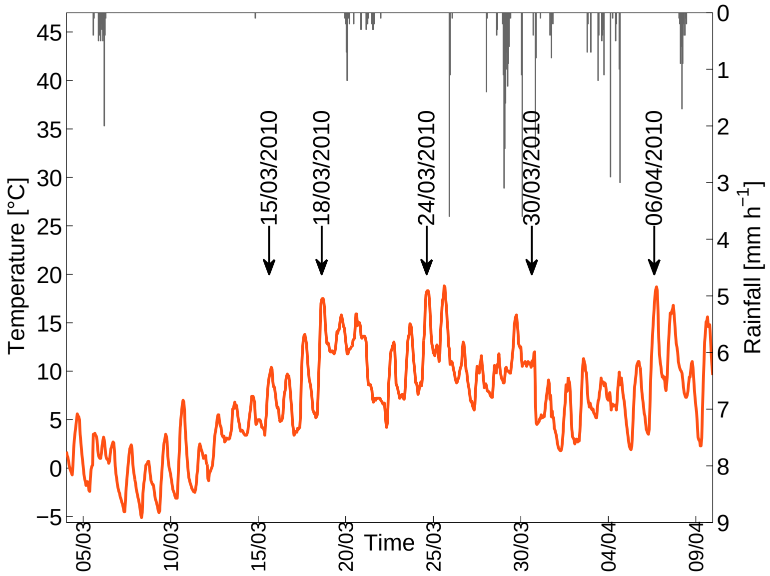

Figure 5.2: Air temperature and precipitation depicted from the 04 March to 10 April 2010.

5.4.2 Soil moisture mapping by ground penetrating radar

Surface soil moisture patterns were retrieved by full-waveform inversion of GPR data, as presented in chapter 4. For field acquisition, we rely on a ultra-wideband radar antenna operating between 200 and 2000 MHz and the lowest frequencies (under 800 MHz) only were used as noise arose at higher frequencies due to soil roughness. We focused on surface soil moisture retrieval by selecting the surface reflection peak of the GPR wave in the time-domain (Lambot *et al.*, 2006b) (see Fig. 4.3). This resulted in a shallow depth of characterization around 4 cm (Jadoon *et al.*, 2010a). GPR-derived surface dielectric permittivities ε were translated into volumetric soil moisture values θ using the relationship of Topp *et al.* (1980) (Eq. (1.16)). Very high soil permittivity values resulting in very large soil moisture values were found in particularly wet conditions in the last two surveys. These values were truncated at a maximum soil moisture of 0.5 m^3m^{-3} which is believed to be the soil moisture at saturation. These high values could originate from model inadequacy with respect to the one-layered configuration, i.e., if the soil is vertically-layered, constructive

Table 5.1: Presentation of the five GPR acquisitions

Date	10-days antecedent rainfalls [mm]	N° of points	Duration
15/03/2010	6.3	1496	1h09'
18/03/2010	0.1	1252	56'
24/03/2010	5.1	1429	1h01'
30/03/2010	29.8	1227	1h32'
06/04/2010	38.4	1759	51'

interferences may occur and affect the measured GPR data. They could also coming from measurements over areas partly covered by ponding water.

Field acquisitions were performed by mounting the GPR system on an all-terrain vehicle (ATV) as presented in chapter 3. For each date, the ATV followed 12 parallel tracks with a spacing of 5 m between the acquisition tracks (see Fig. 4.1), whereas measurements were taken with a spacing of 2 m along the acquisition lines. Table 5.1 indicates the number of points and the duration of the acquisition for each survey. Along an acquisition line, nearly continuous soil moisture measurements were acquired owing to the proximity of the support and resolution scale. Therefore, this proximal GPR method has an intermediate coverage between points measurements and continuous remote sensing acquisition. Soil moisture maps were produced by interpolation of point measurements using ordinary kriging with a rectangular neighboring window in order to deal with the uneven disposition of the points in space. The reader is referred to the previous chapter (chapter 4) for a comprehensive explanation of the field acquisition, GPR data inversions and interpolation of point-measurements. The reliability of the GPR system was also evaluated in the previous chapter.

In order to further validate the accuracy of the GPR soil moisture measurements, surface soil moisture was independently measured by volumetric soil core sampling in the top 5 cm at 20 regularly spaced locations (see Fig. 4.1). Soil samples were oven-dried at 105°C for at least 48h and the dry and wet weights were measured, in order to determine the volumetric moisture.

5.4.3 Temporal stability of soil moisture pattern identification

In this chapter, the temporal stability of the spatial average of soil moisture patterns was analyzed by two methods. First, time-stable locations showing the field-average were revealed by the intersection of the zones where soil moisture is equal to the field-average within a tolerance of ± 0.02 m^{3}m^{-3} for the five dates. This threshold was chosen as it approximately corresponds to the soil moisture uncertainty with interpolated data (see chapter 4). This method was the most intuitive, but it be might affected by a single date showing a different pattern. Even though, given the relatively-small time range on which soil moisture patterns were compared, it was expected that intersection of zones showing field-average between the five dates would exist.

Secondly, temporal stability were revealed by the computation of the mean and standard deviation over time of the relative differences in soil moisture, $\overline{\delta}_i$ and $\sigma(\delta)_i$, respectively, which were firstly introduced by Vachaud *et al.* (1985) and widely used afterward (e.g., Brocca *et al.*, 2009; Jacobs *et al.*, 2004; Hu *et al.*, 2010; Mohanty and Skaggs, 2001). These indicators permit, for each location i, to identify the relative difference in soil moisture with the spatial average over time (t) and are given by:

$$\overline{\delta}_i = \frac{1}{n_t} \sum_{t=1}^{n_t} \frac{\theta_{i,t} - \overline{\theta}_t}{\overline{\theta}_t} \tag{5.1}$$

$$\sigma(\delta)_i = \sqrt{\frac{1}{n_t - 1} \sum_{t=1}^{n_t} \left(\frac{\theta_{i,t} - \overline{\theta}_t}{\overline{\theta}_t} - \overline{\delta}_i \right)^2} \tag{5.2}$$

where $\overline{\theta}_t$ being the spatial average of soil moisture $\theta_{i,t}$ computed as:

$$\overline{\theta}_t = \frac{1}{n_i} \sum_{i=1}^{n_i} \theta_{i,t} \tag{5.3}$$

The time-averaged mean of the relative difference $\overline{\delta}_i$ indicates, for each location, the bias in soil moisture with respect to the spatial average, i.e., whether the location is drier ($\overline{\delta}_i < 0$) or wetter ($\overline{\delta}_i > 0$) on average over time. Locations that show on average the spatial average of the field have $\overline{\delta}_i$ equal to zero. The standard deviation of the relative difference $\sigma(\delta)_i$ gives the degree of variation of the relative difference, that is, time-stable locations have low $\sigma(\delta)_i$. For identifying the most time-stable locations for the spatial average, we may combine these indicators in the root mean square error of the relative differences RMSE$_{\delta_i}$ (Jacobs *et al.*, 2004) which is given by:

$$RMSE_{\delta_i} = \sqrt{\overline{\delta}_i^2 + \sigma(\delta)_i^2} \tag{5.4}$$

The locations showing a high temporal stability for the field-average are thus given by the lowest RMSE$_{\delta_i}$ values. This second method for evaluating the temporal stability of the spatial average integrated the contribution of the five dates in time-averaged indicators. It is worth noting that these indicators were computed based on interpolated values, as the locations of point measurements slightly differed between the five dates.

5.5 Soil moisture patterns

5.5.1 Geostatistical analysis

Figure 5.3 shows the maps of the GPR-derived soil moisture point-measurements for the five surveys. Soil moisture values are depicted by colored circles with a diameter corresponding to the estimated GPR antenna footprint. The coverage rate of the GPR acquisition was estimated at around 9 % of the field area for

Figure 5.3: GPR-derived soil moisture point-measurements depicted with the same color scale for the five GPR surveys.

Table 5.2: Statistics of GPR-derived volumetric soil moisture expressed in [m^{3}m^{-3}] and variograms parameters (Nugget [m^{3}m^{-3}]^2, Sill [m^{3}m^{-3}]^2 and Range [m])

Date	$\mu_{\theta_{GPR}}$	$\text{median}_{\theta_{GPR}}$	$\sigma_{\theta_{GPR}}$
15/03/2010	0.228	0.222	0.067
18/03/2010	0.234	0.227	0.063
24/03/2010	0.240	0.236	0.064
30/03/2010	0.295	0.284	0.114
06/04/2010	0.298	0.296	0.115

Date	Nugget	Sill	Nugget/Sill [%]	Range
15/03/2010	0.0016	0.0039	40	62
18/03/2010	0.0016	0.0034	47	77
24/03/2010	0.0014	0.0036	39	70
30/03/2010	0.0031	0.0115	26	107
06/04/2010	0.0026	0.0113	23	109

this configuration of acquisition, assuming a circular antenna footprint of 1.5 m in diameter. Soil moisture data acquired for the first three dates showed similar patterns and drier conditions than the last two ones (see Table 5.2), which was related to antecedent rainfalls (see Fig. 5.2).

The parallel variograms (Fig. 5.4) were also similar for the first three dates, with respect to nugget and sill variances and ranges (Table 5.2). The soil moisture patterns from the first three dates showed stationarity within the field extent, with a range around 70 m. The last two dates, characterized by wetter conditions, showed different soil moisture patterns with a sharp amplification in nugget and sill variances, as observed in Western *et al.* (1998) in wet conditions. There was also a moderate increase in the variogram range (> 100 m) for the last two dates. However, in the Tarrawarra catchment, Western *et al.* (1998) observed a decrease in the range with wet conditions, which was attributed to the reorganization of soil moisture patterns according to the topography. In our case, a visual inspection of the maps shows that both dry and wet conditions were still characterized by soil moisture patterns that could be partly related to the topography. Actually, the observed increase in the ranges with wet conditions may be not significant when closely inspecting the last two variograms, as similar ranges as in the dry conditions could be fitted on the variogram estimates. Lastly, we observed a decrease in the Nugget/Sill ratio with wet conditions (Table 5.2), denoting the larger soil moisture pattern organization in wet conditions (Grayson *et al.*, 1997).

All the fitted variograms showed large nugget variances, especially in wet conditions. It is usually assumed that nugget effect may be caused by unrevealed small-scale variability due to insufficient sampling resolution or by point-measurement uncertainties. The uncertainties in the GPR sensing of soil moisture were notably evaluated in the same field in chapter 4 (Minet *et al.*, submitted) using three repetitions of the acquisition within three hours. The

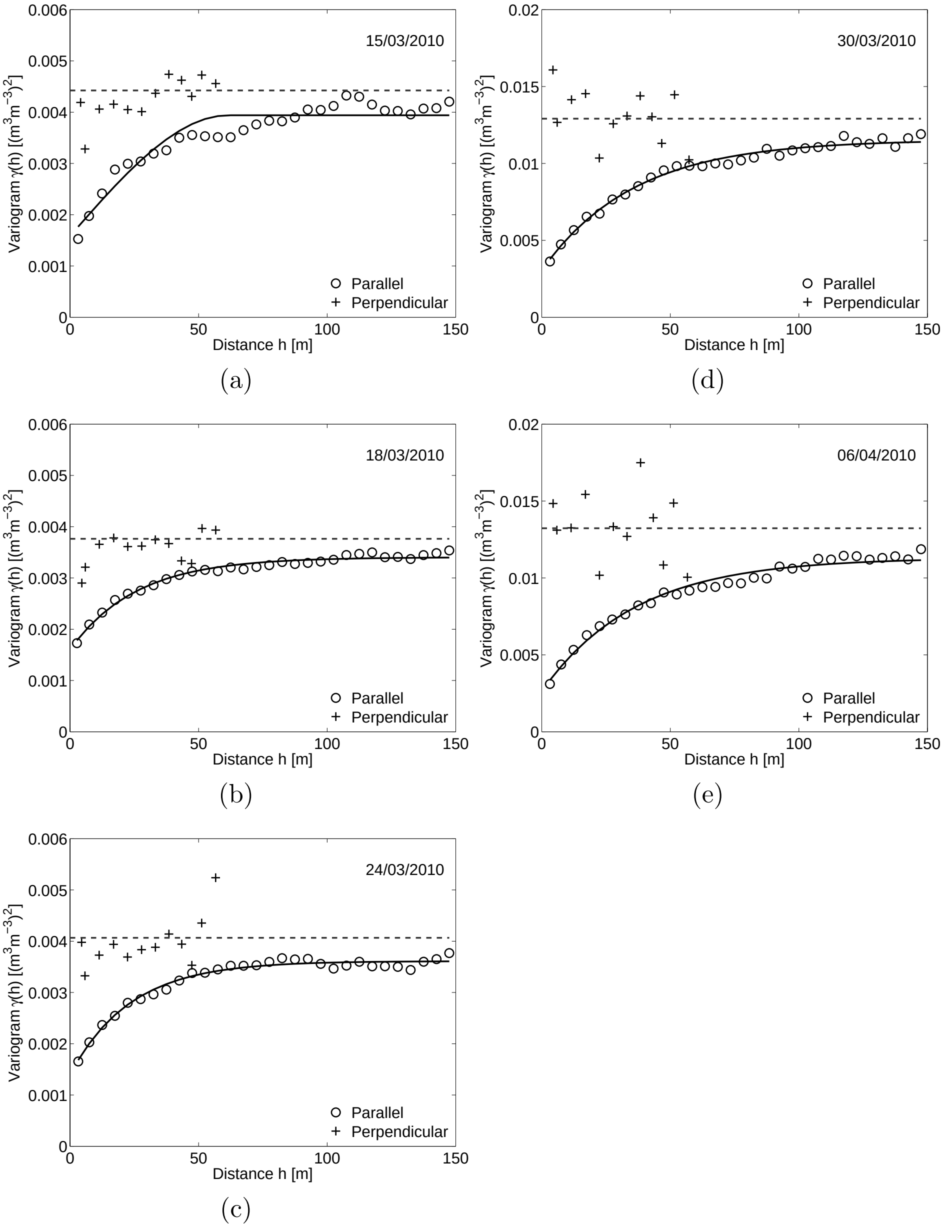

(a) (d)

(b) (e)

(c)

Figure 5.4: Variograms for soil moisture computed for the five field acquisitions along ('o') and perpendicular ('+') to the acquisition lines. Exponential models are fitted for the parallel variograms. The total variance is indicated by the horizontal dashed line.

GPR repetition uncertainties were evaluated as 0.0169 m^3m^{-3} and a large part was attributed to interpolation uncertainties. Therefore, the GPR measurement errors appeared to be too low to explain the relatively large nugget effects observed here. On the other hand, previous studies have shown that unrevealed small-scale variability was the most prominent cause of high nugget effect (Western *et al.*, 1998). Although the spacing (2 m along the acquisition lines) nearly matched the support scale (1.5 m in diameter), unrevealed spatial variability between GPR measurements could explain such large nugget effect. This could also explain why nugget variances are larger for the perpendicular variograms, independently of the line effect.

Soil moisture spatial variability appeared to be maximal in wetter conditions (Table 5.2), albeit soil moisture variability is generally expected to decrease with wet conditions because of the increasing size of areas showing soil saturation (Famiglietti *et al.*, 2008). Actually, it is believed that no saturation conditions were measured by the GPR as the mean soil moisture of the last two dates were still below the expected soil moisture at saturation. This was attributed to the shallow penetration depth of the GPR method and to the rapid drainage of the shallow soil layer. In that respect, De Lannoy *et al.* (2006) already remarked that the decreasing trend in soil moisture variability with high soil moisture was not observed for shallow (0-10 cm) soil layer but only for deeper layers, because of the fast soil moisture dynamics of the shallow layer.

5.5.2 Line effect

The uneven acquisition sampling resulted in striped soil moisture patterns (see Fig. 5.3), i.e, denoting a line effect, which could be observed by a larger spatial coherency of the soil moisture values when looking along the acquisition lines while a smaller spatial coherency was observed when looking in the perpendicular direction to the acquisition lines. We could interestingly notice that this line effect was observed at same locations for repeated dates (Fig. 5.3), i.e., it was related to local soil conditions and not to a sensor drift.

Figure 5.4 presents the variograms computed along and perpendicular to the acquisition lines for the five surveys. The perpendicular variogram estimates were offset by an additional variance corresponding to the line effect. They showed a poorer spatial coherency, especially for the last two dates, with a strong nugget effect nearly equal to the total variance. In addition, the perpendicular variograms were computed over a distance (60 m) that appeared to be too small for reaching the ranges observed in the parallel variograms. The line effect was clearly higher for the last two dates, as it can be observed in the soil moisture maps and in the larger offset between parallel and perpendicular variograms.

This line effect was already observed in chapter 3 (Minet *et al.*, 2011) in a field acquisition in Walhain using the same mobile platform. It was mainly attributed to the soil compaction induced by the ploughing or fertilizer spreading machine, as we followed the same direction with the platform. The largest line effect that was observed here with wet conditions may be related to: 1) the overall largest soil moisture variance in wet conditions or to 2) a real increase in the striped soil moisture patterns due to the repeated passes of the ATV holding the GPR system. It was observed in situ that the passes of the ATV have compacted the soil slightly but sufficiently to affect volumetric soil moisture. In addition, flow paths may have been deviated by these acquisition lines, particularly in flat areas.

5.5.3 Comparison with soil core sampling measurements

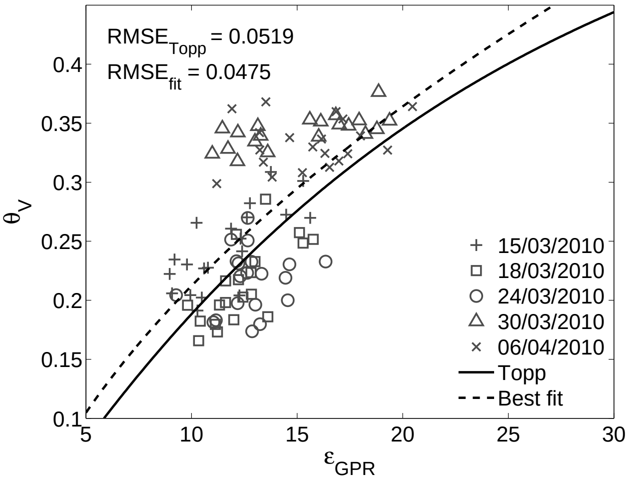

Figure 5.5: Comparison between interpolated GPR-derived soil dielectric permittivity ε_{GPR} and volumetric sampling soil moisture θ_V for all dates.

Figure 5.5 presents the comparison between interpolated GPR-derived soil dielectric permittivity ε_{GPR} and volumetric soil moisture θ_V from the soil sampling measurements. A simple petrophysical model (Ledieu *et al.*, 1986) (Eq. (1.17)) was fitted over the data and the standard relationship of Topp *et al.* (1980) (Eq. (1.16)) was also drawn for comparison. There was an overall moderate agreement between the soil permittivity and volumetric moisture with a RMSE$_{fit}$ of 0.0475 m^{3}m^{-3} when fitting the Ledieu's model and a RMSE$_{Topp}$ of 0.0519 m^{3}m^{-3} when comparing with the Topp's relationship. The Topp's and Ledieu's relationships fitted for all dates together were in good agreement between them. In addition, the Ledieu's model was fitted individually for each date and corresponding RMSE$_{fit}$ are displayed in Table 5.3, as well as RMSE$_{Topp}$ computed for each date. There were poorer agreements with Topp's relationship for the last two dates, which showed a small variation of volumetric soil moisture compared to the large range of GPR-derived dielectric permittivity. The observed discrepancies could be attributed to the different support scales and penetration depths of the techniques, with respect to the small-scale variability of soil moisture. More particularly, the relatively low dielectric permittivity values observed compared to soil core sampling moisture values could be caused by scattering of the GPR waves due to surface roughness or by destructive interferences due to model inadequacy such as soil layering. Nevertheless, as point soil moisture were compared with interpolated dielectric permittivity values, it is worth noting that these discrepancies were within the range of the interpolation uncertainties (chapter 4) (Minet *et al.*, submitted).

Table 5.3: Soil moisture [$\mathrm{m^3m^{-3}}$] statistics from soil core sampling and RMSE of the petrophysical relationships

Date	μ_{θ_V}	σ_{θ_V}	RMSE_{Topp}	RMSE_{fit}
15/03/2010	0.244	0.0343	0.0363	0.0227
18/03/2010	0.213	0.0331	0.0299	0.0227
24/03/2010	0.217	0.0264	0.0390	0.0253
30/03/2010	0.343	0.0133	0.0759	0.0095
06/04/2010	0.333	0.0206	0.0628	0.0197

A decrease in the standard deviation σ_{θ_V} of volumetric soil moisture from core sampling was observed with increasing mean soil moisture (Table 5.3), whereas the standard deviation of GPR measurements $\sigma_{\theta_{GPR}}$ increased with wet conditions. This opposite trend may be due to the different support depths between the two soil moisture measurement methods. GPR measurements have a shallower characterization depth in wet conditions, because of the increasing soil dielectric permittivity. As a result, GPR measurement depth might be smaller than the depth of the ground-truth (i.e., 5 cm) in wet conditions. This latter phenomenon could also explain the poorer agreement with the Topp's petrophysical relationship observed in wet conditions for the last two dates.

5.6 Temporal stability of soil moisture patterns

5.6.1 Intersection of field-average soil moisture areas

Figure 5.6 shows the areas giving the field-average soil moisture for the five dates with a tolerance of ± 0.02 $\mathrm{m^3m^{-3}}$ and their intersection between the five dates (first method). There was a remarkable temporal stability of soil moisture patterns for the sets of the first three and the last two dates, respectively, i.e., the zones outlined by black lines are similar for these two sets of dates. However, due to moderate rainfalls (24.8 mm between 24 and 30 March 2010), the soil moisture pattern greatly changed between the third and fourth dates. The zones indicating the field-average soil moisture shrank from dry to wet conditions as a result of the increase in soil moisture variance with wet conditions. There existed locations that indicated the field-average for all the five dates (red lines), but these locations were split and dispersed within the field. The locations showing the lowest soil moisture values were rather time-invariant as well, whereas highest soil moisture zones moved over the time.

The main thalweg of the field (see Fig. 4.4) is characterized by a temporal stability of the field average for the first three dates. Nevertheless, following rainfall events, the thalweg appeared slightly drier than the rest of the

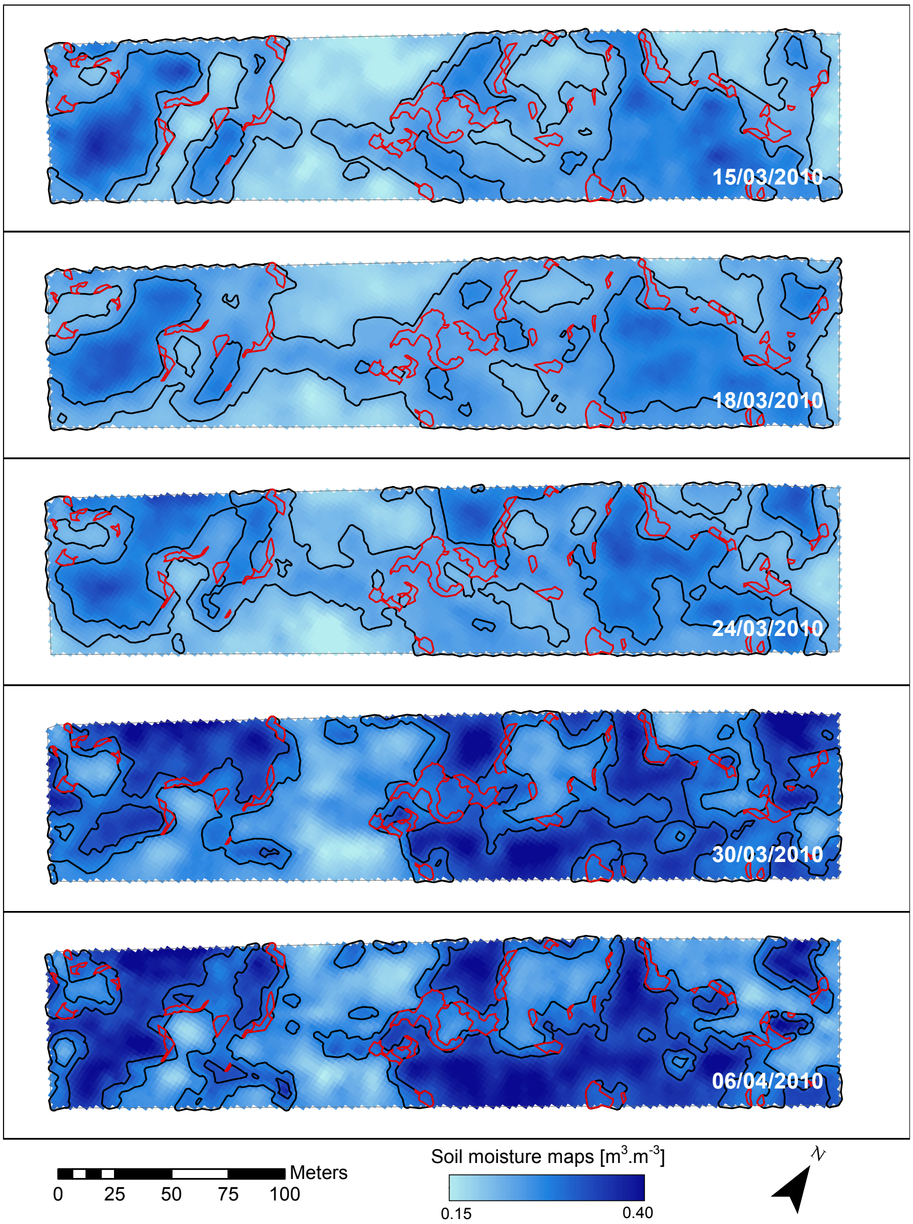

Figure 5.6: Soil moisture maps for the five dates. The locations where soil moisture is equal to the field-average within a tolerance of ± 0.02 m^3m^{-3} are outlined by black lines. The intersection of these zones between the five dates are outlined by red lines.

field, maybe because of its larger slope. Driest patterns appeared the most connected, while Western *et al.* (1998) observed a larger spatial organization of soil moisture patterns in wet conditions. In our case, it is worth noting that the driest conditions were still rather humid. In the last two dates that were characterized by large antecedent rainfalls, the wettest areas may denote the locations where water accumulated and infiltrated due to topography, i.e., these locations are characterized by a small slope and are receiving water from neighboring locations.

5.6.2 Relative difference to field-average

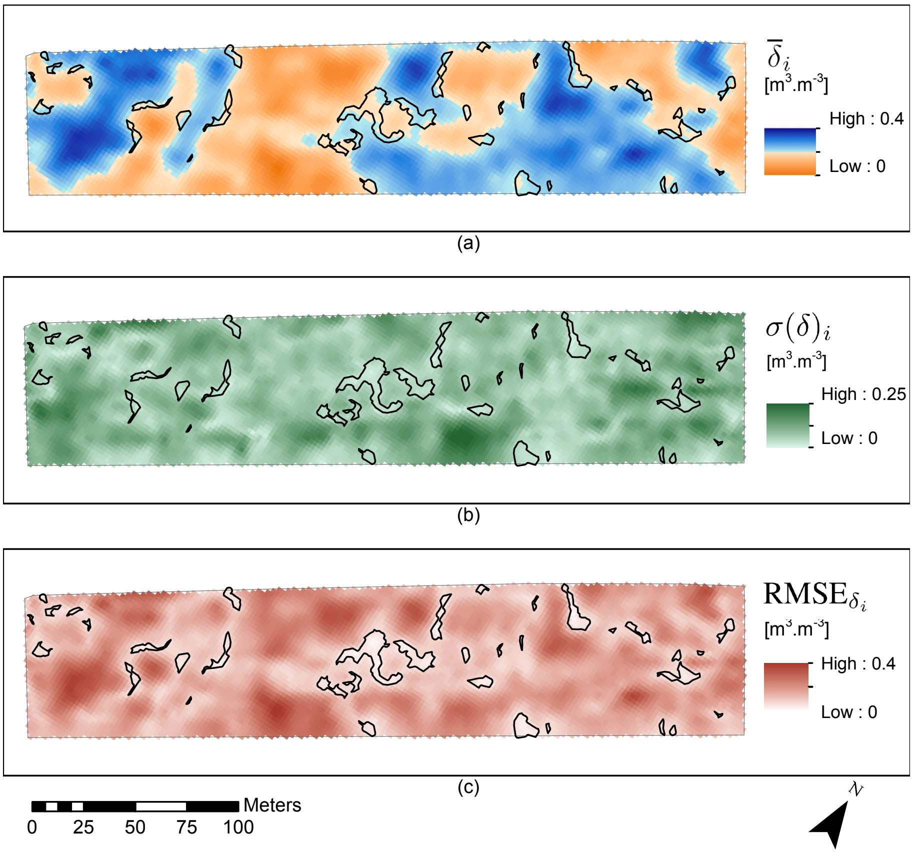

Figure 5.7: Temporal stability of the field-average soil moisture computed by indicators based on the relative difference of soil moisture to the field-average. From top to bottom, the mean of the relative difference $\overline{\delta}_i$, the standard deviation of the relative difference $\sigma(\delta)_i$ and the RMSE of these differences RMSE_{δ_i} are presented. The time-stable zones determined by the first method are outlined by black lines.

Figure 5.7 presents the maps of the time-averaged indicators based on the relative difference of soil moisture to the field-average (second method). The first map (Fig. 5.7 (a)) shows the mean of the relative difference $\overline{\delta}_i$, that is, the bias in soil moisture compared to the field-average. The locations where $\overline{\delta}_i = 0$ gave on average over time the field-average. Persistently drier ($\overline{\delta}_i < 0$) and wetter ($\overline{\delta}_i > 0$) areas are depicted in orange and blue, respectively, and divide the field in almost equal parts. A relatively large part of the locations could serve as time-stable locations of the field-average, i.e., 10% of the field area estimated the field-average soil moisture with a 0.02 $\mathrm{m^3m^{-3}}$ accuracy. The zones of the intersection of the field-average between the five dates (first method) were located in zones where $\overline{\delta}_i$ was close to zero. The time-averaged soil moisture difference pattern could be related to topographic features in some parts of the field. For instance, persistently wetter areas were located in flat areas in the most and less elevated areas of the field. Persistently driest areas were however located where slopes are the largest. This may originate from the poor occurrence of run-on and to the faster drainage of water in slopy areas. In contrast, flat areas are more subject to larger infiltration and run-on and tend to store more water in soil. As a result, time-stable locations showing the field average are located in intermediate slopes.

The second map (Fig. 5.7 (b)) indicates the standard deviation over time of the difference of soil moisture to the field-average $\sigma(\delta)_i$. The locations where $\sigma(\delta)_i$ was low indicated a high time-stability of soil moisture with respect to the field-average. The $\sigma(\delta)_i$ pattern appeared less spatially correlated than the $\overline{\delta}_i$ pattern. Again, there was a rather good match between the locations with lowest $\sigma(\delta)_i$ values and the zones of the intersection of the field-average between the five dates. The third map (RMSE_{δ_i}) (Fig. 5.7 (c)) combines the information of the first two maps and gives an assessment of the temporal stability of the field-average soil moisture. As a result, there was a perfect match between the lowest RMSE_{δ_i} zones and the time-stable zones outlined by the first method. These zones were not located in flat areas, but rather in transition zones between the lowest and highest elevated parts of the field. In particular, the largest time-stable zone appeared to be located in an intermediate slope area (see Fig. 5.1).

The distributions of the mean and the standard deviation of the relative difference ($\overline{\delta}_i$ and $\sigma(\delta)_i$) computed for each interpolated points are presented in Fig. 5.8. The mean of the relative difference was ranging from -0.40 to 0.33 $\mathrm{m^3m^{-3}}$ while the standard deviation was ranging from 0 to 0.27 $\mathrm{m^3m^{-3}}$. Although no clear trend could be drawn from the relationship between these two variables, it could be noticed that the largest $\sigma(\delta)_i$ were encountered for slightly positive $\overline{\delta}_i$, meaning that moderately wet locations were the less time-stable. It is worth noting that extreme values of $\overline{\delta}_i$, that were the persistently driest and wettest locations, showed low $\sigma(\delta)_i$, denoting a high temporal stability. It means that the extremes of soil moisture spatial distribution could be known with a larger confidence than the field-average of soil moisture if grounded sensors are installed. Nevertheless, there was a wide variability in $\sigma(\delta)_i$ for each part of the ranked mean of the difference, i.e., the temporal stability was not clearly linked to the bias in soil moisture to the field-average.

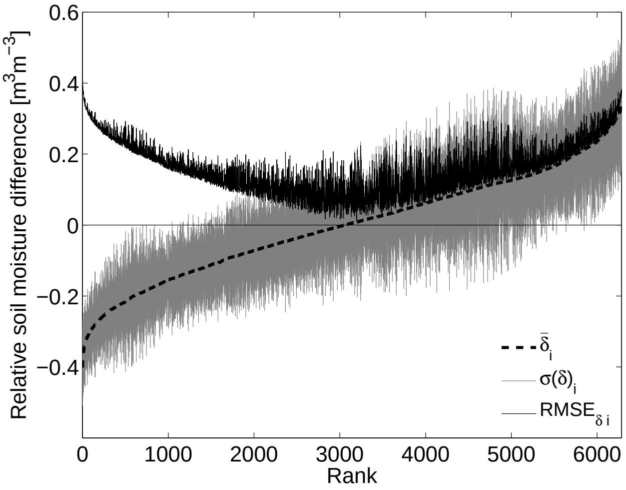

Figure 5.8: Rank ordered mean relative difference of GPR-derived soil moisture to the field-average $\overline{\delta}_i$ (dashed line) depicted with standard deviation $\sigma(\delta)_i$ (in gray). The RMSE of the relative differences RMSE_{δ_i} is presented in a plain line. Results from GPR measurements.

5.6.3 Comparison of the two methods

Locations showing a temporal stability of field-average soil moisture were revealed in accordance by the two methods used for the investigation of the temporal stability of the soil moisture patterns. Nevertheless, the intersection of the area showing the field-average within a tolerance of 0.02 $\mathrm{m^3m^{-3}}$ (first method) concerned only 5 % of the field area whereas 10 % of locations where $|\overline{\delta}_i| < 0.02$ $\mathrm{m^3m^{-3}}$ could be identified with the second method. However, a negligible fraction (<0.1 %) of the field area (5 locations on 6284) was characterized by $\mathrm{RMSE}_{\delta_i} < 0.02$ $\mathrm{m^3m^{-3}}$ when accounting for both $\overline{\delta}_i$ and $\sigma(\delta)_i$. Using the same soil moisture threshold, the first method was thus more restrictive than $\overline{\delta}_i$, but less than RMSE_{δ_i}. It is quite evident that intersected time-stable areas were smaller compared to areas where $|\overline{\delta}_i| < 0.02$ $\mathrm{m^3m^{-3}}$ because the former indicated time-stable areas that were always close to the field-average while the latter indicated areas that were on average over time close to the field-average. As we surveyed the field in a rather short time range (i.e., 22 days), the first method still resulted in intersected locations indicating the field-average between all dates, but over longer period, these locations might not appear by intersection of time-stable zones.

5.6.4 Temporal stability of soil moisture from soil core sampling measurements

The same analysis on the temporal stability using the relative difference method was performed with soil core sampling measurements and results are depicted in Fig. 5.9. The mean of the relative difference was ranging from -0.12 to 0.19

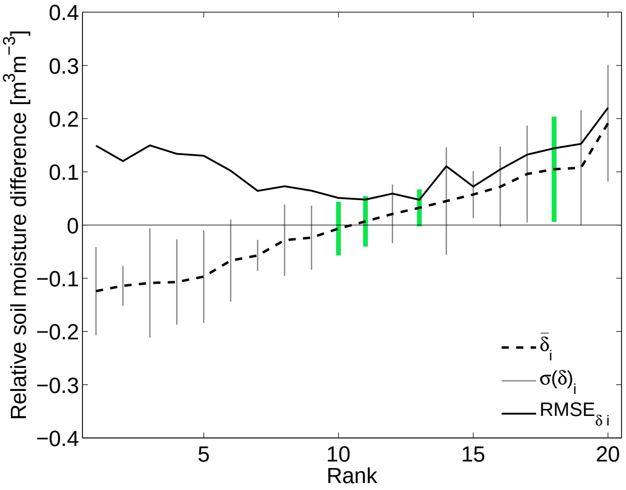

Figure 5.9: Rank ordered mean relative difference of volumetric soil moisture to the field-average $\overline{\delta}_i$ (dashed line) depicted with standard deviation $\sigma(\delta)_i$ (in gray) for the 20 soil core sampling locations. The RMSE of the relative differences RMSE_{δ_i} is presented in a plain line. Results from soil core sampling measurements. The four sampling points that are within the time-stable area are depicted with a thick green errorbar.

m^3m^{-3} while the standard deviation was ranging from 0.11 to 0.29 m^3m^{-3}. There was no clear trend between the $\overline{\delta}_i$ and $\sigma(\delta)_i$. Four sampling points appeared to fall into the area showing the intersection of time-stable locations (first method) and they were outlined with thick green errorbars for $\sigma(\delta)_i$ in Fig. 5.9. Three of these points showed a large temporal stability for the volumetric soil moisture data from soil core sampling as well, as they actually correspond to the three smallest RMSE_{δ_i}. Locations showing temporal stability of field-average soil moisture could thus be also detected using the soil core sampling measurements.

5.6.5 Comparison with previous studies

The relative difference indicators $\overline{\delta}_i$ and $\sigma(\delta)_i$ showed a great temporal stability of field-average soil moisture compared to previous studies. The most comprehensive review about temporal stability of soil moisture was given by Brocca *et al.* (2009, Table 1). Few studies resulted in smaller ranges in terms of $\overline{\delta}_i$ and $\sigma(\delta)_i$ than the ones observed in this study (i.e., $\overline{\delta}_i$ = -0.40 to 0.33 and $\sigma(\delta)_i = 0$ to 0.08 m^3m^{-3}). In Jacobs *et al.* (2004), rather large criteria for highlighting time-stable locations of the field-average were used, that were, time-stable locations were defined by $|\delta_i| < 0.05$ or 0.10 m^3m^{-3} and covered 13-18 % and 27-37% of fields areas, respectively. Applying the same thresholds, time-stable locations could be identified in, respectively, 24% and 46% of the field area in our study. This rather good temporal stability could be mainly attributed to the short time range and the small number of acquisition of the GPR field acquisitions, although, for instance, a shorter time range (14 days) was used in Jacobs *et al.* (2004).

Finally, the time-stable zones indicating the field-average appeared to be located in-between low and high elevated areas, as already noticed in many previous studies (Brocca *et al.*, 2009; Jacobs *et al.*, 2004; Mohanty and Skaggs, 2001). However, the relatively flat topography of the study site impeded to clearly relate the time-stable pattern to topography. Moreover, no high-resolution soil information was available to relate the spatiotemporal pattern to local conditions, but it was expected that soil conditions were rather uniform in the study site, due to its limited extent and as the Belgian soil map did not distinguish different soil types.

5.7 Conclusions

Spatiotemporal patterns of soil moisture were measured by a proximal GPR mobile platform in a 2.5 ha agricultural field at five dates in spring 2010. Time-lapse measurements at high spatial resolution permitted to extensively study the spatiotemporal soil moisture variability and to investigate the temporal stability of soil moisture. The evolution of soil moisture patterns was mainly governed by rainfalls, i.e., similar patterns and variograms were obtained for the different dates unless large rainfalls occurred. Passing from dry to wet conditions, the soil moisture variance increased, in relation with the shallow characterization of the GPR technique. Moderate nugget effects were observed in the soil moisture variograms and they were attributed to unrevealed spatial variability between the resolution and support scales. Soil moisture from soil core sampling were in a good agreement with GPR-derived estimates ($\mathrm{RMSE}_{fit}=$ 0.0475 $\mathrm{m^3m^{-3}}$) given the interpolation uncertainties, although larger discrepancies were found in wet conditions. Soil moisture patterns seemed mainly governed by topography, with wetter areas in flat areas.

Temporal stability of the field-average soil moisture was revealed by two methods, that were: 1) the intersection of zones showing the field-average and by 2) the computation of the mean and standard deviation over time of the relative difference of soil moisture to the field-average, as defined by Vachaud *et al.* (1985). These methods were in accordance, although they showed different degrees of temporal stability extents. Intersection of areas showing the field-average within a tolerance of 0.02 $\mathrm{m^3m^{-3}}$ covered 5 % of the field area, whereas locations where the mean relative difference $|\overline{\delta}_i|$ was below 0.02 $\mathrm{m^3m^{-3}}$ extended up to 10 % of the field area. Soil moisture data from the soil core sampling also exhibited temporal stability of the field-average and some sampling locations were found to be in accordance with the time-stable locations determined using GPR-derived soil moisture data. Compared to previous studies, the temporal stability of the field-average soil moisture was high, with 24 % of locations showing $|\overline{\delta}_i| < 0.05$ $\mathrm{m^3m^{-3}}$, although it was owing to the relatively small time frame over which the field campaigns were performed.

To the best of our knowledge, among the large body of literature about the temporal stability of soil moisture, there were no studies using soil moisture estimates from proximal sensing platform such as GPR. The use of the GPR platform permitted to investigate the temporal stability pattern using a large number of measurements at an unprecedented spatial resolution at the field scale in a limited time frame, such as soil moisture does not change with time between the start and the end of the acquisition. Owing to the proximity of its support scale to its spacing, the technique was able to nearly acquire the continuous soil moisture pattern in the direction of the acquisition. This study showed the potential of the proposed GPR method for the mapping of soil moisture patterns in order to determine time-stable locations where grounded sensors could be installed. These promising results should be nevertheless corroborated by conducting field acquisitions over a larger time frame, e.g., over a year. In addition, the relation of the time-stable locations with local attributes such as topography, soil type and vegetation cover should be investigated.

Chapter 6

Effect of high-resolution spatial soil moisture variability on simulated runoff response using a distributed hydrologic model[*]

6.1 Outline

The importance of spatial variability of antecedent soil moisture conditions on runoff response is widely acknowledged in hillslope hydrology. Using a distributed hydrologic model, this chapter aims at investigating the effects of soil moisture spatial variability on runoff in various field conditions and at finding the structure of the soil moisture pattern that approaches the measured soil moisture pattern in terms of field scale runoff. High spatial resolution soil moisture was surveyed in ten different field campaigns using a proximal ground penetrating radar (GPR) mounted on a mobile platform. Based on these soil moisture measurements, seven scenarios of spatial structures of antecedent soil moisture were used and linked with a field scale distributed hydrological model to simulate field scale runoff. Accounting for spatial variability of soil moisture resulted in general in higher predicted field scale runoff as compared to the case where soil moisture was kept constant. The ranges of possible hydrographs were delineated by extreme scenarios where soil moisture was directly and

---

[*] This chapter is adapted from:
Minet, J.; Laloy, E.; Lambot, S. & Vanclooster, M. Effect of high-resolution spatial soil moisture variability on simulated runoff response using a distributed hydrologic model, in *Hydrology and Earth System Sciences*, **2011**, 15, 1323-1338.

inversely modeled according to the topographic wetness index (TWI). These behaviors could be explained by the sizes and locations of runoff contributing areas, knowing that runoff was generated by infiltration excess over a certain soil moisture threshold. The most efficient scenario for modeling the within field spatial structure of soil moisture appeared to be when soil moisture is directly arranged according to the TWI, especially when measured soil moisture and TWI were correlated. The novelty of this work is to benefit from a large set of high-resolution soil moisture measurements allowing to model effectively the within field distribution of soil moisture and its impact on the field scale hydrograph. These observations contributed to the current knowledge of the impact of antecedent soil moisture spatial variability on field scale runoff.

6.2 Introduction

The antecedent soil moisture condition prior to rainfall is a key factor in determining the hydrological response as it mainly governs the generation of runoff due to its effect on infiltration capacities. In hydrologic modeling, the prediction of runoff is therefore highly sensitive to the description of antecedent soil moisture conditions. The response of the hydrologic models to antecedent soil moisture is moreover often highly non-linear and shows a threshold behavior (Zehe and Blöschl, 2004).

The effect of antecedent soil moisture spatial variability on hydrologic response at the field scale has been widely addressed in numerous studies through hydrologic modeling. The large effect of soil moisture variability on runoff response is to be attributed to the prominent role of soil moisture in runoff generation by either infiltration excess or saturation excess overland flows (Zehe and Blöschl, 2004). The location of runoff contributing areas, which are directly related to the soil moisture state, modulates the hydrologic response as generated runoff can re-infiltrate on its way downhill to the catchment outlet. In particular, Merz and Plate (1997); Merz and Bardossy (1998) and Bronstert and Bardossy (1999) showed that accounting for the spatial variability of antecedent soil moisture yields a greater runoff compared to assuming uniform soil moisture conditions, denoting the non-linear response of the hydrologic model to antecedent moisture conditions. Regarding the type of variability, Merz and Plate (1997); Merz and Bardossy (1998) and Zehe *et al.* (2005) observed that a structured soil moisture pattern results in a greater runoff than a stochastic random variability, especially when large contributing areas were connected by a flow channel to the outlet. In contrast to this, Bronstert and Bardossy (1999) observed the smallest runoff response with structured soil moisture patterns compared to random patterns. This was attributed to the actual poor organization of the structured pattern that was observed in dry conditions. Bronstert and Bardossy (1999) also showed that the introduction of topographic data in modeling of soil moisture was the best strategy to obtain a runoff response close to the measured outlet response. The importance of spatial variability of soil moisture for hydrologic modeling has also received a specific attention in data assimilation studies (Houser *et al.*, 1998; Pauwels *et al.*, 2001; Crow and Ryu, 2009; Brocca *et al.*, 2010).

The way spatial variability of soil moisture impacts runoff is depending on model parameterization, average soil moisture state itself (Zehe *et al.*, 2005, 2010) and type of rainfall which is considered (Bronstert and Bardossy, 1999; Noto *et al.*, 2008). In particular, Noto *et al.* (2008) pointed out that the well-known high sensitivity of the hydrologic model to antecedent soil moisture conditions may be observed only under specific rainfall forcing. In that respect, in a semi-arid catchment, Castillo *et al.* (2003) noticed that runoff response is insensitive to antecedent soil moisture conditions for high intensity rainfalls or for poorly permeable soils. Hence, in some conditions, assuming a constant mean soil moisture may be sufficient to correctly model the rainfall-runoff response, particularly if extreme events are considered (e.g., in flood risks applications). The effect of spatial variability of soil moisture were particularly observed in steep topography (Kuo *et al.*, 1999; Castillo *et al.*, 2003) that allows lateral redistribution of water over the catchment. It is also expected to be substantial in dry conditions as shown in Merz and Plate (1997) where two antecedent soil moisture conditions were compared. It is worth noting that highly wet conditions inherently exhibit low spatial variability because of the bounded behavior of soil moisture by saturation (Famiglietti *et al.*, 2008).

The scale aggregation of soil moisture data as well as other inputs (e.g., digital elevation model) can also highly alter the accuracy of the response of the hydrologic model. Using information theory, Kuo *et al.* (1999) noticed that the deviations in simulated runoff increase proportionally with the grid size of a distributed hydrologic model, especially for steep topography and in wet conditions. Finally, the high sensitivity of runoff response to antecedent soil moisture implies that uncertainty in soil moisture characterization exerts a large effect on the predictability of hydrologic models, similarly to the effect of soil moisture variability (Zehe and Blöschl, 2004). Still, the effect of the variability of soil moisture on runoff response has to be investigated for various conditions of catchment attributes, soil moisture patterns and rainfall forcing.

In the near future, the availability of in-situ measurements of soil moisture for hydrologic applications is expected to greatly increase through the development of soil moisture dedicated remote sensing platforms (Wagner *et al.*, 2007), soil moisture electrical sensors and their implementation in sensor networks (Vereecken *et al.*, 2008; Robinson *et al.*, 2008b) and non-invasive sensors such as ground penetrating radar (GPR) (Huisman *et al.*, 2003; Lambot *et al.*, 2008a). In that respect, GPR has shown great potential to accurately characterize soil moisture at the field scale with high resolution (Serbin and Or, 2005; Weihermüller *et al.*, 2007; Lambot *et al.*, 2008b; Minet *et al.*, 2011). As pointed out by Western *et al.* (1999), high-resolution soil moisture datasets are required to readily assess the effect of antecedent soil moisture conditions, rather than relying on few point values that may not capture the real soil moisture patterns. Nevertheless, hydrologic modeling of processes occurring at an intermediate scale between coarse-scale ($\sim$km) remote sensing and fine-scale ($\sim$m) soil moisture measurement techniques is limited by a scale-gap in soil moisture information. The combination of these two types of information by disaggregating (or downscaling) coarse-scale to fine-scale soil moisture data is thus of particular interest (Crow *et al.*, 2000). In that respect, Loew and

Mauser (2008) investigated the use of prior information on spatially persistent soil moisture patterns to disaggregate coarse-scale remotely-sensed soil moisture data. Disaggregated soil moisture values may be also particularly valuable for soil moisture data assimilation in hydrologic models (Merlin *et al.*, 2006).

6.3 Objectives

To increase our knowledge about the strong nonlinear effect of antecedent soil moisture on field scale hydrological response in temperate climate conditions, this chapter aims to: 1) investigate the effect of different scenarios of the spatial structure of antecedent soil moisture on simulated runoff at the field scale and; 2) find the spatial structure of the within field soil moisture that most closely approaches the measured soil moisture pattern in terms of hydrologic response. Seven scenarios of antecedent soil moisture patterns, together with GPR measured soil moisture patterns, were defined in order to determine which degree of description of soil moisture spatial variability is necessary to get an adequate estimation of the runoff. As no runoff measurements were available, the effect of antecedent soil moisture scenarios could not be compared with real discharge, but they are to be compared to each other by hydrologic simulations. The main novelties of this work compared to the previous studies are: 1) to benefit from a fast soil moisture mapping technique at high resolution ($\sim$m) at the field scale (several ha) and; 2) to rely on ten field acquisitions of soil moisture in different field and moisture conditions. This work may also help when coarse-scale remotely-sensed soil moisture data are to be disaggregated into fine-scale patterns in hydrologic or climatic models (downscaling).

6.4 Materials and Methods

6.4.1 Agricultural fields

In this chapter, we used soil moisture data collected during ten GPR acquisitions performed in five different agricultural fields situated in the center of Belgium and Luxembourg (see Table 6.1). The fields are characterized by relatively similar topography, soil type and land cover but the acquisitions were performed in different moisture conditions. The first three fields, that are called, Burnia, Marbaix and Walhain, pertain to the loess belt area in Belgium and are characterized by a flat topography and a silt loam soil. According to the national Belgian soil database (Van Orshoven and Vandenbroucke, 1993) and following a profile matching technique, the texture of this soil consists of 4 % of sand, 82 % of silt and 14 % of clay for the Burnia and Marbaix soil and 4 % of sand, 79 % of silt and 17 % of clay for the Walhain soil. The last two fields, that are located in Luxembourg and called Keispelt and Walsdorf, are characterized by a gentle topography. They are classified as sandy loam and shaly silt loam soils, respectively.

The GPR acquisitions were performed in spring when fields were covered by barley or wheat, except for the Walsdorf site where acquisition was performed in summer after barley cropping. All the acquisitions were performed on bare or nearly-bare soils with vegetation height less than 10 cm and a soil roughness less than 5 cm, thus avoiding scattering issues in the measured GPR data. In each field surveyed by the GPR, the largest catchment was delineated, as some fields are actually constituted of several catchments. Moreover, the fields were considered as hydrologically isolated from the neighboring plots (i.e., by ditches or rural roads along the field limits). For some fields, that were, Keispelt, Marbaix and Burnia, the delineated catchments encompasses the whole surveyed field. Catchment areas are given in Table 6.1.

Table 6.1: Description of the agricultural fields and resolutions used in hydrologic simulations

Field	Location		Area [ha]	Elevation range [m]	Soil type	Land cover
Burnia	4°38’33”E	50°40’10”N	2.29	14	silt loam	wheat
Marbaix	4°38’40”E	50°40’07”N	5.73	14	silt loam	wheat
Walhain	4°41’32”E	50°36’11”N	5.14	16	silt loam	barley
Keispelt	6°04’57”E	49°41’33”N	3.29	18	sandy loam	wheat
Walsdorf	6°09’19”E	49°55’45”N	2.39	12	shaly silt loam	bare

6.4.2 Sensing of soil moisture by ground penetrating radar

Soil moisture was measured by the proximal off-ground GPR method exposed in chapter 4. Soil surface dielectric permittivity was retrieved using an inversion of time-domain GPR data focused on the surface reflection peak in the 200-800 MHz frequency range. GPR-derived dielectric permittivity was translated into soil moisture using the Topp’s petrophysical relationship (Topp *et al.*, 1980) (Eq. (1.16)). Field acquisitions were performed using the GPR mobile platform exposed in chapter 3. Table 6.2 summarizes the 10 GPR acquisitions and shows the number of measurement points and the duration of the acquisition for each field campaign. Time-lapse measurements were performed in two fields only, i.e., in Marbaix and Burnia, in spring 2009 and 2010, respectively. Soil moisture patterns of the five field campaigns in Burnia were widely analyzed in chapter 5.

The GPR-derived soil moisture reflects the surface soil moisture with a depth of investigation of about 5 cm. This relatively shallow characterization of soil moisture may be a limitation for using the soil moisture data in a hydrologic model, as the hydrological active soil layer extends up to 20 cm in the hydrologic model and because of the possible decoupling of surface and subsurface soil moisture (Capehart and Carlson, 1997; Vereecken *et al.*, 2008). Nevertheless, the use of a proximal GPR operating in a large frequency bandwidth and at relatively low frequencies inherently provides a deeper characterization of soil moisture than remote sensing instruments. Moreover, a deeper characterization could be obtained using a multi-layered soil model, as shown in chapter 3 and Minet *et al.* (2011). In this study, it is assumed that the surface soil moisture reflects the soil moisture of the hydrological active soil layer or, at least, its spatial variability.

6.4.3 Antecedent soil moisture scenarios

Soil moisture spatial variability can be analyzed in terms of stochastic or deterministic variability (Blöschl and Sivapalan, 1995). Stochastic variability (or random, non-structured variability) of soil moisture entails that soil moisture can not be a completely deterministic variable based on local attributes but rather a variable with global statistical properties that can be determined. On the other hand, soil moisture can be viewed as a spatially deterministic (or structured) variable that is uniquely determined by spatial conditions, mainly topography, soil properties, and vegetation cover. The introduction of auxiliary spatial data (e.g., topography) to simulate soil moisture thus results in deterministic soil moisture patterns. Between these two extremes, hydrological systems exhibit soil moisture conditions that can be modeled from pure random variability to highly structured soil moisture patterns, with intermediate degree of organization (Western *et al.*, 1999). It is worth mentioning that a stochastic soil moisture description implies several random realizations while a deterministic soil moisture pattern is usually a unique realization. Except the pure random case, soil moisture patterns can be captured using variograms or connectivity functions.

In this study, soil moisture scenarios are based on point measured data, that are displayed as an example for Marbaix, 15 April 2009 in Fig. 6.1. In order to assess the effect of different antecedent soil moisture conditions in hydrologic modeling, seven different types of antecedent soil moisture maps were constructed (see further explanations in this section below):

1. *Reference*: GPR-derived measured values, $\theta = \theta_{GPR}$;
2. *Constant*: $\theta = \theta_{mean}$ = constant;
3. *Structured*: Measured values sorted according to the TWI;
4. *Structured*$_{inv}$: Measured values inversely sorted according to the TWI;
5. *Random*: Randomly permutated values;
6. *Variogram*: Spatially coherent values using a variogram;
7. *Connected*: Spatially coherent and connected values.

Scenarios 2 to 4 are deterministic scenarios, i.e., they consist of a unique realization, while scenarios 5 to 7 are stochastic scenarios, for which 1000 realizations were produced. These soil moisture scenarios are all based on GPR-derived soil moisture that was measured during field acquisitions. Figure 6.2 presents all soil moisture scenarios (except the *constant*) for the field of Marbaix, 15 April 2009.

The soil moisture values measured by the GPR were not regularly spaced in the field, but rather followed the acquisition tracks (see Fig. 6.1). The hydrologic model however requires as an input perfectly grid-shaped antecedent soil moisture maps. Therefore, the measured values must be rasterised. The first scenario ($reference$, Fig. 6.2 (a)), that is based on the real locations of GPR measured values, was thus made by filling a regular grid with the average of the measured values that fell into each pixel of the grid. The resolutions of the grids (see Table 6.1) were set as the maximum resolution that avoids having an empty pixel in the grid.

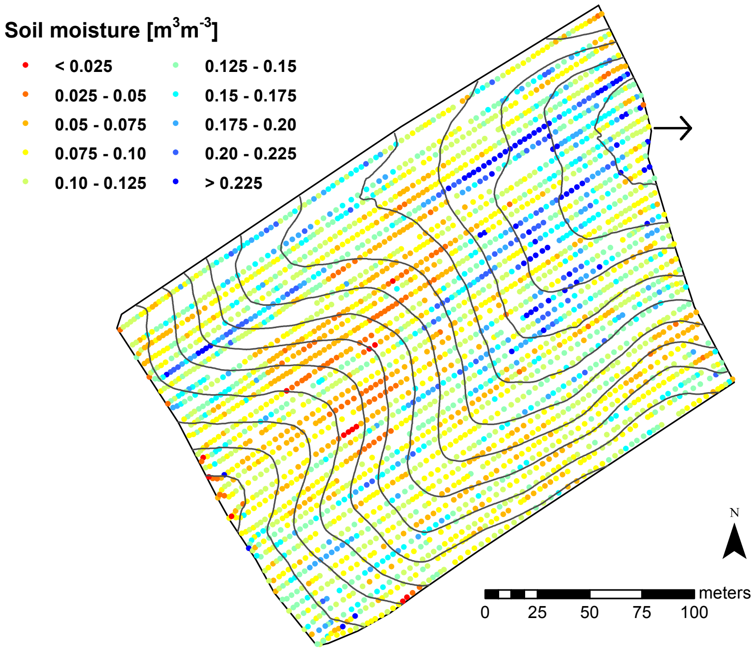

Figure 6.1: Maps of soil moisture point-values retrieved by GPR inversions from the field acquisition in Marbaix, 15 April 2009. Contour lines with an inter-distance of one meter are depicted in black lines. The outlet of the field is indicated by the black arrow. Projected coordinate system: Belgian Lambert 1972.

For the second scenario (*constant*), soil moisture values were set as constant over space and equal to the mean of the measured values from the first map. This map is not presented in Fig. 6.2.

In the third scenario (*structured*, Fig. 6.2 (b)), measured values were sorted according to the topographic wetness index (TWI), as defined by Beven and Kirkby (1979):

$$TWI = \ln\left(\frac{a}{\tan(\beta)}\right) \tag{6.1}$$

where a is the raster of the flow accumulation and β is the raster of the slope expressed in %. We used a single direction algorithm to compute the flow accumulation raster, as was used in previous studies (e.g., Merz and Plate, 1997).

The TWI was preliminary computed over the fields using a digital elevation model of same resolution that was set in the first scenario. Then, moisture and TWI values were ranked and moisture values were attributed to the pixels where the TWI was in the same rank. The fourth scenario ($structured_{inv}$, Fig. 6.2 (c)) is the counterpart of the third one, that is, soil moisture and TWI values were inversely ranked, so that the pixels with the highest TWI values received the lowest soil moisture values.

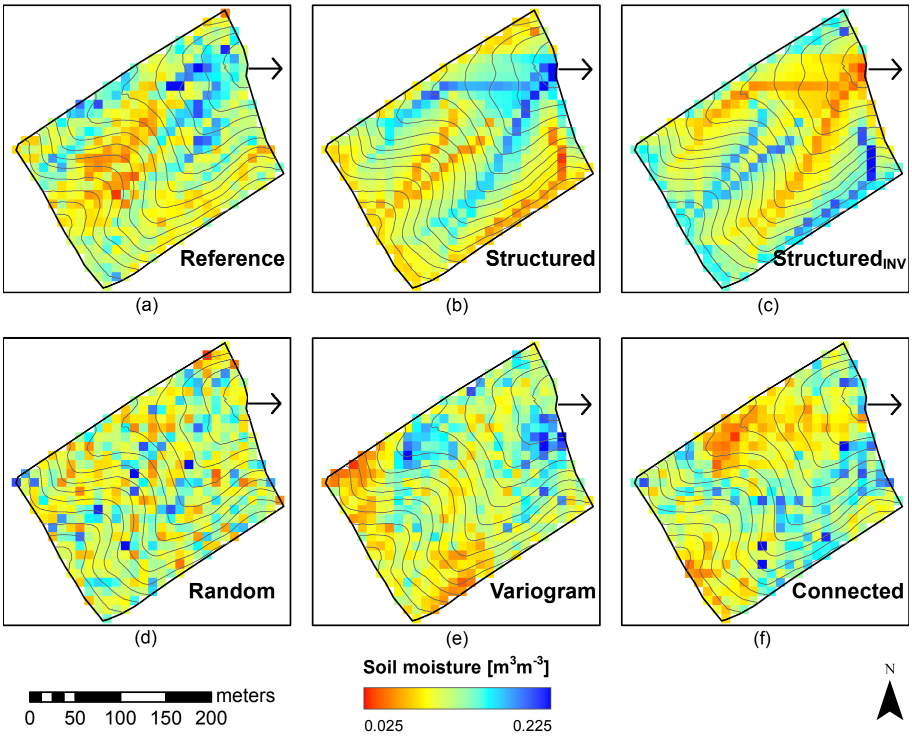

Figure 6.2: Antecedent soil moisture maps for Marbaix, 15 April 2009, used as an input in the hydrologic model with measured grided values (a), measured values rearranged according the TWI (b), measured values inversely rearranged according the TWI (c), randomly permuted values (d), simulated values using a variogram (e) and connected simulated values (f). The outlet location and direction are indicated with an arrow.

The TWI was chosen for modeling structured soil moisture patterns because of the lack of other detailed sources of information for these fields (e.g., soil properties, vegetation) and for its high predictive power in wet conditions (Western *et al.*, 1999). The limited elevation range of the fields may however limit the redistribution of water according to the topography and restrain the explanatory power of the TWI for soil moisture in these fields. Although high-resolution soil information at the field scale could have provided more insights for explaining moisture patterns, no high-resolution soil parameters can be usually found at the catchment scale (> 10 km). We thus investigated the use of topographically-derived indices (i.e., TWI) for soil moisture modeling in a data-scarcity context. As soils were bare or nearly-bare, the influence of vegetation heterogeneities on spatial soil moisture variability might be furthermore limited in our study. In addition, land cover heterogeneities are limited in our study as the fields are managed as single plots. For larger catchment scale (> 10 km), land cover differences among the fields may better explain soil moisture patterns (Western *et al.*, 1999). For drier climatic conditions, when potential evapotranspiration exceeds precipitation, local controls as potential radiative indices have shown better correlations with observed soil moisture (Grayson *et al.*, 1997). Some reviews about the predictive power of the TWI for soil moisture can be found in Western *et al.* (1999) and Sørensen *et al.* (2006).

The fifth scenario (*random*, Fig. 6.2 (d)) maps were made by randomly permuting the measured values over space. As the random process can lead to different maps, 1000 realizations of this scenario were repeated, as well as for the two following scenarios (stochastic variability scenarios).

The sixth scenario (*variogram*, Fig. 6.2 (e)) maps were made by simulating gaussian soil moisture patterns using variograms describing the spatial dependence of soil moisture. Variograms were computed considering the spatial dependence of the data along the acquisition lines only, neglecting the spatial dependence of the data of adjacent lines (Minet *et al.*, 2011). An exponential model accounting for a nugget effect was fitted for all the variograms. Zero-mean gaussian distributed values were then simulated in each grid pixel using an implementation of the sequential non conditional method. Finally, measured values were ranked and attributed to the pixels where the simulated values were in the same rank. This ranking procedure permitted therefore to preserve exactly the same distribution of values as in the $reference$, *random*, *structured* and $structured_{inv}$ scenarios.

The seventh scenario (*connected*, Fig. 6.2 (f)) is characterized by connected patterns of high soil moisture values. It was made following the method of Zinn and Harvey (2003) that was used here to produce a highly connected pattern of a given variable. First, spatially coherent values of a zero-mean gaussian distribution were simulated over the field extent as for the *variogram* scenario. Second, the absolute value of the simulated values were taken, so that the locations where the values were close to zero (i.e., now the lowest values) became connected between them. In order to conserve the spatial properties of the simulated values after taking the absolute value, the parameters of the variogram must be initially modified. Hence, the range was multiplied by the scale factor of 1.86 and the nugget effect was divided by 2. Finally, inversely ranked measured values were attributed to the pixels where simulated values were in the same rank, so that the connected paths (i.e., the lowest simulated values) received the highest soil moisture values.

It is worth noting that all scenarios have the same mean as the $reference$ scenario, and that all scenarios, except the *constant* one, show exactly the same soil moisture distribution as the $reference$ scenario, owing to the ranking procedure. Moreover, the $reference$, *variogram* and *connected* maps were characterized by the same variogram. This allowed to truly compare the modeling discharge between the scenarios. Actually, the *random* scenario can yield exactly the same antecedent soil moisture maps that were realized with the $reference$, *structured*, $structured_{inv}$, *variogram* and *connected* scenarios, as the same values were merely rearranged according to different schemes. But the probability that the *random* scenario yield a particular realization is drastically low, i.e., equals to $\frac{1}{n!}$, where n is the number of grid cells per field, and may not be encountered in our study. The number of 1000 realizations for the stochastic scenarios is thus a tradeoff between the computation time and the desirable variability among realizations.

Other types of auxiliary information could be used to model antecedent soil moisture patterns, such as soil type information. As soil properties may significantly vary within a field, this may largely determine soil moisture patterns, through varying soil hydraulic properties. Nevertheless, detailed soil information was not available at high resolution and it is worth noting that this information is rarely available.

The hydrograph modeled with the $reference$ soil moisture map was assumed to be the reference hydrograph, as no measured discharges were available. Comparison of soil moisture scenarios were performed based on Nash-Sutcliffe efficiency (NSE) coefficients between the hydrographs simulated with the measured soil moisture pattern ($reference$ scenario) and the other scenarios.

The effect of soil moisture spatial variability may also depend on the resolution (grid size) of the distributed hydrologic model. For investigating scale aggregation of antecedent soil moisture maps, hydrologic simulations were also performed with increasing grid sizes for the field campaign of Marbaix, 19 April 2009 for the seven scenarios. Nine grid sizes, uniformly ranging from 10 to 30 m, were selected. The field campaign of Marbaix, 19 April 2009 was chosen as it was performed in the largest field at high resolution, maximizing the grid size range.

6.4.4 Hydrologic model

In this work, we used the hydrological component of the continuous runoff and erosion CREHDYS model (see Laloy and Bielders (2008, 2009) for a comprehensive model description). It can be used at rainfall event scale to simulate high-frequency variability in rainfall-runoff processes. Short time steps are then required to properly capture soil physical dynamics. Consequently, the model requires one minute time step rainfall data as input. The model is spatially distributed and the flow path must be derived from topography through a flow accumulation grid. As we used the model for event-scale simulations only, the relevant modeled processes for runoff prediction are infiltration, soil depressional storage filling and runoff flow. For simplicity, no surface storage was however considered in this study. Infiltration is computed using the Green-Ampt model (Green and Ampt, 1911) which assumes a uniform wetting front infiltrating vertically. A single soil layer is assumed, which results in a single effective hydraulic conductivity along the entire topsoil depth. In its current form, the CREDHYS model therefore simulates infiltration-excess overland flow only and does not simulate saturation-excess runoff caused by shallow impervious layer or perched aquifers. Runoff flow is routed along flow paths using a one-dimensional kinematic wave equation. Although not strictly required by the model to simulate the runoff dynamics at the event scale, note that percolation is computed within and between precipitations using the method of Savabi and Williams (1995). In addition, no evapotranspiration is taken into account within a single rainfall event.

The same rainfall forcing was used for every simulation. It was recorded in central Belgium and corresponds to a short and intensive storm with a return period of 6 years (17.4 mm in 16 minutes). Because no discharge measurements are available, the hydrologic model could not be specifically calibrated for each of the fields. We therefore selected a typical model parameterization for a mildly crusted bare loamy soil. In the absence of surface storage, the soil properties to be considered by the model are the effective saturated soil hydraulic conductivity, KS [mm/h], the absolute value of the Green-Ampt soil matrix potential at the wetting front, ψ [mm], the antecedent soil moisture, θ [$\mathrm{m^3m^{-3}}$], the volumetric soil moisture content at saturation, θ_{SAT} [$\mathrm{m^3m^{-3}}$], the control depth for computing water balance, DF [m], the Manning's n friction coefficient [$\mathrm{m^{-1/3}s}$] and the percolation submodel parameters (see Laloy and Bielders (2008) for details). Based on the values found in Laloy and Bielders (2008); Laloy *et al.* (2010), we fixed KS at 25 mm/h (Burnia site) and 20 mm/h (other fields), ψ to 100 mm, θ_{SAT} to 0.50 $\mathrm{m^3m^{-3}}$, DF to 0.2 m, and n to 0.03 $\mathrm{m^{-1/3}s}$. Those values were used for all field simulations. The KS parameter was set at a slightly higher value for the Burnia site in order to generate runoff responses suitable for a meaningful comparison among fields and antecedent soil moisture scenarios. The KS equal to 20 mm/h was too small for Burnia site for generating differences between scenarios. The KS parameters were thus set accordingly the range of values found in Laloy and Bielders (2008) and Laloy *et al.* (2010) for a similar soil in order to observe different runoff responses according to soil moisture scenarios. Lastly, it is worth mentioning that antecedent soil moisture θ was found to be one of the most sensitive parameters of CREHDYS with respect to runoff production (Laloy and Bielders, 2008). Hence, as the model is spatially-distributed, it is expected that spatial organization of soil moisture strongly affects the runoff prediction at the outlet.

6.5 Results

6.5.1 Soil moisture data measured by ground penetrating radar

Table 6.2 presents the within-field mean and standard deviation of GPR measured soil moisture and the parameters of the fitted variograms for the ten field campaigns. As an example, Fig. 6.1 shows the map of surface soil moisture measured by GPR in Marbaix on the 15 April 2009. It is worth noting that the point-symbols appear around two times larger on the map compared to the real GPR antenna footprint size. Soil moisture conditions were clearly dry for this GPR acquisition, with a corresponding smaller variability compared to the other acquisitions (see Table 6.2).

Soil moisture values appeared globally spatially coherent, although some nugget effect can be observed between neighboring points. In particular, we can notice a line effect with a high spatial coherence for points along the same acquisition line (i.e., the acquisition tracks), whereas there are some abrupt changes when moving to adjacent lines, as already observed and discussed in chapter 3. For other fields, line effects were also observed, but with different degrees of importance. At a larger scale however, soil moisture patterns were mainly related to the topography, that is, hilltops were drier than thalwegs. The wettest areas appeared in the bottom of the thalwegs and near the outlet.

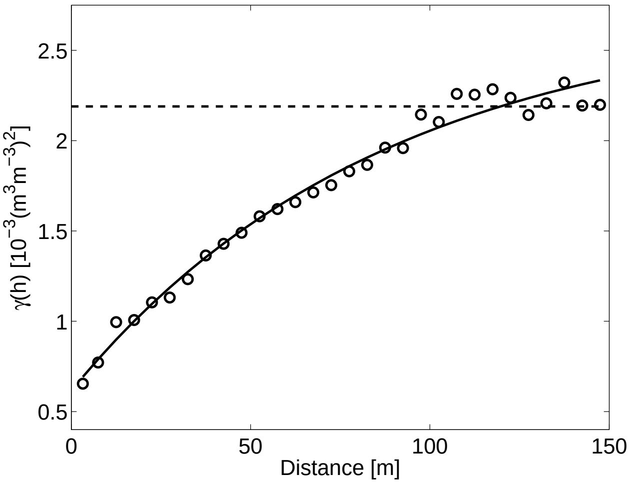

Figure 6.3: Variogram of soil moisture computed for the field campaign in Marbaix, 15 April 2009 with a class distance from 0 to 150 m by a step of 5 m. A variogram using an exponential model is fitted on the data. The total variance of soil moisture is depicted with the dashed line.

Table 6.2: GPR soil moisture ([m^{3}m^{-3}]) acquisitions. The number of measured points, the duration of the acquisition, the mean (μ_θ) and standard deviation (σ_θ) of soil moisture, variogram parameters (Nugget effect [m^{3}m^{-3}]^2, Sill [m^{3}m^{-3}]^2 and Range), the ratio between the nugget effect and the sill (Nug./Sill), the coefficient of correlation between the TWI and soil moisture ($r_{TWI,\theta}$) and the resolution for hydrologic simulations are presented.

		N° of points	Duration	μ_θ	σ_θ	Nug. effect	Sill	Range [m]	Nug./Sill [%]	$r_{TWI,\theta}$	Resolution [m]
Walhain	07/04/2008	1008	4h56’	0.301	0.060	0.0006	0.0028	35	20	-0.064	15
Keispelt	13/03/2009	1311	48’	0.262	0.106	0.0033	0.0076	112	43	0.156	12.5
Marbaix	19/03/2009	3786	1h51’	0.106	0.051	0.0008	0.0023	177	33	0.170	10
Marbaix	15/04/2009	2911	2h02’	0.115	0.047	0.0006	0.0027	260	23	0.385	10
Walsdorf	21/07/2009	3248	1h08’	0.173	0.071	0.0019	0.0038	21	50	-0.235	10
Burnia	15/03/2010	1496	1h09’	0.226	0.067	0.0013	0.0041	79	32	0.139	7
Burnia	18/03/2010	1252	56’	0.234	0.062	0.0016	0.0034	77	47	0.011	7
Burnia	24/03/2010	1429	1h01’	0.238	0.063	0.0014	0.0036	70	39	-0.050	7
Burnia	30/03/2010	1227	1h32’	0.304	0.154	0.0065	0.0248	120	26	0.062	7
Burnia	06/04/2010	1759	51’	0.309	0.155	0.0064	0.0258	175	25	0.120	7

Figure 6.3 shows the variogram of soil moisture values computed along the acquisition lines for the field campaign in Marbaix, 15 April 2009. Spatial coherence was observed, with a regular increase of soil moisture variance with increasing distance classes up to the range, which reached 260 meters, while other field campaigns showed smaller ranges. The nugget effect accounted for 23% of the total sill (Table 6.2). Pearson's coefficients of correlation between the TWI and measured soil moisture from the $reference$ maps were computed ($r_{TWI,\theta}$, Table 6.2) and was equal to 0.385 for Marbaix, 15 April 2009. For the other field campaigns, the correlation between the TWI and soil moisture was always lower and even negative, as for, e.g., Walsdorf.

6.5.2 Effect of antecedent soil moisture on hydrographs

Hydrographs simulated with the deterministic soil moisture maps

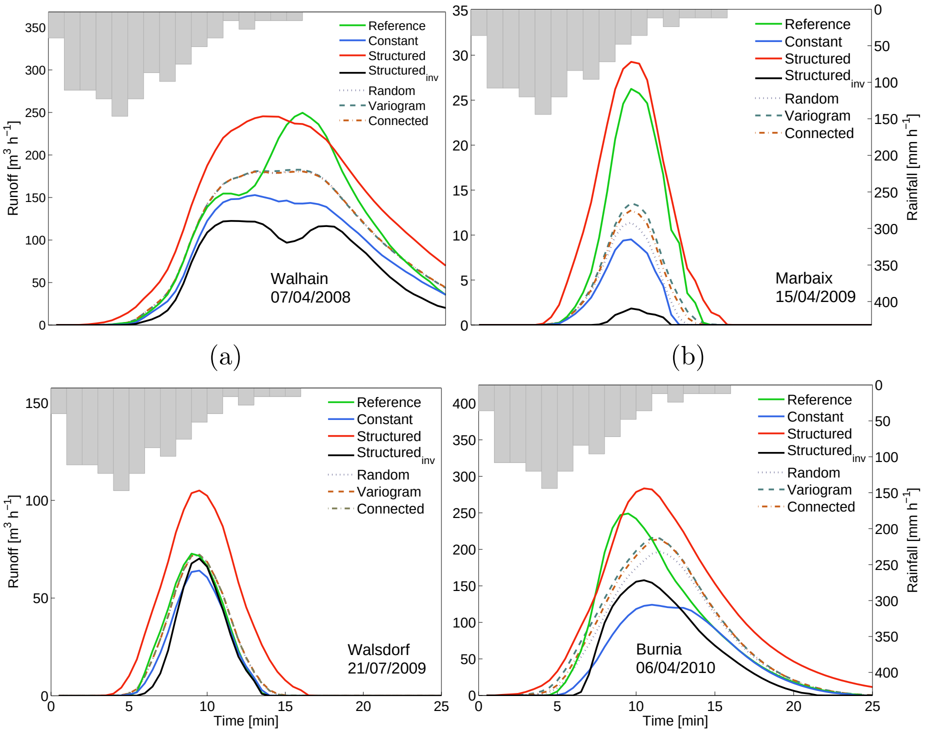

(a) (b)

(c) (d)

Figure 6.4: Hydrographs from hydrologic simulations using the antecedent soil moisture maps from all scenarios for 4 field campaigns: Walhain - 07/04/2008 (a), Marbaix - 15/04/2009 (b), Walsdorf - 21/07/2009 (c) and Burnia - 06/04/2010 (d). For stochastic soil moisture scenarios, i.e., *random*, *variogram*, *connected*, the average hydrographs on the 1000 realizations are depicted. The rainfall is depicted by the bars of the second Y-axis.

Table 6.3 presents the runoff peaks and total runoff volumes resulting from the hydrologic simulations for the ten field campaigns and the seven scenarios. Figure 6.4 shows the hydrographs for four field campaigns only. For stochastic soil moisture scenarios, i.e., *random*, *variogram*, *connected*, the average hydrographs of the 1000 realizations are depicted.

The *constant* scenario, where soil moisture uniformly equals the mean value, showed a lower runoff peak and volume compared to all other scenarios, except the $structured_{inv}$. For Burnia, 30/03/2010 and 06/04/2010, the smallest runoff peaks were found with the *constant* scenario. The hydrographs simulated with the *structured* and $structured_{inv}$ scenarios completely delineated the range of variation of the other hydrographs for Marbaix - 15/04/2009 (Fig. 6.4 (b)) as well as for Marbaix - 19/03/2009 and for the first three dates in Burnia. For the other field campaigns, although some scenarios (e.g., the $reference$) can exceed this range, the hydrographs from the two soil moisture maps based on the TWI (i.e., *structured* and $structured_{inv}$) generally gave the range of variation for the other hydrographs. In terms of runoff volume, the *structured* scenario always resulted in the largest discharge. The $structured_{inv}$ scenario resulted in the lowest runoff volume in 9 out of 10 field campaigns. It is worth noting that large differences in runoff peak and volumes existed between the different dates of the time-lapse acquisitions in Burnia and Marbaix. The amount of runoff appeared to be largely sensitive to the wetness state of the antecedent conditions.

Table 6.3: Runoff peak Q_{max} and total runoff volume V for each antecedent soil moisture scenario for the 10 field campaigns. For the stochastic scenarios, the average Q_{max} and V were computed and the standard deviations are depicted in brackets. Maximum and minimum values for each field campaign are highlighted in bold and italic, respectively.

		Reference	Constant	Structured	Structured$_{inv}$	Random	Variogram	Connected
Walhain	$Q_{max}[m^3h^{-1}]$	**250**	153	246	*122*	192 (15)	199 (22)	195 (18)
07/04/2008	$V[m^3]$	5259	4019	**6945**	*3069*	4886 (231)	4896 (353)	4895 (301)
Keispelt	$Q_{max}[m^3h^{-1}]$	**529**	*327*	460	334	401 (20)	412 (47)	405 (37)
13/03/2009	$V[m^3]$	6454	3986	**6742**	*3554*	5045 (184)	5138 (563)	5079 (419)
Marbaix	$Q_{max}[m^3h^{-1}]$	18	7	**26**	*1*	9 (2)	10 (8)	10 (5)
19/03/2009	$V[m^3]$	150	51	**262**	*4*	66 (18)	81 (68)	71 (41)
Marbaix	$Q_{max}[m^3h^{-1}]$	26	10	**29**	*2*	12 (3)	14 (10)	13 (8)
15/04/2009	$V[m^3]$	223	74	**302**	*10*	90 (21)	115 (94)	105 (68)
Walsdorf	$Q_{max}[m^3h^{-1}]$	73	*64*	**105**	70	72 (6)	73 (8)	73 (7)
21/07/2009	$V[m^3]$	637	545	**1189**	*513*	653 (58)	659 (77)	658 (66)
Burnia	$Q_{max}[m^3h^{-1}]$	**45**	18	43	*15*	25 (4)	31 (16)	28 (11)
15/03/2010	$V[m^3]$	509	142	**739**	*87*	237 (43)	312 (164)	284 (116)
Burnia	$Q_{max}[m^3h^{-1}]$	**49**	22	44	*20*	29 (4)	34 (14)	31 (10)
18/03/2010	$V[m^3]$	534	194	**776**	*127*	300 (45)	355 (149)	327 (105)
Burnia	$Q_{max}[m^3h^{-1}]$	47	26	**49**	*24*	33 (4)	37 (15)	35 (10)
24/03/2010	$V[m^3]$	494	240	**870**	*154*	349 (46)	407 (160)	391 (114)
Burnia	$Q_{max}[m^3h^{-1}]$	240	*112*	**274**	157	195 (16)	250 (52)	230 (41)
30/03/2010	$V[m^3]$	3363	*2025*	**5048**	2170	3172 (128)	3549 (448)	3401 (362)
Burnia	$Q_{max}[m^3h^{-1}]$	249	*124*	**283**	158	200 (17)	261 (55)	242 (43)
06/04/2010	$V[m^3]$	3581	2232	**5146**	*2230*	3255 (129)	3654 (504)	3529 (386)

As mean soil moisture increases, the range of variation of the hydrographs between the two extreme scenarios (*structured* and $structured_{inv}$) tends however to diminish. Figure 6.5 shows the relative difference between *structured* and $structured_{inv}$ runoff volume as a function of the mean soil moisture in the field. There was a good agreement between these two variables considering the Belgian fields (Burnia, Marbaix, Walhain) only, with a coefficient of correlation of -0.920, compared to a coefficient of correlation of -0.729 for all fields. The range of variation of the hydrographs, i.e., the sensitivity of the runoff response to the soil moisture spatial variability, appeared thus to be minimized in wet conditions. It is worth mentioning that repeated measurements in Marbaix and Burnia exhibited a temporal stability of measured soil moisture patterns (see chapter 5 that may explain the good correlation when considering the fields separately.

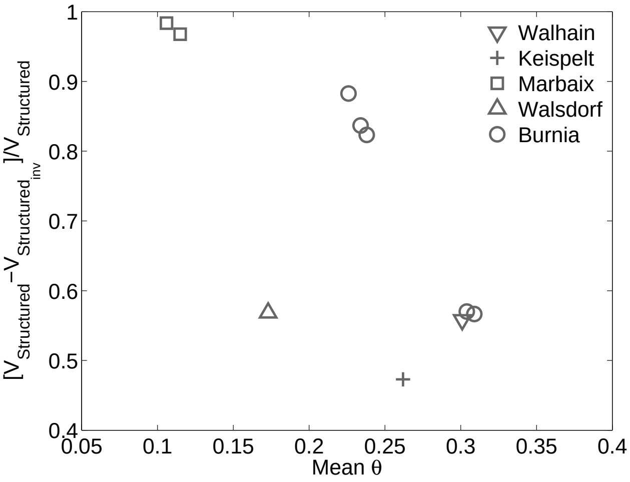

Figure 6.5: Relative difference between *structured* and $structured_{inv}$ runoff volume as a function of the mean soil moisture in the field.

The particular behavior of the $reference$ scenario for Walsdorf, which gave a small runoff peak and volume compared to the other fields, originates from the specific organization of the measured soil moisture. The wettest part of the field in Walsdorf was observed in the plateau of the field whereas the driest part was located near the outlet, which is highlighted by the negative correlation between the TWI and soil moisture (Table 6.2, last column). A part of the runoff which was generated in the wettest part may then have re-infiltrated before reaching the outlet.

Hydrographs simulated with the stochastic soil moisture maps

Figure 6.6 shows the 1000 hydrographs from the *random* scenario for the field campaign in Marbaix, 15 April 2009. The hydrographs from the four first soil moisture scenarios are also plotted, as well as the average *random* hydrograph.

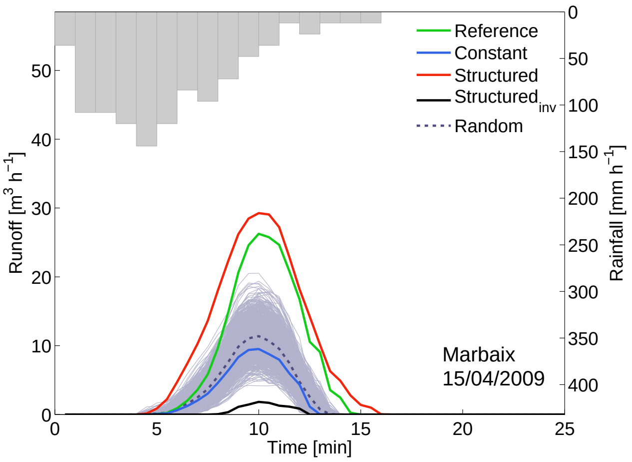

Figure 6.6: Hydrographs from hydrologic simulation using the antecedent soil moisture maps from scenarios 1 to 5 for the field campaign in Marbaix, 15 April 2009. The average *random* hydrograph is depicted as a dotted line on top of the 1000 hydrographs from the random antecedent soil moisture maps.

The 1000 *random* hydrographs cover a wide range of values but the peak discharge is always lower than the $reference$ and *structured* hydrographs, denoting the particular arrangements of soil moisture patterns in these scenarios that produced a high discharge, although random simulation could theoretically provide the same soil moisture map as the ones from the $reference$ or *structured* scenarios.

It is worth noticing that a particular realization of the *random* scenario can result in a hydrograph drastically different from another realization. Other fields than Marbaix, 15 April 2009 showed average *random* hydrographs that were better approaching the $reference$ one, but there were still a large variability between the realizations.

The hydrographs from the *variogram* scenario (Fig. 6.7) cover a wider range of values, largely overlapping the range delineated by the hydrographs from the *structured* and the $structured_{inv}$ scenarios. The antecedent soil moisture map of the *variogram* scenario giving the largest discharge was actually characterized by a well-connected soil moisture pattern with the highest soil moisture values near the outlet (map not shown). It was observed that, for all fields, the highest *variogram* scenario hydrograph showed the largest runoff peak and volume compared to the highest *random* hydrograph. The hydrographs from the *connected* scenarios (Fig. 6.8) cover also a wide range of values, similarly to the *variogram* coverage. The average hydrographs of the stochastic soil moisture scenarios gave on average higher runoff than the *constant* scenario.

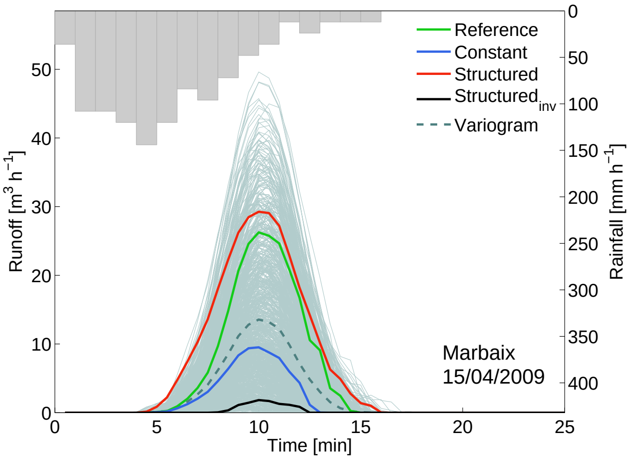

Figure 6.7: Hydrographs from hydrologic simulation using the antecedent soil moisture maps from scenarios 1 to 4 and 6 for the field campaign in Marbaix, 15 April 2009. The average *variogram* hydrograph is depicted in a dashed line on top of the 1000 hydrographs from the simulated antecedent soil moisture maps.

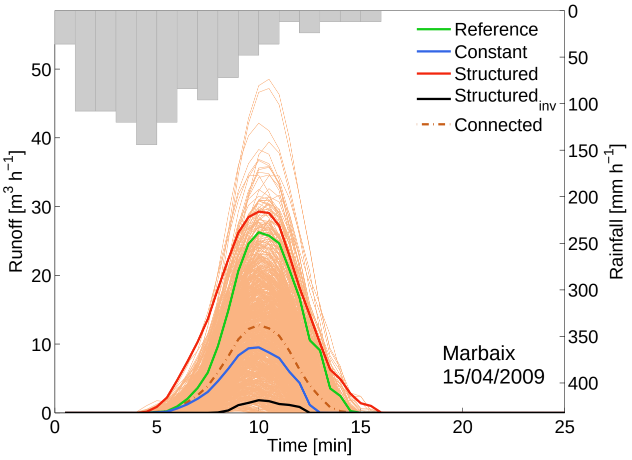

Figure 6.8: Hydrographs from hydrologic simulation using the antecedent soil moisture maps from scenarios 1 to 4 and 7 for the field campaign in Marbaix, 15 April 2009. The average *connected* hydrograph is depicted in a dashed-dotted line on top of the 1000 hydrographs from the simulated antecedent soil moisture maps.

6.5.3 Evaluation of soil moisture modeling scenarios

Table 6.4 shows Nash-Sutcliffe efficiency coefficients (NSE) of the comparison between the different scenarios of antecedent soil moisture maps and the $reference$ scenario, for the ten field campaigns. The comparison of the soil moisture scenarios was performed based on the normalized NSE, that are, the NSE divided by the maximal NSE observed for each field campaign. This normalization was set such that the mean, the standard deviation and the corresponding statistical tests for each soil moisture scenario can be computed.

The stochastic scenarios of soil moisture, i.e., the *random*, *variogram* and *connected* scenarios performed equally (based on a 95% confidence interval) and gave on average higher NSE than the deterministic scenarios, especially for the *variogram* scenario. The *structured* scenario performed the best among the deterministic scenarios. Neglecting the field campaign of Walsdorf, the averages of the normalized NSE of the *structured* and the *constant* scenarios appeared significantly different, with a p-value of 0.0117. Although the *constant* scenario performed better than the *structured* one in two field campaigns, i.e., Waldorf and Burnia - 24/03/2010, the *structured* scenario was found to be a better approach for modeling the soil moisture spatial variability within a catchment than the *constant* scenario.

Table 6.4: Nash-Sutcliffe efficiency coefficients of the different scenarios of antecedent soil moisture maps compared to the $reference$ scenario for the 10 field campaigns. The mean and the standard deviation of normalized Nash-Sutcliffe coefficients were computed for the 10 field campaigns. Maximum and minimum values for each field campaign are highlighted in bold and italic, respectively.

		Constant	Structured	Structured_{inv}	Random	Variogram	Connected
Walhain	07/04/2008	0.853	0.869	*0.686*	0.945	**0.946**	0.943
Keispelt	13/03/2009	0.777	**0.971**	*0.650*	0.903	0.911	0.906
Marbaix	19/03/2009	0.513	0.553	*-0.066*	0.646	**0.755**	0.690
Marbaix	15/04/2009	0.491	**0.894**	*-0.030*	0.592	0.719	0.675
Walsdorf	21/07/2009	0.970	*0.469*	0.937	**0.993**	0.991	0.992
Burnia	15/03/2010	0.431	**0.777**	*0.224*	0.672	0.773	0.755
Burnia	18/03/2010	0.551	0.724	*0.378*	0.764	**0.821**	0.792
Burnia	24/03/2010	0.685	0.555	*0.506*	0.863	**0.903**	0.896
Burnia	30/03/2010	*0.666*	0.763	0.837	0.889	**0.920**	0.915
Burnia	06/04/2010	*0.688*	0.817	0.808	0.887	**0.922**	0.910
Mean*		0.736	0.834	0.531	0.913	0.974	0.951
Standard deviation*		0.136	0.178	0.374	0.101	0.062	0.075

* The mean and standard deviation were computed based on normalized Nash-Sutcliffe coefficients.

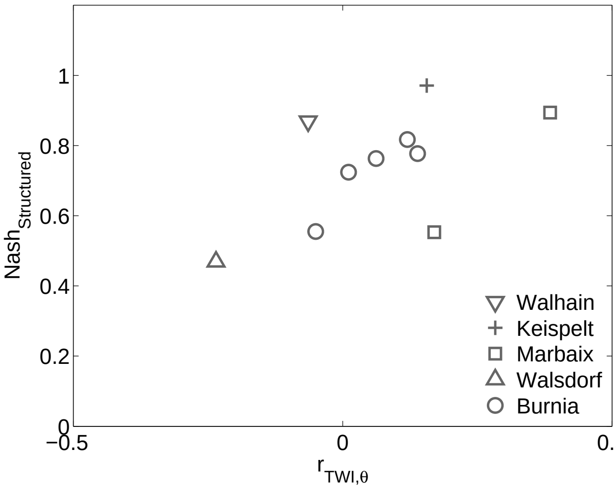

Figure 6.9: Nash-Sutcliffe efficiency coefficients of the *structured* scenario with respect to the *reference* scenario ($NSE_{structured}$) as a function of the correlation between measured soil moisture and the TWI ($r_{TWI,\theta}$).

Figure 6.9 presents the NSE of the *structured* scenario with respect to the *reference*, as a function of the correlation between measured soil moisture and the TWI. The performance of the *structured* scenario in approaching the *reference* hydrograph (i.e., $NSE_{structured}$) appeared to be related to the explanatory power of the TWI for soil moisture (i.e., $r_{TWI,\theta}$), with a coefficient of correlation of 0.581 between these two variables. This correlation increased if we consider only field campaigns performed on the same field, e.g., the correlation rose to 0.898 when field acquisitions in Burnia only were considered. The bad performance of the *structured* scenario in approaching the *reference* scenario for Walsdorf pointed out above can be related to its negative correlation between the TWI and measured soil moisture. Similarly, the proximity of the *reference* and *structured* hydrographs for Marbaix - 15/04/2009 (Fig. 6.4(b)) can be related to the largest correlation between the TWI and soil moisture that was observed for this campaign.

Varying grid sizes did not drastically change the hydrographs that were obtained with the 10 m resolution simulations (see Fig. 6.4(b)). While the correlation between TWI and measured soil moisture slightly increased with grid size, there was not a clear increase of the NSE for the *structured* scenario (Table 6.5).

Table 6.5: Nash-Sutcliffe efficiency coefficients of the different scenarios of antecedent soil moisture maps compared to the $reference$ scenario for Marbaix, 15 April 2010 for varying grid sizes. The coefficients of correlation between the TWI and soil moisture ($r_{TWI,\theta}$) are presented in the second column.

Grid size	$r_{TWI,\theta}$	Constant	Structured	Structured$_{inv}$	Random	Variogram	Connected
10 m	0.385	0.491	0.894	-0.030	0.592	0.719	0.675
12.5 m	0.383	0.611	0.914	0.185	0.689	0.770	0.708
15 m	0.387	0.378	0.913	-0.097	0.485	0.542	0.522
17.5 m	0.427	0.660	0.973	0.294	0.724	0.793	0.748
20 m	0.488	0.550	0.989	0.235	0.618	0.676	0.641
22.5 m	0.393	0.421	0.798	-0.098	0.485	0.551	0.509
25 m	0.488	0.557	0.899	0.219	0.599	0.637	0.613
27.5 m	0.439	0.531	0.945	0.169	0.591	0.608	0.599
30 m	0.668	0.693	0.898	-0.001	0.788	0.815	0.805

6.6 Discussions

6.6.1 Effect of spatial variability of soil moisture on simulated runoff

Hydrologic simulations using different organizations of soil moisture patterns showed a large variability of runoff responses. This behavior can be explained by the location of the runoff contributing and non-contributing (or even re-infiltrating) areas that are determined by antecedent soil moisture conditions (Noto *et al.*, 2008). Runoff is generated at a certain soil moisture threshold because rainfall intensity exceeds the effective infiltration capacity (Hortonian overland flow). Based on single-cell hydrologic simulation, the antecedent soil moisture thresholds that triggered runoff generation were estimated to be approximately 0.25 and 0.20 m^3m^{-3} for the 25 and 20 mm/h initial hydraulic conductivity, respectively. The threshold behavior of the hydrologic model response to antecedent soil moisture results in a non-linear response of the model with soil moisture. Introducing spatial variability of soil moisture creates zones where the initial soil moisture is close or above this threshold, which rapidly become runoff contributing areas. The runoff response of the different soil moisture scenarios can be explained by the locations of runoff contributing areas that modulated the simulated runoff response at the catchment outlet:

- The *constant* scenario resulted in smaller runoff than other spatially variable soil moisture scenarios (except the $structured_{inv}$), denoting the non-linear response of the hydrologic model to soil moisture. Merz and Plate (1997); Merz and Bardossy (1998) and Bronstert and Bardossy (1999) also observed that constant soil moisture conditions resulted in the lowest discharge compared to spatially-variable soil moisture, either organized in a structured (Merz and Plate, 1997; Merz and Bardossy, 1998; Bronstert and Bardossy, 1999) or random (Merz and Bardossy, 1998; Bronstert and Bardossy, 1999) way. However, compared to spatially-constant soil moisture organization, Merz and Plate (1997) observed similar (dry conditions) and smaller (wet conditions) discharge with randomly permuted values. This was explained by the possibility of re-infiltrating pixels placed along the flow channel, but this explanation was incoherent when comparing the results in dry and wet conditions. In our case, although some random realizations resulted in smaller discharge than the *constant* scenarios, the average *random* hydrographs appeared larger than the *constant* ones, maybe due to the larger number of realizations in our study (1000 instead of 3) or to the different model parameterizations.

- The *structured* scenario gave the largest discharge due to the locations of the contributing areas (i.e., the wettest areas) that were situated near the outlet and in the flow channels. However, for the $structured_{inv}$ scenario, the contributing areas were far from the outlet and from the runoff network, so the generated runoff re-infiltrated when propagated to the field outlet.

- The decrease in the range of hydrographs, expressed as the difference between the *structured* and $structured_{inv}$ scenarios, with increasing mean soil moisture (Fig. 6.5) can be explained by the increasing size of the contributing areas in wet conditions. In dry conditions, small contributing areas are located near to and far from the outlet for the *structured* and the $structured_{inv}$ scenarios, respectively. As a result, the difference between these scenarios is maximized in dry conditions. Therefore, field acquisitions (i.e., Marbaix, Walsdorf and the first three dates of Burnia) that showed antecedent soil moisture below the soil moisture thresholds are expected to be more sensitive to spatial variability of soil moisture as thresholds are overtaken during the simulations. In wet conditions, the contributing areas expand and tend to cover the whole field, and as a result, the difference between the two scenarios tends to vanish. At an extreme state of wetness, i.e., for a completely saturated soil, there would be no differences in terms of runoff between the two extreme scenarios. In that respect, Merz and Plate (1997) also pointed out that the effect of simulated spatially structured variability was more important in dry conditions because of the smaller size of the contributing areas.

- The average *random*, *variogram* or *connected* hydrographs (i.e., the model outputs) appeared larger from the *constant* hydrograph, although the average *random*, *variogram* or *connected* antecedent soil moisture maps (i.e., the model inputs) are theoretically equals to the *constant* one, denoting the non-linearity of the hydrologic model.

- The *variogram* and *connected* soil moisture scenarios gave a wider range of hydrographs and on average higher runoff peak and volume compared to the *random* soil moisture scenario because of the spatial coherence of contributing areas, as it was also stated in Merz and Bardossy (1998). This wide range is to be attributed to the spatial clustering of non-contributing re-infiltrating pixels that can be placed on or completely outside the flow channel, resulting in a small or great discharge, respectively. The probability that numerous re-infiltrating pixels are present on the flow channel is smaller in the *random* scenario than in the *variogram* and *connected* scenarios because of the grouping of similar pixels.

- It was shown that a unique realization of the *random* scenario can not be used to properly model soil moisture patterns because of the large variability in modeled discharges. From a practical point of view, the *random* scenario may suffer from the large requirement in computing resources, due to the need of several repetitions. This large variability between the realizations with the *random* scenario compared to a structured soil moisture organization was not observed in Merz and Plate (1997) and Merz and Bardossy (1998). It seems that the threshold effect of soil moisture on runoff was stronger in our study than in these two previous ones, allowing for more re-infiltration and a larger impact of the locations of the contributing areas.

The second objective of this paper was to evaluate which description of soil moisture organization is the most appropriate for hydrologic modeling at the field scale. The comparability of the fields may be limited by soil, topographic, resolution and moisture conditions differences. Nevertheless, the good performance of the *structured* soil moisture scenario was observed for different field and moisture conditions, even in cases when measured soil moisture was poorly correlated with the TWI. It was shown that there was a larger comparability between the different soil moisture conditions for field campaigns performed on same fields (Burnia and Marbaix), even though there was a large variability of the runoff peak and volume amounts depending on the wetness conditions. Varying grid sizes did not alter the order of performance of the antecedent soil moisture scenarios (Table 6.5). It was thus shown that, to some extent, the effect of spatial variability of antecedent soil moisture can be observed in various field conditions at the field scale, under a specific rainfall.

6.6.2 Soil moisture patterns and its relation with topographic wetness index

In this study, the TWI appeared to be a poor predictor of the measured soil moisture spatial distribution (see Table 6.2). Although some studies have shown that the explanatory power of the TWI for soil moisture may increase with scale aggregation (Sørensen *et al.*, 2006) or by comparing grid cells accounting for an uncertainty in the location of the cells (Güntner *et al.*, 2004), this was only slightly observed when increasing the resolution scale (i.e., for Marbaix, 15 April 2009 only). Meanwhile, the use of multidirectional flow accumulation algorithms could also improve the computation of the TWI and its correlation with measured soil moisture (Quinn *et al.*, 1995; Tarboton, 1997; Seibert and McGlynn, 2007). The explanatory power of the TWI for soil moisture may be limited in dry conditions, as observed for Walsdorf. Indeed, for this case, the soil moisture pattern may be better explained by soil type or radiative indices, as it was the only field campaign that was conducted in summer.

The predictive power of the *structured* scenario appeared to be related to the correlation between the measured soil moisture and the TWI (Fig. 6.9). Nevertheless, for some field campaigns, this weak negative correlation contrasted with the rather good NSE of the $reference$ scenario compared to the *structured* scenario, as for, e.g., Walhain, 07 April 2008, which has $r_{TWI,\theta}$ = -0.064 and $NSE_{structured} = 0.869$. This can be explained by the non-unicity of the hydrologic model with respect to the antecedent soil moisture maps for a particular hydrograph, that is, a large number of antecedent soil moisture maps can result in the same hydrograph. In that respect, a measured soil moisture pattern which is poorly correlated with the TWI could still result in a runoff response close to the one of the *structured* scenario.

In the hydrologic simulations using CREHDYS, flow paths are governed by topography, but it is worth noticing that in reality, deviating structure within (e.g., wheel tracks) and between (e.g., ditches, roads) fields may limit the use of solely topographically-driven hydrologic modeling. If not accounted for in real case experiment, it would reduce the relationship between the explanatory power of the TWI for soil moisture and the runoff response using the *structured* scenario. In these simulations, the same topography information (e.g., same grid resolution) is used for both hydrological modeling and reordering soil moisture in the *structured* scenario. This might have increased the correlation between the $NSE_{structured}$ and the explanatory power of the TWI for measured soil moisture.

Grayson *et al.* (1997) showed that soil moisture patterns tend to be characterized by a larger stochastic variability in dry conditions while they appear more structured in wet conditions. Nevertheless, for the 10 soil moisture datasets presented here, there was no clear trend between the mean soil moisture and the importance of the nugget effect (Table 6.2), except for Burnia where a decrease in the Nugget/Sill ratio is observed with increasing soil moisture. The overall poor relation may originate from the different field conditions in terms of soil type and topography and from the limited soil moisture range of the field campaigns.

6.6.3 Disaggregation of soil moisture

Disaggregating coarse-scale soil moisture data into fine-scale patterns needs to account for the importance of spatial variability on runoff responses. For large catchments ($>$ 10 km), spatial distribution of soil moisture can not be measured at high resolution (e.g., $\sim$m) at the field scale. Nevertheless, coarse-scale remotely-sensed soil moisture data could be disaggregated by combining a geostatistical description of fine-scale soil moisture patterns with other sources of fine-scale information (e.g., topography as in Pellenq *et al.* (2003)), if soil moisture patterns could be explained by this information. In that respect, several authors have proposed empirical relationships between the mean soil moisture and its corresponding standard deviation for different extent scales using soil moisture data from remote sensing estimates and invasive sensors at various extent scales (Western *et al.*, 2003; Vereecken *et al.*, 2007; Famiglietti *et al.*, 2008). Therefore, fine-scale antecedent soil moisture maps are to be modeled from coarse-scale remotely-sensed soil moisture data according to the effects of soil moisture spatial variability on runoff response.

6.7 Conclusions

We investigated the effect of antecedent soil moisture spatial variability on runoff response using a distributed hydrologic model at the field scale. Ten field acquisitions of soil moisture at high resolution were obtained using a mobile proximal GPR platform. Based on these soil moisture data, seven scenarios of antecedent soil moisture maps were constructed with different spatial organizations. Hydrologic simulations were then performed for each field acquisition with seven antecedent soil moisture scenarios.

The first objective of this study was to investigate the effect of different antecedent soil moisture scenarios on field scale runoff response. The high sensitivity of antecedent soil moisture spatial variability on the runoff response was clearly shown for all the field acquisitions in various field and moisture conditions, but in a larger extent in dry conditions. Spatially constant antecedent soil moisture conditions (*constant* scenario) resulted in a smaller discharge than scenarios exhibiting soil moisture spatial variability, except for the $structured_{inv}$ scenario. When soil moisture was arranged according to the TWI (*structured* scenario), the runoff volume was the largest for all field campaigns. At the opposite, when soil moisture was inversely arranged according to the TWI ($structured_{inv}$ scenario), the runoff volume was in general the lowest. Stochastic scenarios of antecedent soil moisture (i.e., *random*, *variogram* and *connected*) gave on average similar and intermediate hydrographs, but there was a wide variability between the stochastic realizations. The observed effects of soil moisture spatial variability on the runoff could be explained in terms of contributing areas, with respect to their sizes and their locations within the field, as runoff is triggered above a soil moisture threshold. The spatial variability of antecedent soil moisture conditions therefore resulted in different runoff responses compared to field-averaged values because of the non-linearity of the runoff production to antecedent soil moisture.

The second objective of this study was to find the soil moisture scenarios that most closely approach the measured soil moisture pattern in terms of runoff response. The average hydrograph from the *variogram* scenario was the best soil moisture modeling scenario. Yet, it is worth noting that a particular realization can perform very badly. Among the deterministic soil moisture scenarios, *structured* performed the best, which was moderately related to the correlation of measured soil moisture and the TWI itself.

Except few particular cases, the effects of spatial variability of soil moisture on runoff response which were already analyzed in previous studies (Merz and Plate, 1997; Merz and Bardossy, 1998; Bronstert and Bardossy, 1999) could be generalized for various field and moisture conditions. In the absence of other detailed source of information, organizing the soil moisture pattern accordingly to the TWI appeared to be the best soil moisture modeling method, even when TWI was poorly correlated to measured soil moisture. Given the high availability of topographic data at high resolution, disaggregating remotely-sensed soil moisture data using TWI information might be valuable. Nevertheless, these findings may be better validated against real discharge measurements.

Conclusions and Perspectives

Soil moisture plays an important role in many hydrologic, climatic and environmental processes. Management of terrestrial systems needs an accurate characterization of the determinant state variables at the appropriate scale of time and space. Knowing the spatiotemporal distribution of soil moisture at various scales is therefore essential for the modeling and understanding of theses processes. Soil moisture measurements techniques range from small-scale invasive sensors to large-scale remote sensing instruments. Hence, there is still a scale gap in the soil moisture measurement techniques. In that respect, ground penetrating radar (GPR) has shown interesting capacities for proximal soil sensing at the field scale.

This thesis aimed at applying and validating the advanced GPR method developed by Lambot *et al.* (2004b) for soil moisture sensing and mapping in field conditions, in support of hydrological modeling at the field scale. The first main objective was to evaluate the reliability of the GPR method for soil moisture determination through numerical, laboratory and field experiments. The second main objective was to investigate the spatiotemporal patterns of soil moisture at the field scale and the importance of taking them into account in hydrologic modeling.

Summary

In the first chapter, a frequency domain reflectometry (FDR) system was developed and modeled using the modeling approach initially developed for GPR by Lambot *et al.* (2004b). The medium sensed by the FDR probe was assumed as a multi-element transmission line, with each element being characterized by its own electromagnetic parameters, and probe head effects were accounted for by three frequency-dependent transfer functions (global reflection and transmission coefficients functions). Only three measurements in known media are sufficient to determine the probe transfer functions and the FDR waveforms could be well modeled after probe calibration. The technique permitted to retrieve the relative dielectric permittivity of humid sand media with a good accuracy (RMSE=0.514 in terms of permittivity), as well as frequency-dependent electrical conductivity.

In chapters 2 and 3, we investigated the use of one-layered, two-layered or continuous profile model inversions for soil moisture retrieval by numerical, laboratory and field experiments. In the presence of shallow soil layering or vertically-varying soil moisture conditions, interferences may occur and affect the backscattered GPR wave. The purpose of these experiments was both to determine in which conditions a one-layered model permits to retrieve surface soil moisture information and to investigate the retrieval of profile soil moisture by two-layered or profile models. In chapter 2, numerical experiments showed that surface soil moisture of a two-layered medium could be retrieved using a one-layered model with a good accuracy while the contrast between the layers remained sufficiently low (< 0.10 m^{3}m^{-3}). These results were corroborated by the laboratory experiments, with an increasing error in shallow soil moisture retrieval with increasing contrast between the layers. Two-layered inversions were able to retrieve soil moisture of the two layers, as well as the first layer thickness with an accuracy of 2 cm. The importance of full-waveform inversions on a large frequency bandwidth were pointed out, as errors increased when inverting the data over limited frequency bandwidths. In chapter 3, we demonstrated by numerical experiments that two-layered GPR data inversion permitted to address continuous profile conditions, that was, two-layered inversions could retrieve soil moisture values at the top and bottom of the profile. Using GPR data acquired in field conditions, two-layered and profile characterization of soil moisture were also in good agreement between them and in accordance with field observations, that were, soil moisture increased with depth.

The GPR system was comprehensively validated for field acquisition of surface soil moisture in chapter 4. For field acquisition, the GPR system was mounted on a mobile platform that allowed for a high acquisition rate (5-10 km/h) at high resolution over several ha. In that chapter and the followings, only one-layered model inversion for the characterization of surface soil moisture was considered. The uncertainties in GPR-derived soil moisture mapping were evaluated by three different methods. First, GPR inversion uncertainties were computed and appeared to be very low, i.e., a field-average standard deviation of 0.0039 m^{3}m^{-3}. Second, the repeatability of soil moisture mapping was assessed and the field-average root mean square repetition error was found to be equal to 0.0169 m^{3}m^{-3}, with a large part of this error attributed to the interpolation of soil moisture points. Lastly, comparison with soil core sampling resulted in a RMSE of 0.0233 m^{3}m^{-3}. In conclusion, soil moisture mapping by GPR appeared very precise, repeatable and in a good agreement with independent soil moisture data.

In chapter 4, a linear approximation of the inverse problem was sufficient to assess the inverted parameter uncertainties (i.e., the soil moisture standard deviation), owing to the low dimensionality of the inverse problem (two parameters). Nevertheless, in case of a larger number of parameters to invert for, the inverse problems could not be reasonably linearly approximated and a Markov Chain Monte Carlo sampling of the parameter space was necessary, as used in chapter 2. This sampling permitted to assess the complete posterior distributions of inverted parameters and to evaluate the cross-correlation between the parameters, therefore allowing for a sensitivity analysis of the parameters to the electromagnetic model. However, it is worth mentioning that this Markov Chain Monte Carlo sampling remains considerably computationally intensive compared to linear methods.

In chapter 5, using the GPR mobile platform, soil moisture was surveyed at five different dates in the same field. These campaigns permitted to reveal spatiotemporal patterns of surface soil moisture with an unprecedented resolution at the field scale. The temporal stability of these patterns were investigated and some locations of the field showed temporal stability of soil moisture, either for the field-average or for the extremes of soil moisture distributions. The intersection of the areas showing the field-average ± 0.02 m^3m^{-3} for each date covered 5 % of the field area whereas the less restrictive criterion based on the average over time of the relative difference of soil moisture to the field-average showed 10 % of the field locations where this difference was below 0.02 m^3m^{-3}. The time-stable soil moisture patterns could be related to topography and might inform about surface hydrologic processes occurring in the field.

Ten soil moisture maps obtained by GPR field campaigns were used in chapter 6 to investigate the effect of the spatial variability of antecedent soil moisture on the runoff response using a distributed hydrologic model. This chapter aimed at knowing which description of soil moisture variability was the more suited for an accurate hydrologic modeling at the field scale. The high sensitivity of antecedent soil moisture spatial variability on runoff response was clearly shown for all field acquisitions. In general, spatially constant antecedent soil moisture conditions resulted in smaller discharges than scenarios exhibiting soil moisture spatial variability. When sorting the soil moisture directly or inversely according to the topographic wetness index (TWI), this delineated the range of possible hydrographs. Stochastic simulations of soil moisture variability, either randomly arranged or spatially-structured, resulted in a wide variability of runoff responses among the stochastic realizations. In the absence of other detailed source of information, organizing the soil moisture pattern accordingly to the TWI appeared to be the best soil moisture modeling method, and this was moderately related to the correlation of measured soil moisture and the TWI itself. This last chapter was particularly appealing for disaggregating (or downscaling) remotely-sensed coarse-scale soil moisture data into fine-scale patterns in a data assimilation framework.

In conclusion, an efficient proximal GPR was applied to field conditions for soil moisture sensing and mapping. The method was found to be accurate and precise, in addition to its high practicability. This tool has an intermediate support scale between invasive sensors and active radar remote sensing, i.e., the antenna footprint is 1.5 meter in diameter. Field measurements were performed with spacings ranging from 2 to 15 meters, but other spacings could be used. More than one thousand of points could be acquired per hour, which resulted in extents covering up to several ha within few hours. Hence, the developed GPR is characterized by an unprecedented scale triplet, showing a high spatial resolution at the field scale. Regarding the processing time, a full-waveform inversion using a one-layered model for surface soil moisture determination takes around 0.5 s on a PC with a single processor, allowing for real-time soil moisture mapping during the acquisition if needed.

Compared to traditional GPR methods (e.g., the ground-wave method), the proposed GPR approach shows larger capacities in information retrieval in terms of accuracy and vertically-varying soil moisture. These larger capacities originate from the full-waveform inversion of ultra-wideband radar data, which inherently increases the information content in the GPR data compared to GPR systems operating in small frequency bandwidths, and from the accurate modeling of the GPR system, which avoids shortcomings in the modeling of the propagation of electromagnetic waves. For field acquisition, the off-ground configuration also permits to use the GPR system in digital soil mapping applications, helping for the mapping of larger areas compared to traditional on-ground GPR systems.

The proposed GPR method has provided new soil moisture measurements in terms of support, resolution and extent scales. It has shown that the spatial variability of surface soil moisture remains important, even if a 1 m^2-support scale is used. Although measurement and modeling errors appeared relatively low (e.g., 0.017 m^3m^{-3} of repetition error in chapter 4), large nugget effects (e.g., 0.04 m^3m^{-3}) were observed and they were explained by unrevealed small-scale ($\sim$ m) spatial variability. Knowing the spatial variability of soil moisture at the intermediate scales between the support and resolution scales may help for elucidating this issue. More generally, when soil moisture measurements are to be compared, for instance between remote sensing and ground-truth measurements, scale gap between support and resolution scales of each instrument should be avoided.

Ground penetrating radar limitations and perspectives

The application of the electromagnetic model to a TDR probe resulted in good retrievals of soil electromagnetic properties. However, it is worth noting that the media that were analyzed by the FDR analysis were simple and that the FDR approach did not outperform the classical TDR approach for determining the dielectric permittivity. The developed FDR modeling approach is theoretically exact in terms of the propagation of the electromagnetic fields and could be used to retrieve the complete profile of soil electromagnetic parameters along the FDR probe. Nevertheless, in practice, this asset may be limited by the narrow frequency bandwidth in which the probe is efficient, thereby limiting the information content in the FDR waveform. In that respect, the design and construction of an optimal probe is particularly important.

In this thesis, the GPR inversion appeared poorly sensitive to the soil electrical conductivity, because of the low sensitivity of the electromagnetic model to the relatively-low conductivity encountered in the study areas. However, in case of more conductive soils, insensitivity of the model to the electrical conductivity may affect the retrieval of soil dielectric permittivity and correlated soil moisture (Giroux and Chouteau, 2010). Electromagnetic induction (EMI) instruments, operating at lower frequency ($\sim$ kHz) are known to be better effective tools for electrical conductivity sensing. One may notice that there is actually a frequency gap in the EMI-GPR sensors in the kHz-MHz frequency range. Knowing that increasing the bandwidth increases the information content, it would be particularly relevant to benefit from a single sensor capable of sensing the dielectric permittivity and electrical conductivity simultaneously.

GPR antenna and soil-antenna interactions effects are accounted for in the electromagnetic modeling of the GPR system for a far-field configuration. This means that the GPR antenna should be placed far enough from the main reflector (e.g., the soil surface) in order to assume a planar propagation of the electromagnetic waves at the antenna reception. For the 200-2000 MHz radar antenna used for field measurements (chapters 3 to 6), the far-field configuration starts at around 1.10 meter above the soil surface, in relation with the antenna dimension. However, at this height, a part of the energy that is reflected from the soil surface is not received by the antenna because of the geometrical spreading of the waves. The modeling of the GPR system in the near-field configuration as initiated in Lambot *et al.* (2010) would permit to lower the antenna and increase the part of the reflected energy sent back to the antenna, thereby increasing the signal-noise ratio. This would permit to increase the depth of penetration of the electromagnetic waves by increasing the information content from the reflection of deeper soil layers.

Concerning the GPR setup, it is worth noting that its components, i.e., the VNA, the GPR antenna and the cable, were not designed for field utilization. Therefore, the development of rugged instruments would facilitate the practicability of the method and may reduce measurements errors. In particular, the calibration of the VNA is known to be sensitive to temperature changes, although this was not observed during fields campaigns. The normal incidence of the GPR waves is also required, while the orientation of the antenna may change during field acquisition.

As discussed in chapter 4, lateral and vertical heterogeneities within the GPR antenna footprint may affect the GPR reflected signal. The absence of lateral heterogeneity at the footprint scale is a strong hypothesis in field conditions and it is still not known how this affect the retrieval of footprint soil moisture. As a result, the unique soil moisture value that is retrieved at the support scale might be different from the arithmetic average of footprint soil moisture. Laboratory and field experiments have to be performed in order to investigate how soil moisture is integrated within the GPR footprint. Forward and inverse modeling of the GPR wave in a discretized 3-D medium could permit to get a complete characterization of heterogeneous media, but it is worth noting that the information content in a single GPR wave may not be sufficient to fully characterize within footprint heterogeneities. Lastly, a smaller support scale may be valuable given the high soil moisture variability at the meter scale. In that respect, modeling the GPR system in a near-field configuration would permit to decrease the height of the GPR antenna, resulting in a decrease of the antenna footprint.

A great issue in the sensing of soil moisture by electromagnetic waves is the depth of characterization (or sampling depth). In case of multi-layered medium configurations in the electromagnetic model, depth-dependent information can be retrieved, as shown in chapters 2 and 3, and the depth of penetration for a particular frequency only depends on the power of the electromagnetic wave in relation with the antenna characteristics. However, for GPR data inversion focused on the surface reflection peak (one-layered model) as used in chapters 4 to 6, the backscattered GPR data that are considered pertain to the air-soil interface only. For the surface reflection method, the depth of characterization d of an electromagnetic wave is proportional to its wavelength λ, that is, the Rayleigh criterion assumes $d = \lambda/8$. The depth of characterization is thus inversely linearly related to the electromagnetic wave frequency and to the square root of the permittivity. Therefore, the depth of characterization increases with decreasing soil moisture and, as a result, is actually varying within a field as a function of soil moisture. This drawback could be surmounted owing to the ultra-wideband GPR data by inverting the GPR data within different frequency ranges according to the soil moisture. According to Jadoon *et al.* (2010a), by comparing the GPR-derived soil moisture with near-surface horizontal TDR measurements, the depth of characterization using the same GPR antenna with the surface reflection data inversion was found to be about 4 cm. Further investigations, combining theoretical and experimental studies, are needed to more precisely determine this depth.

The impact of surface soil roughness on the GPR data was widely discussed in chapter 3. In this thesis, surface roughness interferences and scattering were avoided by operating at sufficiently low frequencies. However, for larger surface roughness, these phenomenons should be taken into account by an appropriate modeling. Proximal radar sensing could be also used for surface roughness characterization, in support to radar remote sensing operating at larger frequencies. Similarly, the effect of vegetation was not addressed in this thesis and field campaigns were performed in fields with few vegetation cover. In order to monitor the soil moisture over the full vegetation period, it would be interesting to deal with GPR measurements over a significant vegetation cover. In that respect, treating the canopy as an additional layer or using Rayleigh scattering approaches as in remote sensing applications should be investigated. Both for surface roughness and vegetation cover issues, proximal GPR research could benefit from the great developments that were achieved in the field of spaceborne radar remote sensing.

According to Huisman *et al.* (2003), one of the main limitations of GPR techniques for soil moisture sensing is the petrophysical relationship used to convert GPR-derived dielectric permittivity into soil moisture values. Nevertheless, during this thesis, the petrophysical relationships that were determined in laboratory and field conditions showed in general good agreements between GPR-derived permittivities and soil moisture determined by volumetric sampling. More appropriate petrophysical models could be used by adding auxiliary information (porosity, texture, etc.). It is worth noting that the petrophysical model parameters could be also optimized in the GPR inversion in order to directly retrieve the soil moisture (Tran *et al.*, submitted).

Perspectives in soil moisture sensing

Mounted on a mobile platform, this proximal GPR was proven to be an efficient tool for digital soil mapping at high resolution. It is worth noting that time-lapse soil moisture measurements can provide insights about soil properties, such as soil structure and hydraulic properties, these latter being dependent upon time-invariant properties such as soil texture. Therefore, high-resolution soil properties could be indirectly mapped using GPR measurements.

It is of particular interest to rely on high-resolution soil properties data for precision agriculture applications (Adamchuk *et al.*, 2004). Information about the spatial variability of soil properties could help for a reasonable application of nutrients to crops in environments facing contamination of soil and water and increasing scarcity of non-renewable resources such as phosphore and potassium. Precision agriculture could also help to reduce input costs or to avoid overdosing of nutrients. High-resolution soil information could be known before agricultural intervention or in real-time during the application of inputs. In order to facilitate the data acquisition, the GPR system could be mounted on agricultural machines on the occasion of usual farming operations. This tool could be also directly used for the optimisation of irrigation systems, allowing for the distribution of the right amount of water to crops in real-time according to the soil wetness.

Despite the huge development in instruments and retrieval algorithms, quantitative remote sensing of soil moisture remains a complicated task. Validation campaigns of remote sensing instruments often require a large number of point-measurements over large areas in a limited time frame, as surface soil moisture evolves rapidly. In that respect, the proposed GPR method could improve high-resolution remote sensing data products, by providing efficient soil moisture mapping, as initiated in Lievens *et al.* (submitted) for RADARSAT-2 and ENVISAT ASAR sensors. In particular, two-layered and profile inversions (chapters 2 and 3) could be of particular interest to differentiate between surface and subsurface soil moisture and to infer the relationships between shallowly-retrieved soil moisture from remote sensing and the root-zone soil moisture (Li and Islam, 2002). Moreover, remote sensing backscattered coefficients could be compared directly with the GPR-derived dielectric permittivity, without the use of petrophysical relationships.

A large number of studies have investigated downscaling or disaggregating of large-scale remotely-sensed soil moisture data for soil moisture characterization at a finer scale (e.g., Merlin *et al.*, 2006). Knowing small-scale spatiotemporal patterns of soil moisture and their relation with terrain attributes or soil information could be used to properly disaggregate soil moisture. Owing to its intermediate scale of characterization, this GPR method could be used for a more accurate downscaling of soil moisture data through the knowledge of temporally-persistent soil moisture patterns (Loew and Mauser, 2008).

So far, a large majority of soil moisture studies at the field scale relied on point-measurements using invasive methods. On the other hand, the huge development in remote sensing of soil moisture techniques resulted in a great number of studies about soil moisture characterization, but at larger scales.

More recently, wireless sensor networks have shown promising perspectives for soil moisture characterization at the field scale, as installed sensors permit to acquire soil moisture data with a considerable temporal resolution. An exciting perspective would be to combine the large temporal resolution of grounded sensors network with the large spatial resolution of the proximal GPR developed in this thesis. As demonstrated in chapter 5, time-lapse measurements using GPR can be used to determine the best locations for grounded sensors in terms of temporal stability. The combination of well-located grounded sensors with occasional GPR field measurements would therefore result in an unprecedented characterization of soil moisture patterns.

Appendices

Bibliography

Adamchuk, V. I., Hummel, J. W., Morgan, M. T., and Upadhyaya, S. K. 2004. On-the-go soil sensors for precision agriculture. Computers and Electronics in Agriculture, 44(1):71–91.

Alumbaugh, D., Chang, P., Paprocki, L., Brainard, J., Glass, R. J., and Rautman, C. A. 2002. Estimating moisture contents in the vadose zone using cross-borehole ground penetrating radar: A study of accuracy and repeatability. Water Resources Research, 38:1309.

Annan, A. P. 2002. GPR - History, Trends, and Future Developments. Subsurface Sensing Technologies and Applications, 3(4):253–270.

Benedetto, A. 2010. Water content evaluation in unsaturated soil using GPR signal analysis in the frequency domain. Journal of Applied Geophysics, 71(1):26–35.

Beven, K. J. and Kirkby, M. J. 1979. A physically based, variable contributing area model of basin hydrology. Hydrological Sciences Bulletin, 24:43–69.

Bikowski, J., van der Kruk, J., Huisman, J. A., Vereecken, H., and Vrugt, J. A. 2010. Inversion and sensitivity analysis of GPR data with waveguide dispersion using Markov Chain Monte Carlo simulation. In *Proceedings of the XIII International Conference on Ground Penetrating Radar*, pages 722–726. Lecce (Italy), 21-25 June 2010.

Binley, A., Winship, P., Middleton, R., Pokar, M., and West, J. 2001. High-resolution characterization of vadose zone dynamics using cross-borehole radar. Water Resources Research, 37(11):2639–2652.

Binley, A., Winship, P., West, L. J., Pokar, M., and Middleton, R. 2002. Seasonal variation of moisture content in unsaturated sandstone inferred from borehole radar and resistivity profiles. Journal of Hydrology, 267(3-4):160–172.

Birchak, J. R., Gardner, C. G., Hipp, J. E., and Victor, J. M. 1974. High dielectric constant microwave probes for sensing soil moisture. Proc. IEEE, 62:93–102.

Blöschl, G. and Sivapalan, M. 1995. Scale Issues in Hydrological Modeling - A Review. Hydrological Processes, 9(3-4):251–290.

Bogena, H., Herbst, M., Huisman, J., Rosenbaum, U., Weuthen, A., and Vereecken, H. 2010. Potential of Wireless Sensor Networks for Measuring Soil Water Content Variability. Vadose Zone Journal, 9:1002–1013.

Bogena, H. R., Huisman, J. A., Oberdoerster, C., and Vereecken, H. 2007. Evaluation of a low-cost soil water content sensor for wireless network applications. Journal of Hydrology, 344(1-2):32–42.

Borgogno, F., D'Odorico, P., Laio, F., and Ridolfi, L. 2010. A stochastic model for vegetation water stress. Ecohydrology, 3(2, Sp. Iss. SI):177–188.

Brocca, L., Melone, F., Moramarco, T., Wagner, W., Naeimi, V., Bartalis, Z., and Hasenauer, S. 2010. Improving runoff prediction through the assimilation of the ASCAT soil moisture product. Hydrology and Earth System Sciences, 14(10):1881–1893.

Brocca, L., Morbidelli, R., Melone, F., and Moramarco, T. 2007. Soil moisture spatial variability in experimental areas of central Italy. Journal of Hydrology, 333(2-4):356–373.

Brocca, L., Melone, F., Moramarco, T., and Morbidelli, R. 2009. Soil moisture temporal stability over experimental areas in Central Italy. Geoderma, 148(3-4):364–374.

Bronstert, A. and Bardossy, A. 1999. The role of spatial variability of soil moisture for modelling surface runoff generation at the small catchment scale. Hydrology and Earth System Sciences, 3(4):505–516.

Campbell, G. S., Calissendorff, C., and Williams, J. H. 1991. Probe for measuring soil specific-heat using a heat-pulse method. Soil Science Society of America Journal, 55(1):291–293.

Campbell, J. E. 1990. Dielectric properties and influence of conductivity in soils at one to fifty megahertz. Soil Science Society of America Journal, 54:332–341.

Capehart, W. J. and Carlson, T. N. 1997. Decoupling of surface and near-surface soil water content: A remote sensing perspective. Water Resources Research, 33(6):1383–1395.

Castillo, V. M., Gomez-Plaza, A., and Martinez-Mena, M. 2003. The role of antecedent soil water content in the runoff response of semiarid catchments: a simulation approach. Journal of Hydrology, 284(1-4):114–130.

Ceballos, A., Scipal, K., Wagner, W., and Martinez-Fernandez, J. 2005. Validation of ERS scatterometer-derived soil moisture data in the central part of the Duero Basin, Spain. Hydrological Processes, 19(8):1549–1566.

Chanzy, A., Tarussov, A., Judge, A., and Bonn, F. 1996. Soil water content determination using digital ground penetrating radar. Soil Science Society of America Journal, 60:1318–1326.

Chung, C. C. and Lin, C. P. 2009. Apparent Dielectric Constant and Effective Frequency of TDR Measurements: Influencing Factors and Comparison. Vadose Zone Journal, 8(3):548–556.

Crow, W. T. and Ryu, D. 2009. A new data assimilation approach for improving runoff prediction using remotely-sensed soil moisture retrievals. Hydrology and Earth System Sciences, 13(1):1–16.

Crow, W. T., Wood, E. F., and Dubayah, R. 2000. Potential for downscaling soil moisture maps derived from spaceborne imaging radar data. Journal of Geophysical Research - Atmospheres, 105(D2):2203–2212.

Das, N. N. and Mohanty, B. P. 2006. Root zone soil moisture assessment using remote sensing and vadose zone modeling. Vadose Zone Journal, 5(1):296–307.

De Lannoy, G. J., Verhoest, N. E., Houser, P. R., Gish, T. J., and Van Meirvenne, M. 2006. Spatial and temporal characteristics of soil moisture in an intensively monitored agricultural field (OPE3). Journal of Hydrology, 331(3-4):719–730.

Dobson, M. C., Ulaby, F. F., Hallikainen, M. T., and El-Rayes, M. A. 1985. Microwave dielectric behavior of wet soil - Part II: Dielectric mixing models. IEEE Transactions on Geoscience and Remote Sensing, 23:35–46.

D'Odorico, P., Laio, F., Porporato, A., and Rodriguez-Iturbe, I. 2003. Hydrologic controls on soil carbon and nitrogen cycles. II. A case study. Advances in Water Resources, 26(1):59–70.

Doolittle, J. A., Jenkinson, B., Hopkins, D., Ulmer, M., and Tuttle, W. 2006. Hydropedological investigations with ground-penetrating radar (GPR): Estimating water-table depths and local ground-water flow pattern in areas of coarse-textured soils. Geoderma, 131(3-4):317–329.

D'Urso, G. and Minacapilli, M. 2006. A semi-empirical approach for surface soil water content estimation from radar data without a-priori information on surface roughness. Journal of Hydrology, 321(1-4):297–310.

Ernst, J. R., Maurer, H., Green, A. G., and Holliger, K. 2007. Full-waveform inversion of crosshole radar data based on 2-D finite-difference time-domain solutions of Maxwell's equations. IEEE Transactions on Geoscience and Remote Sensing, 45(9):2807–2828.

ESA. 2002. Mission Objectives and Scientific Requirements of the Soil Moisture and Ocean Salinity (SMOS) Mission, Version 5. Technical report, ESA.

Evett, S. and Parkin, G. 2005. Advances in soil water content sensing: The continuing maturation of technology and theory. Vadose Zone Journal, 4(4):986–991.

Famiglietti, J. S., Ryu, D., Berg, A. A., Rodell, M., and Jackson, T. J. 2008. Field observations of soil moisture variability across scales. Water Resources Research, 44:W01423.

Famiglietti, J. S., Rudnicki, J. W., and Rodell, M. 1998. Variability in surface moisture content along a hillslope transect: Rattlesnake Hill, Texas. Journal of Hydrology, 210(1-4):259–281.

Feng, W., Lin, C. P., Deschamps, R. J., and Drnevich, V. P. 1999. Theroretical model of a multisection time domain reflectometry measurement system. Water Ressources Research, 35:2321–2331.

Fitzjohn, C., Ternan, J. L., and Williams, A. G. 1998. Soil moisture variability in a semi-arid gully catchment: implications for runoff and erosion control. Catena, 32(1):55–70.

Galagedara, L. W., Parkin, G. W., Redman, J. D., P., and Endres, A. L. 2005. Field studies of the GPR ground wave method for estimating soil water content during irrigation and drainage. Journal of Hydrology, 301:182–197.

Garrido, F., Ghodrati, M., and Chendorain, M. 1999. Small-scale measurement of soil water content using a fiber optic sensor. Soil Science Society Of America Journal, 63(6):1505–1512.

Giese, K. and Tiemann, R. 1975. Determination of the complex permittivity from thin-sample time domain reflectometry. Improved analysis of the step response waveform. Advances in Molecular Relaxation Processes, 7(1):45–59.

Giroux, B. and Chouteau, M. 2010. Quantitative analysis of water-content estimation errors using ground-penetrating radar data and a low-loss approximation. Geophysics, 75(4):WA241–WA249.

Güntner, A., Seibert, J., and Uhlenbrook, S. 2004. Modeling spatial patterns of saturated areas: An evaluation of different terrain indices. Water Resources Research, 40(5):W05114.

Grayson, R. B. and Western, A. W. 1998. Towards areal estimation of soil water content from point measurements: time and space stability of mean response. Journal of Hydrology, 207(1-2):68–82.

Grayson, R. B., Western, A. W., Chiew, F. H. S., and Blöschl, G. 1997. Preferred states in spatial soil moisture patterns: Local and nonlocal controls. Water Resources Research, 33(12):2897–2908.

Green, W. and Ampt, G. 1911. Studies on soil physics: 1, flow of air and water through soils. Journal of Agricultural Science, 4:1–24.

Grote, K., Hubbard, S. S., and Rubin, Y. 2003. Field-scale estimation of volumetric water content using GPR ground wave techniques. Water Resources Research, 39(11):1321.

Grote, K., Anger, C., Kelly, B., Hubbard, S., and Rubin, Y. 2010. Characterization of Soil Water Content Variability and Soil Texture using GPR Groundwave Techniques. Journal of Environmental and Engineering Geophysics, 15(3, Sp. Iss. SI):93–110.

Guber, A. K., Gish, T. J., Pachepsky, Y. A., Van Genuchten, M. T., Daughtry, C. S. T., Nicholson, T. J., and Cady, R. E. 2008. Temporal stability in soil water content patterns across agricultural fields. CATENA, 73(1):125–133.

Hawley, M. E., Jackson, T. J., and McCuen, R. H. 1983. Surface soil-moisture variation on small agricultural watersheds. Journal of Hydrology, 62(1-4):179–200.

Heimovaara, T. J. 1993. *Time domain reflectometry in soil science: theoretical backgrounds, measurements and models*. Ph.D. thesis, Amsterdam University, Amsterdam, The Netherlands.

Heimovaara, T. J. 1994. Frequency domain analysis of time domain reflectometry waveforms, 1, Measurements of the complex dielectric permittivity of soils. Water Resources Research, 30(2):189–199.

Heimovaara, T. J. and Bouten, W. 1990. A Computer-Controlled 36-Channel Time Domain Reflectometry System for Monitoring Soil Water Contents. Water Resources Research, 26(10):2311–2316.

Heimovaara, T. J., Huisman, J., Vrugt, J. A., and Bouten, W. 2004. Obtaining the Spatial Distribution of Water Content along a TDR Probe Using the SCEM-UA Bayesian Inverse Modeling Scheme. Vadose Zone Journal, 3:1128–1145.

Herbst, M., Prolingheuer, N., Graf, A., Huisman, J. A., Weihermueller, L., and Vanderborght, J. 2009. Characterization and Understanding of Bare Soil Respiration Spatial Variability at Plot Scale. Vadose Zone Journal, 8(3):762–771.

Herkelrath, W. N., Hamburg, S. P., and Murphy, F. 1991. Automatic, real-time monitoring of soil moisture in a remote field area with time domain reflectometry. Water Resources Research, 27(5):857–864.

Hook, W. R. and Livingston, N. J. 1996. Errors in converting time domain reflectometry measurements of propagation velocity to estimates of soil water content. Soil Science Society of America Journal, 60:35–41.

Houser, P. R., Shuttleworth, W. J., Famiglietti, J. S., Gupta, H. V., Syed, K. H., and Goodrich, D. C. 1998. Integration of soil moisture remote sensing and hydrologic modeling using data assimilation. Water Resources Research, 34(12):3405–3420.

Hu, W., Shao, M., Han, F., Reichardt, K., and Tan, J. 2010. Watershed scale temporal stability of soil water content. Geoderma, 158(3-4):181–198.

Huisman, J. A. and Bouten, W. 2003. Accuracy and reproducibility of measuring soil water content with the ground wave of ground-penetrating radar. Journal of Environmental and Engineering Geophysics, 8(2):65–73.

Huisman, J. A., Sperl, C., Bouten, W., and Verstraten, J. M. 2001. Soil water content measurements at different scales: accuracy of time domain reflectometry and ground penetrating radar. Journal of Hydrology, 245:48–58.

Huisman, J. A., Snepvangers, J. J. J. C., Bouten, W., and Heuvelink, G. B. M. 2002a. Mapping spatial variation in surface soil water content: comparison of ground-penetrating radar and time domain reflectometry. Journal of Hydrology, 269:194–207.

Huisman, J. A., Weerts, A. H., Heimovaara, T. J., and Bouten, W. 2002b. Comparison of travel time analysis and inverse modeling for soil water content determination with time domain reflectometry. Water Resources Research, 38(6):1224.

Huisman, J. A., Hubbard, S. S., Redman, J. D., and Annan, A. P. 2003. Measuring soil water content with ground penetrating radar: A review. Vadose Zone Journal, 2:476–491.

Huisman, J. A., Bouten, W., and Vrugt, J. A. 2004. Accuracy of frequency domain analysis scenarios for the determination of complex dielectric permittivity. Water Resources Research, 40.

Huisman, J. A., Lin, C. P., Weihermüller, L., and Vereecken, H. 2008. Accuracy of bulk electrical conductivity measurements with time domain reflectometry. Vadose Zone Journal, 7(2):426–433.

Hupet, F. and Vanclooster, M. 2002. Intraseasonal dynamics of soil moisture variability within a small agricultural maize cropped field. Journal of Hydrology, 261(1-4):86–101.

Hupet, F., Lambot, S., Javaux, M., and Vanclooster, M. 2002. On the identification of macroscopic root water uptake parameters from soil water content observations. Water Resources Research, 38(12):1556, doi:10.1029/2001WR001224.

Huyer, W. and Neumaier, A. 1999. Global optimization by multilevel coordinate search. Journal of Global Optimization, 14(4):331–355.

Jackson, T. J., Schmugge, J., and Engman, E. T. 1996. Remote sensing applications to hydrology: soil moisture. Hydrological Sciences, 41(4):517–530.

Jacob, R. W. and Hermance, J. F. 2004. Assessing the precision of GPR velocity and vertical two-way travel time estimates. Journal of Environmental and Engineering Geophysics, 9(3):143–153.

Jacobs, J. M., Mohanty, B. P., Hsu, E. C., and Miller, D. 2004. SMEX02: Field scale variability, time stability and similarity of soil moisture. Remote Sensing of Environment, 92(4):436–446.

Jadoon, K. Z., Lambot, S., Scharnagl, B., van der Kruk, J., Slob, E., and Vereecken, H. 2010a. Quantifying field-scale surface soil water content from proximal GPR signal inversion in the time domain. Near Surface Geophysics, 8:483–491.

Jadoon, K. Z., Lambot, S., Slob, E., and Vereecken, H. 2010b. Investigation of the frequency dependent antenna transfer functions and phase center position for modeling off-ground GPR. IEEE Transactions on Geoscience and Remote Sensing, In press.

Jonard, F., Weihermüller, L., Jadoon, K., Schwank, M., Vereecken, H., and Lambot, S. 2010. Mapping field-scale soil moisture with L-band radiometer and ground-penetrating radar over bare soil. IEEE Transactions on Geoscience and Remote Sensing, In press.

Kao, C.-P., Li, J., Wang, Y., Xing, H., and Liu, C. R. 2007. Measurement of layer thickness and permittivity using a new multilayer model from GPR data. IEEE Transactions on Geoscience and Remote Sensing, 45(8):2463–2470.

Kelleners, T. J., Robinson, D. A., Shouse, P. J., Ayars, J. E., and Skaggs, T. H. 2005. Frequency dependence of the complex permittivity and its impact on dielectric sensor calibration in soils. Soil Science Society of America Journal, 69(1):67–76.

Kool, J. B. and Parker, J. C. 1988. Analysis of the Inverse Problem for Transient Unsaturated Flow. Water Resources Research, 24:817–830.

Kuo, W. L., Steenhuis, T. S., McCulloch, C. E., Mohler, C. L., Weinstein, D. A., DeGloria, S. D., and Swaney, D. P. 1999. Effect of grid size on runoff and soil moisture for a variable-source-area hydrology model. Water Resources Research, 35(11):3419–3428.

Lagarias, J. C., Reeds, J. A., Wright, M. H., and Wright, P. E. 1998. Convergence properties of the Nelder-Mead Simplex method in low dimensions. Siam Journal on Optimization, 9(1):112–147.

Laloy, E. and Bielders, C. L. 2008. Plot scale continuous modelling of runoff in a maize cropping system with dynamic soil, surface properties. Journal of Hydrology, 349(3-4):455–469.

Laloy, E. and Bielders, C. L. 2009. Modelling intercrop management impact on runoff and erosion in a continuous maize cropping system: Part I. Model description, global sensitivity analysis and Bayesian estimation of parameter identifiability. European Journal of Soil Science, 60(6):1005–1021.

Laloy, E., Fasbender, D., and Bielders, C. L. 2010. Parameter optimization and uncertainty analysis for plot-scale continuous modeling of runoff using a formal Bayesian approach. Journal of Hydrology, 380(1-2):82–93.

Lambot, S., Javaux, M., Hupet, F., and Vanclooster, M. 2002. A global multilevel coordinate search procedure for estimating the unsaturated soil hydraulic properties. Water Resources Research, 38(11):1224.

Lambot, S., Rhebergen, J., van den Bosch, I., Slob, E. C., and Vanclooster, M. 2004a. Measuring the soil water content profile of a sandy soil with an off-ground monostatic ground penetrating radar. Vadose Zone Journal, 3(4):1063–1071.

Lambot, S., Slob, E. C., van den Bosch, I., Stockbroeckx, B., and Vanclooster, M. 2004b. Modeling of ground-penetrating radar for accurate characterization of subsurface electric properties. IEEE Transactions on Geoscience and Remote Sensing, 42:2555–2568.

Lambot, S., van den Bosch, I., Stockbroeckx, B., Druyts, P., Vanclooster, M., and Slob, E. C. 2005. Frequency dependence of the soil electromagnetic properties derived from ground-penetrating radar signal inversion. Subsurface Sensing Technologies and Applications, 6:73–87.

Lambot, S., Antoine, M., Vanclooster, M., and Slob, E. C. 2006a. Effect of soil roughness on the inversion of off-ground monostatic GPR signal for noninvasive quantification of soil properties. Water Resources Research, 42:W03403.

Lambot, S., Weihermüller, L., Huisman, J. A., Vereecken, H., Vanclooster, M., and Slob, E. C. 2006b. Analysis of air-launched ground-penetrating radar techniques to measure the soil surface water content. Water Resources Research, 42:W11403.

Lambot, S., Slob, E., and Vereecken, H. 2007. Fast evaluation of zero-offset Green's function for layered media with application to ground-penetrating radar. Geophysical Research Letters, 34:L21405, doi:10.1029/2007GL031459.

Lambot, S., Binley, A., Slob, E. C., and Hubbard, S. 2008a. Ground penetrating radar in hydrogeophysics. Vadose Zone Journal, 7(1):137–139.

Lambot, S., Slob, E. C., Chavarro, D., Lubczynski, M., and Vereecken, H. 2008b. Measuring soil surface water content in irrigated areas of southern Tunisia using full-waveform inversion of proximal GPR data. Near Surface Geophysics, 6:403–410.

Lambot, S., André, F., Jadoon, K., Slob, E., and Vereecken, H. 2010. Full-waveform modeling of ground-coupled GPR antennas for wave propagation in multilayered media: the problem solved ? In *13th International Conference on Ground Penetrating Radar (GPR 2010), 5 pp.*.

Lasne, Y., Paillou, P., Freeman, A., Farr, T., McDonald, K. C., Ruffie, G., Malezieux, J.-M., Chapman, B., and Demontoux, F. 2008. Effect of salinity on the dielectric properties of geological materials: Implication for soil moisture detection by means of radar remote sensing. IEEE Transactions on Geoscience and Remote Sensing, 46(6):1674–1688.

Ledieu, J., De Ridder, P., De Clercq, P., and Dautrebande, S. 1986. A method of measuring soil moisture by time domain reflectometry. Journal of Hydrology, 88:319–328.

Li, J. K. and Islam, S. 2002. Estimation of root zone soil moisture and surface fluxes partitioning using near surface soil moisture measurements. Journal of Hydrology, 259(1-4):1–14.

Lievens, H., Heitz, S., Minet, J., Lambot, S., Vanclooster, M., Matgen, P., Hissler, C., Hoffmann, L., and Verhoest, N. E. C. submitted. Mapping within-field soil moisture variability with high-resolution C-band SAR and GPR. Canadian Journal of Remote Sensing.

Lin, C.-P. 2003. Frequency Domain versus Travel Time Analyses of TDR Waveforms for Soil Moisture Measurements. Soil Science Society of America Journal, 67:720–729.

Lin, C. P., Chung, C. C., Huisman, J. A., and Tang, S. H. 2008. Clarification and calibration of reflection coefficient for electrical conductivity measurement by time domain reflectometry. Soil Science Society of America Journal, 72(4):1033–1040.

Loew, A. and Mauser, W. 2008. On the disaggregation of passive microwave soil moisture data using a priori knowledge of temporally persistent soil moisture fields. IEEE Transactions on Geoscience and Remote Sensing, 46:819–834.

Logsdon, S. D. 2005. Soil dielectric spectra from vector network analyzer data. Soil Science Society of America Journal, 69(4):983–989.

Looms, M. C., Jensen, K. H., Binley, A., and Nielsen, L. 2008. Monitoring unsaturated flow and transport using cross-borehole geophysical methods. Vadose Zone Journal, 7(1):227–237.

Lunt, I. A., Hubbard, S. S., and Rubin, Y. 2005. Soil moisture content estimation using ground-penetrating radar reflection data. Journal of Hydrology, 307(1-4):254–269.

Marquardt, D. W. 1963. An algorithm for least-squares estimation of nonlinear parameters. Journal of the Society for Industrial and Applied Mathematics, 11:431–441.

Martinez, G., Vanderlinden, K., Giráldezb, J. V., Espejoa, A. J., and Muriela, J. L. 2010. Field-scale soil moisture pattern mapping using electromagnetic induction. Vadose Zone Journal, 9:871–881.

Mattei, E., De Santis, A., Di Matteo, A., Pettinelli, E., and Vannaroni, G. 2005. Time domain reflectometry of glass beads/magnetite mixtures: A time and frequency domain study. Applied Physics Letters, 86(22).

Mattei, E., De Santis, A., Di Matteo, A., Pettinelli, E., and Vannaroni, G. 2008. Electromagnetic Parameters of Dielectric and Magnetic Mixtures Evaluated by Time-Domain Reflectometry. IEEE Geoscience and Remote Sensing Letters, 5(4):730–734.

Meissner, T. and Wentz, F. J. 2004. The complex dielectric constant of pure and sea water from microwave satellite observations. IEEE Transcations on Geoscience and Remote Sensing, 42(9):1836–1849.

Merlin, O., Chehbouni, A., Boulet, G., and Kerr, Y. 2006. Assimilation of disaggregated microwave soil moisture into a hydrologic model using coarse-scale meteorological data. Journal of Hydrometeorology, 7(6):1308–1322.

Merz, B. and Bardossy, A. 1998. Effect of spatial variability on the rainfall runoff process in a small loess catchment. Journal of Hydrology, 212:304–317.

Merz, B. and Plate, E. J. 1997. An analysis of the effects of spatial variability of soil and soil moisture on runoff. Water Resources Research, 33(12):2909–2922.

Michalski, K. A. and Mosig, J. R. 1997. Multilayered media Green's functions in integral equation formulations. IEEE Transactions on Antennas and Propagation, 45(3):508–519.

Michot, D., Benderitter, Y., Dorigny, A., Nicoullaud, B., King, D., and Tabbagh, A. 2003. Spatial and temporal monitoring of soil water content with an irrigated corn crop cover using surface electrical resistivity tomography. Water Resources Research, 39(5).

Minet, J., Lambot, S., Slob, E., and Vanclooster, M. 2010a. Soil surface water content estimation by full-waveform GPR signal inversion in the presence of thin layers. IEEE Transactions on Geoscience and Remote Sensing, 48:1138 – 1150.

Minet, J., Patriarca, C., Slob, E., Vanclooster, M., and Lambot, S. 2010b. Characterization of layered media using full-waveform inversion of proximal GPR data. In *Proceedings of the URSI International Symposium on Electromagnetic Theory - EMTS2010*. Berlin (Germany), 16-19 August 2010.

Minet, J., Wahyudi, A., Bogaert, P., Vanclooster, M., and Lambot, S. 2011. Mapping shallow soil moisture profiles at the field scale using full-waveform inversion of ground penetrating radar data. Geoderma, 161:225–237.

Minet, J., Bogaert, P., Vanclooster, M., and Lambot, S. submitted. Validation of ground penetrating radar full-waveform inversion for field scale soil moisture mapping. Journal of Hydrology.

Moghadas, D., André, F., Vereecken, H., and Lambot, S. 2010. Efficient loop antenna modeling for zero-offset, off-ground electromagnetic induction in multilayered media. Geophysics, 75(4).

Mohanty, B. P. and Skaggs, T. H. 2001. Spatio-temporal evolution and time-stable characteristics of soil moisture within remote sensing footprints with varying soil, slope, and vegetation. Advances in Water Resources, 24(9-10):1051–1067.

Noborio, K. 2001. Measurement of soil water content and electrical conductivity by time domain reflectometry: a review. Computers and Electronics in Agriculture, 31:213–237.

Noto, L. V., Ivanov, V. Y., Bras, R. L., and Vivoni, E. R. 2008. Effects of initialization on response of a fully-distributed hydrologic model. Journal of Hydrology, 352(1-2):107–125.

Oden, C. P., Olhoeft, G. R., Wright, D. L., and Powers, M. H. 2008. Measuring the electrical properties of soil using a calibrated ground-coupled GPR system. Vadose Zone Journal, 7(1):171–183.

Pauwels, V. R. N., Hoeben, R., Verhoest, N. E. C., and De Troch, F. P. 2001. The importance of the spatial patterns of remotely sensed soil moisture in the improvement of discharge predictions for small-scale basins through data assimilation. Journal of Hydrology, 251(1-2):88–102.

Pellenq, J., Kalma, J., Boulet, G., Saulnier, G., Wooldridge, S., Kerr, Y., and Chehbouni, A. 2003. A disaggregation scheme for soil moisture based on topography and soil depth. Journal of Hydrology, 276(1-4):112–127.

Pepin, S., Livingston, N. J., and Hook, W. R. 1995. Temperature-dependent measurement errors in time-domain reflectometry determinations of soilwater. Soil Science Society of America Journal, 59(1):38–43.

Porporato, A., D'Odorico, P., Laio, F., and Rodriguez-Iturbe, I. 2003. Hydrologic controls on soil carbon and nitrogen cycles. I. Modeling scheme. Advances in Water Resources, 26(1):45–58.

Quinn, P. F., Beven, K. J., and Lamb, R. 1995. The LN(A/tan-BETA) index - How to calculate it and how to use it within the TOPMODEL framework. Hydrological Processes, 9(2):161–182.

Redman, J. D., Davis, J. L., Galagedara, L. W., and Parkin, G. W. 2002. Field studies of GPR air launched surface reflectivity measurements of soil water content. In Koppenjan, S. and Hua, L., editors, *Proceedings of the Ninth International Conference on Ground Penetrating Radar*, pages SPIE 4758:156–161. Santa Barbara, California, USA.

Rhoades, J. D., Raats, P. A. C., and Prather, R. J. 1976. Effects of liquid-phase electrical conductivity, water content, and surface conductivity on bulk soil electrical conductivity. Soil Science Society of America Journal, 40:651–655.

Robinson, D. A., Jones, S. B., Wraith, J. M., Or, D., and Friedman, S. P. 2003. A review of advances in dielectric and electrical conductivity measurement in soils using time domain reflectometry. Vadose Zone Journal, 2:444–475.

Robinson, D. A., Bell, J. P., and Batchelor, C. H. 1994. Influence of iron minerals on the determination of soil-water content using dielectric techniques. Journal of Hydrology, 161(1-4):169–180.

Robinson, D. A., Kelleners, T. J., Cooper, J. D., Gardner, C. M. K., Wilson, P., Lebron, I., and Logsdon, S. 2005. Evaluation of a capacitance probe frequency response model accounting for bulk electrical conductivity: Comparison with TDR and network analyzer measurements. Vadose Zone Journal, 4(4):992–1003.

Robinson, D. A., Binley, A., Crook, N., Day-Lewis, F. D., Ferre, T. P. A., Grauch, V. J. S., Knight, R., Knoll, M., Lakshmi, V., Miller, R., Nyquist, J., Pellerin, L., Singha, K., and Slater, L. 2008a. Advancing process-based watershed hydrological research using near-surface geophysics: a vision for, and review of, electrical and magnetic geophysical methods. Hydrological Processes, 22(18):3604–3635.

Robinson, D. A., Campbell, C. S., Hopmans, J. W., Hornbuckle, B. K., Jones, S. B., Knight, R., Ogden, F., Selker, J., and Wendroth, O. 2008b. Soil moisture measurement for ecological and hydrological watershed-scale observatories: A review. Vadose Zone Journal, 7(1):358–389.

Roth, C. H., Malicki, M. A., and Plagge, R. 1992. Empirical-evaluation of the relationship between soil dielectric-constant and volumetric water-content as the basis for calibrating soil-moisture measurements by TDR. Journal of Soil Science, 43(1):1–13.

Sambuelli, L. 2009. Uncertainty propagation using some common mixing rules for the modelling and interpretation of electromagnetic data. Near Surface Geophysics, 7(4, Sp. Iss. SI):285–296.

Savabi, M. and Williams, J. 1995. Water balance and percolation. In: Flanagan, D.C., Nearing, M.A. (Eds.), USDA - Water Erosion Prediction Project: Hillslope profile model documentation (Chapter 5). Nserl report no. 2. Technical report, USDA-ARS National Soil Erosion Research Laboratory, West Lafayette, Indiana.

Schaap, M. G., Robinson, D., Friedman, S., and Lazar, A. 2003. Measurement and modeling of the TDR signal propagation through layered dielectric media. Soil Science Society of America Journal, 67:1113:1121.

Schumann, G., Lunt, D. J., Valdes, P. J., de Jeu, R. A. M., Scipal, K., and Bates, P. D. 2009. Assessment of soil moisture fields from imperfect climate models with uncertain satellite observations. Hydrology and Earth System Sciences, 13(9):1545–1553.

Seibert, J. and McGlynn, B. L. 2007. A new triangular multiple flow direction algorithm for computing upslope areas from gridded digital elevation models. Water Resources Research, 43(4):W04501.

Seneviratne, S. I., Corti, T., Davin, E. L., Hirschi, M., Jaeger, E. B., Lehner, I., Orlowsky, B., and Teuling, A. J. 2010. Investigating soil moisture-climate interactions in a changing climate: A review. Earth-Science Reviews, 99(3-4):125–161.

Serbin, G. and Or, D. 2003. Near-surface water content measurements using horn antenna radar: methodology and overview. Vadose Zone Journal, 2:500–510.

Serbin, G. and Or, D. 2004. Ground-penetrating radar measurement of soil water content dynamics using a suspended horn antenna. IEEE Transactions on Geoscience and Remote Sensing, 42:1695–1705.

Serbin, G. and Or, D. 2005. Ground-penetrating radar measurement of crop and surface water content dynamics. Remote Sensing of Environment, 96:119–134.

Shuai, X., Wendroth, O., Lu, C., and Ray, C. 2009. Reducing the Complexity of Inverse Analysis of Time Domain Reflectometry Waveforms. Soil Science Society Of America Journal, 73(1):28–36.

Sihvola, A. H. and Kong, J. A. 1988. Effective Permittivity of dielectric mixtures. IEEE Transactions on Geoscience and Remote Sensing, 26(4):420–429.

Slob, E., Sato, M., and Olhoeft, G. 2010. Surface and borehole ground-penetrating-radar developments. Geophysics, 75(5):A103–A120.

Slob, E. C. and Fokkema, J. 2002. Coupling effects of two electric dipoles on an interface. Radio Science, 37(5):1073, doi:10.1029/2001RS2529.

Sørensen, R., Zinko, U., and Seibert, J. 2006. On the calculation of the topographic wetness index: evaluation of different methods based on field observations. Hydrology and Earth System Sciences, 10(1):101–112.

Steelman, C. M. and Endres, A. L. 2010. An examination of direct ground wave soil moisture monitoring over an annual cycle of soil conditions. Water Resources Research, 46.

Steelman, C. M. and Endres, A. L. 2010. Comparison of petrophysical relationships for soil moisture estimation using GPR ground waves. Vadose Zone Journal, In press.

Stevens, A., van Wesemael, B., Bartholomeus, H., Rosillon, D., Tychon, B., and Ben-Dor, E. 2008. Laboratory, field and airborne spectroscopy for monitoring organic carbon content in agricultural soils. Geoderma, 144(1-2):395–404.

Stillman, D. and Olhoeft, G. 2008. Frequency and temperature dependence in electromagnetic properties of Martian analog minerals. Journal of Geophysical Research - Planets, 113(E9).

Strobbia, C. and Cassiani, G. 2007. Multilayer ground-penetrating radar guided waves in shallow soil layers for estimating soil water content. Geophysics, 72(4):J17–J29.

Sun, Z. J., Young, G. D., McFarlane, R. A., and Chambers, B. M. 2000. The effect of soil electrical conductivity on moisture determination using time-domain reflectometry in sandy soil. Canadian Journal of Soil Science, 80(1):13–22.

Tarboton, D. 1997. A new method for the determination of flow directions and upslope areas in grid digital elevation models. Water Resources Research, 33(2):309–319.

Topp, G. C., Davis, J. L., and Annan, A. P. 1980. Electromagnetic Determination of Soil Water Content: Measurements in Coaxial Transmission Lines. Water Resources Research, 16:574–582.

Topp, G. C., Davis, J. L., and Annan, A. P. 2003. The Early Development of TDR for Soil Measurements. Vadose Zone Journal, 2:492–499.

Tran, A. P., Ardekani Mahmouzadeh, M. R., and Lambot, S. submitted. Coupling of Soil Mixing Models with full-wave Ground-Penetrating Radar Signal Inversion to Study the Frequency Dependence of the Sand Conductivity and Permittivity. Geophysical Research Letters.

Vachaud, G., Passerat de Silans, A., Balabanis, P., and Vauclin, M. 1985. Temporal stability of spatially measured soil-water probability density function. Soil Science Society Of America Journal, 49(4):822–828.

van Dam, R. L., Schlager, W., Dekkers, M. J., and Huisman, J. A. 2002. Iron oxides as a cause of GPR reflections. Geophysics, 67(2):536–545.

van der Kruk, J. 2006. Properties of surface waveguides derived from inversion of fundamental and higher mode dispersive GPR data. IEEE Transactions on Geoscience and Remote Sensing, 44(10):2908–2915.

van der Kruk, J., Arcone, S. A., and Liu, L. 2007. Fundamental and higher mode inversion of dispersed GPR waves propagating in an ice layer. IEEE Transactions on Geoscience and Remote Sensing, 45(8):2483–2491.

van der Kruk, J., Jacob, R. W., and Vereecken, H. 2010. Properties of precipitation-induced multilayer surface waveguides derived from inversion of dispersive TE and TM GPR data. Geophysics, 75(4):WA263–WA273.

van Genuchten, M. T. 1980. A closed-form equation for predicting the hydraulic conductivity of unsaturated soils. Soil Science Society of America Journal, 44:892–898.

Van Orshoven, J. and Vandenbroucke, D. 1993. Guide de l'utilisateur d'AARDEWERK, base de données pédologiques, Institute for land and water management, K.U. Leuven, Leuven, Belgium. Technical report.

Vereecken, H., Maes, J., Feyen, J., and Darius, P. 1989. Estimating the soil-moisture retention characteristic from texture, bulk-density, and carbon content. Soil Science, 148(6):389–403.

Vereecken, H., Kamai, T., Harter, T., Kasteel, R., Hopmans, J., and Vanderborght, J. 2007. Explaining soil moisture variability as a function of mean soil moisture: a stochastic unsaturated flow perspective. Geophysical Research Letters, 34(22):L22402–1–6.

Vereecken, H., Huisman, J. A., Bogena, H., Vanderborght, J., Vrugt, J. A., and Hopmans, J. W. 2008. On the value of soil moisture measurements in vadose zone hydrology: A review. Water Resources Research, 44:W00D06.

Verhoest, N. E. C., Lievens, H., Wagner, W., Alvarez-Mozos, J., Moran, M. S., and Mattia, F. 2008. On the soil roughness parameterization problem in soil moisture retrieval of bare surfaces from synthetic aperture radar. Sensors, 8(7):4213–4248.

Vrugt, J. A., ter Braak, C. J. F., Diks, C. G. H., Robinson, B. A., Hyman, J. M., and Higdon, D. 2009. Accelerating Markov Chain Monte Carlo Simulation by Differential Evolution with Self-Adaptive Randomized Subspace Sampling. International Journal of Nonlinear Sciences and Numerical Simulation, 10(3):273–290.

Wagner, W., Lemoine, G., and Rott, H. 1999. A method for estimating soil moisture from ERS scatterometer and soil data. Remote Sensing of Environment, 70(2):191–207.

Wagner, W., Blöschl, G., Pampaloni, P., Calvet, J. C., Bizzarri, B., Wigneron, J. P., and Kerr, Y. 2007. Operational readiness of microwave remote sensing of soil moisture for hydrologic applications. Nordic Hydrology, 38(1):1–20.

Weerts, A. H., Huisman, J. A., and Bouten, W. 2001. Information content of time domain reflectometry waveforms. Water Resources Research, 37:1291–1299.

Weihermüller, L., Huisman, J. A., Lambot, S., Herbst, M., and Vereecken, H. 2007. Mapping the spatial variation of soil water content at the field scale with different ground penetrating radar techniques. Journal of Hydrology, 340:205–216.

Wendroth, O., Pohl, W., Koszinski, S., Rogasik, H., Ritsema, C. J., and Nielsen, D. R. 1999. Spatio-temporal patterns and covariance structures of soil water status in two northeast German field sites. Journal of Hydrology, 215(1-4):38–58.

West, L. J., Handley, K., Huang, Y., and Pokar, M. 2003. Radar frequency dielectric dispersion in sandstone: Implications for determination of moisture and clay content. Water Resources Research, 39(2):1026.

Western, A., Grayson, R., Blöschl, G., and Wilson, D. 2003. *Spatial Variability of Soil Moisture and Its Implications for scaling*, chapter 8, pages 119–142. CRC PRESS.

Western, A. W., Blöschl, G., and Grayson, R. B. 1998. Geostatistical characterisation of soil moisture patterns in the Tarrawarra catchment. Journal of Hydrology, 205(1-2):20–37.

Western, A. W., Grayson, R. B., Blöschl, G., Willgoose, G. R., and McMahon, T. A. 1999. Observed spatial organization of soil moisture and its relation to terrain indices. Water Resources Research, 35(3):797–810.

Wigneron, J. P., Calvet, J. C., Pellarin, T., Van de Griend, A. A., Berger, M., and Ferrazzoli, P. 2003. Retrieving near-surface soil moisture from microwave radiometric observations: current status and future plans. Remote Sensing of Environment, 85(4):489–506.

Yang, S., Yoo, S. H., Yang, R., Mitchell, K. E., van den Dool, H., and Higgins, R. W. 2007. Response of seasonal simulations of a regional climate model to high-frequency variability of soil moisture during the summers of 1988 and 1993. Journal of Hydrometeorology, 8(4):738–757.

Yu, C., Warrick, A. W., and Conklin, M. H. 1999. Derived functions of time domain reflectometry for soil moisture measurement. Water Resources Research, 35(6):1789–1796.

Zehe, E. and Blöschl, G. 2004. Predictability of hydrologic response at the plot and catchment scales: Role of initial conditions. Water Resources Research, 40(10):W10202.

Zehe, E., Becker, R., Bardossy, A., and Plate, E. 2005. Uncertainty of simulated catchment runoff response in the presence of threshold processes: Role of initial soil moisture and precipitation. Journal of Hydrology, 315(1-4):183–202.

Zehe, E., Graeff, T., Morgner, M., Bauer, A., and Bronstert, A. 2010. Plot and field scale soil moisture dynamics and subsurface wetness control on runoff generation in a headwater in the Ore Mountains. Hydrology and Earth System Sciences, 14(6):873–889.

Zhang, R., Yang, J., and Ye, Z. 1996. Solute transport through the vadose zone: A field study and stochastic analyses. Soil Science, 161(5):270–277.

Zhou, C., Liu, L., and Lane, J. W. 2001. Nonlinear inversion of borehole-radar tomography data to reconstruct velocity and attenuation distribution in earth materials. Journal of Applied Geophysics, 47:271–284.

Zinn, B. and Harvey, C. F. 2003. When good statistical models of aquifer heterogeneity go bad: A comparison of flow, dispersion, and mass transfer in connected and multivariate Gaussian hydraulic conductivity fields. Water Resources Research, 39(3):1051.

Soil moisture maps

The surface soil moisture maps presented here are a selection of the soil moisture maps that were produced for the HYDRASENS research project and along this thesis. Surface soil moisture values were retrieved using time-domain inversions focused on surface reflection, as presented in chapter 4. Soil moisture values were interpolated using ordinary kriging, with a rectangular neighboring window for the maps in Burnia (see chapter 4). These maps and others are presented in a dynamic webmap on http://sites.uclouvain.be/MappingResearch.

The following table summarizes the soil moisture data used to produce these maps. The mean $\mu_{\theta_{GPR}}$ and standard deviation $\sigma_{\theta_{GPR}}$ of soil moisture [m^{3}m^{-3}] data are presented in the last two columns.

Field	Watershed	Date	N° of points	$\mu_{\theta_{GPR}}$	$\sigma_{\theta_{GPR}}$
Walhain	Dyle	31/03/2008	1041	0.314	0.0807
Walhain	Dyle	04/07/2008	2947	0.307	0.0713
Cruchten	Alzette	13/03/2009	3572	0.309	0.1178
Keispelt	Alzette	13/03/2009	1311	0.261	0.1017
Marbaix	Dyle	19/03/2009	3999	0.108	0.0514
Walhain	Dyle	23/03/2009	4157	0.110	0.0412
Marbaix	Dyle	15/04/2009	3250	0.116	0.0488
Walsdorf	Alzette	21/07/2009	3629	0.172	0.0687
Burnia	Dyle	15/03/2010	1699	0.228	0.0670
Burnia	Dyle	18/03/2010	1586	0.234	0.0629
Burnia	Dyle	24/03/2010	1593	0.240	0.0644
Burnia	Dyle	30/03/2010	1385	0.295	0.1143
Burnia	Dyle	06/04/2010	1980	0.298	0.1153

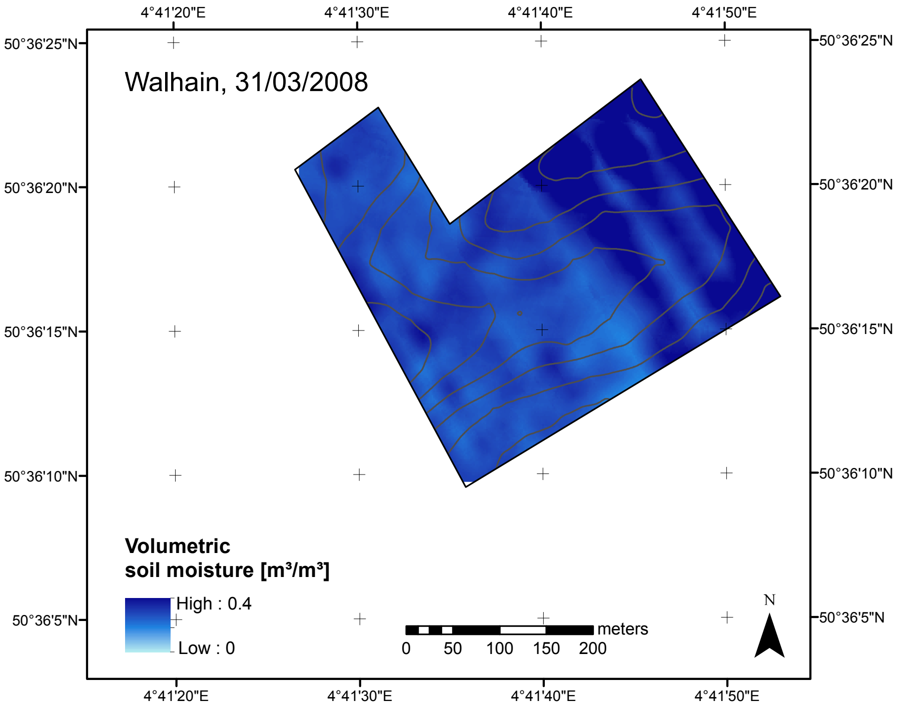
Walhain, 31/03/2008
4°41'20"E
4°41'30"E
4°41'40"E
4°41'50"E
50°36'25"N
50°36'20"N
50°36'15"N
50°36'10"N
50°36'5"N
Volumetric
soil moisture [m³/m³]
High : 0.4
Low : 0
0 50 100 150 200
meters
N

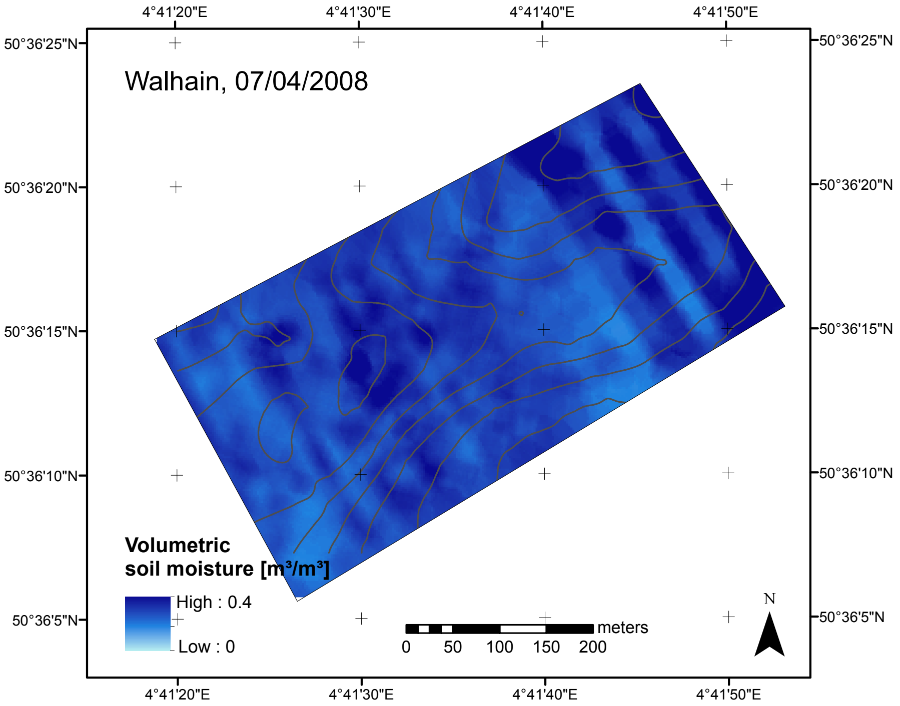
Walhain, 07/04/2008
4°41'20"E
4°41'30"E
4°41'40"E
4°41'50"E
50°36'25"N
50°36'20"N
50°36'15"N
50°36'10"N
50°36'5"N
Volumetric
soil moisture [m³/m³]
High : 0.4
Low : 0
0 50 100 150 200
meters
N

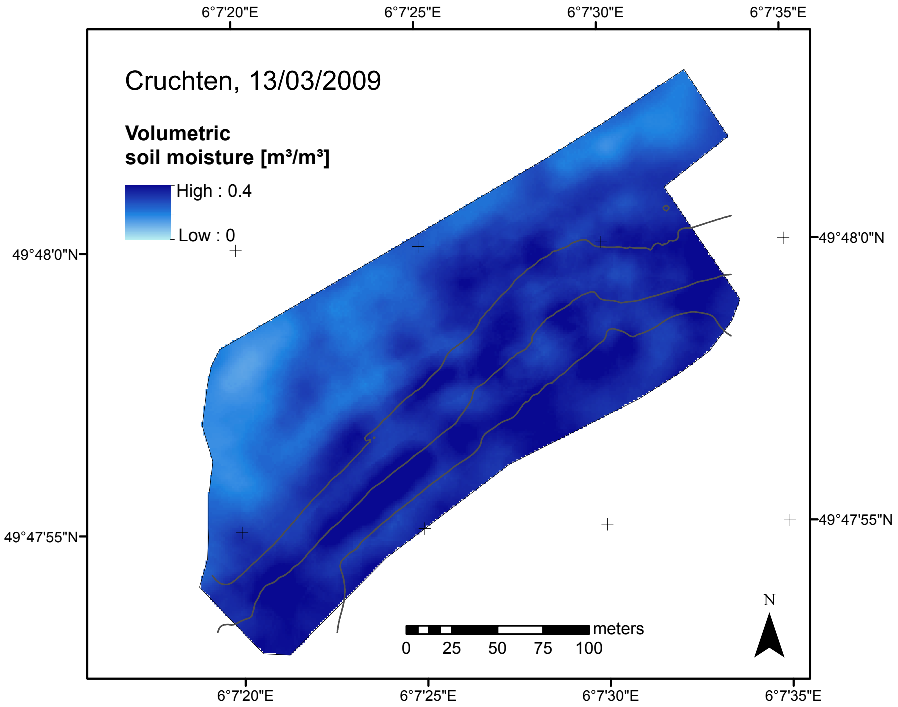
6°7'20"E
6°7'25"E
6°7'30"E
6°7'35"E
Cruchten, 13/03/2009
Volumetric soil moisture [m³/m³]
High : 0.4
Low : 0
49°48'0"N
49°47'55"N
N
meters
0
25
50
75
100

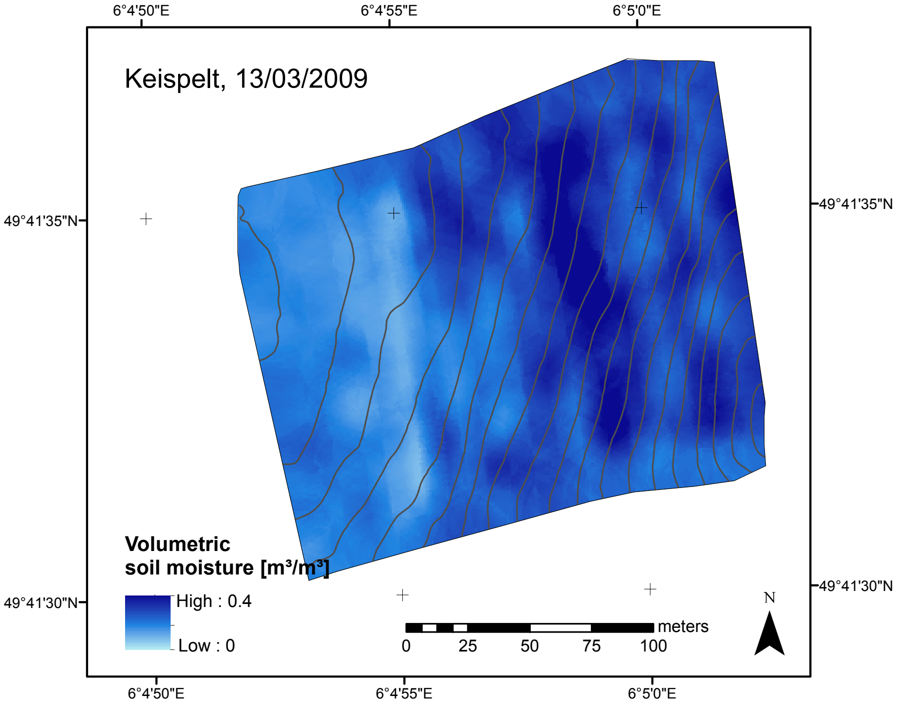
6°4'50"E
6°4'55"E
6°5'0"E
Keispelt, 13/03/2009
49°41'35"N
49°41'30"N
Volumetric soil moisture [m³/m³]
High : 0.4
Low : 0
N
meters
0
25
50
75
100

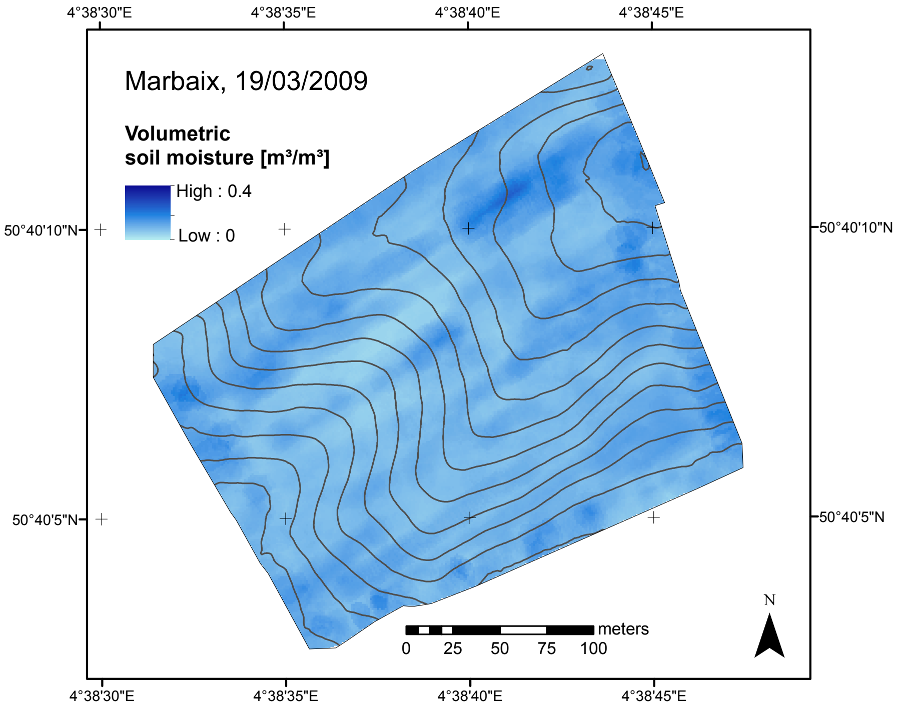
Marbaix, 19/03/2009
Volumetric soil moisture [m³/m³]
High : 0.4
Low : 0
4°38'30"E
4°38'35"E
4°38'40"E
4°38'45"E
50°40'10"N
50°40'5"N
0
25
50
75
100
meters
N

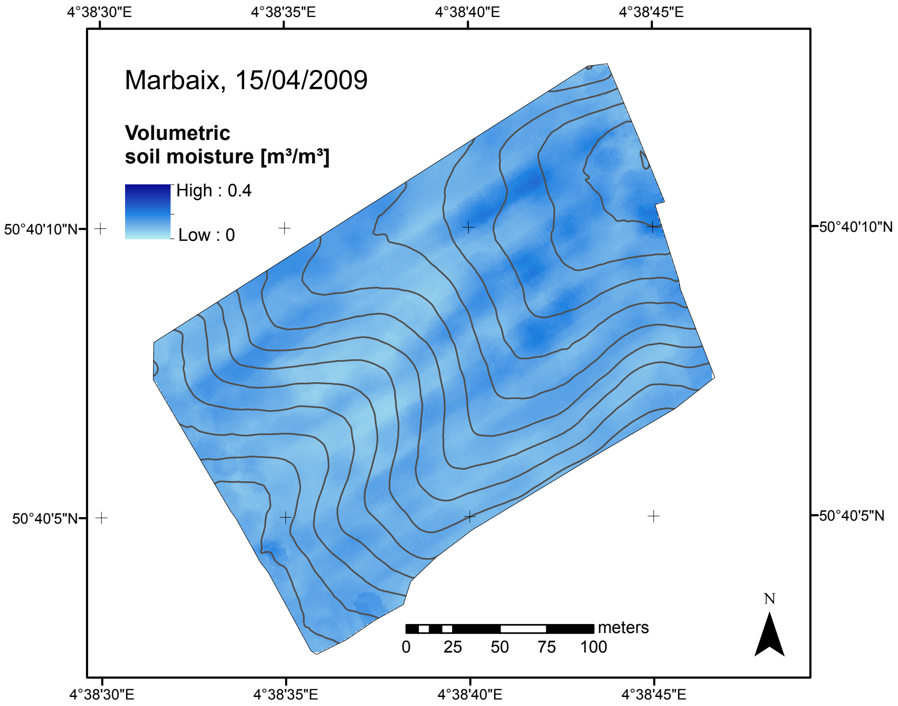
Marbaix, 15/04/2009
Volumetric soil moisture [m³/m³]
High : 0.4
Low : 0
4°38'30"E
4°38'35"E
4°38'40"E
4°38'45"E
50°40'10"N
50°40'5"N
0
25
50
75
100
meters
N

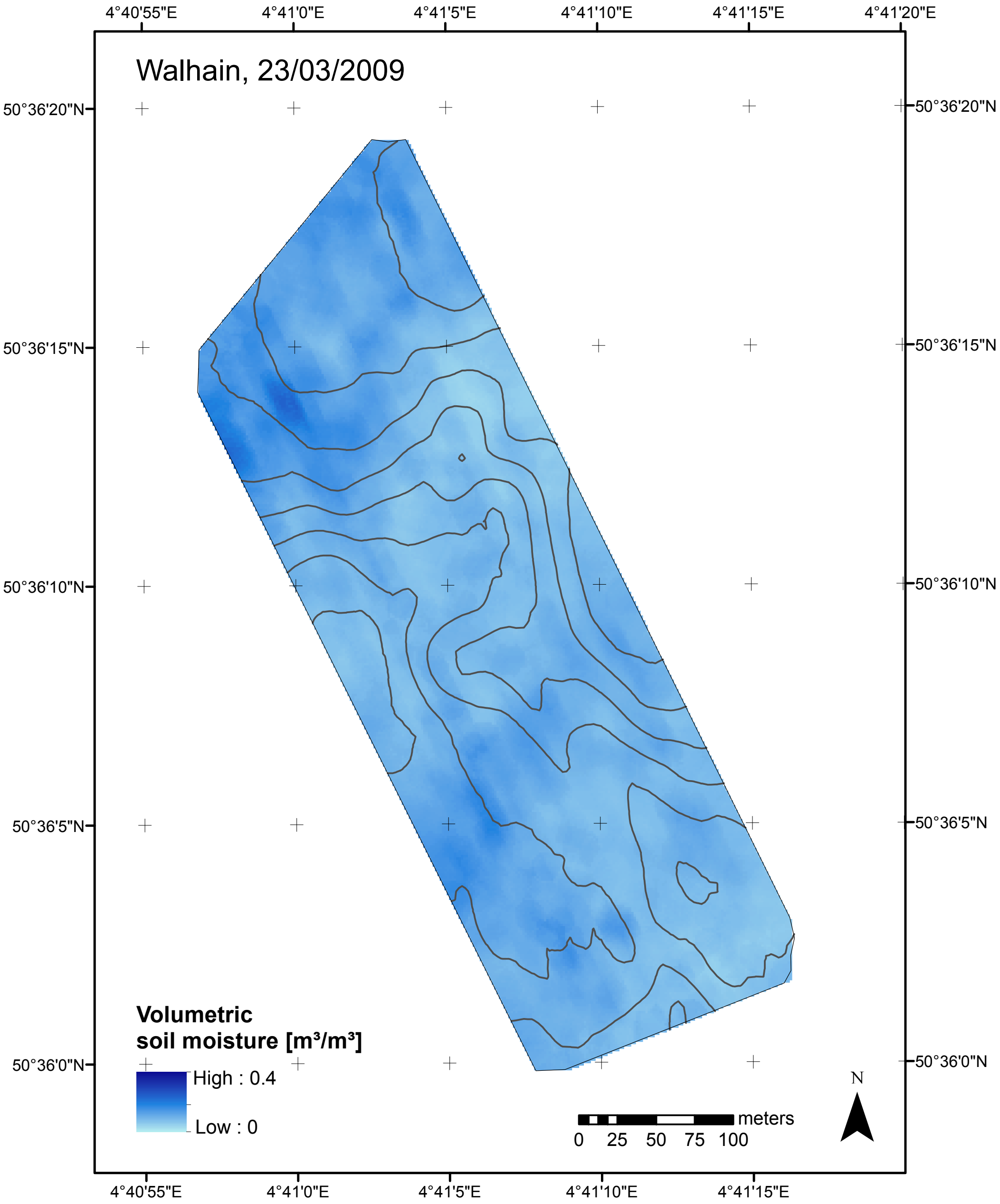
Walhain, 23/03/2009
4°40'55"E
4°41'0"E
4°41'5"E
4°41'10"E
4°41'15"E
4°41'20"E
50°36'20"N
50°36'15"N
50°36'10"N
50°36'5"N
50°36'0"N
Volumetric
soil moisture [m³/m³]
High : 0.4
Low : 0
0 25 50 75 100
meters
N

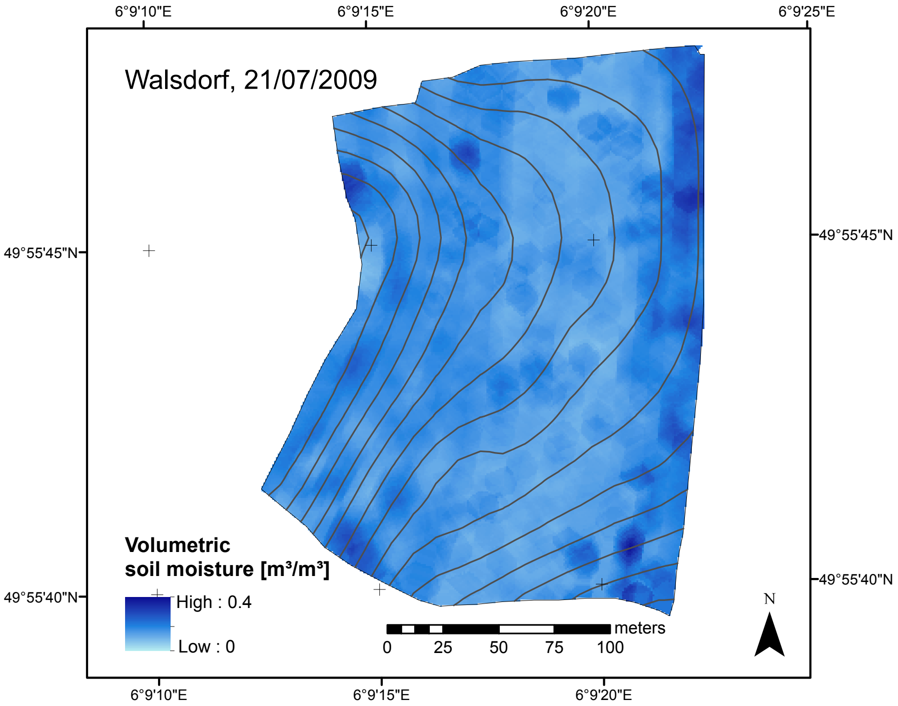
6°9'10"E
6°9'15"E
6°9'20"E
6°9'25"E
Walsdorf, 21/07/2009
49°55'45"N
49°55'45"N
49°55'40"N
49°55'40"N
Volumetric
soil moisture [m³/m³]
High : 0.4
Low : 0
0
25
50
75
100
meters
N
6°9'10"E
6°9'15"E
6°9'20"E

Burnia, 15/03/2010 to 06/04/2010

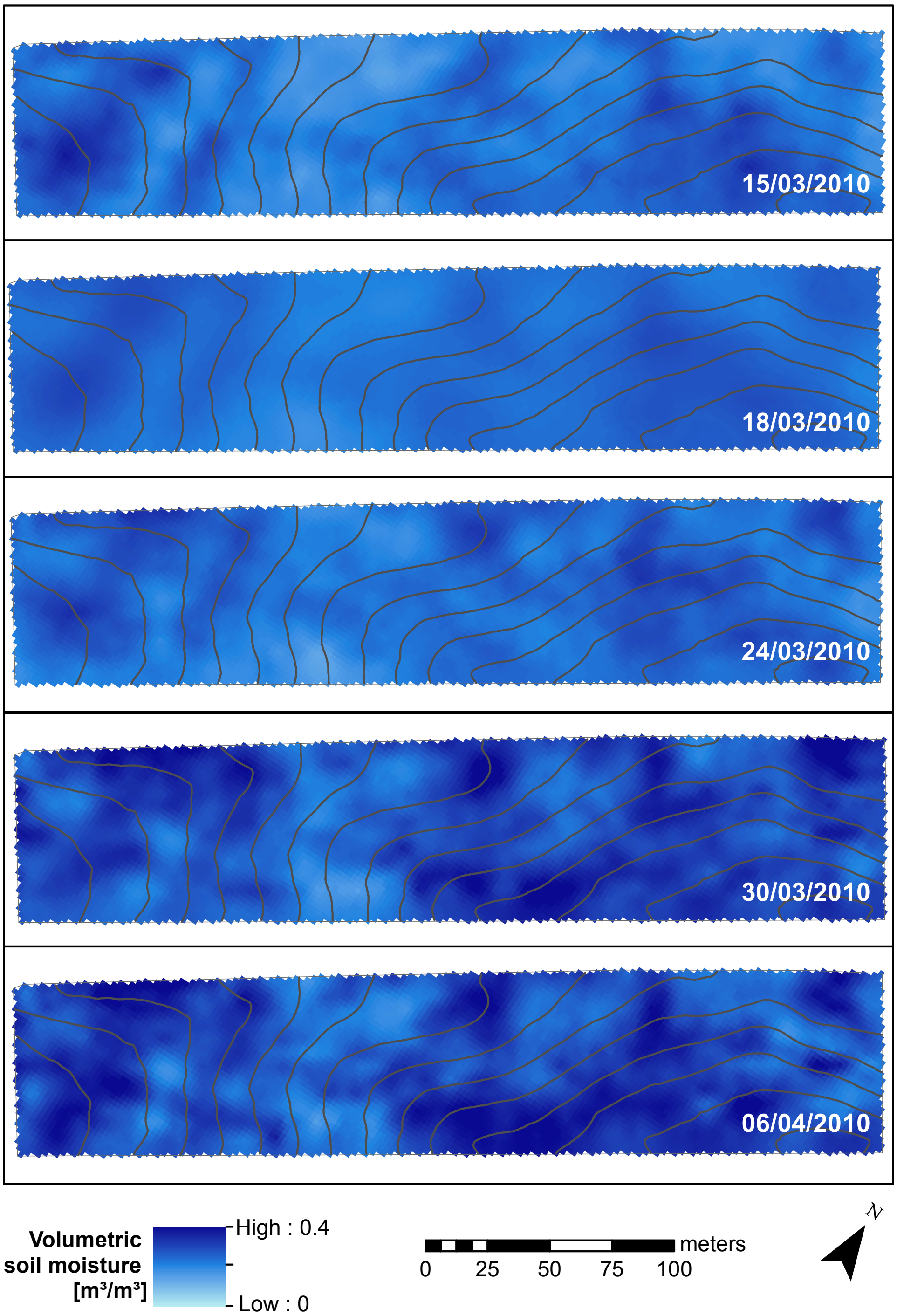

Publications and Conferences

Publications in international peer-reviewed journals

- Minet J., Lambot S., Slob E.C. and Vanclooster M. Soil surface water content estimation by full-waveform GPR signal inversion in the presence of thin layers, *IEEE Transactions on Geoscience and Remote Sensing*, **2010**, 48, 1138-1150.
- Minet J., Lambot S., Delaide G., Huisman J. A., Vereecken H. and Vanclooster M. A generalized frequency domain reflectometry forward and inverse modeling technique for soil electrical properties determination, *Vadose Zone Journal*, **2010**, 9(4), 1063-1072.
- Minet J., Wahyudi A., Bogaert P., Vanclooster M. and Lambot S. Mapping shallow soil moisture profiles at the field scale using full-waveform inversion of ground penetrating radar data, *Geoderma*, **2011**, 161, 225-237.
- Minet J., Laloy E., Lambot S. and Vanclooster M. Effect of high-resolution spatial soil moisture variability on simulated runoff response using a distributed hydrologic model, *Hydrology and Earth System Sciences*, **2011**, 15, 1323-1338.
- Patriarca C., Lambot S., Mahmoudzadeh M.R., Minet J. and Slob E.C. Reconstruction of sub-wavelength fractures and physical properties of masonry media using full-waveform inversion of proximal penetrating radar, *Journal of Applied Geophysics*, in press.
- Lievens H., Heitz S., Minet J., Lambot S., Vanclooster M., Matgen P., Hissler C., Hoffmann, L. and Verhoest N.E.C. Mapping within-field soil moisture variability with high-resolution C-band SAR and GPR, *Canadian Journal of Remote Sensing*, submitted.
- Minet J., Bogaert P., Vanclooster M. and Lambot S. Validation of ground penetrating radar full-waveform inversion for field scale soil moisture mapping, *Journal of Hydrology*, submitted.

- Vernieuwe H., De Baets B., Minet J., Pauwels V., Lambot S., Vanclooster M. and Verhoest N.E.C. Integrating coarse-scale uncertain soil moisture data into a fine-scale hydrological modelling scenario, *Hydrology and Earth System Sciences*, submitted
- Minet J., Vanclooster M. and Lambot S. Temporal stability of soil moisture patterns measured by a proximal ground penetrating radar in an agricultural field, to be submitted.

Book chapters

- Lambot S., Slob E.C., Minet J., Jadoon K.Z., Vanclooster M. and Vereecken H. Full-Waveform Modeling and Inversion of Ground Penetrating Radar Data for Non-Invasive Characterization of the Soil Hydrogeophysical Properties, in: Proximal Soil Sensing, Developments in Soil Science Series, Viscara Rossel R.A., A.B. McBratney and B. Minasny ed(s), Springer.
- Minet J., Jadoon K.Z., Jonard F., Mahmoudzadeh M.R., Tran P.A. and Lambot S. Advanced Ground Penetrating Radar for Soil Moisture Retrieval, in: Advances in Hydrologic Remote Sensing for Monitoring Global Changes, in review.

Conferences and workshops

Oral presentations

- Lambot, S., J. Minet, K. Z. Jadoon, E. C. Slob, H. Vereecken, Advanced Ground-Penetrating Radar for Digital Soil Mapping, *European Geophysical Union*, Vienna, Austria, April 2009.
- Lambot, S., J. Minet, K. Z. Jadoon, D. Moghadas, F. André, E. C. Slob, H. Vereecken, M. Vanclooster, Advanced Characterization Monitoring of Soil Water Content Salinity using Integrated, Full-Waveform Inversion of Off-Ground Ground Penetrating Radar Electromagnetic Induction, *Atelier Qualité des sols et des eaux: outils de suivi et surveillance de la variabilité spatiotemporelle*, Rabat, Morocco, January 2009.
- Lambot, S., J. Minet, E. Slob, K. Z. Jadoon, M. Vanclooster, H. Vereecken, Full-Waveform Modeling Inversion of Proximal Ground Penetrating Radar Data for Soil Hydrogeophysical Characterization, *First Global Workshop on High Resolution Digital Soil Sensing & Mapping*, Sydney, Australia, February 2008.
- Lambot, S., J. Minet, E. C. Slob, H. Vereecken, M. Vanclooster, High-Resolution, Real-Time Mapping of Surface Soil Moisture at the Field Scale using Ground Penetrating Radar, *American Geophysical Union*, San Francisco, CA, US, December 2008.

- Lievens, H., J. Minet, S. Lambot, M. Vanclooster, P. Matgen, M. Montanari, L. Hoffmann, P. Marzahn, R. Ludwig, F. Mattia, et al. Soil Moisture Retrieval Based on SAR-Derived Effective Roughness Parameters, *3rd ALOS Joint PI Symposium*, Kona, Hawaii, US, November 2009.

- Minet, J. A. Besson, M. Vanclooster, S. Lambot, Analysis of a Frequency Domain Reflectometry Forward Inverse Modelling Technique for Complete Characterization of a Water Content Profile, *European Geophysical Union*, Vienna, Austria, April 2008.

- Minet, J., S. Lambot, E. C. Slob, M. Vanclooster, Surface soil water content estimation by GPR signal inversion facing shallow soil layering, *GPR conference 2008*, Birmingham, UK, June 2008.

- Minet, J., S. Lambot, E. C. Slob, H. Vereecken, M. Vanclooster, High-resolution digital mapping of surface soil water content at the field scale using Ground Penetrating Radar, *American Geophysical Union - Spring Assembly*, Toronto, Canada, May 2009.

- Minet, J., S. Lambot, M. Vanclooster, Cartographie digitale de la teneur en eau de surface du sol à l'échelle du champ par Ground Penetrating Radar, *34èmes Journées Scientifiques du GFHN*, Aix-en-Provence, France, November 2009.

- Minet, J., S. Lambot, M. Vanclooster, Mapping of soil moisture at the field scale using full-waveform inversion of proximal Ground Penetrating Radar data, *European Geophysical Union*, Vienna, Austria, May 2010.

- Minet, J., C. Patriarca, E. C. Slob, M. Vanclooster, S. Lambot, Characterization of layered media using full-waveform inversion of proximal GPR data, *URSI International Symposium on Electromagnetic Theory - EMTS2010*, Berlin, Germany, August 2010, invited presentation.

- Minet, J., S. Lambot, M. Vanclooster, Evaluation of a proximal ground penetrating radar technique for soil moisture mapping at the field scale, *European Geophysical Union Leonardo Topical Conference*, Luxembourg, Luxembourg, November 2010.

- Minet, J., A. Wahyudi, P. Bogaert, S. Lambot, M. Vanclooster, Amélioration de la cartographie de la teneur en eau du sol mesurée par télédétection radar rapprochée grâce à l'élimination des effets de lignes par un outil géostatistique, *GFHN 2010: Transferts en milieux poreux: hétérogénéité des processus et des propriétés*, Louvain-la-Neuve, Belgium, November 2010.

- Patriarca, C., S. Lambot, M. R. Mahmoudzadeh, J. Minet, E. C. Slob, Potential of Monostatic Proximal Penetrating Radar for Non-Destructive Inspection of Concrete Structures, *10th Workshop on subsurface electromagnetic measurement*, Tokyo, Japan, October 2009.

- Vande Kerkhove, C., M. Vanclooster, S. Lambot, J. Minet, F. André, M. Lahlou, Caractérisation spatio-temporelle de la salinité dans une parcelle irriguée du Tadla, Maroc, par EM38, *Atelier Qualité des sols et des eaux: outils de suivi et surveillance de la variabilité spatiotemporelle*, Rabat, Morocco, January 2009.
- Verhoest, N., H. Lievens, J. Minet, M. Vanclooster, S. Lambot, H. Vernieuwe, B. De Baets, L. Giustarini, P. Matgen, L. Hoffmann, et al. Integrating Radar Remote Sensing, Hydrologic and Hydraulic Modelling for Surface Water Management, *Flemish Water Forum*, Antwerpen, Belgium, October 2010.

Poster presentation

- Besson A., J. Minet, M. Vanclooster, Characterization of the Soil Water Content Profile Along a Frequency Domain Reflectometry Probe using Advanced Forward Inverse Modeling Techniques. *EuroSoil*, Vienna, Austria, September 2008.
- Heitz, S., P. Matgen, H. Lievens, J. Minet, L. Pfister, L. Hoffmann, Potential of Radarsat-2-Data for Retrieving Spatially Distributed Surface Soil Moisture, *3rd Radarsat-2 Workshop*, Montreal, Canada, September 2010.
- Lievens, H., N.E.C. Verhoest, M. Vanclooster, B. De Baets, L. Hoffmann, V. Pauwels, S. Lambot, J. Minet, H. Vernieuwe, P. Matgen, et al. Integrating Radar Remote Sensing, Hydrologic and Hydraulic Modelling for Surface Water Management, *Luxembourg Earth Observation Day*, Luxembourg, November 2008.
- Minet, J., S. Lambot, E. C. Slob, M. Vanclooster, Soil Surface Water Content Estimation by Full-Waveform GPR Signal Inversion in the Presence of Thin Layers, *3rd PhD Student Day of the Graduate School ENVITAM*, Namur, Belgium, January 2010.
- Minet, J., S. Lambot, E. C. Slob, M. Vanclooster, Soil Surface Water Content Estimation by Full-Waveform GPR Signal Inversion in Presence of Thin Layers. *European Geophysical Union*, Vienna, Austria, April 2009.
- Minet, J., M. Vanclooster, S. Lambot, Real-Time Mapping of Soil Water Content using GPR, *SSSB thematic day*, Brussels, Belgium, December 2007.
- Wahyudi, A., J. Minet, P. Bogaert, S. Lambot, Geostatistical Tool for Line Effect Removal on Field Water Content Estimation using Ground Penetrating Radar (GPR), *GFHN 2010: Transferts en milieux poreux: hétérogénéité des processus et des propriétés*, Louvain-la-Neuve, Belgium, November 2010.

Summary

Soil moisture is an important state variable acting in many environmental, hydrologic and climatic processes. There is thus a pressing scientific demand for revealing the soil moisture dynamics in the biosphere at various temporal and spatial scales. Despite the huge development of remote sensing of soil moisture techniques, there is still a lack of soil moisture measurement techniques available at high spatial resolution ($\sim$ m). This thesis aimed to validate and apply advanced proximal ground penetrating radar (GPR) for soil moisture sensing at the field scale.

For field acquisition, the GPR system was mounted on a mobile platform that allowed for a fast acquisition rate at high resolution. The impact of shallow soil layering on the GPR backscattered signal was investigated in numerical and laboratory experiments and the best GPR data inversions strategies for dealing with shallow soil layering were determined. Then, coherent two-layered and continuous soil moisture profiles could be characterized in field conditions, owing to the large frequency bandwidth in which the GPR operates. The uncertainties in soil moisture sensing and mapping were comprehensively evaluated in field conditions, and the proposed GPR method appeared to be highly precise and accurate. In that respect, the GPR method showed a high repeatability for soil moisture sensing.

This advanced GPR method permitted to characterize spatiotemporal patterns of soil moisture in an agricultural field and to investigate their temporal stability. Locations showing temporal stability of field-average soil moisture could be revealed. Lastly, the effect of the spatial variability of antecedent soil moisture on runoff response using a distributed hydrologic model was studied in various field and moisture conditions. Benefiting from an unprecedented spatial resolution, the proposed GPR method bridges the scale gap between large-scale remote sensing instruments and small-scale invasive sensors for an accurate soil moisture determination.